Title

Disentangling physical and biological drivers of optical signals for improved monitoring of evergreen needleleaf photosynthesis

Author

Pierrat, Zoe Amie

Publication Date
2023

UNIVERSITY OF CALIFORNIA
Los Angeles

Disentangling physical and biological drivers of optical signals for improved monitoring of evergreen needleleaf photosynthesis

A dissertation submitted in partial satisfaction
of the requirements for the degree
Doctor of Philosophy in Atmospheric and Oceanic Sciences

by

Zoe Amie Pierrat

2023

ABSTRACT OF THE DISSERTATION

Disentangling physical and biological drivers of optical signals for improved monitoring of evergreen needleleaf photosynthesis

by

Zoe Amie Pierrat
Doctor of Philosophy in Atmospheric and Oceanic Sciences
University of California, Los Angeles, 2023
Professor Jochen P. Stutz, Chair

The largest source of uncertainty in global climate models is terrestrial carbon cycle feedbacks. One of the most important but most poorly understood vegetation types in the global carbon cycle is evergreen needleleaf forests (ENFs). To address this challenge, a growing appreciation for the stress physiology of photosynthesis has inspired emerging techniques to detect ENF photosynthetic activity with optical signals. This includes the use of solar-induced chlorophyll fluorescence (SIF), a small light signal emitted by plants during the photosynthetic process. SIF has shown a marked improvement over traditional reflectance-based vegetation indices in tracking ENF photosynthesis. However, SIF, as well as other optical signals, in ENF are complicated by photon-plant interactions over complex canopy structures (physical) and unique adaptations to deal with the seasonal stress of winter while retaining their needles (biological).

In this dissertation, we identify the physical and biological drivers of optical signals in ENF and connect remote sensing observations with physiological processes to improve monitoring of evergreen needleleaf photosynthesis. In Chapter 2, we provide a broad overview

for non-specialists of the biological basis for using optical signals to track evergreen needleleaf photosynthesis. We then explore these topics in more detail by using tower-based remote sensing data across four ENF sites which span the climatic gradient experienced by ENF (details in Chapter 3). In Chapters 4 and 5 we zoom in to a single site in Canada and explore the temporal dynamics of different optical metrics and their biological underpinnings. In Chapter 6 we then show how to combine multiple metrics across multiple sites to improve predictions of forest carbon uptake.

Ultimately this work advances our understanding of ENF photosynthesis and our ability to predict the fate of ENFs in a changing climate. Future work will help scale and integrate the understandings gleaned in this dissertation to satellite and modeling frameworks.

The dissertation of Zoe Amie Pierrat is approved.

Christian Frankenberg

Marcelo Chamecki

Ulli Seibt

Jochen P. Stutz, Committee Chair

University of California, Los Angeles

2023

To Mother Earth

"I always knew there was an order to this
The wind in the trees whispering mathematics"
- Willow Smith (curious/furious)

TABLE OF CONTENTS

LIST OF FIGURES

LIST OF TABLES

ACKNOWLEDGMENTS

Funding:

I thank the following grants and organizations for their financial contributions to the material presented in this dissertation.

National Science Foundation Graduate Research Fellowship (Grant No. DGE-1650604 and DGE2034835). National Science Foundation Macrosystems Biology and NEON-Enabled Science (Award 1926090). National Science Foundation Division of Environmental Biology (Award 1929709). National Science Foundation Macrosystems Biology program (awards EF-1065029 and EF-1702697). The National Ecological Observatory Network is a major facility fully funded by the National Science Foundation. Any opinion, findings, and conclusions or recommendations expressed in this material are those of the authors(s) and do not necessarily reflect the views of the National Science Foundation.

National Aeronautics and Space Administration Earth Science Division IDS (awards 80NSSC17K0108 at UCLA, 80NSSC17K0110 at JPL). National Aeronautics and Space Administration ABoVE programs (Award 80NSSC19M0130). National Aeronautics and Space Administration ABoVE (Award 80NSSC19M0129). National Aeronautics and Space Administration OCO Science team projects (Award 80NSSC18K0895). National Aeronautics and Space Administration Postdoctoral Program at the Jet Propulsion Laboratory, administered by Oak Ridge Associated Universities under contract with NASA.

I acknowledge the following Canadian organizations which helped support and data collection efforts in Canada. The Canadian Space Agency and Natural Sciences and Engineering Research Council of Canada (NSERC). Canada Research Chairs and Natural Sciences and Engineering Research Council Discovery Grants programs. Global Institute for Water Security, University of Saskatchewan.

Scientific Contributions:

I would like to thank my many collaborators and co-authors for their time, energy, and effort in contributing to the work presented in this dissertation. This dissertation was made possible through collaborative efforts in data collection, scientific input, funding acquisition, writing, and editing. Thank you to: Alan Barr, Jacob Bortnik, David R. Bowling, Rui Cheng, Christian Frankenberg, Katja Grossmann, Jeremy A. Hoyne Grosvenor, Warren Helgason, Bruce Johnson, Colin Laroque, Barry A. Logan, Troy Magney, Andrew J. Maguire, Magali F. Nehemy, Sara E. Nelson, Alexander Norton, Christoforos Pappas, Nicholas C. Parazoo, Alexandra Ramirez, Mukund Rao, Andrew D. Richardson, Alexandre Roy, Ulli Seibt, Oliver Sonnentag, Jochen Stutz, Anneka F. Williams, and Christopher Y.S. Wong.

Additionally, I thank the National Ecological Observatory Network staff and technicians for their efforts in support of this work. Their efforts enabled the collection of data presented in this dissertation.

I thank my science friends and organizations for their support in my educational journey. Specifically from my graduate education I would like to thank the Society for Gender Equity in Geoscience, the Center for Diverse Leadership in Science, The UCLA Mildred E. Mathias Botanical Garden, and the Fluxcourse 2022 cohort and instructors. From my undergraduate education I would like to thank the Colorado College Physics Department, the Boulder Solar Research Experience for Undergraduates Program, and Frontiers Abroad.

Personal:

I would like to thank my friends and family for everything they have done for me. Specifically I would like to thank my parents Julie and Marc Pierrat, my grandparents Lyn and George Kutzelman, my fabulous roommate Drew Ceglinski, my wonderful girlfriend Payton Rund, and my perfect cat Nova.

VITA

2013–2017	BA in Physics: Environmental Emphasis, Minor in Chemistry, Colorado College
2018–2020	MS in Atmospheric and Oceanic Sciences, The University of California, Los Angeles

PUBLICATIONS

Z. A. Pierrat, M. F. Nehemy, A. Roy, T. Magney, C. Parazoo, C. Laroque, C. Pappas, O. Sonnentag, D. R. Bowling, U. Seibt, A. Ramirez, W. Helgason, A. Barr, and J. Stutz. Tower-based remote sensing reveals mechanisms behind a two-phased spring transition in a mixed-species boreal forest. *Journal of Geophysical Research: Biogeosciences*, 2021.

Z. A. Pierrat, T. S. Magney, N. C. Parazoo, K. Grossmann, D. R. Bowling, U. Seibt, B. Johnson, W. Helgason, A. Barr, J. Bortnik, A. Norton, A. Maguire, C. Frankenberg, J. Stutz. Diurnal and Seasonal Dynamics of Solar-Induced Chlorophyll Fluoresence, Vegetation Indices, and Gross Primary Productivity in the Boreal Forest. *Journal of Geophysical Research: Biogeosciences,* 2022

Z. A. Pierrat, J. Bortnik, B. Johnson, A. Barr, T. Magney, D. R. Bowling, N. Parazoo, C. Frankenberg, U. Seibt, J. Stutz. Forests for forests: combining vegetation indices with solar-induced chlorophyll fluoresence in random forest models improves gross primary productivity prediction in the boreal forest. *Environmental Research Letters*, 2022

Z. A. Pierrat, T. Magney, R. Cheng, A. J. Maguire, C. Y. S. Wong, M. F. Nehemy, M. Rao, S. E. Nelson, A. F. Williams, J. A. H. Grosvenor, K. R. Smith, J. S. Reblin, J. Stutz, A. D. Richardson, B. A. Logan, D. R. Bowling. The biological basis for using optical signals to track evergreen needleleaf photosynthesis. *In review at BioScience*

CHAPTER 1

Introduction

1.1 Motivation and Science Questions

Carbon cycle feedbacks are the largest source of uncertainty in future climate projections. These carbon cycle uncertainties are largely driven by uncertainties in terrestrial ecosystem feedbacks (Friedlingstein et al., 2014, 2022). Among the most poorly understood are evergreen needleleaf forests (ENFs) which store a significant amount of carbon (an uptake of 2 billion tons of CO2 each year, Köhl et al., 2015) and are one of the vegetation types most sensitive to environmental change (Thurner et al., 2014; Bonan, 2008). Therefore, understanding environmental controls on ENF productivity is critical to predicting the future of these forests and their role in the global carbon cycle (Anav et al., 2015; Parazoo et al., 2018).

Climate change has progressively altered the winter environment of ENFs with increased temperature, altered precipitation, and earlier snowmelt in many locations (Bowling et al., 2018). These changes have led to an earlier spring green-up across the northern hemisphere (Barichivich et al., 2013; Piao et al., 2011). This earlier spring onset and longer growing season could lead to increased total ecosystem carbon uptake, or to an earlier depletion of water resources and restricted carbon uptake (Trahan and Schubert, 2016). Therefore, improved understanding of the spring onset, drivers of this onset, and plant's response to water stress is critical for understanding the future of this ecosystem. Despite it's importance, climate models currently fail to accurately predict the onset of spring photosynthesis (Commane et al., 2017; Peng et al., 2014; Parazoo et al., 2018; Richardson et al., 2010). This is partly due to difficulties in accurately measuring the onset of spring photosynthesis and partly due to uncertainties in understanding the environmental controls on the timing and rate of spring photosynthetic recovery (Jeong et al., 2011, 2017).

Optical metrics are a powerful tool for understanding plant productivity and environmental controls on productivity across space and time (Frankenberg and Berry, 2017; Gamon et al., 1997, 2016; Jeong et al., 2017; Tucker, 1979). However, traditional optical remote sensing measures sensitive to canopy greenness often fail to predict photosynthetic carbon uptake (also known as gross primary productivity, GPP) in ENF which remain annually verdant (Magney et al., 2019a; Walther et al., 2016; Jeong et al., 2017). In contrast, satellite observations of solar-induced chlorophyll fluorescence (SIF) have been shown to be an excellent proxy for GPP across a variety of ecosystems (Frankenberg and Berry, 2017; Sun et al., 2018, 2017). In ENFs, structurally complex canopies, spatial inhomogeneities, varied vegetation cover, and high solar zenith angles complicate remotely sensed observations and make these systems particularly difficult to study from satellite observations alone. As a result, small-scale leaf and tower-based measurements have highlighted nuance to the relationship between SIF and GPP, thereby raising questions over its utility as a proxy for GPP (Maguire et al., 2020; Marrs et al., 2020; Kim et al., 2021). In summary, photon-plant interactions over complex canopy structures (*physical*) create significant challenges for interpreting remotely sensed optical signals and connecting them to plant productivity (*biological*).

Tower-based spectrometer systems can take measurements at finer spatial and temporal scales than spatially averaged once-per-day satellite overpasses, but not as fine as leaf level measurements (Grossmann et al., 2018; Gamon, 2015). Therefore, they allow for a deeper investigation of the physical and biological drivers of optical metrics while aiding our ability to scale measurements from the leaf/needle to orbit. Tower-based SIF spectrometer systems have already provided valuable insights into the SIF-GPP relationship in cropping (Magney et al., 2019b; He et al., 2020), temperate (Kim et al., 2021; Yang et al., 2017, 2015), and sub-alpine evergreen systems (Magney et al., 2019a; Cheng et al., 2020; Seyednasrollah et al., 2020). However, there is a significant need for such measurements in ENFs, particularly in the boreal ecozone where site-level observations are extremely limited.

By disentangling the physical and biological drivers of optical signals in evergreen needleleaf forests with tower-based spectrometer systems, this dissertation builds a framework for understanding and monitoring evergreen needleleaf photosynthesis in a changing climate. Specifically, I seek to answer:

1. What environmental conditions drive changes in photochemical and biochemical regulation of photosynthesis in ENFs?
2. What are the fundamental biological and physical processes influencing observed optical metrics?
3. How do the relationships among different optical metrics and underlying biologic processes change across varying temporal scales?
4. How can we improve our ability to track ENF photosynthesis by combining optical metrics?

1.2 Outline

In order to answer my main motivating science questions, this dissertation is structured as follows:

Chapter 2 gives a broad overview designed for non-specialists on the biological basis for using optical signals to track evergreen needleleaf photosynthesis. This overview is based on Pierrat et al., 2023 *in review*, and summarizes how fundamental plant biological and biophysical processes control the fate of photons from leaf to globe, ultimately enabling remote estimates of ENF photosynthesis. We demonstrate this using data across four ENF sites spanning a broad range of environmental conditions and link leaf- and stand-scale observations of photosynthesis (i.e., needle biochemistry and flux towers) with tower- and satellite-based remote sensing. This overview summarizes the more detailed knowledge gleaned in Chapters 4, 5, and 6 and places the work in the broader context of multi-scale observations for an integrated understanding of evergreen needleleaf biology.

Chapter 3 provides a methodological overview for data used in this dissertation, including that used in Chapters 2, 4, 5, & 6. We describe the field locations in more detail including elevation, mean annual temperature, precipitation, over and understory vegetation, and soil characteristics. We also describe the instrumentation used to collect tower-based remote sensing data (PhotoSpec) and a broad overview of the processing details. We describe the meteorological data available at the sites, including eddy-covariance data, soil moisture and temperature, and air temperature data. Here, we provide the details of eddy-covariance gap-filling and partitioning to get to GPP.

Chapter 4 focuses on the spring transition in the boreal forest and is based on Pierrat et al. (2021a). Because the boreal forest is a major contributor to the global climate system, and a key biome for ENF, reducing uncertainties in how this forest will respond to a changing climate is critical. One source of uncertainty is the timing and drivers of the spring transition. Remote sensing can provide important information on this transition, but persistent foliage greenness, seasonal snow cover, and a high prevalence of mixed forest stands (both deciduous and evergreen species) complicate interpretation of these signals. We collected tower-based remotely sensed data (reflectance-based vegetation indices and SIF), stem radius measurements, gross primary productivity, and environmental conditions in a boreal mixed forest stand. Evaluation of this data set shows a two-phased spring transition. The first phase is the reactivation of photosynthesis and transpiration in evergreens, marked by an increase in relative SIF, and is triggered by thawed stems, warm air temperatures, and increased available soil moisture. The second phase is a reduction in bulk photoprotective pigments in evergreens, marked by an increase in the Chlorophyll-Carotenoid Index. Deciduous leaf-out occurs during this phase, marked by an increase in all remotely sensed metrics. The second phase is controlled by soil thaw. Our results demonstrate that remote sensing metrics can be used to detect specific physiological changes in boreal tree species during the spring transition. The two-phased transition explains inconsistencies in remote sensing estimates of the timing and drivers of spring recovery. Our results imply that satellite-based observations will improve by using a combination of vegetation indices and SIF, along with species distribution information.

Chapter 5 focuses on the diurnal and seasonal dynamics of SIF, vegetation indices, and gross primary productivity in the boreal forest and is based on Pierrat et al. (2022a). Remote sensing of SIF provides a powerful proxy for GPP. It is particularly promising in boreal ecosystems where seasonal downregulation of photosynthesis occurs without significant changes in canopy structure or chlorophyll content. The use of SIF as a proxy for GPP is complicated by inherent non-linearities due to both physical (illumination effects) and ecophysiological (light use efficiencies) controls at fine spatial (tower/leaf) and temporal (half-hourly) scales. To study the SIF-GPP relationship, we investigated the diurnal and seasonal dynamics of continuous tower-based measurements of SIF, GPP, and common vegetation indices at the Southern Old Black Spruce Site (SOBS) in Saskatchewan, CA over the course of two years. We find that SIF outperforms other vegetation indices as a proxy for GPP at all temporal scales but shows a non-linear relationship with GPP at a half-hourly resolution. At small temporal scales, SIF and GPP are predominantly driven by light and non-linearity between SIF and GPP is due to the light saturation of GPP. Averaged over daily and monthly scales, the relationship between SIF and GPP is linear due to a reduction in the observed PAR range. Seasonal changes in the light responses of SIF and GPP are driven by changes in light-use-efficiency which co-vary with changes in temperature, while illumination and canopy structure partially linearize the SIF-GPP relationship. Additionally, we find that the SIF-GPP relationship has a seasonal dependency. Our results help to clarify the utility of SIF for estimating carbon assimilation in boreal forests.

Chapter 6 combines SIF and VIs using random forest models to improve GPP prediction across ENF sites and is based on Pierrat et al. (2022b). The success of remote sensing measurements can be attributed to their ability to capture valuable information on plant structure (physical) and function (physiological), both of which impact GPP. However, no single remote sensing measure provides a universal constraint on GPP and the relationships between remote sensing measurements and GPP are often site specific, thereby limiting broader usefulness and neglecting important nuances in these signals. Improvements must be made in how we connect remotely sensed measurements to GPP, particularly in boreal ecosystems which have been traditionally challenging to study with remote sensing. In this chapter we improve GPP prediction by using random forest models as a quantitative framework that incorporates physical and physiological information provided by SIF and vegetation indices (VIs). We analyze 2.5 years of tower-based remote sensing data (SIF and VIs) across two field locations at the northern and southern ends of the North American boreal forest. We find (a) remotely sensed products contain information relevant for understanding GPP dynamics, (b) random forest models capture quantitative SIF, GPP, and light availability relationships, and (c) combining SIF and VIs in a random forest model outperforms traditional parameterizations of GPP based on SIF alone. Our new method for predicting GPP based on SIF and VIs improves our ability to quantify terrestrial carbon exchange in boreal ecosystems and has the potential for applications in other biomes.

Chapter 7 closes by revisiting my main motivating science questions and summarizing the work presented in this dissertation. I discuss future research directions inspired by this work and long-term aspirations. Ultimately advancements in vegetation remote sensing, such as those presented in this dissertation, lead to improved monitoring of ecosystems and reduced uncertainty in their role in the global carbon cycle.

CHAPTER 2

The biological basis for using optical signals to track evergreen needleleaf photosynthesis

2.1 Why should we care about tracking evergreen needleleaf photosynthesis?

Evergreen needleleaf forests (ENFs) are one of the largest forest biomes in the world and are an important sink in the global carbon cycle (Smith et al., 2009). Notably, the carbon sequestration potential of ENFs is high, with an uptake of ∼2 billion tons of CO_2 each year (Köhl et al., 2015). They also provide critical ecosystem services, including climate regulation, wildlife habitat, sustenance, and timber (Keenan et al., 2015; Felipe-Lucia et al., 2018). Anthropogenic climate change has shifted baseline environmental conditions for ENFs, but the impacts of these changes on carbon budgets and ecosystem services remain uncertain (Liu et al., 2020a). Rising temperature and carbon fertilization have increased canopy greenness in some ENFs, suggesting enhanced potential for photosynthetic carbon uptake (Wang and Friedl, 2019; Berner et al., 2020). However, the future of ENF carbon assimilation is threatened by a myriad of climate-related factors including widespread drought (Bentz et al., 2019; Anderegg et al., 2020; Trugman et al., 2021), changes to growing season length, increased wildfire potential, and biotic agents of mortality (Anderegg et al., 2015; Kautz et al., 2017). In regions where warmer springs and drier summers are becoming more prevalent, ENFs have become more productive in the spring and less productive in the summer/fall, ultimately impacting long-term trends in the seasonality, magnitude, and sign of net carbon exchange

(Buermann et al., 2018; Fisher et al., 2018; Butterfield et al., 2020). Our understanding of the ENF carbon cycle is encumbered by limited observations of plant photosynthesis (i.e., carbon assimilation) at high spatio-temporal resolutions globally. Consequently, our predictions of the future carbon cycle remain highly uncertain, with some Earth System Models (ESMs) suggesting that the terrestrial biosphere may even transition to a net carbon source by the end of the twenty-first century (Friedlingstein et al., 2022).

Optical remote sensing plays a critical role in detecting changes in evergreen photosynthesis and can provide an important constraint on our ability to predict and understand the future of ENFs (Schimel et al., 2019). Remote sensing can help scale leaf- and site-level observations across both space and time, enabling more robust quantification of ENF photosynthesis across the globe. Optical remote sensing is sensitive to both changes in plant physiology and the biophysics of how incident photons are reflected or emitted from vegetation (Zeng et al., 2022).

The goal of this Overview is to review the fundamental biological and physical processes that inform the use of optical remote sensing data for tracking photosynthesis in ENFs. We provide non-specialists with an understanding of how these data can be used to better inform our understanding of the ENF carbon cycle. To do this, we use a suite of data (Figure 2.1) collected from four ENF sites spanning a climate gradient across North America (Figure 2.2). We begin by reviewing the mechanisms controlling the diurnal and seasonal dynamics of photosynthesis in ENFs and the physical and physiological controls on the fate of absorbed light at the leaf/needle level (Section 2.2). These biological mechanisms are then scaled to the canopy level using a variety of different measurement approaches. We show how an integrated measurement approach can provide a more complete picture of carbon assimilation at the canopy scale (Section 2.3). We further scale these measurements and their biologic underpinnings to the biome level with satellite-based remote sensing (Section 2.4). We end this overview by discussing the need for multi-scale and multi-disciplinary research - spanning from leaf-level biology to physics and remote sensing - for advancing our understanding of the processes underpinning global change impacts on ENFs (Section 2.5).

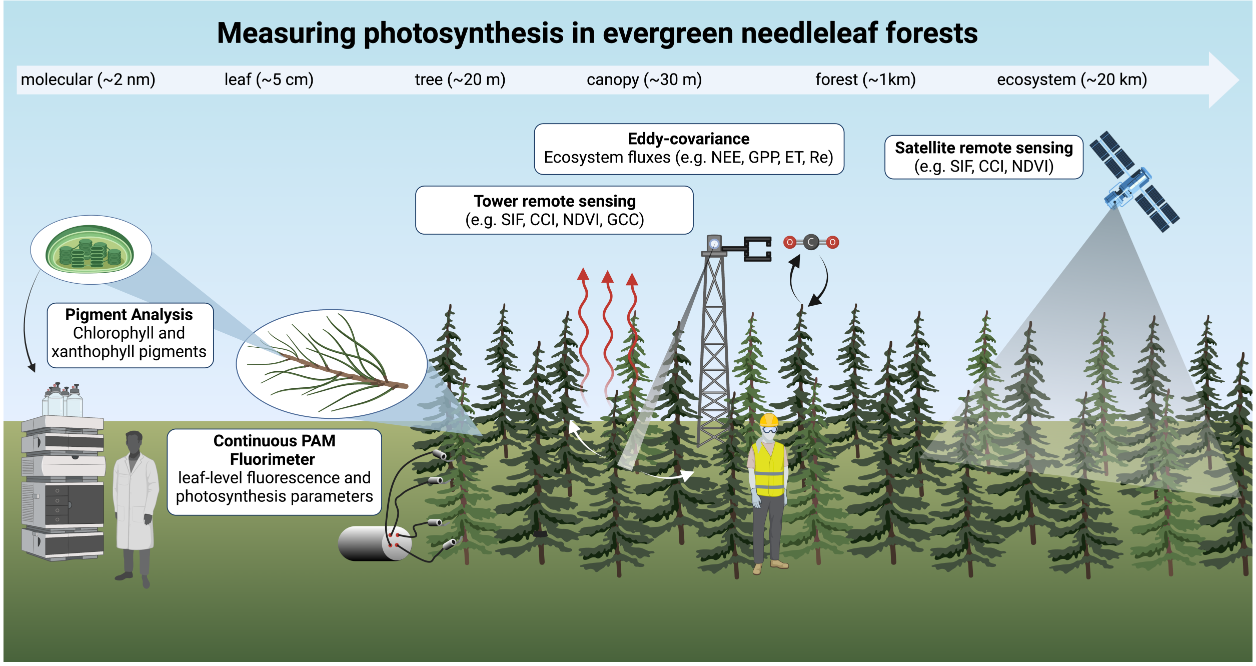

Figure 2.1: Summary of ways to measure ENF photosynthesis from the molecular to ecosystem scale and data types highlighted in this overview. Pigment analyses provides direct insight into light absorption and partitioning but has limited temporal resolution (samples must be collected and processed manually) (Section 2.2). Continuous pulse amplitude modulated (PAM) fluorometry provides leaf-level information on the photosynthetic activity of plant photosystems including information on the partitioning of light energy among different pathways (Section 2.2). Tower-based remote sensing provides proxies for many variables related to photosynthetic carbon uptake including forest chlorophyll and xanthophyll pigment content and net carbon uptake at a high spatiotemporal resolution (half-hourly, tree-canopy scale) (Section 2.3). Eddy-covariance derived CO_2 fluxes are the best available measure for carbon uptake via photosynthesis (gross primary production, GPP) at the canopy scale and can be derived at a half-hourly resolution (Section 2.3). Satellite-based remote sensing is the only way we can detect photosynthesis at large spatial scales but is limited in its spatial and temporal resolutions (Section 2.4).

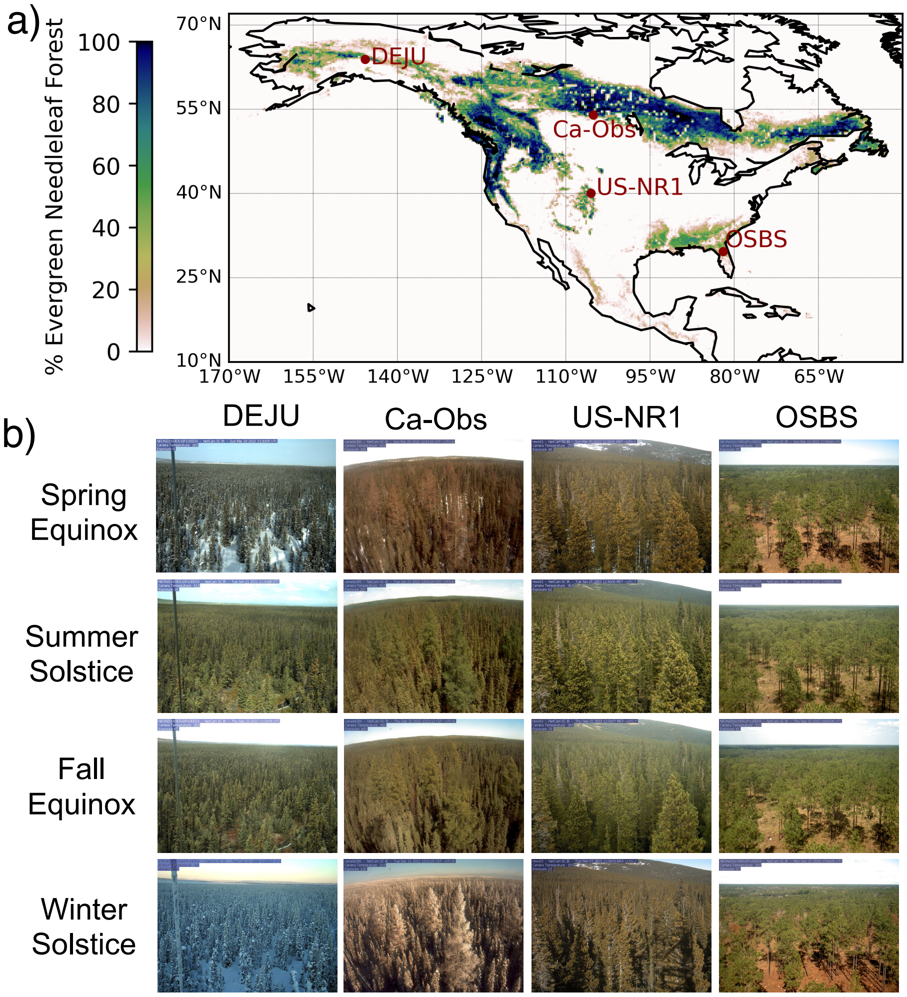

Figure 2.2: Overview of ENF sites used in this overview. Part a) shows the spatial extent and percent cover of ENFs across North America, as well as the locations of the four field sites used in this study. ENF percent cover was derived from the Moderate Resolution Imaging Spectroradiometer (MODIS) International Geosphere-Biosphere Programme (IGBP) Land Cover 2019 dataset at 500m resolution (Friedl and Sulla-Menashe, 2019). The four sites include boreal forest locations in Alaska (DEJU, mean annual temperature = 0.4 °C, latitude = 63.9 °N) and Saskatchewan, Canada (Ca-Obs, 1.3 °C, 54.0 °N), a high elevation forest in Colorado (US-NR1, 2.8 °C, 40.0 °N), and a longleaf pine forest in Florida (OSBS, 21.1 °C, 29.7 °N). Part b) shows images of the four sites across seasons highlighting that canopy structure does not change with season in ENFs. Images are obtained from the PhenoCam Network (https://phenocam.nau.edu/webcam/) and brightened for clarity.

2.2 Needle-scale mechanisms controlling the daily and seasonal physiology of evergreen needleleaf forests

Photosynthesis uses light from the sun to drive the conversion of carbon dioxide and water into energy-rich organic compounds (sugars and starch). Through this process, plants use solar power to sustain nearly all life on earth. Light, temperature, and the availability of water control photosynthesis (Figure 2.3, Berry and Bjorkman, 1980; Farquhar et al., 1980). Within a daily cycle, a plant's ability to photosynthesize varies with changes in sunlight, temperature, and evaporative demand. Over days to weeks, plants acclimate to their environment and allocate resources to optimize photosynthesis during the active season, thus adjusting to seasonal changes (e.g., Logan et al., 1998; Huxman et al., 2003). To properly explain the mechanisms controlling the daily and seasonal photosynthetic physiology of ENFs, we begin by discussing the fate of sunlight.

Light travels from the sun through Earth's atmosphere and into a forest canopy. Only a portion of the sun's electromagnetic spectrum can be used to drive photosynthesis, known as Photosynthetically Active Radiation (PAR, 400-700 nm). A portion of PAR is incident upon soil, branches, and other non-photosynthesizing media, whereas the remaining fraction of this light ($f\mathrm{PAR}_{\mathrm{chl}}$) is absorbed by chlorophyll molecules in foliage and is known as absorbed photosynthetically active radiation ($\mathrm{APAR}_{\mathrm{chl}}$) such that:

$$\mathrm{APAR}_{\mathrm{chl}} = f\mathrm{PAR}_{\mathrm{chl}} \times \mathrm{PAR} \tag{2.1}$$

Chlorophyll molecules have a unique spectral signature in that they reflect more light in the green region of the spectrum and absorb strongly in the red and blue, thus plants appear green. Optical metrics can approximate the fraction of light absorbed by chlorophyll ($f\mathrm{PAR}_{\mathrm{chl}}$) by probing the ratios of reflected light in the red, blue and green spectral regions (more in Section 2.3). While $\mathrm{APAR}_{\mathrm{chl}}$ can vary seasonally due to changes in PAR, in ENFs,

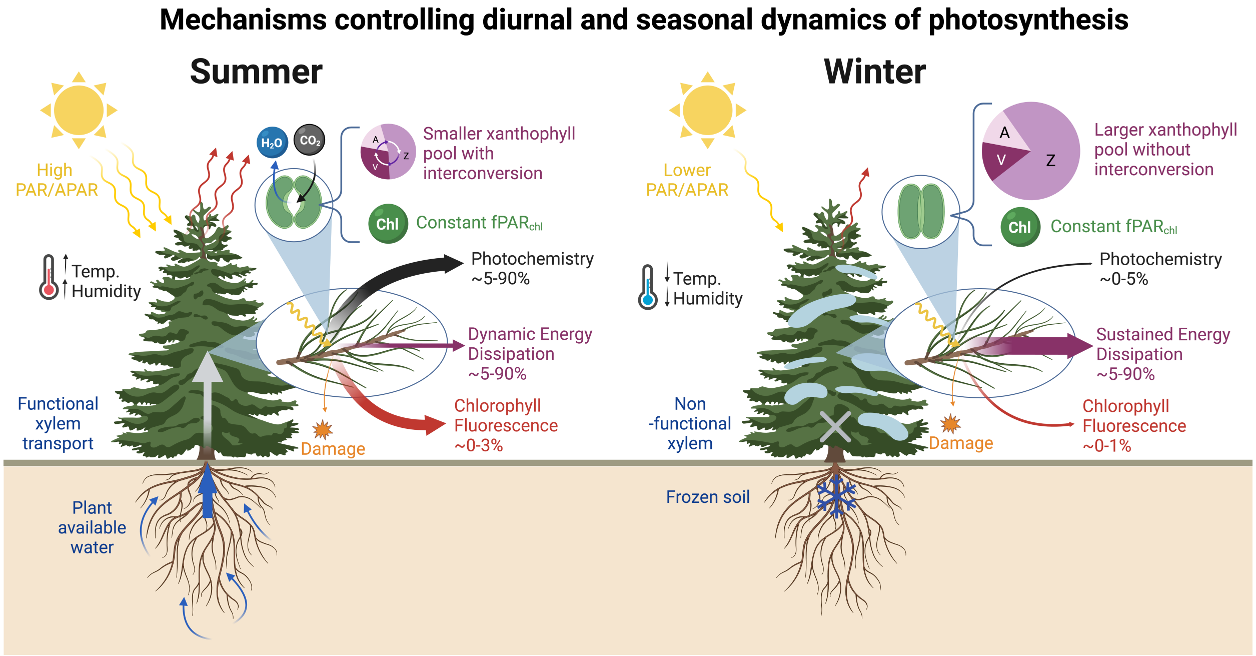

Figure 2.3: Overview of the mechanisms controlling the daily and seasonal physiology of evergreen needleleaf forests as well as their environmental controls. The summer and winter examples highlight the biological mechanisms associated with most extreme environmental conditions ENFs experience at higher latitudes and altitudes.

$f\mathrm{PAR}_{\mathrm{chl}}$ tends to remain seasonally constant. This is because seasonal changes in chlorophyll content (Figure 2.4) and canopy structure are small. Therefore, we cannot rely on optical metrics sensitive to $f\mathrm{PAR}_{\mathrm{chl}}$ alone and need to understand not just how much light is absorbed, but the fate of the energy of absorbed light.

When absorbing a photon, chlorophyll enters an excited state and will partition the energy to one of four potential pathways: photochemistry, damage via the formation of reactive oxygen species, thermal energy dissipation, and fluorescence (Figure 2.3 Niyogi, 1999). In order to maintain energy conservation, the yield of each pathway (ϕ) must add up to 1 such that:

$$1 = \phi_{\mathrm{P}} + \phi_{\mathrm{D}} + \phi_{\mathrm{N}} + \phi_{\mathrm{F}} \tag{2.2}$$

where ϕ_{P} is the yield of photochemistry, ϕ_{D} is the yield of damage, ϕ_{N} is the yield of thermal

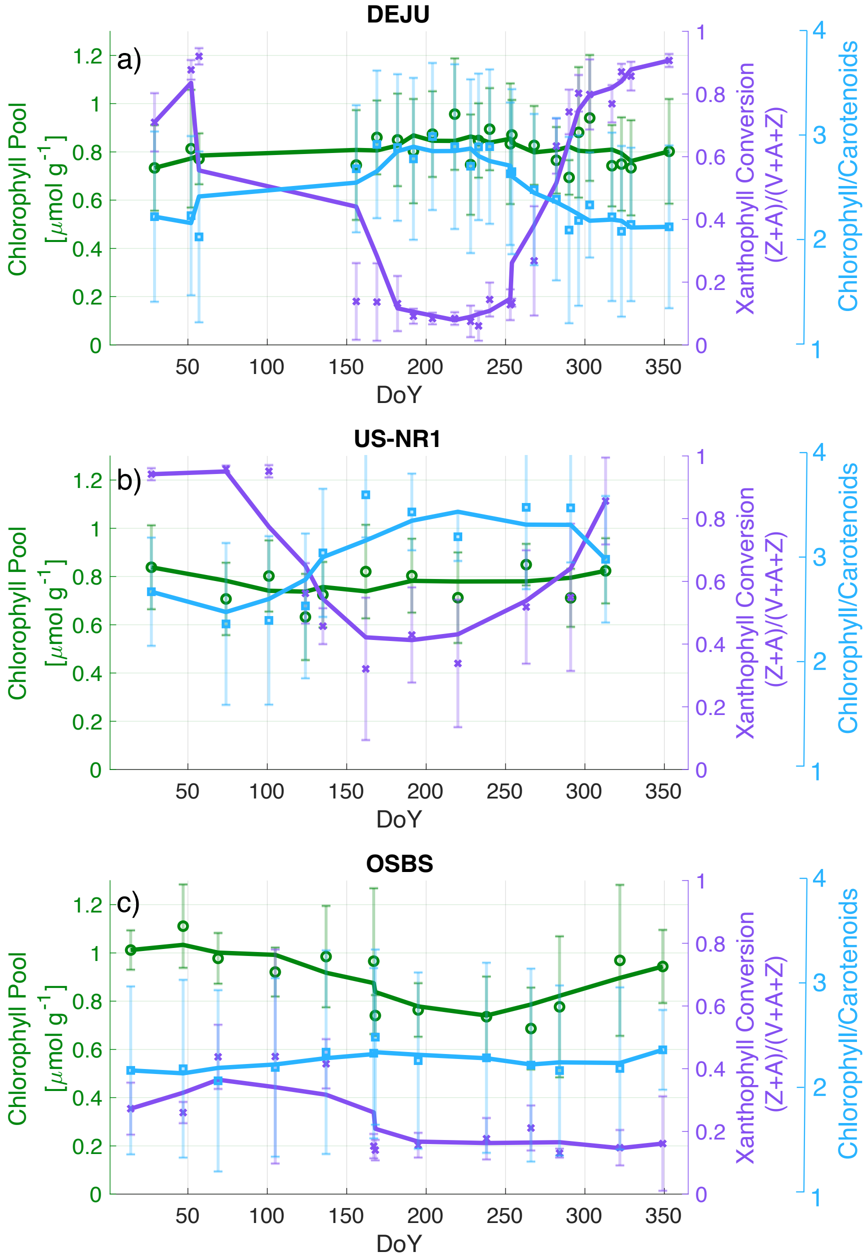

Figure 2.4: Pigments collected from a) DEJU, b) US-NR1, and c) OSBS field sites. The chlorophyll pool remains relatively constant year-round at all 3 sites (DEJU, US-NR1, and OSBS). The relatively cold sites (DEJU and US-NR1) exhibit much larger seasonal variability in xanthophyll conversion state than the warm site (OSBS). Pigment analysis is performed by collecting needle tissue from 8-10 different trees at each site, immediately flash-frozen in liquid nitrogen (LN2) and stored in a -80o freezer until analysis. Pigments are then extracted in acetone and analyzed by HPLC as described in Bowling et al. (2018).

energy dissipation, and ϕ_{F} is the yield of fluorescence (Frankenberg and Berry, 2017). The amount of photochemistry (which is tightly linked to subsequent carbon uptake) a plant can perform depends on both the absorption of light by chlorophyll (i.e., $\mathrm{APAR_{chl}}$), as well as the partitioning of light among these four pathways such that:

$$\text{Photosynthesis} \approx \mathrm{APAR_{chl}} \times \phi_{\mathrm{P}} \tag{2.3}$$

and

$$\phi_{\mathrm{P}} = 1 - \phi_{\mathrm{D}} - \phi_{\mathrm{N}} - \phi_{\mathrm{F}} \tag{2.4}$$

Optical techniques can probe photosynthesis by approximating $\mathrm{APAR_{chl}}$, ϕ_{P}, or both. While ϕ_{P} cannot be directly observed with optical methods, we can rely on techniques that are sensitive to other pathways - namely ϕ_{N} and ϕ_{F} - which tend to co-vary in predictable ways with ϕ_{P} in ENFs as a response to environmental controls. Much of our understanding of the partitioning of light among these pathways has come from pulse amplitude modulated (PAM) fluorometry (Maxwell and Johnson, 2000). PAM fluorometry employs a pulsed measuring source of weak light, in combination with saturating pulses of light, measuring the subsequent fluorescence emissions to derive a variety of parameters that can tell us about photochemical performance and how light energy is being partitioned (we refer readers to Schreiber (2004) for details on PAM fluorometry). By understanding how ϕ_{N} and ϕ_{F} pathways operate in ENFs, we can relate the biology of photochemistry (ϕ_{P}) to what can be detected with optical methods.

The dynamics of ENF photosynthesis are unique because they absorb light year-round, but can experience seasonal stress in their ability to perform photosynthesis. For example, sub-zero temperatures in winter (e.g., DEJU in Alaska, Ca-Obs in Canada, and US-NR1 in Colorado) inhibit enzyme activity and drive a lack of liquid water availability due to ice forming in the soil, within the roots, the trunk, and the distal stems (Figure 2.3, Sevanto et al., 2006; Bowling et al., 2018; Pierrat et al., 2021a; Nehemy et al., 2022). Repeated freeze-thaw events can also lead to damage to the water transport pathway via embolism of xylem (Sperry and Sullivan, 1992). Due to the combination of cold temperature stress and water limitation, many plants in cold locations down regulate the biochemical processes of photosynthesis during winter (Figure 2.3, Adams et al., 2004). Because absorbed light energy cannot be used for photochemistry, it must be sent down alternative energy pathways.

When a plant absorbs more light than can be used to drive photochemistry (ϕ_{P}), excess energy can damage plant tissue (ϕ_{D}). Excited chlorophyll molecules can pass energy to oxygen, transforming it into singlet oxygen (Niyogi, 1999). This is an unstable form in the family of reactive oxygen species, which can irreversibly modify proteins, membrane lipids, and chlorophyll itself, potentially setting off a cascade of harmful cellular oxidation reactions (Logan, 2007). Singlet oxygen formation via energy transfer from chlorophyll is a low-probability biophysical event (i.e., $\phi_{\mathrm{D}}{\approx}0$ for healthy plants); however, it can occur at appreciable and problematic levels when chlorophyll molecules remain in the excited state when photochemistry is unable to "claim" that energy. It is advantageous, then, for plants to have systems in place to deal with light absorbed in excess of what can be used to perform photochemistry.

All plants possess a well-regulated pathway to safely divert excess absorbed light energy as heat (Demmig-Adams and Adams, 2006). This pathway, known as thermal energy dissipation, is modulated by three xanthophyll pigment molecules, zeaxanthin (Z), antheraxanthin (A), and violaxanthin (V), which interconvert through a process known as the xanthophyll cycle (Demmig-Adams and Adams, 2006). Z and A undergo exothermic chemical reactions, which facilitate the conversion of excitation energy into heat that can be dissipated to the surrounding environment (Holt et al., 2004; Holzwarth and Jahns, 2014). The portion of light energy dissipated via this pathway (ϕ_{N}) is controlled by the ratio of Z+A to chlorophyll. This ratio is modulated via enzyme-catalyzed interconversions between Z, A and V; the latter pigment is unable to carry out energy dissipation (Niyogi et al., 1998). When temperature allows enzymatic activity (i.e., during the warm season), plants interconvert xanthophyll pigments to dissipate light absorbed in excess (Figure 2.3, Demmig-Adams and Adams, 1992). This type of dynamic thermal energy dissipation happens over shorter periods of time, from minutes to hours and can help plants prevent damage during short-term stress and routine absorption of light in excess (e.g., midday).

ENFs also use a form of sustained thermal energy dissipation over winter (Demmig-Adams and Adams, 1992; Huner et al., 1993). Because low temperature inhibits enzyme-catalyzed interconversion of xanthophyll cycle pigments, evergreens retain high levels of Z+A over winter in relation to the total xanthophyll pool (V+A+Z) ((Figure 2.3, Verhoeven, 2014). This induces a sustained form of thermal energy dissipation marked by an increase in (Z+A)/(V+A+Z) evident in winter dormant ENFs (DEJU and US-NR1 in Figure 2.4 a, b). In addition to the change in xanthophyll pigment ratios, ENFs also increase the total amount of xanthophyll pigments which is most often quantified as the ratio between chlorophyll and carotenoid pigments (including xanthophylls). Winter dormant ENFs thus exhibit a decrease in chlorophyll/carotenoid ratios over winter (Figure 2.4 a,b). ENFs experiencing mild winters (e.g., the OSBS site in Florida) do not require sustained energy dissipation, and therefore do not exhibit dramatic seasonal variation in pigment pools (Figure 2.4 c). Because the yield of photochemistry (ϕ_{P}) depends on the yield of thermal energy dissipation (ϕ_{N}), and ϕ_{N} is modulated by xanthophyll pigment concentrations, we can use the spectral signatures of xanthophyll pigments to probe photosynthesis (further explained in Section 2.3).

The final path for the energy of excited chlorophyll is fluorescence emission (ϕ_{F}) (Figure 2.3). Excited chlorophyll can fall back to its unexcited state with the emission of a red/near infrared photon, i.e., fluorescence. The intensity of the fluorescence emission is thus a function of $\mathrm{APAR}_{\mathrm{chl}}$ and the yields of alternative energy partitioning pathways. Fluorescence never accounts for more than a small fraction (typically 1-3%) of $\mathrm{APAR}_{\mathrm{chl}}$ and is not a method for plants to safely dissipate appreciable excess energy. Rather, it is a byproduct of chlorophyll excited electrons falling back to their ground state and varies in predictable ways with ϕ_{P}, depending on the light environment. Under extremely low-light conditions, such as dusk and dawn, photosynthesis is typically limited by the amount of light absorbed rather than biochemical capacities. Under light-limited conditions, light energy is thus almost entirely sent down the photochemistry pathway (known as photochemical quenching 'PQ' phase) with essentially no energy being dissipated as heat ($\phi_{\mathrm{N}}\approx 0$). During the PQ phase, the yields of photochemistry (ϕ_{P}) and the yields of fluorescence (ϕ_{F}) will exhibit an inverse relationship (Figure 2.5a, Equation 2.3, Porcar-Castell et al., 2014; Van Der Tol et al., 2014; Magney et al., 2020; Maguire et al., 2020). Under moderate/typical-light conditions, thermal energy dissipation mechanisms (ϕ_{N}, known as non-photochemical quenching 'NPQ' phase) regulate the amount of light used for photochemistry. Because ϕ_{N} pulls energy away from ϕ_{P} and ϕ_{F}, during the NPQ phase ϕ_{P} and ϕ_{F} exhibit a direct relationship (Figure 2.5 a, Porcar-Castell et al., 2014; Van Der Tol et al., 2014; Magney et al., 2020; Maguire et al., 2020). In ENFs where seasonal changes in sustained thermal energy dissipation (ϕ_{N}) drive changes in ϕ_{P} and ϕ_{F} (Porcar-Castell, 2011) we observe strong covariation between the seasonal cycles of ϕ_{P} and ϕ_{F} (Figure 2.5 b). Remote sensing observations of fluorescence also typically occur under 'NPQ phase' conditions and can serve as a robust proxy for photosynthesis when averaged over longer temporal scales (i.e., seasonally).

2.3 Canopy-scale measures of photosynthesis and remote sensing proxies

Carbon uptake via photosynthesis can be studied at the canopy scale with instruments mounted above the vegetation on towers using the eddy covariance technique (reviewed by Baldocchi (2020)). This technique uses high-frequency observations of atmospheric turbulence to derive vertical fluxes of CO_2 (and other variables) between a forest and the atmosphere within a varying footprint range around the tower. The eddy covariance technique provides a measure of the net CO_2 flux (Net Ecosystem Exchange, NEE) which is the combination of CO_2 uptake by photosynthesis (Gross Primary Production, GPP) and the release

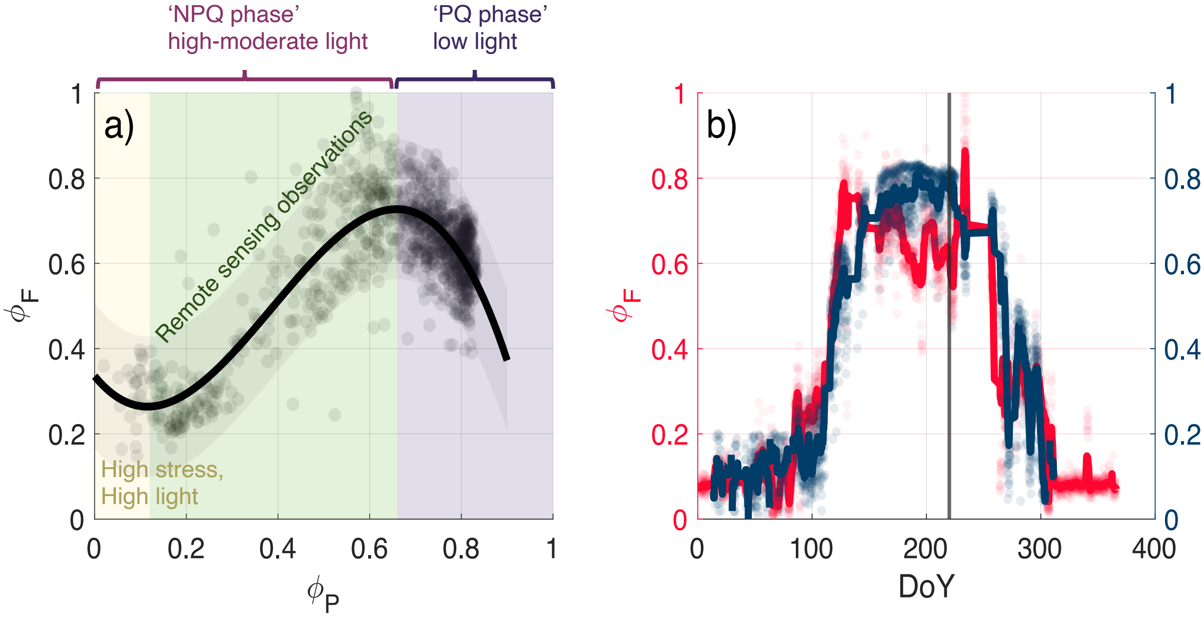

Figure 2.5: Continuous pulse amplitude modulated (PAM) measurements made at DEJU. a) The relationship between normalized steady state fluorescence yield (ϕ_{F}) and photosystem II yield (ϕ_{P}) during the warm season (DoY 100-250) fit with a third order polynomial showing 95% confidence intervals. Data is in good agreement with the theorized relationship from Magney et al. (2020) and observed relationship in Maguire et al. (2020). We observe an inverse relationship under low-light conditions and a direct relationship under moderate light conditions where remote sensing observations are typically made. b) Seasonal co-variation between ϕ_{F} and ϕ_{P}. The PAM measurements were recorded every 10 seconds with a saturating pulse every 2 hours using a Walz Monitoring PAM (MONI-PAM). MONI-PAM heads were affixed to four needle clumps on branches of three different trees, facing all cardinal directions. The data were averaged on a two-hourly basis from August 2021 through fall 2022.

of CO_2 through respiration (ecosystem respiration). NEE can be split into its component parts (GPP and ecosystem respiration) using a wide variety of models based on a combination of temperature, sunlight, and evaporative demand (Reichstein et al., 2005; Desai et al., 2008; Lasslop et al., 2010; Tramontana et al., 2020), all of which carry uncertainties (Wutzler et al., 2018; Papale et al., 2006)).

Carbon uptake via photosynthesis at the canopy scale can be described using the light-use efficiency model of GPP (Monteith, 1972; Monteith et al., 1997):

$$\mathrm{GPP} = \mathrm{PAR} \times f\mathrm{PAR}_{\mathrm{chl}} \times \mathrm{LUE}_{\mathrm{P}} \tag{2.5}$$

where $\mathrm{LUE}_{\mathrm{P}}$ is the light-use efficiency of photosynthesis at the canopy scale (canopy level ϕ_{P}). As at the leaf level, GPP is dependent on light ($\mathrm{APAR}_{\mathrm{chl}} = \mathrm{PAR}\times f\mathrm{PAR}_{\mathrm{chl}}$), temperature, and the availability of water (both of which will impact $\mathrm{LUE}_{\mathrm{P}}$) (Luyssaert et al., 2007; Beer et al., 2010). This is observed across our four study sites. The first three sites (DEJU, Ca-Obs, US-NR1) experience cold winters with sub-zero temperature (Figure 2.6 a-d) but differ in the amount of light they receive (Figure 2.6 e-h). During winter, these cold weather sites are photosynthetically dormant (slightly positive NEE, no GPP) (Figure 2.6 i-p) and therefore use the thermal energy dissipation pathway (ϕ_{N}) to dissipate excess energy. This results in a seasonal cycle in $\mathrm{LUE}_{\mathrm{P}}$ (Figure 2.6 q-t) where plants can safely divert excess energy from sunlight while remaining photosynthetically dormant. The extent to which ϕ_{N} is necessary to prevent damage also depends on the intensity of the light over winter. Specifically, the high elevation of US-NR1 in Colorado ensures a cold winter - despite the lower latitude – resulting in dramatically higher PAR in the winter compared to the more northerly sites. This combination amplifies the need for sustained thermal energy dissipation in comparison with more high-latitude sites. The warmest site, OSBS in Florida, photosynthesizes year-round and thus does not employ sustained energy dissipation. Based on the light-use efficiency model, canopy level remote sensing metrics for tracking photosynthesis are typically sensitive to either $f\mathrm{PAR}_{\mathrm{chl}}$ or approximate $\mathrm{LUE}_{\mathrm{P}}$ based on the partitioning of energy into thermal dissipation (ϕ_{N}) or fluorescence (ϕ_{F}) pathways.

Reflectance-based vegetation indices are the most common type of optical measure capable of tracking changes in photosynthesis. These are typically calculated using a normalized

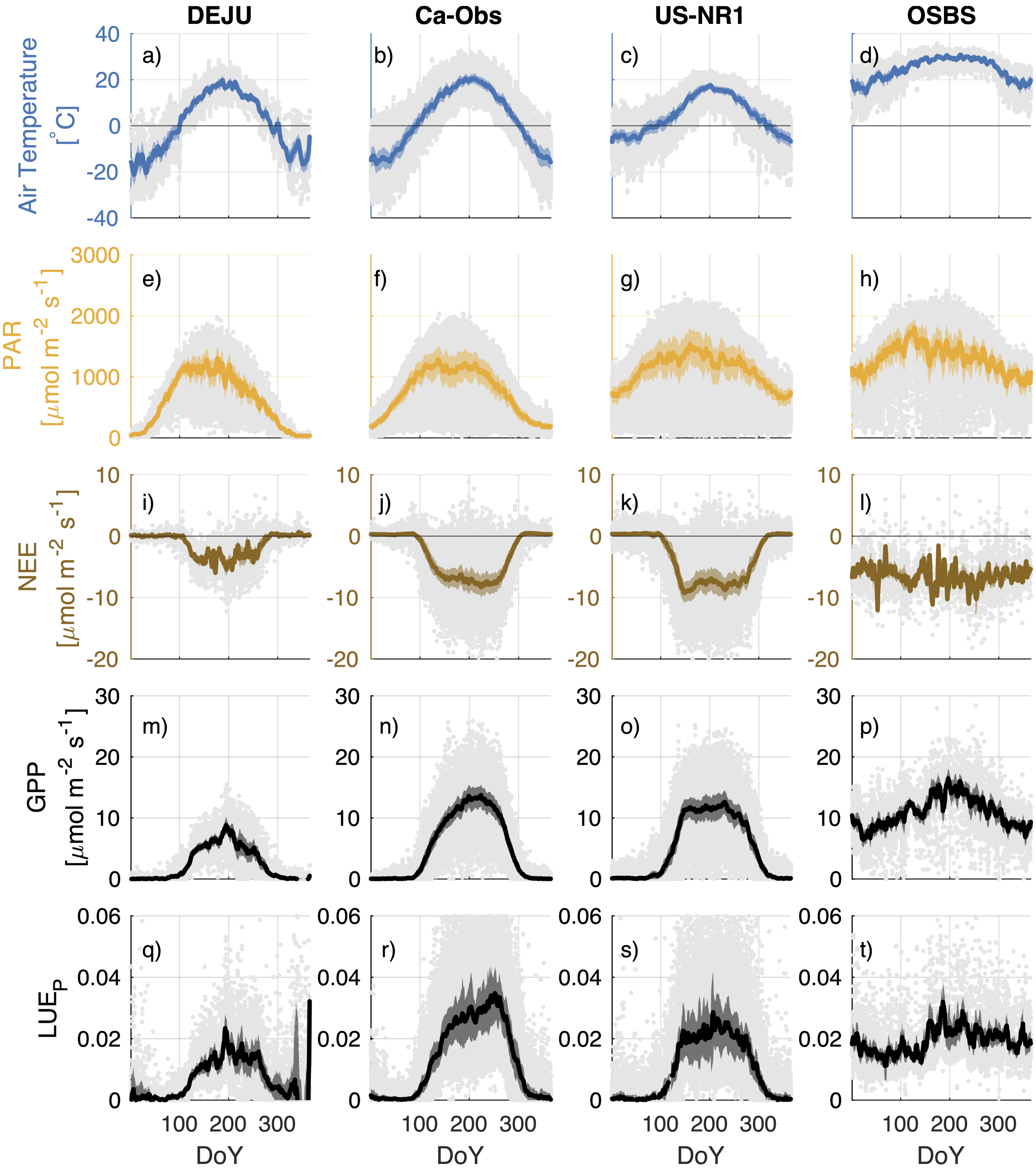

Figure 2.6: Midday (10:00-14:00) stand-level a-d) Air Temperature, e-h) PAR, i-l) NEE, m-p) GPP, and q-t) LUE$_P$ data from the 4 field sites. LUE$_P$ is approximated by assuming fPAR≈0.5 and seasonally invariant, thus LUE$_P$ = $\frac{\text{GPP}}{\text{PAR}\times 0.5}$. Gray dots are individual data points, colored lines are average inter-annual midday values and shaded regions are the inter-annual midday standard deviation.

difference formula:

$$\text{Index} = \frac{\rho_1 - \rho_2}{\rho_1 + \rho_2} \tag{2.6}$$

where ρ_1 and ρ_2 are reflectance in the wavelength bands of interest. The first of these reflectance-based metrics to be widely used was the Normalized Difference Vegetation Index (NDVI) (Tucker, 1979). NDVI takes advantage of the difference in reflectance between the red (sensitive to chlorophyll absorption; ∼620-670 nm) and near infrared (∼830-860 nm) regions of the spectrum (Figure 2.7 Tucker, 1979). It provides a good measure of canopy structure, particularly the presence/absence of chlorophyll (Figure 2.8 a-d), and thus $f\text{PAR}_{\text{chl}}$. The sensitivity of NDVI to $f\text{PAR}_{\text{chl}}$ means that NDVI is a good proxy for GPP in systems where changes in $f\text{PAR}_{\text{chl}}$ are significantly greater than changes in LUE_{P} (Equation 2.5) and thus, canopy structure and carbon uptake are closely linked (e.g., crops, deciduous ecosystems). However, it fails to detect changes in GPP in ENFs due to minimal seasonal change in canopy chlorophyll content, and thus $f\text{PAR}_{\text{chl}}$ (Magney et al., 2019a; Pierrat et al., 2022a). In addition, NDVI is highly sensitive to the presence of snow cover due to the large difference in reflectance between vegetation and snow in the NIR (Figure 2.7, Figure 2.8 a-d), Myers-Smith et al., 2020). This complicates interpretation of NDVI in ENFs which are commonly impacted by snow contamination within the sensor viewing window. Derivations of NDVI that also use the difference between the red and near infrared regions of the spectrum, such as the near-infrared reflectance of vegetation (NIRv) (Badgley et al., 2017, 2019) and the enhanced vegetation index (EVI), among others, have been able to account for background and soil contamination, but still fail to capture changes in photosynthetic phenology of ENFs due to the decoupling between chlorophyll content and photosynthesis (Sims et al., 2006a; Garbulsky et al., 2010; Gamon et al., 2013).

Reflectance-based indices that are sensitive to xanthophyll pigment activity in ENFs have shown a marked improvement in tracking the photosynthetic phenology of ENFs over greenness-based metrics. This is because xanthophyll pigment activity modulates how much light energy is sent down the thermal energy dissipation pathway (ϕ_{N}), which can inform

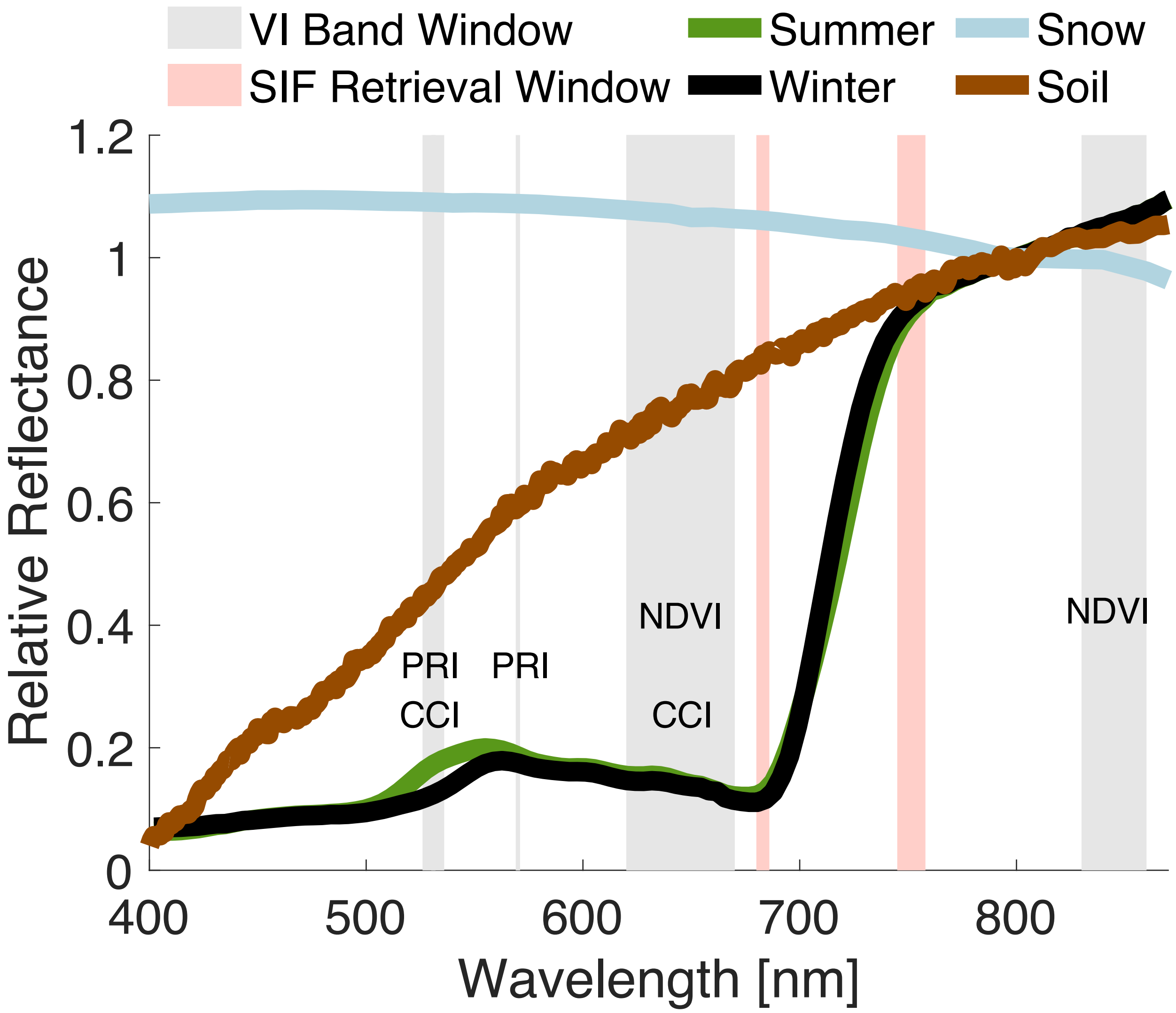

Figure 2.7: Spectral regions where reflectance-based vegetation indices (VIs) are commonly calculated (shaded gray), SIF retrievals are commonly performed (shaded red), and example reflectance data of vegetation and snow normalized at 800 nm. Vegetation reflectance data are from US-NR1 and processed following Cheng et al. (2020). Snow and soil reflectance data are from the Advanced Spaceborne Thermal Emission and Reflection Radiometer (ASTER) Spectral Library (Baldridge et al., 2009; Meerdink et al., 2019).

$\mathrm{LUE_P}/\phi_\mathrm{P}$. The first of these to be developed, the Photochemical (or Physiological) Reflectance Index (PRI), exploits a narrow band at 531 nm (which is sensitive to the conversion state of xanthophyll cycle pigments) in reference to a narrow band at 570 nm (which does not change with xanthophyll interconversion) (Gamon et al., 1992, 1997). This is noticeable in the difference in reflectance spectra in the 531 nm region from the US-NR1 site (Figure 2.7) between summer (when Z concentrations are lower) and winter (when Z concentrations are higher). Over short temporal scales (e.g., over the course of a day in the growing season), PRI is sensitive to rapidly reversible thermal energy dissipation dynamics (ϕ_N) in ENFs, making it effective for tracking diurnal changes in $\mathrm{LUE_P}$ (Gamon et al., 2015; Yang et al., 2020). Over longer temporal scales (seasons), PRI is sensitive to sustained thermal energy dissipation due to winter increases in Z + A pigments (Figure 2.8 e-h, Wong and Gamon, 2015a,b). PRI is also highly sensitive to the presence of snow on the canopy which presents a significant challenge in ENFs. It is also not presently measured from spaceborne platforms. The best available satellite proxy for PRI, the chlorophyll-carotenoid index (CCI), was specifically developed to track the seasonal changes in the ratio of chlorophylls to carotenoids (including xanthophyll pigments) using reflectance bands from the Moderate Resolution Imaging Spectroradiometer (MODIS, Band 11 526-536 nm; and Band 1 620-670 nm, Gamon et al., 2016). By tracking the ratio of chlorophylls to carotenoids, CCI is also able to track sustained energy dissipation in ENFs (Figure 2.8 i-l) and is thus a good proxy for ENF carbon uptake (Gamon et al., 2016).

In addition to reflectance-based metrics which employ narrow wavelength bands, digital repeat photography can be used to track seasonal changes in canopy color, and thus the photosynthetic phenology of ENFs. Specifically, the Green Chromatic Coordinate (Gcc) can be calculated from images as:

$$\mathrm{Gcc} = \frac{\mathrm{G}}{\mathrm{R} + \mathrm{G} + \mathrm{B}} \tag{2.7}$$

where G, R, and B are the mean intensity of the green, red, and blue color channels (Richardson, 2019). Prior work has shown that Gcc is sensitive to the changes in canopy color asso-

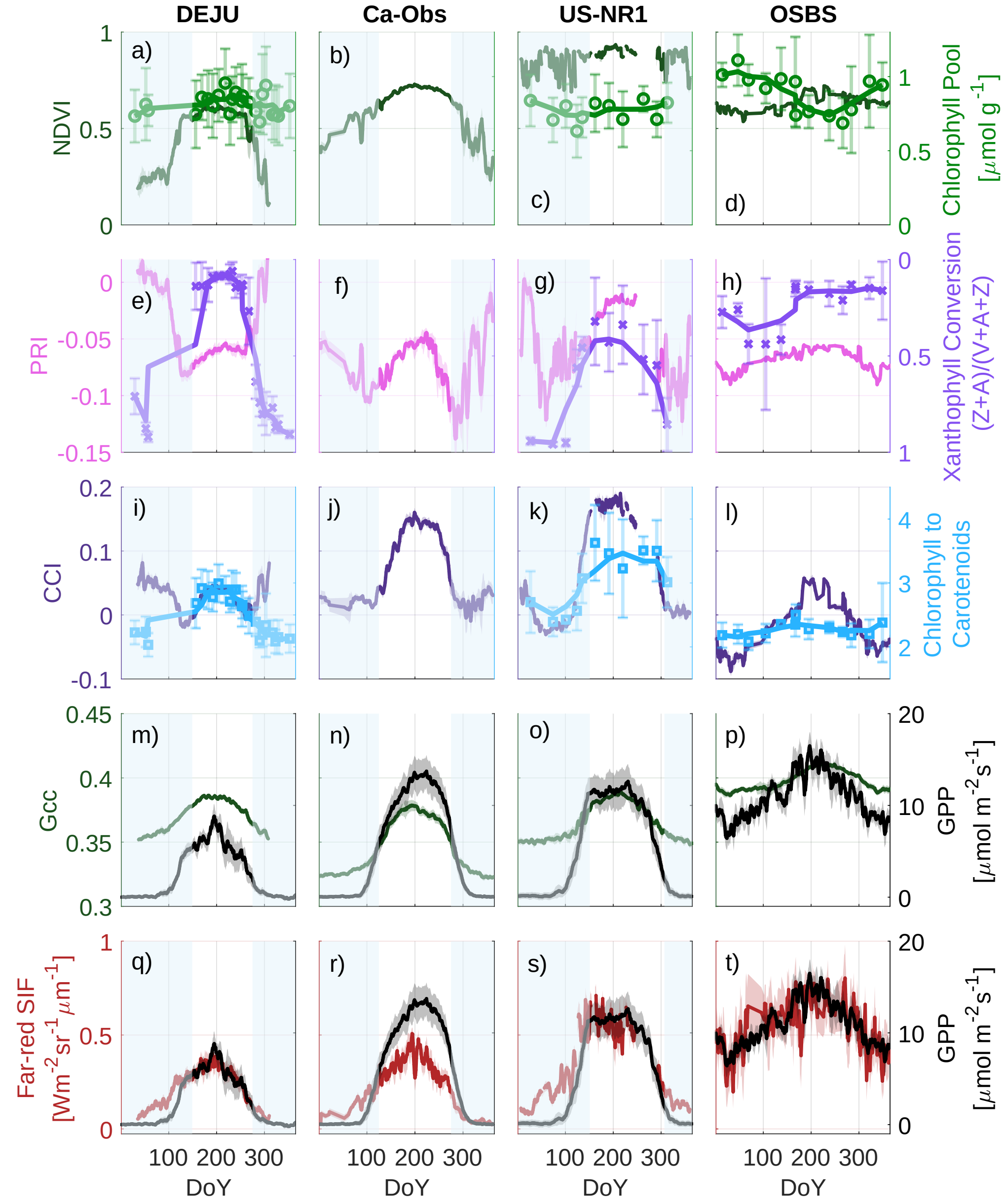

Figure 2.8: Tower-based remote sensing combined with leaf-level pigment data and eddy-covariance derived GPP. a-d) NDVI and chlorophyll concentration, (e-h) PRI and xanthophyll conversion state, (i-l) CCI and chlorophyll/carotenoid ratio, m-p) Gcc and GPP, and q-t) SIF and GPP. NDVI, PRI, CCI, and SIF data were collected using PhotoSpec. Additional measurement and data processing details from PhotoSpec can be found in Grossmann et al. (2018); Magney et al. (2019a); Pierrat et al. (2022a, 2021a). Gcc data were obtained from the PhenoCam Network (https://phenocam.nau.edu/webcam/). Shaded blue regions indicate days where snow on the canopy obscures remote sensing observations.

ciated with variation in leaf pigment ratios (including the ratio of chlorophyll to xanthophyll pigments) in ENFs (Seyednasrollah et al., 2020). Due to this sensitivity, Gcc can probe thermal energy dissipation, and thus tracks the seasonality of GPP. Start of season and end of season transition dates derived from Gcc are well aligned with start of season and end of season transition dates derived from eddy-covariance GPP as well as the onset of transpiration, as determined by stem-radius measurements in ENFs (Seyednasrollah et al., 2020; Nehemy et al., 2023). Gcc from our four experimental sites shows good agreement with the seasonal cycle of GPP, but does not show a consistent ratio between Gcc and GPP (Figure 2.8 m-p). Snow cover impacts Gcc values by obscuring the canopy in the region of interest and making it less green, but values only shift down by approximately 10% (Seyednasrollah et al., 2020). A major advantage of Gcc is the ease of measurement at the canopy scale and the accessibility of images and data from 600 sites globally with a standardized processing approach through the PhenoCam Network (Richardson et al., 2018). This level of standardization and accessibility is currently unavailable for most other canopy-level remotely sensed data.

A more direct approach to probe photosynthesis remotely is the use of the fluorescence emitted by excited chlorophyll. Under natural sunlight conditions, this is referred to as sun- or solar-induced chlorophyll fluorescence (SIF). SIF has shown significant potential for tracking GPP in ENFs (Figure 2.8 a-d, Magney et al., 2019a; Pierrat et al., 2021a, 2022a,b). Canopy level SIF is expressed similarly to GPP (Equation 2.5) using the light-use efficiency model as:

$$\mathrm{SIF} = \mathrm{PAR} \times f\mathrm{PAR}_{\mathrm{chl}} \times \mathrm{LUE}_{\mathrm{F}} \times f_{\mathrm{esc}} \tag{2.8}$$

where $\mathrm{LUE}_{\mathrm{F}}$ is the light-use efficiency of fluorescence (ϕ_{F} integrated over all leaves/needles within the sensor field of view) and f_{esc} is the fraction of SIF photons that escape the canopy and reach the detector. We can relate SIF and GPP by combining Equations 5 and 8:

$$\mathrm{GPP} = \mathrm{SIF} \times \frac{\mathrm{LUE}_{\mathrm{P}}}{\mathrm{LUE}_{\mathrm{F}} \times f_{\mathrm{esc}}} \tag{2.9}$$

SIF and GPP are therefore linked by both shared drivers ($\mathrm{APAR_{chl}} = \mathrm{PAR} \times f\mathrm{PAR_{chl}}$), as well as leaf-level biological parameters (ϕ_P and ϕ_F) that can be scaled to the canopy level ($\mathrm{LUE_P}$ and $\mathrm{LUE_F}$). Under typical conditions for remote sensing observations, when thermal energy dissipation regulates photochemistry ('NPQ' phase) leading to co-variation between ϕ_P and ϕ_F (Figure 2.5 a) and f_esc is invariant, the $\frac{\mathrm{LUE_P}}{\mathrm{LUE_F} \times f_\mathrm{esc}}$ term becomes approximately constant. This leads to a linear relationship between SIF and GPP (Sun et al., 2018). Therefore, SIF generally does an excellent job tracking both the seasonality (Figure 2.8 q-t) and diurnal dynamics of GPP (Pierrat et al., 2022a). Further, because SIF is an emitted signal vs. a reflectance-based metric, it is less sensitive to the presence of snow (Figure 2.8 q-t) and cloud cover (Frankenberg et al., 2011; Mohammed et al., 2019; Chang et al., 2020). The ability to use SIF as a proxy for GPP in ENFs has led to substantial advances in our understanding of ENF carbon dynamics.

Studies at fine spatio-temporal resolutions (leaf and tower) have highlighted nuance to the SIF-GPP relationship which can be attributed to a combination of decoupling between ϕ_P and ϕ_F (and subsequently $\mathrm{LUE_P}$ and $\mathrm{LUE_F}$) modulated by thermal energy dissipation dynamics (Figure 2.5 a, Magney et al., 2020; Maguire et al., 2020; Marrs et al., 2020; Pierrat et al., 2022a), and variation in f_esc. In ENFs with strong seasonal temperature variations, such as DEJU, Ca-OBS, and US-NR1, the GPP-SIF relationship changes throughout the year due to sustained energy dissipation dynamics. In addition, in winter when photochemistry shuts down at these sites, SIF still exhibits a small light response when GPP is absent, which leads to a non-zero SIF signal and an increase in SIF prior to changes in GPP (Figure 2.8 q-t, Magney et al., 2019a; Pierrat et al., 2022a; Yang et al., 2022). The winter SIF light response can be explained as persistent photosystem activity that does not reflect carbon assimilation (ie. zero $\phi_\mathrm{P}/\mathrm{LUE_P}$ and non-zero $\phi_\mathrm{F}/\mathrm{LUE_F}$). The nuances in the SIF-GPP relationship does not preclude the use of SIF as a proxy for GPP, but it does motivate future work to understand when and where divergence between SIF and GPP occurs and how we can best account for it.

Given that remote sensing metrics can contain information on both plant structure ($f\mathrm{PAR}_{\mathrm{chl}}$, f_{esc}) and function (light partitioning among ϕ_{P}, ϕ_{N}, and ϕ_{F}), combining multiple metrics can help paint a more complete picture of ENF photosynthesis. Specifically, combining SIF with reflectance-based indices improves our ability to predict GPP beyond the use of any one metric alone (Wang et al., 2020; Hikosaka and Tsujimoto, 2021; Pierrat et al., 2022b; Wong et al., 2022). This can be attributed to the fact that while some metrics are sensitive to similar physical parameters ($f\mathrm{PAR}_{\mathrm{chl}}$, f_{esc}), they describe different physiological parameters, i.e., reflectance-based metrics are sensitive to leaf/needle composition that controls thermal energy dissipation (ϕ_{N}), while SIF depends on fluorescence yields ($\mathrm{LUE}_{\mathrm{F}}$ and ϕ_{F}). In combination, these metrics provide a more complete description of the fate of photons absorbed by canopies. Both statistical (Zeng et al., 2019; Cheng et al., 2020; Liu et al., 2020b; Wong et al., 2022) and machine learning approaches (Bai et al., 2022; Pierrat et al., 2022b) have been used to incorporate information from both SIF and vegetation indices to predict GPP. There is not yet a universal quantitative framework for relating these metrics, nevertheless, these approaches typically result in improved predictive capacity for GPP over any single metric alone.

2.4 Global-scale satellite remote sensing of evergreen needleleaf forests

The high cost of flux tower observations and restrictions on site suitability limit the locations where eddy-covariance and other canopy-scale measurements can be applied. To scale site-level observations across the terrestrial land surface, satellite remote sensing observations are therefore necessary (Jung et al., 2011, 2020; Zeng et al., 2022). Satellite remote sensing products (e.g., NDVI, CCI, SIF) are sensitive to the same underlying physical and physiological processes that can be measured at the leaf/needle and site levels (Sections 2.2 & 2.3) but offer expanded spatio-temporal monitoring of vegetation (Schimel et al., 2015; Zeng et al., 2022). The spatial resolutions of satellite products range from meters to kilometers and temporal resolutions from sub-daily (geostationary) to daily and >8 days (global coverage) depending on platform. Satellite observations offer applications for monitoring and understanding both short (diurnal, seasonal) and long term (annual, decadal) dynamics of whole landscape/biome processes at a spatial scale much broader than a single site. Some satellite missions also offer long-term data availability with certain missions dating as far back as the 1970s (e.g., Landsat, Xiao et al., 2019). Long-term satellite records have been used to evaluate changes in annual carbon uptake (Myneni et al., 2001; Dong et al., 2003) and phenology (Zhang et al., 2003; White et al., 2009; Keenan et al., 2014). Additionally, monitoring ecosystem function from space has applications for assessing long-term trends in forest stress severity and recovery (e.g., fires, pests, drought, French et al., 2008; Eklundh et al., 2009; Beck et al., 2011; Michaelian et al., 2011). The expansion of the spatio-temporal range that satellite data provides, however, typically comes at the expense of spatio-temporal resolution. Therefore, it is necessary to consider both the spatial and temporal scaling benefits and limitations of satellite data.

Satellite reflectance-based metrics, such as NDVI from MODIS and Landsat reflectance data have been used for many years to monitor the global biosphere. For example, maps of NDVI reveal the spatial and seasonal variation of ecosystem structure across North America (Figure 2.9 a,b). However, care has to be taken with these observations, as satellites aggregate optical signals from multiple sources in a given area, often called ground pixel, into a single measurement (Zeng et al., 2022). This makes interpretation of reflectance-based observations challenging in structurally complex and heterogeneous ecosystems such as ENFs with multiple overstory species and contributions from understory vegetation, soil, and snow (Maguire et al., 2021). Mixed forest sites contain evergreen and deciduous trees with contrasting adaptive strategies (e.g., phenology, photosynthetic capacity, Givnish, 2002) – also complicating the seasonal interpretation of satellite data. Depending on the dominant vegetation type, satellite remote sensing may be biased to the dominant optical signal based

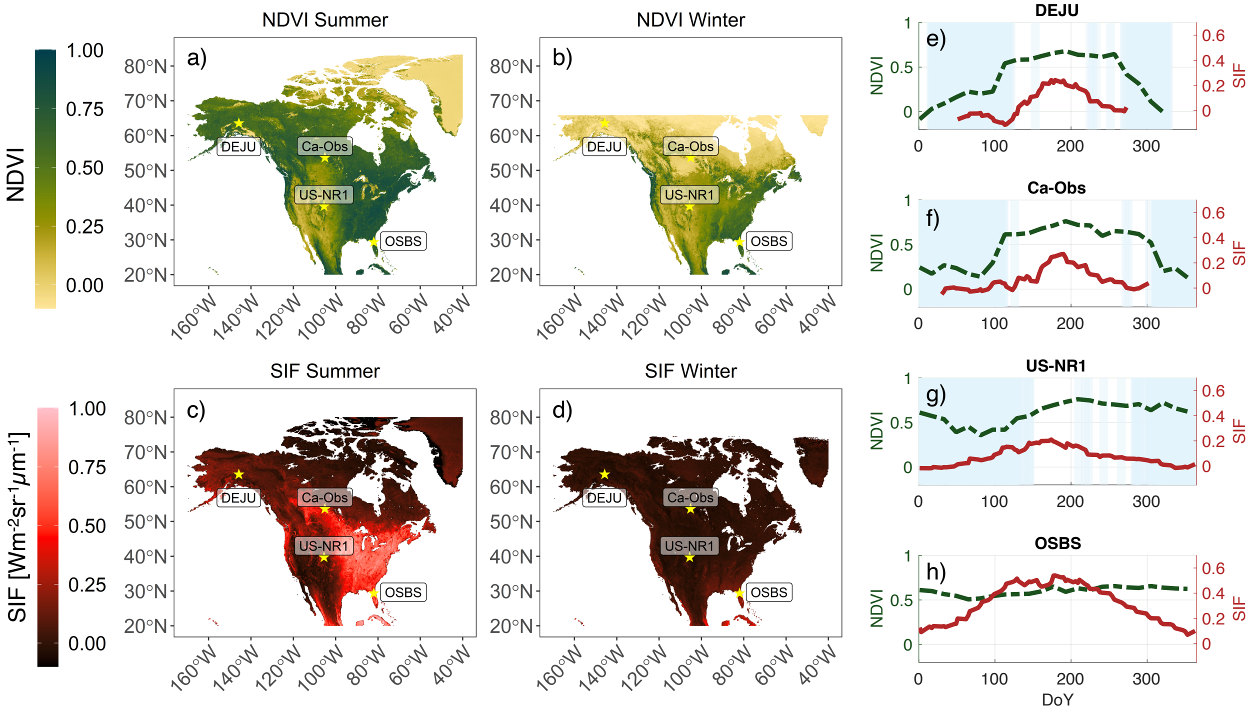

Figure 2.9: a-d) Average summer (June-September) and winter (December-March) MODIS NDVI and TROPOMI SIF. Yellow stars represent site locations. e-h) 16-day MODIS NDVI (unitless) and 16-day daily corrected TROPOMI SIF (in $Wm^{-2}sr^{-1}\mu m^{-1}$) both averaged annually from 2018-2021. Blue regions indicate days with snow present based on daily MODIS NDSI. Winter maps show limited spatial coverage of the northern extent due to high solar zenith angles leading to inadequate solar irradiation.

on density and leaf area (Atherton et al., 2017; Pierrat et al., 2021a). In sparse canopies, understory plants, rock, and soil impact reflectance-based indices like NDVI. For this reason, correction factors (Eitel et al., 2006) or new vegetation indices (e.g., EVI and NIRv) are useful in minimizing the influence of understory components. Reflectance-based metrics are also highly sensitive to cloud cover which may contaminate observations, even for partial cover in a pixel, leading to data gaps (Walther et al., 2016; Cheng et al., 2022). Finally, the sensitivity of reflectance-based metrics to snow (Figure 2.7), can lead to a seasonal signal in reflectance-based metrics that is not associated with changes in photosynthetic phenology. This is, for example, noticeable across three of our study sites (Figure 2.9 e-g). Despite these limitations, global reflectance based remote sensing products have successfully been used to parameterize and constrain model predictions of carbon uptake (Gonsamo et al., 2012; Smith et al., 2020), and remain one of our most important tools to reduce uncertainties in future climate predictions (Friedlingstein et al., 2014, 2022).

The measurement of SIF from space has led to considerable advances in monitoring ENF photosynthesis in recent years. Due to the underlying physical ($\mathrm{APAR_{chl}} = \mathrm{PAR} \times f\mathrm{PAR_{chl}}$, f_{esc}) and physiological drivers ($\mathrm{LUE_F}$) of SIF, SIF can reveal the spatial and seasonal variation of ecosystem structure and function across North America (Figure 2.9 c-h). SIF observations across our study sites show a comparable seasonal cycle to tower-based SIF and eddy-covariance GPP (Figure 2.9 e-h) illustrating the potential of satellite SIF observations over larger spatial scales. As an emitted signal, SIF has a lower sensitivity to cloud (Frankenberg et al., 2014; Doughty et al., 2019) and snow cover (Luus et al., 2017), therefore making it more robust across the seasons (Figure 2.9 e-g). This is especially important during the onset of photosynthesis which often coincides with the snowmelt period (Pierrat et al., 2021a; Nehemy et al., 2022). SIF has also shown significant potential for detecting the impacts of drought, even before changes in canopy greenness (NDVI) are detected (Shen et al., 2021; Mohammadi et al., 2022). This enables potentially real-time evaluations of ecosystem health. In analogy with tower-based results, combining SIF with reflectance-based metrics has the potential to overcome many of the limitations presented by any individual metric alone, however, this has yet to be fully investigated.

Integrating satellite products from different sensors should also be considered with care as overpass time and pixel locations may not align temporally and spatially, leading to spatio-temporal mismatch (Gao et al., 2006; Alcaraz-Segura et al., 2010). In addition, the seasonal variation in solar radiance and high solar-zenith angles results in unequal availability of satellite data between winter and summer (Figure 2.9 a-d), which may bias interpretation of the seasonality of photosynthesis. Forests at higher latitudes will also be more sensitive to sun-sensor geometry, requiring post-processing steps such as bidirectional reflectance distribution function (BRDF) and atmospheric corrections (Asner, 1998).

Satellites offer datasets that expand the spatio-temporal range of tower-based observations. Despite the challenges imposed by mixed-pixels, snow and cloud contamination, satellites are essential tools to better monitor ENFs and to inform global carbon models. More research is needed to fully understand and interpret satellite-based data products for tracking photosynthesis in ENFs. There remains a need for mechanistic validations at a high spatio-temporal resolution (Nelson et al., 2022) with measurements such as those discussed in Sections 2.2 and 2.3.

2.5 Multi-scale observations for an integrated understanding of evergreen needleleaf biology

Climate change is likely to have complex and multifaceted impacts on ENF photosynthesis, which could alter the structure, composition, and productivity of these ecosystems in ways that are not yet fully understood (Seidl et al., 2017). Understanding both the nuances and potential of integrating the aforementioned measurements will create a more complete picture of the ENF carbon cycle. This is critical as both climate change and land-use decisions make the future of forests largely uncertain (Anderegg et al., 2020; Brodribb et al., 2020). Long-term carbon storage and biodiversity of ENFs are hindered by interannual changes in temperature and precipitation as well as disturbance events linked to extreme weather, biotic agents, and large-scale demographic shifts (Allen et al., 2010; Seidl et al., 2017; Anderegg et al., 2020). Both modeling and monitoring these changes have been challenging, with a recent study suggesting wide divergence in projections of future global forest vulnerability using the best available data and mechanistic models (Anderegg et al., 2022). Understanding how climate-sensitive disturbances might impact ENF vegetation physiology going forward will require multidisciplinary efforts for scaling and interpreting observations from the leaf to the globe.

We can glean essential knowledge on the environmental and physiological controls on the seasonality of ENF photosynthesis by combining fundamental theory of plant physiological ecology with a diverse combination of observations at scales from conifer needle to flux tower to satellite. In this paper, we have shown how pigment-based thermal energy dissipation of excess sunlight is an integrative general property of ENFs response to adverse environmental conditions over both mild and harsh winters. Additionally, we show that the steady-state emission of chlorophyll fluorescence can be a physiological indicator of ENF photosynthesis. Interpreting these processes from satellite data alone leaves out important nuances in these signals due to the low spatio-temporal resolution of satellite measurements. Thus, without careful measurements of, and expertise in, plant pigments, gas-exchange, and chlorophyll fluorescence at the site level interpretations of satellite products might over- or under-estimate ENF photosynthetic seasonality. Co-located measurements of footprint-tower spectroscopy and needle biochemistry can provide an explanation for how seasonal adjustments in needle pigments and light energy partitioning are mechanistically linked to photosynthetic capacity. These crucial ground observations enable developers of satellite data products to correct for impacts of sun-sensor geometry and background noise that might confound researchers' interpretation of SIF or pigment-based signals.

While eddy covariance currently provides the best ground-validation of remote sensing derived ENF GPP products, both flux measurements and remote sensing products carry uncertainties (Hollinger and Richardson, 2005; Tramontana et al., 2015). Because flux measurements represent net exchanges of carbon, water and energy at the ecosystem scale, flux data alone do not explicitly tell us the spatio-temporal contributions to, nor the partitioning of fluxes between, different ecosystem components (Baldocchi, 2003). Linking remote sensing with needle-scale measurements can help scientists interpret site-specific flux measurements by providing contextual information on community composition and vegetation function, and help scale estimate fluxes globally (Ustin et al., 2009). Taken together, seasonal measurements of plant biochemistry/physiology, eddy-covariance, and remote sensing can help paint a more complete picture on where uncertainties arise and how we might account for them going forward.

This overview shows how coordinated measurement campaigns (Figure 2.1) allow for a better understanding of the environmental controls on ENF physiology and ultimately how this can be scaled using remote sensing products. With the rapid proliferation of new satellites and researchers using these data to draw conclusions about ecosystem response to climate change, the need for multi-disciplinary efforts to better reconcile when, where, and to what extent remote sensing can be used to track changes in the carbon cycle is critical. The multi-disciplinary efforts discussed here comprised experts in plant ecophysiology, leaf and tower-scale carbon flux observations, tower and satellite remote sensing. Going forward, empirical data from these efforts should be used to help inform modeling efforts or used in model-data fusion frameworks, requiring close collaboration with the ecosystem modeling community (Stofferahn et al., 2019; Gettelman et al., 2022). Accurate scaling of carbon cycle parameters from the site to the ecosystem to the biome is a major challenge but can be accomplished by well instrumented and monitored sites that encompass a broad range of ENFs. Doing so will ultimately enable scientists to better understand both the biological and physical drivers of changes in ENF photosynthesis, and how we can accurately monitor and measure these processes under future climate scenarios.

CHAPTER 3

Methods: field locations, data collection and processing

In this chapter, we provide a general methodological overview of the sites, instrumentation, and general data processing used throughout this dissertation. More details of measurements and data processing can be found in specific chapters where relevant.

3.1 Field Locations

The data presented in this dissertation was collected across a network of field locations in North American evergreen needleleaf forests spanning a latitudinal and climate gradient (Figure 2.2, Table 3.1). The majority of this work (Chapters 2, 4, 5, 6, & 7) uses original data collected at the Southern Old Black Spruce site (SOBS, FLUXNET ID Ca-Obs) in Saskatchewan, Canada. We also collected original data from two sites within the National Ecological Observatory Network (NEON) in Alaska at Delta Junction (DEJU, Chapters 2, 6, & 7) and Florida at the Ordway-Swisher Biological Station (OSBS, Chapters 2, & 7). Finally, we present data previously collected in Colorado at Niwot Ridge (FLUXNET ID, US-NR1). All sites are equipped with scaffolding towers well above the canopy height which collect eddy-covariance and meterological data (Section 3.2).

Table 3.1: Summary of climate and vegetation at field sites

Site	**DEJU**	**Ca-Obs, SOBS**	**US-NR1**	**OSBS**
Lat/Lon	63.88°N, 145.75°W	53.98°N, 105.12°W	40.03 °N, 105.55 °W	29.69 °N, 81.99 °W
Elevation	517 m	629 m	3050 m	46 m
Mean Air Temp.	0.4 °C	1.4°C	2.8 °C	20.9 °C
Mean Precipitation	305 mm	427.7 mm	800 mm	1302 mm
Canopy Height	10 m	16 m	13 m	23 m
Overstory Vegetation	black and white spruce (*Picea mariana & Picea glauca*)	mixed forest stand with stem density predominantly (90%) black spruce (*Picea mariana*) and scattered (10%) larch (*Larix laricina*)	lodgepole pine (*Pinus contorta*), Engelmann spruce (*Pinus engelmannii*), and subalpine fir (*Abies lasiocarpa*)	predominantly long-leaf pine (*Pinus palustris*) with scattered turkey oak (*Quercus laevis*)

Continued on next page

Table 3.1: Summary of climate and vegetation at field sites (Continued)

Site	**DEJU**	**Ca-Obs, SOBS**	**US-NR1**	**OSBS**
Understory Vegetation	sedges, mosses, and low-growing shrubs including lingonberry (*Vaccinium vitis-idaea*), crowberry (*Empetrum nigrum*), bog blueberry (*Vaccinium uliginosum*), bog Labrador tea (*Ledum palustre*), false toadflax (*Geocaulon lividum*) , and bearberry (*Arctostaphylos uva-ursi*)	mixed feather mosses (*Hylocomium splendens, Pleurozium schreberi, Ptilium cristacastrensis*), with some peat moss (*Sphagnum* spp.) and lichen (*Cladina* spp.)	mainly non-vegetated	wiregrass (*Aristida stricta Michx.*)
Soils	gravelly glacial till and outwash covered by a thin layer of loess	moderately-to-poorly drained with a 20-30 cm thick peat layer overlying waterlogged sand	granitic-rocky-podzolic soil, loamy sand overlain by a shallow layer (≈10 cm of organic material)	well-drained and sandy

3.2 Data

3.2.1 Tower-based Remote Sensing: PhotoSpec

We collected tower-based remotely sensed measurements including red and far-red SIF and reflectance based metrics (NDVI, NIRv, CCI, PRI) using PhotoSpec (see Grossmann et al. (2018) for detailed instrument description). Measurements ran from August 2019-present at DEJU, September 2018-present at Ca-Obs, June 2017-June 2018 at US-NR1, and March 2020-present at OSBS. The following sections describe the experimental setup at each site, retrieval approach, and data processing.

Photospec was installed atop the scaffolding/eddy-covariance tower facing due north at all sites. PhotoSpec has a narrow field of view (0.7°), 2-D scanning capabilities, and simultaneously measures SIF and VIs at the same point in the canopy (Grossmann et al., 2018). Individual measurements take approximately 20 seconds.

Reflectance-based vegetation indices (VIs) were calculated as follows, with $\rho_{nm:nm}$ = the average reflectance across a wavelength range in nm:

$$\text{NDVI} = \frac{(\rho_{830:860} - \rho_{620:670})}{(\rho_{830:860} + \rho_{620:670})} \tag{3.1}$$

$$\text{NIRv} = \frac{(\rho_{830:860} - \rho_{620:670})}{(\rho_{830:860} + \rho_{620:670})} \times \rho_{830:860} \tag{3.2}$$

$$\text{PRI} = \frac{(\rho_{569:571} - \rho_{520:532})}{(\rho_{569:571} + \rho_{520:532})} \tag{3.3}$$

$$\text{CCI} = \frac{(\rho_{520:532} - \rho_{620:670})}{(\rho_{520:532} + \rho_{620:670})} \tag{3.4}$$

SIF was retrieved in the red (680-686 nm) and far-red (745-758 nm) wavelength ranges using a Fraunhofer-line based retrieval (Grossmann et al., 2018; Magney et al., 2019b,a; He et al., 2020). Retrieval errors are calculated as outlined in Grossmann et al. (2018) and propagated through all calculations.

To decouple the physical (light, structure, viewing and solar geometries) from the physiological SIF signal, and account for variations in incident light and sun/shade fraction within the field of view, we calculated $\mathrm{SIF}_{\mathrm{relative}}$ (a proxy for $\mathrm{SIF}_{\mathrm{yield}}$) in both the red and far-red wavelength ranges as:

$$\mathrm{SIF}_{\mathrm{relative}} = \frac{\mathrm{SIF}}{\mathrm{I}}$$

where I is the near-infrared (NIR) radiance in the SIF retrieval window (680-686 nm for red and 745-758 nm for far-red) (e.g. Parazoo et al., 2020; Magney et al., 2019b).

We collected 1 second Photosynthetically Active Radiation (PAR) data and used these data to remove PhotoSpec measurements where PAR conditions changed significantly ($\mathrm{PAR}_{\mathrm{std}} > 0.2 \times \mathrm{PAR}_{\mathrm{avg}}$) over the PhotoSpec integration time. We excluded low-quality retrievals where the SIF retrieval error was > 0.2 $\mathrm{Wm^{-2}sr^{-1}\mu m^{-1}}$ and where SIF < -0.1 $\mathrm{Wm^{-2}sr^{-1}\mu m^{-1}}$ or SIF > 10 $\mathrm{Wm^{-2}sr^{-1}\mu m^{-1}}$. Finally, we only considered data where the Solar Zenith Angle (SZA) < 80° to remove data where low light conditions increase retrieval uncertainty.

We developed a clear sky comparison metric, Df, to separate sunny (direct) from cloudy (diffuse) illumination conditions (Pierrat et al., 2021b). Df reflects the deviation of PAR at a given solar zenith angle from the expected PAR during a clear sky reference day so that Df = 1 is clear sky conditions. We used Df to classify measurements with Df<0.6 as cloudy (diffuse) and Df>0.8 as sunny (direct). Df values were calculated for every PhotoSpec measurement (~20 second resolution) but averaged together in 30-minute windows to compare with canopy averages.

We took canopy representative scans across all field locations with either a 30 or 60-minute repeat time to compare with the temporal resolution of eddy-covariance data and environmental variables. Data were then averaged to a half-hourly or hourly resolution for either species-specific averages (Chapter 4) or canopy representative averages (Chapters 5, 6, 7). Data were then averaged again to a daily resolution or mid-day (10:00-14:00) daily averages to explore seasonal trends and compare with satellite data.

Days with significant snow cover were identified visually using phenocam images (`https://phenocam.sr.unh.edu/webcam`).

3.2.2 Eddy-covariance and meteorological data

Eddy-covariance and meterological data were collected across all four field locations and processed as described in Table 3.2

Table 3.2: Summary of methods for measurement and data processing

Measurement	**SOBS/Ca-Obs**	**DEJU, US-NR1, OSBS**
GPP		
Eddy-covariance	Taken using a 3-D sonic anemometer (CSAT3, Campbell Scientific, Logan, UT) in combination with a closed-path infrared gas (CO2/H2O) analyzer (LI-7200 analyzer, Li-Cor, Lincoln, NE) operated in absolute mode.	Obtained from National Ecological Observatory Network (NEON) (2022a) using a Campbell Scientific CSAT-3 3-D Sonic Anemometer and LI-COR - LI7200 gas analyzer.
	We performed quality assurance on the data using the standard Fluxnet-Canada method following (Barr et al., 2004, 2006)	We performed quality assurance on carbon fluxes based on turbulent and storage fluxes separately, using a bivariate statistical procedure for each, to overcome quality flag restrictions in the ”expanded” NEON eddy-covariance bundle.

Continued on next page

Table 3.2: Summary of methods for measurement and data processing (Continued)

Measurement	SOBS/Ca-Obs	DEJU, US-NR1, OSBS
		3% outliers (3% of rarest events from the tails of each distribution) were excluded from joint probability distributions for all available data for 1) turbulent flux and PPFD, and separately for 2) storage flux and time of day. NEE data were considered valid if both the turbulent and storage fluxes passed this quality control step (and NEE is equal to their sum).
Partitioning	Data for NEE and meteorological variables were filtered to remove low turbulence (low friction velocity) periods and then gap-filled via the R package REddyProc (Wutzler et al., 2018). REddyProc was used to partition NEE into GPP and Reco using the method of Lasslop et al. (2010), with air temperature used as the driving temperature for Reco.	Data for NEE and meteorological variables were filtered to remove low turbulence (low friction velocity) periods and then gap-filled via the R package REddyProc (Wutzler et al., 2018). REddyProc was used to partition NEE into GPP and Reco using the method of Lasslop et al. (2010), with air temperature used as the driving temperature for Reco.
Air Temperature (Tair) & Relative Humidity (RH)	Vaisala HMP45C probe at 6 m	Vaisala HUMICAP Humidity and Temperature Probe - HMP 155 at 22 m (National Ecological Observatory Network (NEON), 2022b)

Continued on next page

Table 3.2: Summary of methods for measurement and data processing (Continued)

Measurement	**SOBS/Ca-Obs**	**DEJU, US-NR1, OSBS**
Soil Temperature (Tsoil)	Type-T (copper-constan) thermocouples at a 10 cm depth	Thermometrics - Climate RTD 100-ohm Probe at 6 cm depth (National Ecological Observatory Network (NEON), 2022c)
Soil Volumetric Water Content (SWC)	Cambell Scientific CS615 Water Content Reflectometers at a 7.5 cm depth	Sentek - EnviroSCAN TriSCAN at 6 cm depth (National Ecological Observatory Network (NEON), 2022d)

CHAPTER 4

Tower-based remote sensing reveals mechanisms behind a two-phased spring transition in a mixed-species boreal forest

4.1 Introduction

The boreal forest is a major contributor to the global carbon and water cycles and is one of the regions most sensitive to environmental change (Thurner et al., 2014; Bonan, 2008). Climate change has led to an earlier spring onset and longer growing season, but the potential impacts of this change on the annual carbon balance and seasonal vegetation phenology remain uncertain (Schaefer et al., 2014; Fisher et al., 2018; Goetz et al., 2005; Fu et al., 2017; Richardson et al., 2010). Contributing to this uncertainty, global climate models currently fail to accurately predict the onset of spring photosynthesis (Commane et al., 2017; Peng et al., 2014; Parazoo et al., 2018; Richardson et al., 2012). This is partly due to difficulties in accurately measuring the onset of spring photosynthesis through remotely sensed products, and partly due to uncertainties in understanding the environmental controls on the timing and rate of spring photosynthetic recovery (Jeong et al., 2017, 2011). Overcoming these challenges is therefore critical for understanding the fate of the boreal region in the context of climate change.

Studying the boreal forest spring recovery is challenging, in large part, because it has widespread mixed forest stands with both deciduous and evergreen species. Trees within these stands experience the same environmental conditions but exhibit vastly differing life strategies in both their short-term (daily) functioning (Pappas et al., 2018) and their long-term (monthly) seasonal dynamics (Reich, 2014). During fall, deciduous species drop their leaves and go into a long-term winter dormancy before regrowing them in the spring. This strategy allows deciduous plants to avoid both damage due to freezing and photodamage caused by the absorption of winter sunlight which they are unable to use to drive photosynthesis. Evergreen trees, on the other hand, retain their needles, and must undergo biochemical changes to downregulate photosynthesis in the winter months while still absorbing appreciable sunlight (Ensminger et al., 2004). To do this, evergreens transition from rapidly reversible non-photochemical quenching (NPQ), typical of summer, to sustained NPQ for winter by changing their photoprotective pigments associated with the xanthophyll cycle (Adams et al., 2004; Verhoeven, 2014). During winter, to support sustained NPQ, needles accumulate and retain zeaxanthin and there is an overall increase in the xanthophyll pigment pool size (Gilmore and Ball, 2000). Therefore, in spring, evergreens decrease their bulk carotenoid pigments (including xanthophyll pigments), but maintain high levels of zeaxanthin and antheraxanthin so they can rapidly shift their photoprotective state during the day for protection during high light conditions. Throughout the year, changes in chlorophyll can be much smaller than changes in carotenoid pigments (Gilmore and Ball, 2000; Bowling et al., 2018) and as a result, there is an increase in the ratio of chlorophyll to carotenoid pigments (Chl:Car) in spring and a decrease in winter (Oh et al., 2013; Ottander et al., 1995; Adams III et al., 2002; Öquist and Huner, 2003). The difference in the spring recovery process between evergreen and deciduous species, and the multiple biochemical processes evergreen species undergo, has led to several remotely sensed products, from the leaf to the satellite scale, to investigate the spring transition, each with their own advantages and disadvantages.

Greenness based indices such as the Normalized Difference Vegetation Index (NDVI) and the Near-Infrared Reflectance from Vegetation (NIRv), among others (EVI, GEMI, SAVI, etc.), have been used to successfully track vegetation cover and productivity across biomes (Tucker, 1979; Badgley et al., 2019). NDVI provides an estimate of canopy chlorophyll content in a pixel and therefore tracks the spring onset well in deciduous forests and grasslands (Yang et al., 2017; Wang et al., 2019). However, NDVI is sensitive to non-vegetated surfaces such as clouds, snow and water, and saturates at high leaf area index (LAI) - all of which present challenges for decoupling vegetation productivity from other artifacts that are particularly present in the boreal forest (Gamon et al., 2013). NIRv goes a step beyond NDVI in that it isolates the vegetated signal by amplifying the near-infrared reflectance, and is therefore less sensitive to snow cover and other confounding signals (Badgley et al., 2017, 2019). However, greenness based indices do not provide plant functional information related to photosynthetic activity or light use efficiency (LUE) (Gitelson and Gamon, 2015). Therefore, they may fail to capture the photosynthetic activity of evergreen species that remain green year round despite a complete downregulation of photosynthesis (Magney et al., 2019a; Badgley et al., 2019; Sims et al., 2006b; Garbulsky et al., 2010).

Two other vegetation indices, the Photochemical Reflectance Index (PRI) and the Chlorophyll Carotenoid Index (CCI), are also promising metrics for detecting seasonal changes in evergreen photosynthesis because they are connected to photosynthetic phenology of evergreen conifers and have been shown to be viable indices for tracking seasonal photosynthetic activity at leaf and canopy scales for evergreen species (Wong and Gamon, 2015b; Gamon et al., 2016; Springer et al., 2017; Gamon et al., 1992). PRI acts as an indicator of short-term xanthophyll cycle activity while CCI is sensitive to the seasonal behavior of bulk carotenoid pigment pools - including the seasonal retention of xanthophyll pigments (Gamon et al., 1992, 2016). However, several studies have shown that PRI can vary substantially over longer time scales and the PRI/LUE relationship can change dramatically under changing environmental conditions such as altered nutrient status, (Gamon et al., 1997), water status (Filella et al., 2004; Sims et al., 2006a), and temperature (Porcar-Castell et al., 2012). Furthermore, variability in PRI across different species outweighs biochemical responses of

PRI in one species (Atherton et al., 2017). This poses a significant challenge for spatially averaged measurements over mixed forest stands where changes in PRI could merely reflect changes in species breakdown. These potentially confounding and decoupled effects pose significant challenges for using PRI and/or CCI to determine the spring transition.

Finally, Solar-Induced Chlorophyll Fluorescence (SIF) is the small emission of red and far-red light from excitepd chlorophyll-a molecules. It is frequently used as a proxy for GPP, and has been used to represent the timing of spring GPP onset in Alaskan ecosystems from satellite measurements (Parazoo et al., 2018; Commane et al., 2017; Jeong et al., 2017; Luus et al., 2017; Walther et al., 2016). These satellite measurements, however, are spatially averaged over multiple vegetation types at a much coarser spatial resolution than traditional vegetation indices (e.g., 10 m - 500 m for Sentinel and MODIS reflectance; 2 km - 500 km for OCO2, TROMOMI, GOME-2 SIF). Satellite SIF is therefore more susceptible to mixing species specific information within the spring transition. In addition, spatial averaging is often inconsistent between satellites, thus worsening the problem. In fact, satellite-based morning overpasses show a delay in SIF onset relative to daily mean GPP from towers (Parazoo et al., 2018). In contrast, tower-based measurements of SIF have shown slight increases in SIF preceding changes in GPP, suggesting respiratory recycling of CO_2 before water transport and stomatal opening (Magney et al., 2019a). These contrasting results highlight the need for a more in-depth investigation of the linkages between SIF and carbon uptake during the spring transition.

To verify these remotely sensed products, photosynthesis, carbon uptake, and other plant functions can be locally inferred by eddy-covariance (EC) measurements (Baldocchi et al., 1988) as well as tree-specific stem radius measurements (Drew and Downes, 2009). EC measurements of net ecosystem exchange (NEE), and derived measurements of GPP, can be used to study reactivation of photosynthetic function. However, EC derived GPP is subject to large uncertainties, particularly during the spring transition in arctic ecosystems and mixed forest stands where initial fluxes can be especially small relative to the growing season maximum (Parazoo et al., 2018; Baldocchi, 2003). Within the EC footprint, the spring recovery of understory, deciduous, and evergreen species is captured in a spatially averaged product that cannot distinguish between species-specific recovery (Baldocchi, 2003). Therefore, EC derived GPP measurements are less effective at probing the species-dependent recovery of the widespread mixed forest stands found in the boreal region. Assessment of stem radius change with dendrometers, on the other hand, provides hourly-resolution, tree-specific measurements of growth and tree water relations (Zweifel and Häsler, 2001; Steppe et al., 2006; Zweifel, 2016). Stem radius measurements have been widely recognized as a useful indicator of drought stress but have more recently been used to study fundamental mechanisms underlying whole-plant functioning and growth (De Swaef et al., 2015). Stem radius change measurements can provide information on water uptake by trees during winter (Sevanto et al., 2006) and reveal a shift to springtime stem re-hydration (Turcotte et al., 2009). Therefore, stem radius measurements can allow us to better understand the species-specific spring recovery in mixed forest stands. Finally, the timing of the onset of growth from stem radius measurements provides additional valuable information on long-term sequestration of carbon and how this may change under future climate scenarios (Zweifel et al., 2010).

The variety of remotely sensed products and potential limitations of spatially integrated GPP measurements have led to large uncertainties in the timing of the spring recovery in needleleaf forests, and a broad range of proposed environmental controls for what drives this recovery. Proposed drivers include warmer air temperatures, increases in plant available soil water content, photoperiod, and thawing stems, needles, and soils (Ensminger et al., 2004; Parazoo et al., 2018; Öquist and Huner, 2003; Tanja et al., 2003; Wu et al., 2013). The exact controls of the spring recovery, however, remain uncertain (Ensminger et al., 2004). By understanding how evergreen and deciduous species respond to the spring recovery separately, we can better understand the information contained in spatially integrated remote sensing measures and more accurately determine the specific environmental controls relevant for the recovery of each species. Therefore, our ability to accurately determine the timing and drivers of the onset of the spring transition depends on our ability to utilize remote sensing metrics sensitive to physiological changes occurring in the boreal forest during this time.

The goal of this study is to explore how we can best utilize existing sets of remote sensing metrics to better characterize the timing and drivers of the spring transition in a boreal mixed forest. This includes utilizing a multivariate approach combining tower-based remote sensing with tree-level ecophysiological data to characterize: the onset of photosynthesis, pigment transitions, deciduous leaf-out, stem rehydration, the onset of transpiration, and the start of radial wood growth for individual species. Specifically, we seek to answer:

1. How can tower-based remote sensing products be used to determine the spring transition and what physiological mechanisms are they sensitive to?
2. What environmental conditions are driving changes in photochemical and biochemical regulation of the spring transition?

We explore the efficacy of remotely sensed metrics (NDVI, NIRv, PRI, CCI, and SIF) for determining the spring transition for both deciduous and evergreen species in the boreal forest. We compare co-located and concurrently recorded tower-based remote sensing metrics and ground measurements of stem radius change and tower-based measurements of GPP, all collected at a half-hourly resolution, to determine relevant physiological changes during the spring transition, and which of these changes can be measured with remote sensing. Using this information, we examine different environmental conditions that drive various stages of the spring transition. We used a random forest model to quantify the importance of different environmental conditions and qualitatively connected these conditions to periods of increased productivity to provide an explanation for what controls the spring transition.

4.2 Materials and Methods

4.2.1 Site Description: Southern Old Black Spruce

The study site (Southern Old Black Spruce, SOBS, Fluxnet ID CA-Obs) is located near the southern limit of the boreal forest ecotone in Saskatchewan, Canada (53.98°N, 105.12°W) (Figure 4.1). It is a mixed forest stand with stem density predominantly (90%) black spruce (*Picea mariana*), and scattered (10%) larch (*Larix laricina*) (Pappas et al., 2020a). Average canopy height at the site is ∼16 m for larch and ∼11 m for black spruce with a canopy leaf area index of ∼3.8 m^2m^{-2} (Chen et al., 2006). Wild rose (*Rosa woodsii*) and Labrador tea (*Ledum groenlandieum*) are the main understory vegetation, with ground cover consisting mainly of mixed feather mosses (*Hylocomium splendens, Pleurozium schreberi, Ptilium cristacastrensis*), with some peat moss (*Sphagnum* spp.) and lichen (*Cladina* spp.) (Gaumont-Guay et al., 2014). The soil is moderately-to-poorly drained with a 20-30 cm thick peat layer overlying waterlogged sand. The site is equipped with a twin scaffold tower at 25 m above ground level (agl), approximately twice the height of the forest canopy.

4.2.2 Remote Sensing: PhotoSpec

We collected co-located remotely sensed products (NDVI, NIRv, PRI, CCI, red SIF, far-red SIF) using PhotoSpec (see Grossmann et al. (2018) for detailed instrument description) in the spring of 2019 and 2020. PhotoSpec was installed at the top of the scaffolding tower (25m agl) facing due north. It has a narrow field of view (0.7 degrees) and a 2-D scanning capability which permits independent measurements of both black spruce and larch, giving it a unique advantage over spatially averaged satellite measurements. Our scanning strategy had three 'elevation scans' (scanning vertically) at 35°W (10 measurements), 0°N (24 measurements), and 35°E (10 measurements) that observed predominantly black spruce, and three individual targets on a larch (Figure 4.1). Individual measurements take approximately 20 seconds and the complete scan cycle repeats on a 30 minute loop.

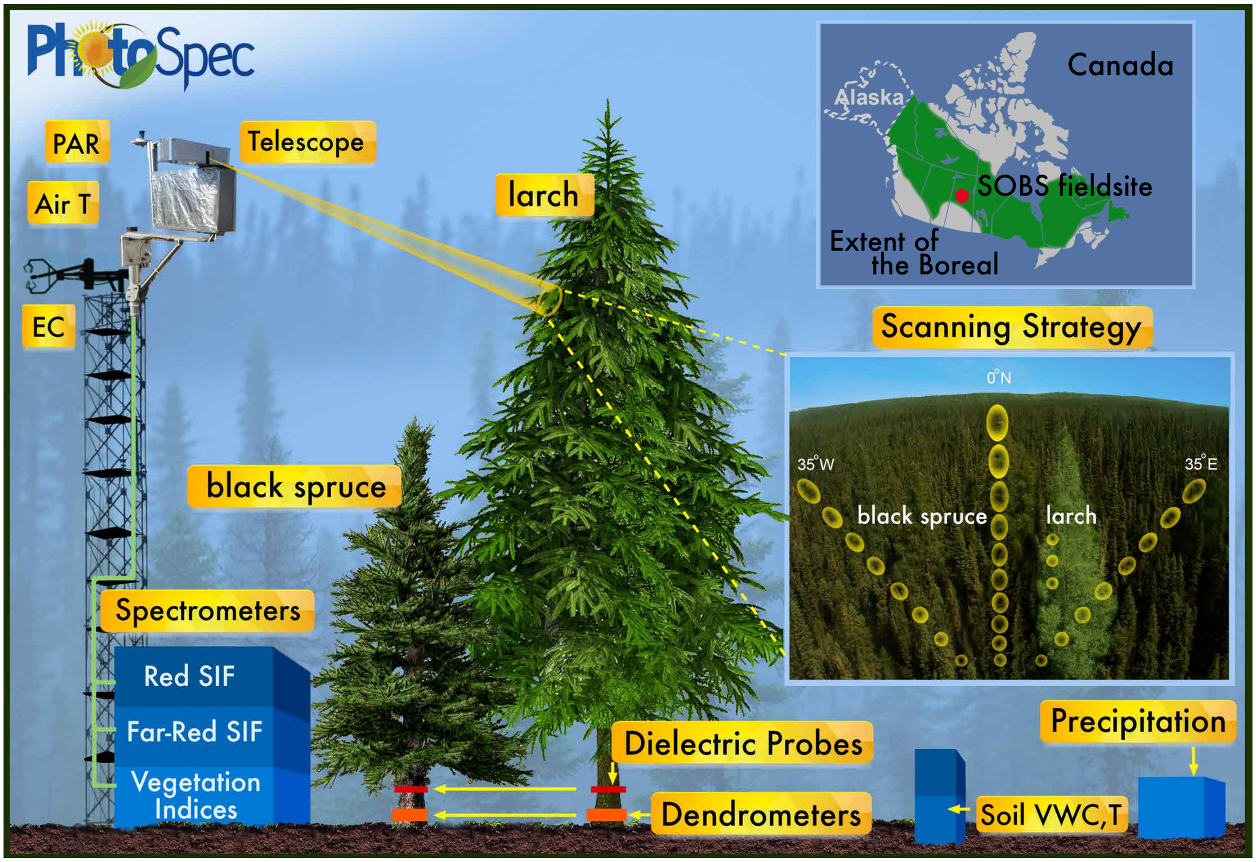

Figure 4.1: Field site location with PhotoSpec and support measurements at the Southern Old Black Spruce (SOBS) site in Saskatchewan, Canada. PhotoSpec set up is shown with an inset of the scanning strategy and measurement points on both black spruce and larch.

Vegetation indices were calculated as the following, with $\rho_{nm:nm}$ = the average reflectance across a wavelength range in nm:

$$\mathrm{NDVI} = (\rho_{830:860} - \rho_{620:670})/(\rho_{830:860} + \rho_{620:670}) \text{ (Tucker, 1979).}$$

$$\mathrm{NIRv} = (\rho_{830:860} - \rho_{620:670})/(\rho_{830:860} + \rho_{620:670}) \times \rho_{830:860} \text{ (Badgley et al., 2017)}$$

$$\mathrm{PRI} = (\rho_{569:571} - \rho_{520:532})/(\rho_{569:571} + \rho_{520:532}) \text{ (Gamon et al., 1992)}$$

$$\mathrm{CCI} = (\rho_{520:532} - \rho_{620:670})/(\rho_{520:532} + \rho_{620:670}) \text{ (Gamon et al., 2016)}$$

SIF was retrieved in the red (680-686 nm) and far-red (745-758 nm) wavelength ranges using a Fraunhofer-line based retrieval (Grossmann et al., 2018). Retrieval errors are calculated as outlined in Grossmann et al. (2018) and propagated through any calculation in this study. Our retrieval approach is comparable to those in Magney et al. (2019b,a); He et al. (2020). To decouple the physical (light, structure, viewing and solar geometries) from the physiological SIF signal, and account for variations in incident light and sun/shade fraction within the field of view, we calculated $\mathrm{SIF}_{\mathrm{relative}}$ (a proxy for $\mathrm{SIF}_{\mathrm{yield}}$) in both the red and far-red wavelength ranges as:

$$\mathrm{SIF}_{\mathrm{relative}} = \mathrm{SIF}/I$$

Where I is the near-infrared (NIR) radiance in the SIF retrieval window (680-686 nm for red and 745-758 nm for far-red) e.g.(Parazoo et al., 2020; Magney et al., 2019b).

We collected 1 second Photosynthetically Active Radiation (PAR) data and used these data to remove PhotoSpec measurements where PAR conditions changed significantly ($PAR_{std} > 0.2 * PAR_{avg}$) over the PhotoSpec integration time. We then filtered all data points for NDVI > 0.5 in order to remove points that were mostly obscured by snow or non-green vegetation (soil, branches, stems), although this process left some measurements with mixed pixels. A lower NDVI threshold (NDVI > 0.2) did not change results of our study and merely increased the scatter and snow responses of vegetation indices. We excluded low-quality retrievals where the SIF retrieval error was > 0.1 $Wm^{-2}sr^{-1}\mu m^{-1}$ and where SIF $<$ -0.1 $Wm^{-2}sr^{-1}\mu m^{-1}$ or SIF > 10 $Wm^{-2}sr^{-1}\mu m^{-1}$. Finally, we only considered data where the Solar Zenith Angle (SZA) $< 80°$ to remove data where low light conditions increase retrieval uncertainty.

We calculated species specific averages over each 30 minute period which were again averaged to report daily averages of $\mathrm{SIF}_{\mathrm{relative}}$ and reflectance measurements for both black spruce and larch in 2019 and 2020 (Figures 4.2 & 4.3).

Finally, days with significant snow cover, were identified visually using phenocam images at the site (`https://phenocam.sr.unh.edu/webcam/sites/canadaOBS/`) and highlighted in Figures 4.2 & 4.3. Our filtering strategy allowed us to effectively isolate remote sensing pixels predominantly filled with plants and identify periods with potential snow contamination.

4.2.3 Tree Water Status

4.2.3.1 Freeze/Thaw State: Dielectric Probes

The freeze-thaw state of the tree trunks was determined with dielectric probes inserted into three tree trunks (two black spruce, one larch). Three ruggedized soil moisture sensors (model GS-3; Decagon Devices, Pullman, Washington, USA) were installed directly into 5.6 cm pre-drilled holes (length of probes) within tree trunks, in order to provide a measure tree relative dielectric constant and tree skin surface temperature. The probes are sensitive to liquid water, as liquid water has a near constant dielectric constant compared to frozen water. The dielectric constant (D) follows ambient temperature in winter, but is near constant when trunks are thawed in the spring (Roy et al., 2020; Matheny et al., 2015). We defined a daily range in the dielectric constant, $\Delta \mathrm{D} = \mathrm{D}_{max} - \mathrm{D}_{min}$, and classified trunks as frozen for $\Delta \mathrm{D} > 0.3$ and thawed for $\Delta \mathrm{D} < 0.3$ in 2019 and frozen for $\Delta \mathrm{D} > 0.5$ and thawed for $\Delta \mathrm{D} < 0.5$ in 2020 after reinstalling following probe failures in 2019. Re-calibration of the ΔD threshold in 2020 yielded no significant difference in the results.

4.2.3.2 Stem Radius: Dendrometers

We monitored stem radius change of 13 black spruce and 13 larch trees to determine water storage dynamics and the onset of transpiration. We used automatic dendrometers (DC3; Ecomatik, Dachau, Germany) to obtain half-hourly measurements of stem radius change at breast height. The data were recorded using HOBOUX120-006M data loggers, where each logger was connected to four dendrometers. The average stem diameter at breast height of monitored trees was 13 cm for black spruce and 18 cm for larch. We converted dendrometer measurements to μm and corrected for thermal sensitivity according to manufacturer's specifications. The recorded data were further processed to identify errors and sensor malfunctioning as a result of wildlife chewing wires, logger battery failure, and moisture interference. Identified periods of sensor malfunction and abnormal jumps were removed creating gaps in the specific sensor data record, which remained unfilled.

We investigated stem radius diurnal cycles and hydraulic signals to determine the timing of stem re-hydration and the onset of transpiration in the spring following the empirical approach proposed by King et al. (2013). We obtained diurnal cycle information by subtracting the daily mean from each measurement and removing growth trend. This provides only reversible stem radius change, attributable to tree water relations. In winter, when trees are dehydrated, the mean stem diurnal cycle shows a negative sinusoidal phase with patterns of minimum stem radius observed in the morning and maximum stem radius observed in the afternoon (daytime SR_{max} & nighttime SR_{min}). This cycle reflects changes in temperature as it induces nighttime frost-shrinkage and daytime bark swelling (Kozlowski and Winget, 1964; Loris et al., 1999; Tardif et al., 2001; Zweifel and Häsler, 2000; Ameglio et al., 2001) and is an important mechanism for winter acclimation (Pearce, 2001; Wisniewski et al., 2014). During the growing season, the mean stem diurnal cycle reverses and follows a positive sinusoidal phase which reflects the balance between water loss from transpiration at the canopy level and water uptake from the soil through the roots at night (Kozlowski and Winget, 1964; Zweifel and Häsler, 2001). Therefore, trees experience stem expansion at night when they refill internal storage and stem shrinkage during the day as water stores are depleted by transpiration that increases the tree water deficit (daytime SR_{min} & nighttime SR_{max}) (Zweifel et al., 2016; Steppe et al., 2006). Thus, tree radius varies daily because of transpiration-induced changes in water storage and potential in the stem (Perämäki et al., 2001). We used the shift in the diurnal cycle of tree trunk radii to indicate the onset of transpiration in the spring (Sevanto et al., 2006; Pappas et al., 2020b; King et al., 2013).

We infer radial growth of the trees following the zero-growth (ZG) approach (Zweifel et al., 2016). The ZG approach defines radial growth as the difference between the current measured stem radius (SR_t) and the maximum measured stem radius in the past (SR_0) so that ($SR = SR_t - SR_0$). We determined the onset of radial growth when SR exceeded the maximum radii from the previous growing season ($SR > 0$). The extracted growth signal is the total radial increment in tree diameter in μm per day. This approach assumes that radial growth only occurs when trees are fully hydrated without water deficit. This approach results in comparable patterns to other methods to determine tree radial growth (B. Eller et al., 2018).

4.2.4 Gross Primary Production

Eddy-covariance (EC) measurements of net ecosystem exchange (NEE) (μmol C m^{-2} s^{-1}) and friction velocity u* (m s^{-1}) were made from atop the site's 25m scaffold tower. The EC system consisted of a 3-D sonic anemometer (CSAT3, Campbell Scientific, Logan, UT) in combination with a closed-path infrared gas (CO_2/H_2O) analyzer (LI-7200 analyzer, Li-Cor, Lincoln, NE)) operated in absolute mode. The 30-min eddy fluxes were computed using the Eddy-Pro software (version 7.0.6, Li-Cor, Lincoln, NE). NEE was calculated as the sum of the measured CO_2 eddy flux at the instrument height and the change in CO_2 storage in the air layer between the instruments and the surface (Barr et al., 2006). Nighttime NEE values were rejected under calm conditions using a u* threshold of 0.30 m s^{-1}. Net Ecosystem Production (NEP) was estimated as -NEE assuming no losses via dissolved organic carbon. Finally, gaps in NEP were filled and NEP was partitioned into gross primary production GPP (μmol C m^{-2} s^{-1}) and total ecosystem respiration R_e (μmol C m^{-2} s^{-1}) using the standard Fluxnet-Canada method (Barr et al., 2004). After processing, we report daily average GPP for only 2020 (Figure 4.3 j), as 2019 GPP data were not recorded.

4.2.5 Environmental Variables

Air temperature and relative humidity were recorded in the canopy at 6 m height with a Vaisala HMP45C probe. Soil temperature measurements were taken with Type-T (copper-constant) thermocouples at two locations at a 10 cm depth below the living-moss layer and averaged together. Soil volumetric water content (VWC) was recorded at two locations at a 7.5 cm depth with Cambell Scientific CS615 Water Content Reflectometers and averaged together. Vapour pressure deficit (VPD) was calculated from air temperature and relative humidity. All environmental variables were recorded at a 30 minute time resolution and averaged together for daily resolution.

4.3 Results and Discussion

4.3.1 Remote Sensing and Stem Radius Results

Daily time series of vegetation indices, $\mathrm{SIF}_{\mathrm{relative}}$, ΔD, stem radius, environmental conditions, and GPP in 2019 and 2020 are presented in Figures 4.2 and 4.3, respectively. Snow days (as identified with phenocam images) are highlighted with shaded vertical gray bars. Important transitions in stem radius and water use are identified with vertical dashed lines and expanded upon in Figures 4.4, 4.5 & 4.6. Shaded error bars indicate the 5 day moving mean of twice the standard deviation of diurnal variability. In general, larch exhibit a larger standard deviation than spruce due to a more limited number of data points. Our results highlight the large seasonal differences between black spruce and larch and the variations between remotely sensed products.

During the winter to spring transition, NDVI and NIRv are relatively invariant for black spruce, but show rapid increases during larch leaf-out (Figures 4.2 a, b&4.3 a, b). Black spruce NDVI decreases as a response to snow days, despite filtering for NDVI > 0.5. These snow dates occur on April 7-10 and May 1-5 in 2019 (Figure 4.2 a), and March 31-April 2,

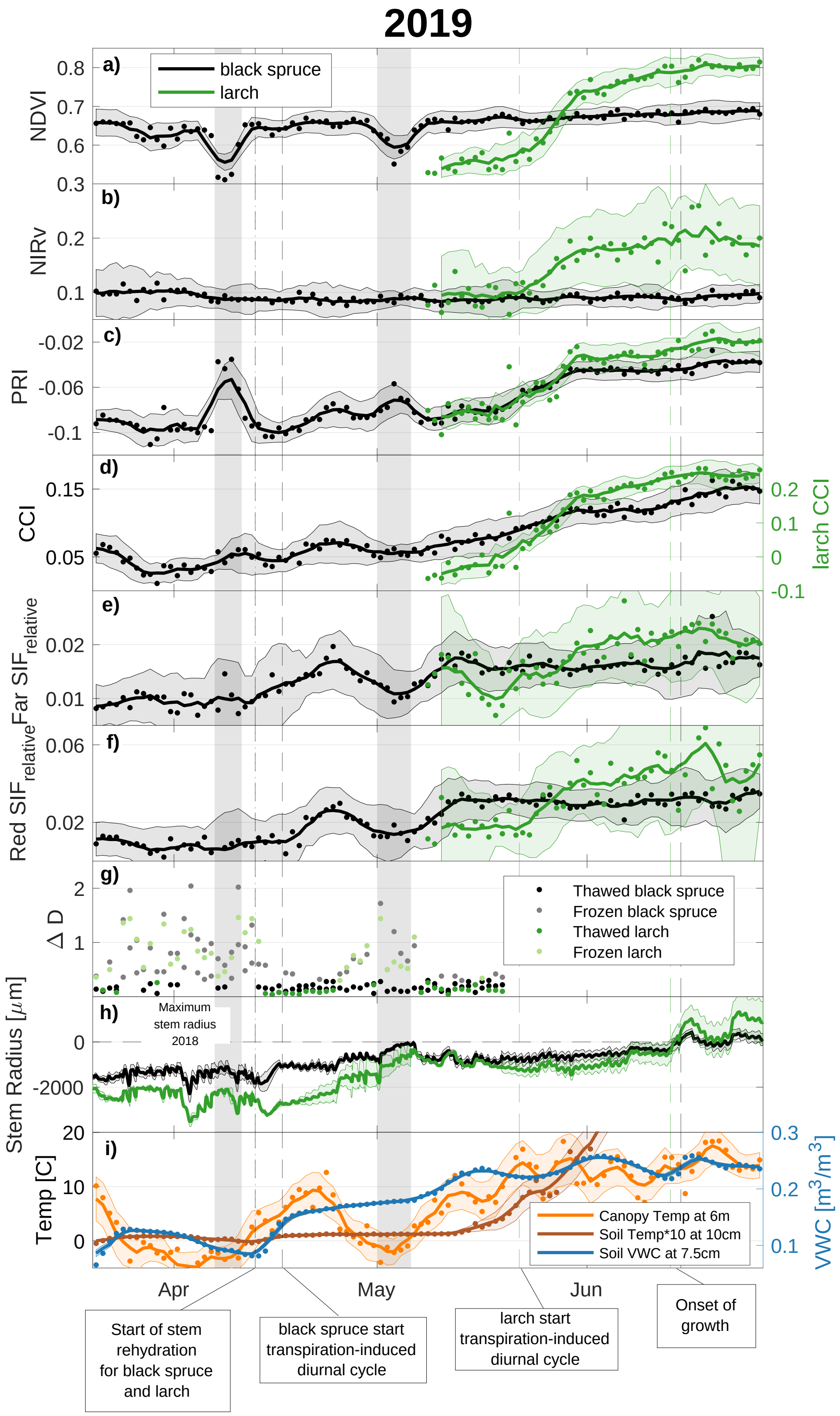

Figure 4.2: Data collected for the 2019 spring transition for both black spruce and larch. Periods of snow cover are shaded in gray. a)-f) show daily averaged PhotoSpec remotely sensed products with a 5 day moving mean. Shaded error bars are the 5 day moving mean of twice the standard deviation of the diurnal variability. g) shows the daily range in the dielectric constant. h) shows stem radius measurements. The zero line is the maximum stem radius from 2018. Shaded regions are twice the standard deviation among species specific dendrometers. i) shows daily average environmental conditions.

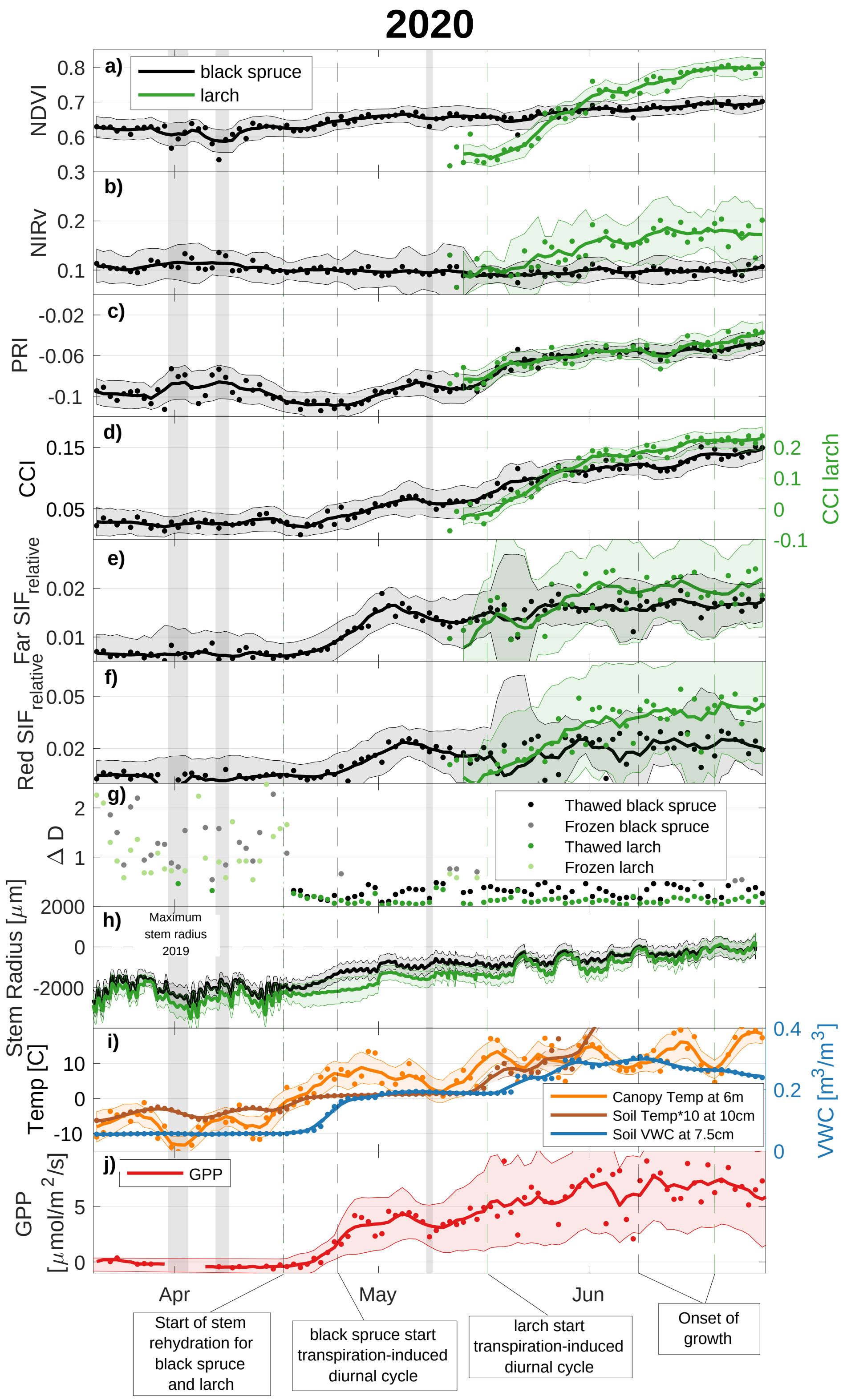

Figure 4.3: Data collected for the 2020 spring transition for both black spruce and larch. Periods where snow cover obscured remotely sensed products are shaded in gray. a)-i) are the same as Figure 2, but for 2020. j) shows daily average GPP.

April 7 & 8, and May 8 in 2020 (Figure 4.3 a). NIRv in black spruce does not show snow variability (Figures 4.2 b & 4.3 b). Larch leaf-out on May 22 in 2019, and May 17 in 2020 was captured with NDVI and NIRv and is supported by visual inspection of the phenocam data (Figures 4.2 a, b & 4.3 a, b).

PRI, CCI, red and far-red $\text{SIF}_{\text{relative}}$ show ecophysiologically relevant changes for both black spruce and larch (Figures 4.2 c, d, e, f & 4.3 c, d, e, f). Black spruce PRI increases as a response to snow cover in 2019 and 2020 (Figures 4.2 c & 4.3 c). In 2020, these responses are more subtle in the 5 day moving mean because periods of snow cover are much shorter than in 2019. Black spruce PRI increases slightly beginning April 17, 2019 and April 25, 2020, followed by large increases beginning May 22, 2019 and May 17, 2020. The PRI signal then levels off by June 1, 2019 and May 25, 2020. For larch, changes in PRI closely follow the timing of the leaf-out in both 2019 and 2020. CCI shows remarkably similar patterns to PRI, however, it is unaffected by snow cover in both 2019 and 2020. Black spruce CCI shows small increases beginning April 17, 2019 and April 25, 2020, that coincide with the small changes in PRI. CCI then decreases slightly in 2019 and levels off in 2020 for a short period of time, before increasing again around May 22, 2019 and May 17, 2020. This second increase in CCI is largely consistent with the larch leaf-out and the second increase in PRI. Larch CCI again follows the timing of leaf-out (Figures 4.2 d & 4.3 d). Black spruce red and far-red $\text{SIF}_{\text{relative}}$ increase prior to larch leaf-out in both 2019 and 2020 (Figures 4.2 e, f & 4.3 e, f). In 2019, $\text{SIF}_{\text{relative}}$ begins to increase starting April 17 and continues to increase through April 25. After April 25, $\text{SIF}_{\text{relative}}$ decreases through May 5 before increasing again and leveling off by May 13 (Figure 4.2 e, f). In 2020, $\text{SIF}_{\text{relative}}$ begins to increase on April 25 and continues to increase through May 2. $\text{SIF}_{\text{relative}}$ then decreases slightly May 2 through May 11, before increasing again slightly and leveling off by May 15 (Figure 4.3 e, f).

The daily range in the dielectric constant, ΔD, shows periods of frozen and thawed stems. In 2019, stem thaw began April 13, followed by a brief freeze starting April 25, and a thaw again on May 6 (Figure 4.2g). One of the black spruce trees remained thawed through the

April 25-May 6 re-freeze, which suggests an uneven freeze-thaw distribution among trees, although with only three points sampled this may merely be a reflection of tree diameter at the measurement point. In 2020, stem thaw occurred April 18 and stems remained thawed with a few exceptions on May 11, 12, and 15 (Figure 4.3). The freeze-thaw state of the stems in both 2019 and 2020 closely follows increases and decreases in air temperature (Figures 4.2 i & 4.3 i) as well as increases and decreases in $\mathrm{SIF}_{\mathrm{relative}}$ in black spruce.

Investigation of stem radius change shows typical patterns for winter and summer in both black spruce and larch in 2019 and 2020. Monthly average diurnal cycle (Figure 4.4) shows a temperature driven diurnal cycle in March, and a transpiration-induced cycle in June. King et al. (2013) observed similar patterns in diurnal cycle of Norway spruce (*Picea abies*) and European larch (*Larix decidua*) in the Swiss Alps.

During the transition months (April & May), the shift from temperature driven to transpiration-induced diurnal cycle in stem radius is tracked at a daily resolution for both black spruce and larch in Figures 4.5 a, d & 4.6 a, d for 2019 and 2020 respectively. Stem radius change for both species follows diurnal changes in air temperature (typical of winter) prior to April 13, 2019 and April 17, 2020. During this period in early spring, large variations in air temperature between day and night also result in large stem radius change amplitudes (Turcotte et al., 2009). This daily stem radius cycle is reversed on April 13 in 2019 and on April 17 in 2020, when stem radius maximum values are observed at predawn and stems have thawed according to ΔD. This indicates the onset of stem rehydration. Rainfall events induced an increase in stem radius and tree water storage refill for both species on April 15 & 16, May 10 & 15, 2019, and May 21, 2020.

Black spruce show a clear onset of the transpiration-induced diurnal cycle in stem radius on April 17 in 2019 and on April 25 in 2020 (Figure 4.5 a & 4.6 a). Larch do not show any clear cycle (beyond occasional stem rehydration) until later in the season, with the onset dates of May 22 in 2019 and May 18 in 2020 (Figures 4.5 d & 4.6). The switch to a transpiration-induced diurnal cycle on April 17 in black spruce corresponds with the start

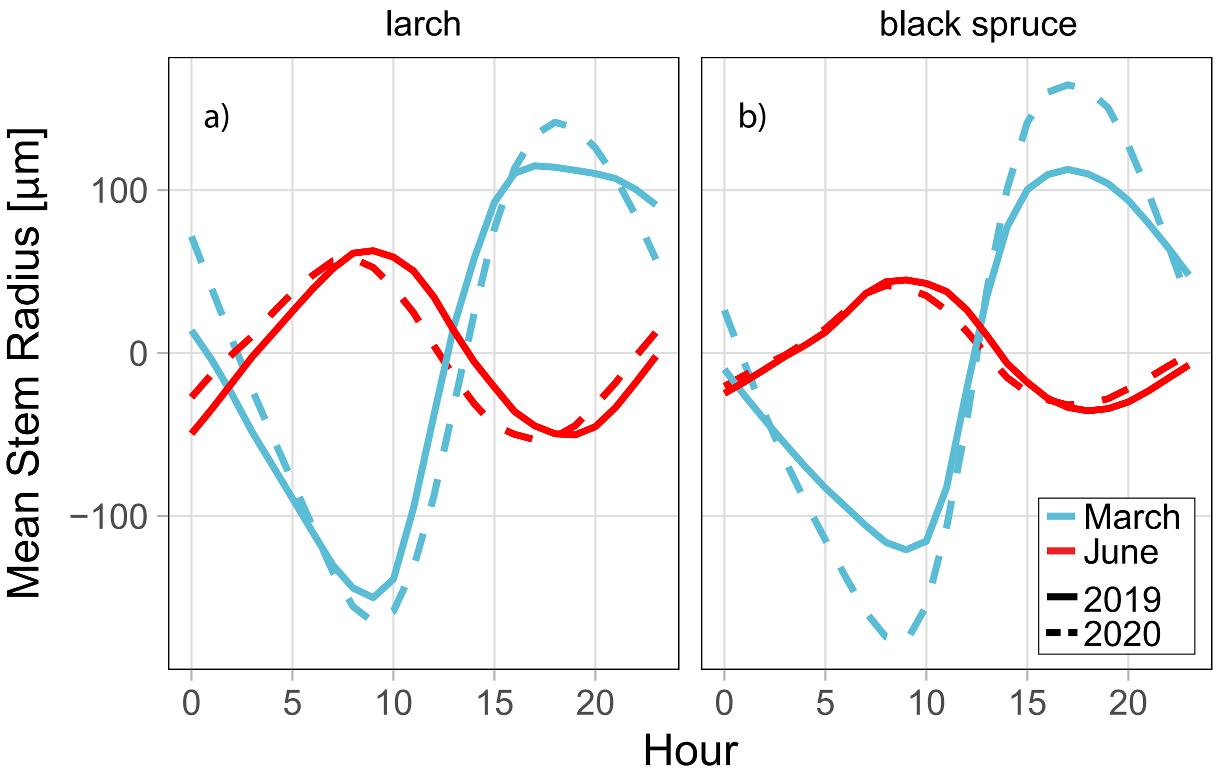

Figure 4.4: Mean monthly diurnal cycle of larch (a) and black spruce (b) in 2019 and 2020. Data show temperature driven diurnal cycle during March (winter) and a reversed pattern in June (summer) showing transpiration-induced cycle.

of the increasing $\text{SIF}_{\text{relative}}$ signals (Figure 4.2 e, f), while the transpiration-induced diurnal cycle in larch corresponds with the timing of the leaf-out, as observed in all larch metrics.

GPP data, reported for 2020, begins to increase around the same time as the switch to a transpiration-driven diurnal cycle in black spruce, and increasing black spruce $\text{SIF}_{\text{relative}}$ (Figure 4.3j). Furthermore, it shows a brief dip, consistent with the small dip in $\text{SIF}_{\text{relative}}$ from May 2 through May 11. GPP then continues to increase after the larch switch to a transpiration-driven diurnal cycle on May 17, while black spruce $\text{SIF}_{\text{relative}}$ levels off.

Stem radius measurements show the onset of radial growth occurring on June 13 for larch and June 14 for black spruce in 2019 (Figure 4.2 h) and June 8 for black spruce and June 19 for larch in 2020 (Figure 4.3 h). The onset of growth does not correspond with any changes

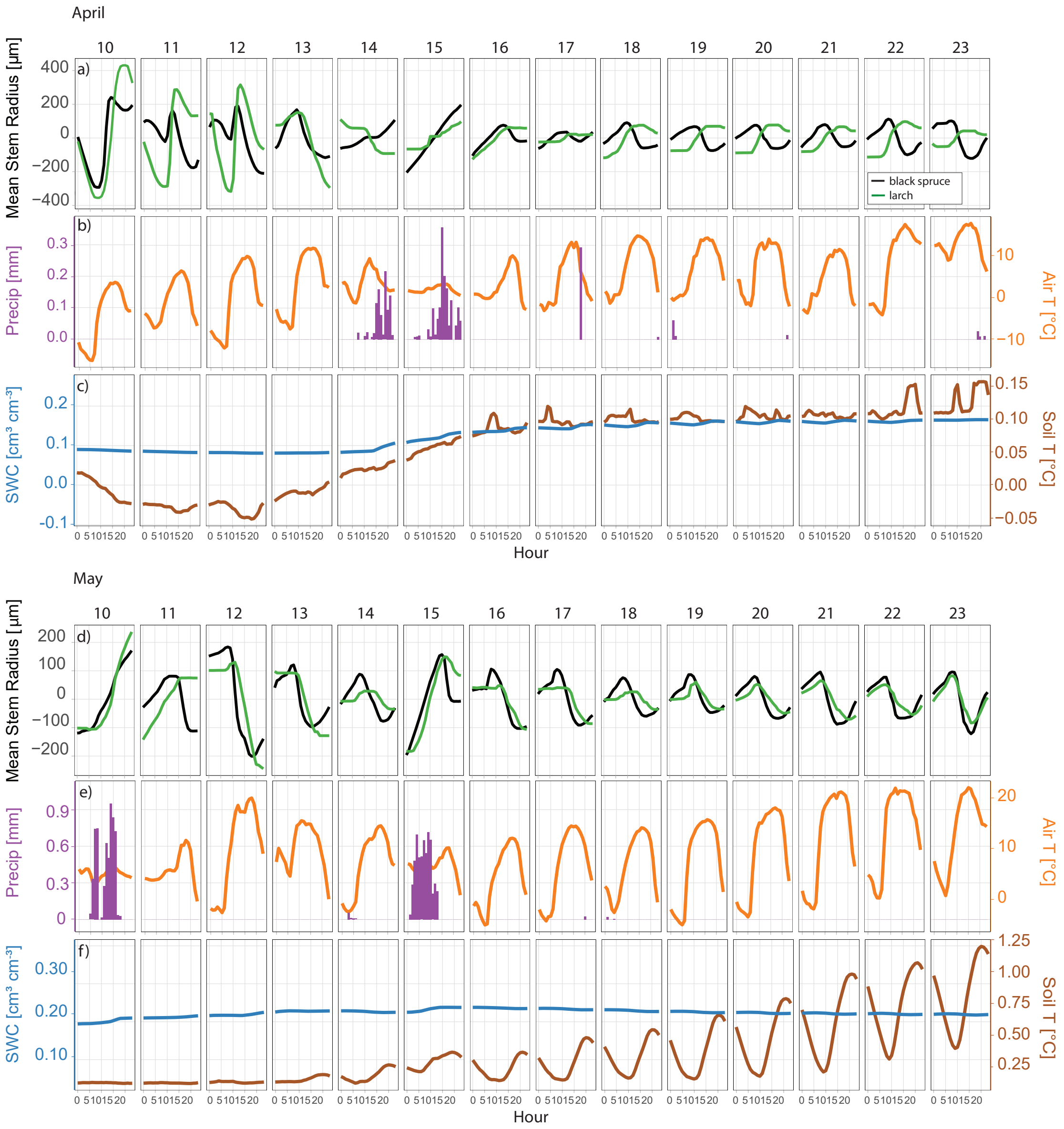

Figure 4.5: Half-hourly mean environmental variables and stem diurnal cycle during the onset of transpiration in April (a-c) and May (d-f) 2019. Panel a and d show mean stem radius (Mean SR) for black spruce and larch. Panel b and e show precipitation (Precip) and air temperature (Air T) during same time interval. Lower panels show soil volumetric water content (SWC) and soil temperature (Soil T). The number on the top of each panel indicates the day of the month.

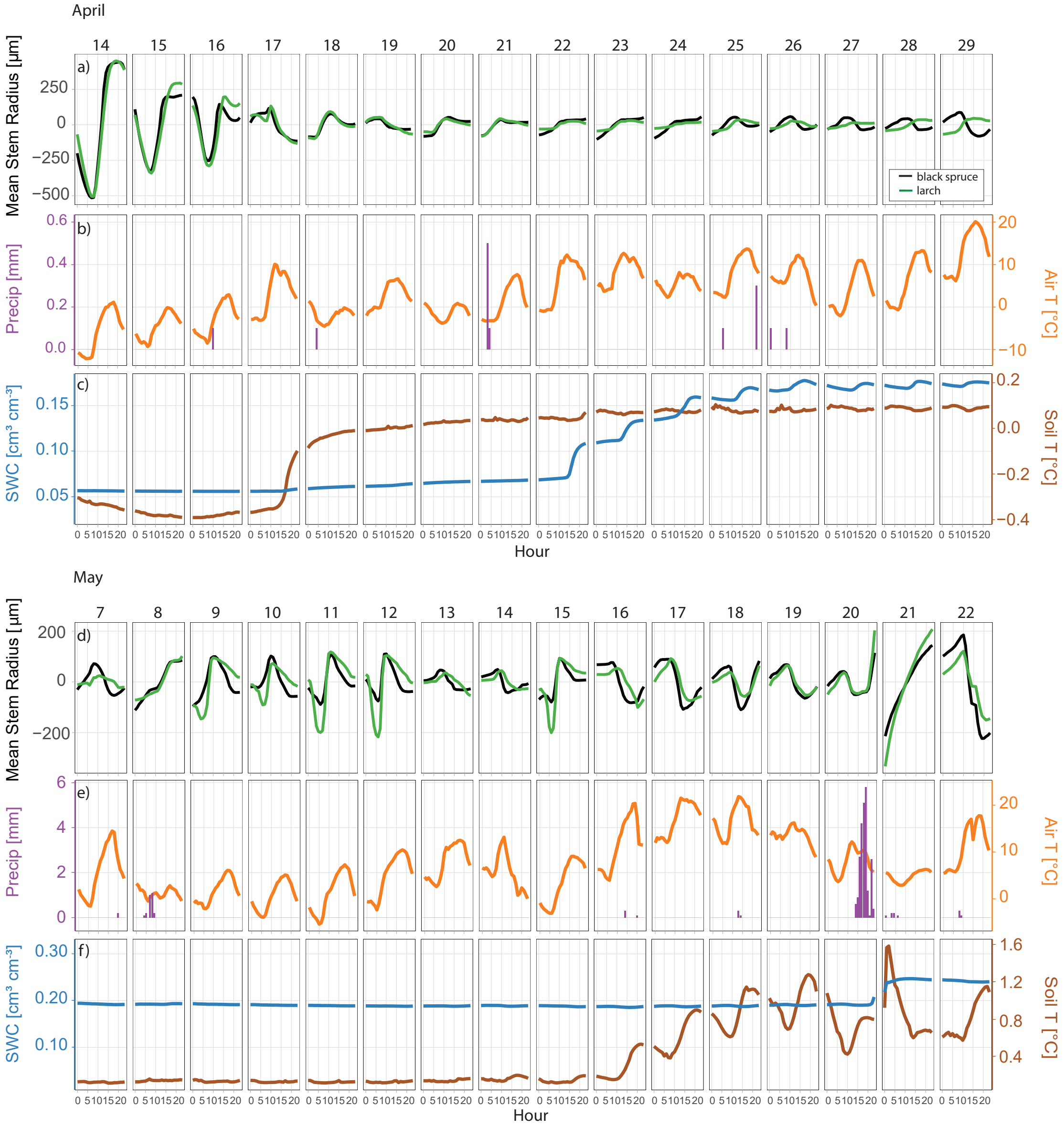

Figure 4.6: Half-hourly mean environmental variables and stem diurnal cycle during the onset of transpiration in April (a-c) and May (d-f) 2020. Panel a and d show mean stem radius (Mean SR) for black spruce and larch. Panel b and e show precipitation (Precip) and air temperature (Air T) during same time interval. Lower panels show soil volumetric water content (SWC) and soil temperature (Soil T). The number on the top of each panel indicates the day of the month.

in remotely sensed metrics.

These results indicate two periods of ecological importance for the spring transition, summarized in the first four rows of Figure 4.7. We propose the following ecophysiological explanation for this two-phased transition and what each remotely sensed product tells us about the spring transition.

4.3.2 Evaluation of Remotely Sensed Indices: A two-phase transition

During the spring transition, NDVI and NIRv show no physiologically relevant changes for black spruce which reflects a lack of variation in chlorophyll content throughout the transition (Magney et al., 2019a). Both indices do however successfully capture the larch leaf-out. NDVI fails to capture photosynthetic activity in evergreen species, and has an overall high sensitivity to snow cover (Magney et al., 2019a; Stylinski et al., 2002; Gamon et al., 2013) which is reflected in our results. NIRv overcomes the general sensitivity to snow cover (Badgley et al., 2017), making it a useful tool for separating snow and vegetation signals in the boreal forest where snow cover is particularly prevalent. NIRv scales well at sites where canopy structure co-varies with GPP (Baldocchi et al., 2020; Dechant et al., 2020). This explains why it tracks the larch leaf-out so well but fails to capture photosynthetic reactivation of black spruce, where canopy structure and crown architecture are a minor and de-coupled fraction of carbon uptake (Pappas et al., 2018, 2020a). Because NDVI and NIRv signals are mostly only variable for larch, and more specifically to changes in leaf presence, we suggest that satellite NDVI and NIRv measurements will be largely driven by the growth and senescence of the larch, or other deciduous species in the region. Other measured remotely sensed products (PRI, CCI, $\text{SIF}_{\text{relative}}$) show two periods of physiological changes that coincide with changes in stem radius and GPP.

The first phase of the transition is from April 13-May 23, 2019 and April 25-May 17, 2020. It is characterized by a variable $\text{SIF}_{\text{relative}}$ signal that closely tracks the freeze-thaw state of the stems, slight increases in PRI and CCI, a transpiration-induced cycle in black spruce

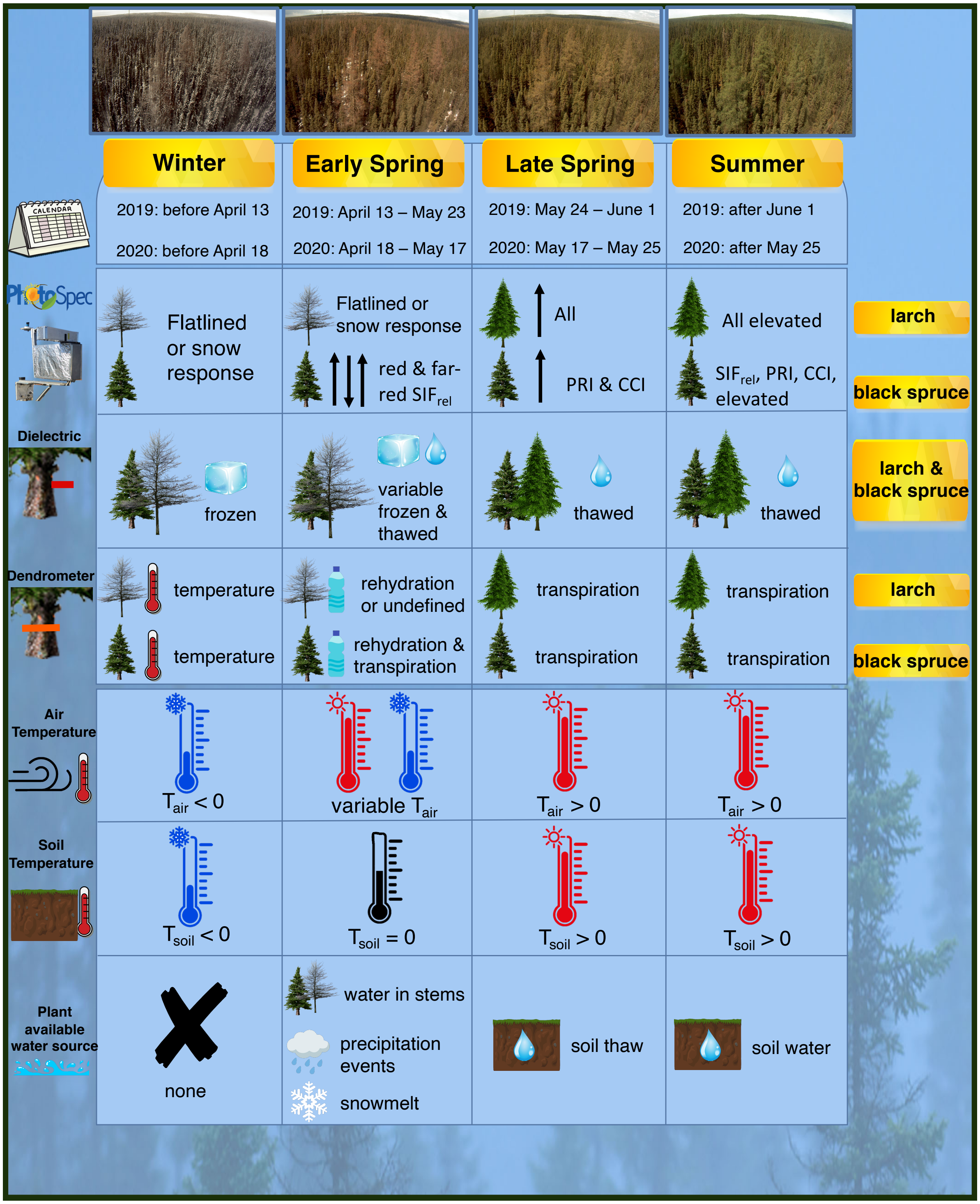

	Winter	Early Spring	Late Spring	Summer	
	2019: before April 13 2020: before April 18	2019: April 13 – May 23 2020: April 18 – May 17	2019: May 24 – June 1 2020: May 17 – May 25	2019: after June 1 2020: after May 25	
PhotoSpec	Flatlined or snow response	Flatlined or snow response	↑ All	All elevated	larch
		↑↓↑ red & far-red SIF_{rel}	↑ PRI & CCI	SIF_{rel}, PRI, CCI, elevated	black spruce
Dielectric	frozen	variable frozen & thawed	thawed	thawed	larch & black spruce
Dendrometer	temperature	rehydration or undefined	transpiration	transpiration	larch
	temperature	rehydration & transpiration	transpiration	transpiration	black spruce
Air Temperature	$T_{air} < 0$	variable T_{air}	$T_{air} > 0$	$T_{air} > 0$	
Soil Temperature	$T_{soil} < 0$	$T_{soil} = 0$	$T_{soil} > 0$	$T_{soil} > 0$	
Plant available water source	none	water in stems precipitation events snowmelt	soil thaw	soil water	

Figure 4.7: Summary of relevant periods in the winter to summer transition. Shown are relevant dates from 2019 and 2020; measured quantities from PhotoSpec, dielectric probes, and dendrometers; ecophysiologically relevant environmental conditions for each phase.

stem radius measurements, and elevated GPP (summarized in Figure 4.7). We propose that this first period can be explained by the re-activation of the rapidly reversible xanthophyll cycle and photosynthetic function in black spruce. Changes in black spruce red and far-red $\mathrm{SIF}_{\mathrm{relative}}$ during this time align closely with the shift from a temperature driven to a water flux driven (both rehydration and transpiration-induced) diurnal cycle in stem radius (Figure 4.7). Additionally, in 2020, this period coincides with the initial increase in GPP, supporting our use of dendrometers for determining the onset of transpiration and carbon uptake. In spring, the combination of transpiration (as shown by stem radius measurements and supported by GPP) and photosystem II activity (as suggested by increasing $\mathrm{SIF}_{\mathrm{relative}}$), suggests a change in photochemical efficiency and a reactivation of the rapidly reversible xanthophyll cycle. We therefore interpret changes in $\mathrm{SIF}_{\mathrm{relative}}$ (a proxy for $\mathrm{SIF}_{\mathrm{yield}}$) as signifying an increase in photochemistry and a subsequent drop in non-photochemical quenching, consistent with Porcar-Castell et al. (2014). Finally, red and far-red $\mathrm{SIF}_{\mathrm{relative}}$ signals agree well because at seasonal timescales, the ratio of red to far-red SIF in evergreen needles is primarily determined by chlorophyll concentration (Magney et al., 2019b), of which we observe little change in black spruce (represented by invariant NDVI and NIRv signals). Therefore, either red or far-red $\mathrm{SIF}_{\mathrm{relative}}$ will be effective at capturing the first phase of the transition.

Magney et al. (2019a) reported an increase in SIF prior to an increase in GPP in a subapline evergreen forest. This is not observed in our results (Figure 4.3). We suggest that the discontinuity observed by Magney et al. (2019a) may be attributable to the fact that GPP is spatially averaged over the flux footprint and will be influenced by recovery of understory following soil thaw and snow melt. Therefore, the recovery of understory may play a less important role at the SOBS site, however, the understory recovery has yet to be explored.

The second phase of the transition is from May 24-June 1, 2019 and May 17-May 25, 2020 (Figure 4.7). It is characterized by additional increases in PRI and CCI in black spruce, as well as the larch leaf-out and shift to a transpiration-induced stem radius cycle in larch.

Based on previous studies connecting PRI and CCI to changes in Chl:Car pigment ratios (Cheng et al., 2020; Wong and Gamon, 2015a; Stylinski et al., 2002; Filella et al., 2009; Garrity et al., 2011; Porcar-Castell et al., 2012), we interpret the increasing black spruce PRI and CCI signals as reflective of a decrease in bulk carotenoid pigments, which indicates a decrease in sustained photoprotection and a more permanent physiological shift for the growing season. Changes in CCI represent the seasonal behavior of Chl:Car pigment ratios (Gamon et al., 2016). Since NDVI is relatively invariant, we assume chlorophyll concentration and canopy structure remain largely stable. Therefore, increases in CCI are driven by a decrease in carotenoid concentrations (Gamon et al., 2016). PRI on the other hand is influenced by three distinct processes: the short term response related to the operation of the xanthophyll cycle, seasonally changing Chl:Car pigment ratios, and a shifting leaf albedo during periods of deep cold (Wong and Gamon, 2015a; Gamon and Berry, 2012). In spring, while the forest experiences both changes in the rapidly reversible xanthophyll cycle and increasing Chl:Car pigment ratios, increasing Chl:Car pigment ratios are the dominant driver of changes in PRI (Wong and Gamon, 2015a; Stylinski et al., 2002; Filella et al., 2009; Garrity et al., 2011; Porcar-Castell et al., 2012). This is why changes in PRI during the first phase of the transition with the reactivation of the xanthophyll cycle are smaller and more variable than the subsequent changes during the second phase.

To further test our interpretation of PRI, and a reactivation of the rapidly reversible xanthophyll cycle during the first phase of the spring transition prior to changes in pigment ratios, we analyzed light response curves using the 30 minute average data for PRI vs. PAR over a 10 day period during winter, spring, and summer in 2019 and 2020 (data not shown). The winter light response curves showed no appreciable change in PRI at high light levels indicative of sustained NPQ, as expected in winter (Gamon and Berry, 2012). Summer PRI light response curves showed a clear decrease in PRI at high light levels, indicative of rapidly reversible NPQ, as expected in summer (Gamon and Berry, 2012). Spring light response curves during all phases of the spring transition were highly variable and therefore inconclusive. We attribute the variability of the spring light response curves to a mixture of offsetting responses to temperature, direct/diffuse light conditions, and viewing direction effects. Given these potential sources of error, and findings from previous studies on drivers of PRI during spring (Wong and Gamon, 2015a; Porcar-Castell et al., 2012), we attribute the changes in PRI as consistent with a shift in bulk Chl:Car pigment ratios, which is further supported by our analysis of CCI.

This two-phased interpretation of the spring transition supports previous work which proposes a decoupling of the reactivation of the diurnal xanthophyll cycle and increasing Chl:Car pigment ratios for evergreens in spring, with the reactivation of the xanthophyll cycle occurring as an early step (Wong and Gamon, 2015b; Porcar-Castell et al., 2012). We observe a slow increase in CCI and PRI during the first phase of the transition. However, these indices don't dramatically increase and level off before the second stage of the spring transition as we observe in the $\text{SIF}_{\text{relative}}$ signals (Figures 4.2&4.3). Therefore, we propose that the secondary (and more pronounced) increase in CCI and PRI signifies major changes in the Chl:Car pigment ratios. This change in pigment ratios marks the second stage of the spring transition as a more permanent shift away from sustained photoprotection for the growing season. Finally, we propose that CCI is a more useful measure of seasonal pigments behavior over winter and during the transition seasons compared with PRI due to its resiliency against snow contamination, and its fewer potential drivers.

The onset of radial growth occurs after the two phases of the spring transition and is not captured by any remote sensing metrics in this study. This is consistent with Eitel et al. (2020), who showed changes in PRI prior to radial stem growth and Zweifel et al. (2010), who showed photosynthetic carbon uptake before radial growth in evergreen species. This highlights the inherent inability of remote sensing to account for long-term above ground carbon storage and carbon partitioning following C assimilation through photosynthesis.

4.3.3 Environmental Drivers of the Spring Transition

4.3.3.1 Statistical Identification of Important Environmental Drivers

To explore the environmental drivers of the two phases of the spring transition, we used random forest models and a qualitative analysis of environmental conditions and the forest's ecophysiological response. A random forest model was chosen because it is non-parametric and is more suitable for approximating nonlinear relationships in complex systems. We used Matlab's TreeBagger function to train 1000 random forest models, each with 100 regression trees using the daily average data from March 20th-June 27th, for 2019 and 2020 separately, to capture the full spring transition and to allow a qualitative comparison with the time series of the two years. Input variables were daily averaged PAR, soil volumetric water content (VWC), soil temperature, air temperature, and vapor pressure deficit (VPD). Response variables were either daily averaged red $\mathrm{SIF}_{\mathrm{relative}}$, far-red $\mathrm{SIF}_{\mathrm{relative}}$, PRI, or CCI, for both black spruce and larch. We removed all data points that had snow contamination (as identified with visual examination of phenocam images and indicated in Figure 4.2). We averaged the unbiased predictor importance estimates and out-of-bag R^2 values of the 1000 trials to arrive at the data presented in Figure 4.8.

The random forest model identified important environmental drivers for the spring transition, as characterized by remotely sensed products, shown in Figures 4.8 & 4.9. In black spruce, the important predictor variables were different depending on the physiologically sensitive remotely sensed response variable in question, with some small differences between 2019 and 2020. Black spruce red $\mathrm{SIF}_{\mathrm{relative}}$ in 2019 and black spruce far-red $\mathrm{SIF}_{\mathrm{relative}}$ in 2019 and 2020 are best predicted by soil temperature, soil VWC, and air temperature (Figures 4.8 a, c & 4.9 c). Black spruce red $\mathrm{SIF}_{\mathrm{relative}}$ in 2020 has a more even distribution of dependencies, with soil VWC and soil temperature most important (Figure 4.9a). We hypothesize that black spruce red $\mathrm{SIF}_{\mathrm{relative}}$ in 2020 shows slightly different predictor variables than all other $\mathrm{SIF}_{\mathrm{relative}}$ measurements because it is more poorly predicted (R^2 = 0.66) than other

$\mathrm{SIF}_{\mathrm{relative}}$ measurements (black spruce red $\mathrm{SIF}_{\mathrm{relative}}$ 2019 $R^2 = 0.87$, black spruce far-red $\mathrm{SIF}_{\mathrm{relative}}$ in 2019 $R^2 = 0.71$, black spruce far-red $\mathrm{SIF}_{\mathrm{relative}}$ $R^2 = 0.87$). Predictor importances for black spruce PRI and CCI are remarkably similar in 2019 and 2020 and have soil temperature as the most important predictor (Figures 4.8 e, g & 4.9 e, g). In 2020 they also show a strong dependency on soil VWC and larger dependencies on air temperature than in 2019. The 2020 dependency is explained by a qualitative analysis of the environmental conditions present in the time series. The random forest model identified soil temperature as the dominant predictor for all larch variables in 2019 and 2020 (Figures 4.8 b, d, f, h & 4.9 b, d, f, h). Additionally, larch variables in 2020 show a greater dependence on soil VWC (Figure 4.9 b, d, f, h). The results from the random forest analysis support a qualitative analysis of the 2019 and 2020 time series (Figures 4.2 & 4.3) and daily breakdowns (Figures 4.5 & 4.6), and imply that the two phases of the spring transition are controlled by different environmental conditions as explained below and summarized in Figure 4.7.

4.3.3.2 Environmental Drivers of the two-phased transition

Phase 1: The Onset of Black Spruce Photosynthesis The first phase of the spring transition, the onset of black spruce photosynthesis, is marked by changes in black spruce red and far-red $\mathrm{SIF}_{\mathrm{relative}}$ which were best predicted by soil temperature, soil water content, and air temperature in the random forest model. Figures 4.2 & 4.3 show that this period of time for both 2019 and 2020 is characterized by the following environmental conditions: variable air temperatures above and below zero, soil temperatures at zero, and slow increases in soil water content following precipitation events (summarized in Figure 4.7). During this time, changes in energy balance, including air temperature effects, drive the freeze-thaw state of the stems (Figures 4.2 g, i & 4.3 g, i). Soil temperatures are approximately 0°C and do not follow diurnal variations in air temperature as observed later in the season due to the insulating properties of snow and the latent heat of frozen water (Figures 4.5 b & 4.6 b). Soil water content increases during precipitation events on April 14, 15, 16 in 2019, which

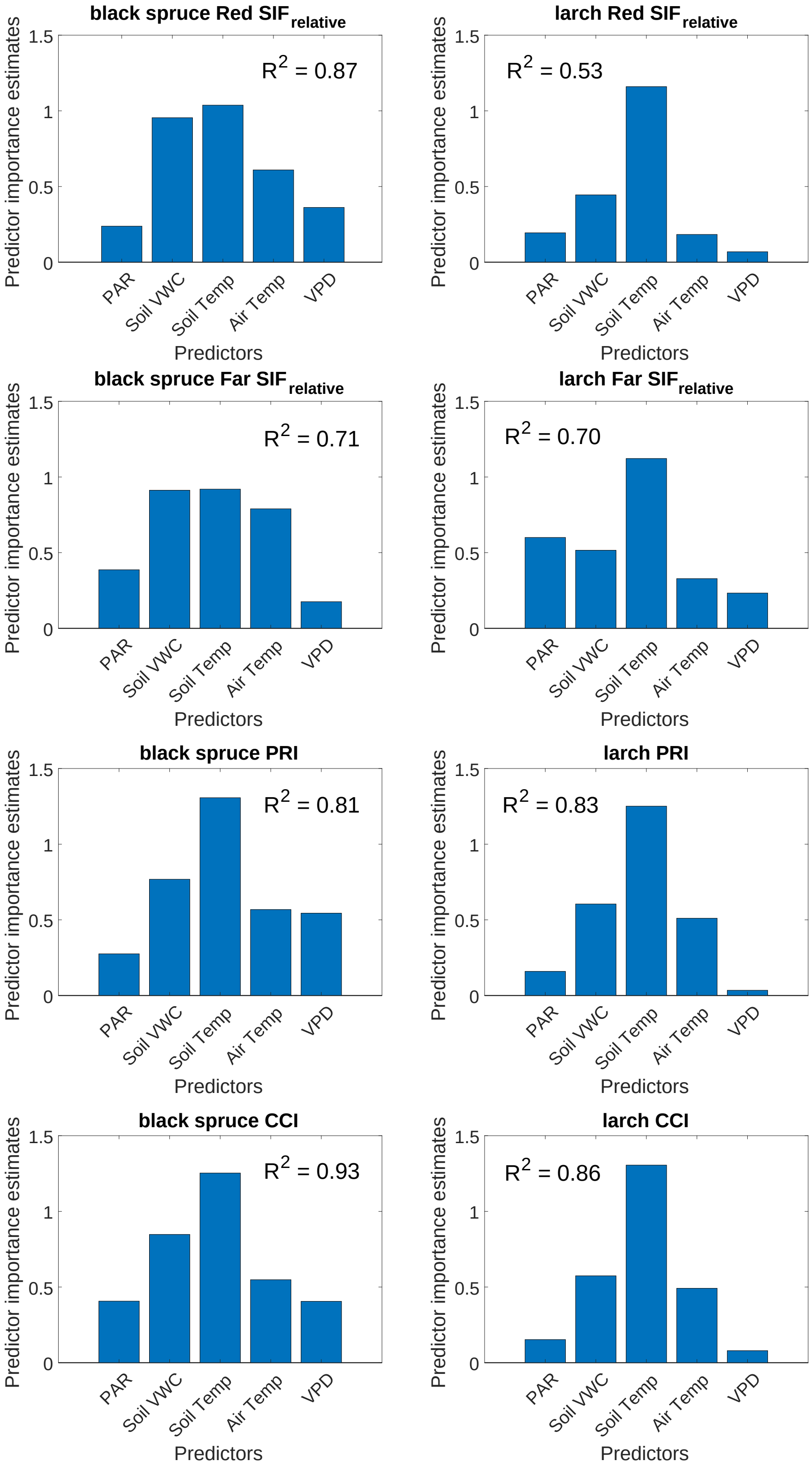

Figure 4.8: Averaged unbiased predictor importance estimates from 1000 repetitions of a random forest model from March 20th through June 27th 2019 for both black spruce and larch with snow days removed.

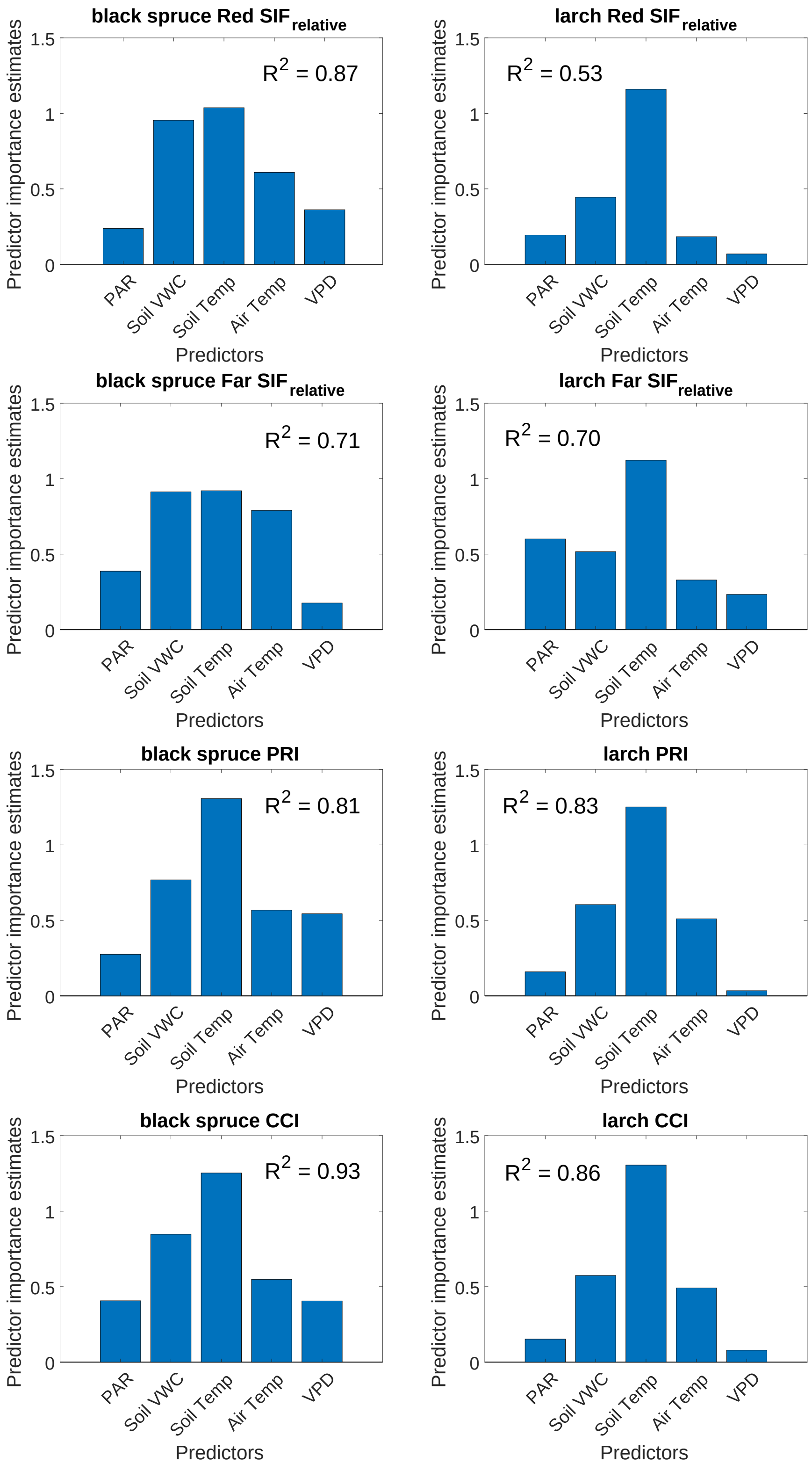
black spruce Red SIF$_{relative}$

larch Red SIF$_{relative}$

black spruce Far SIF$_{relative}$

larch Far SIF$_{relative}$

black spruce PRI

larch PRI

black spruce CCI

larch CCI

Figure 4.9: Averaged unbiased predictor importance estimates from 1000 repetitions of a random forest model from March 20th through June 27th 2020 for both black spruce and larch with snow days removed.

add water to the soil and aid in snow melt (Figure 4.5b). Following these precipitation events, we observe rapid stem rehydration shown in Figure 4.5a, similar to what has been previously observed with stem radius measurements following precipitation events (Tardif et al., 2001; Kozlowski et al., 1962; Kozlowski and Winget, 1964). Finally, increases and decreases in $\text{SIF}_{\text{relative}}$ closely follow increases and decreases in air temperature and small increases in soil water content during this time (Figures 4.2 e, f, i & 4.3 e, f, i). Therefore, we propose that the first phase of the spring onset is driven by the combination of increases in air temperature above 0°C, which thaws tree stems, coupled with small increases in soil water content, due to either precipitation events or snow melt (Figure 4.7). These favorable growing conditions drive the onset of photosynthesis in black spruce, and allow it to take advantage of early spring prior to larch leaf-out and the completion of soil thaw.

These results are consistent with previous studies that suggest that frozen stems both constrain the spring recovery and limit photosynthetic activity in winter, therefore making air temperature a key driver of photosynthetic reactivation in boreal systems (Bowling et al., 2018; Sevanto et al., 2006; Ensminger et al., 2004; Tanja et al., 2003). In a boreal Scots pine stand in Finland, the onset of stand photosynthesis was triggered by a rise in air temperature prior to complete soil thaw, much like what is observed at SOBS (Sevanto et al., 2006; Ensminger et al., 2004). Furthermore, the role of frozen stems as a key blockage to the water transport system, beyond availability of water, was highlighted in a Colorado evergreen system by Bowling et al. (2018). At SOBS, spring temperatures have additionally been most closely associated with inter-annual variability in GPP (Liu et al., 2019a). This highlights not only the importance of the timing of the spring onset of photosynthesis for the overall carbon balance, but also the importance of air temperature and the timing of stem thaw as important predictors of the spring onset of photosynthesis (Liu et al., 2019a; Bowling et al., 2018).

Severe intermittent low-temperature episodes during early spring have been found to not only halt but reverse the physiological recovery (Ensminger et al., 2004). In 2019, a cold snap from April 25-May 1 froze tree stems and led to a subsequent drop in $\mathrm{SIF}_{\mathrm{relative}}$ (Figure 4.2 i, g, e, f). This indicates a potential reversal of physiological recovery. There was a similar period of cold in 2020 from May 2-May 11, however temperatures during this period did not drop well below 0°C, and therefore did not lead to a freeze in the tree stems. The subsequent drop in $\mathrm{SIF}_{\mathrm{relative}}$ was therefore greatly reduced (Figure 4.3 i, g, e, f). Increased air temperatures and the freeze/thaw state of the stems alone, however, is insufficient for fully determining the reactivation of photosynthesis. This is highlighted by the difference in timing between stem rehydration and the onset of transpiration in 2019 vs. 2020.

In 2019 and 2020, trunk thaw coincided with the timing of stem rehydration in both black spruce and larch (Figures 4.2 & 4.3). This further supports the idea that air temperature is a key driver for a tree's access to water, through its influence on stem and soil thawing. In 2019, strong rehydration patterns for both black spruce and larch followed major rainfall events (4.73 mm total) and led to a rapid exponential increase in stem size (Figures 4.2 h and 4.5 a). In 2020 only minor precipitation events (1.79 mm total) occurred and did not lead to the same rapid increase in stem size (Figures 4.3 h and 4.6 a). Therefore, the black spruce transpiration-induced cycle (and increases in $\mathrm{SIF}_{\mathrm{relative}}$) started only four days after the onset of stem rehydration in 2019 (Figure 4.2). In 2020 it began seven days after the onset of stem rehydration and followed a slight increase in available soil VWC. The increase in available soil VWC was likely due to snowmelt or soil temperatures reaching a freeze/thaw equilibrium (Figure 4.3). These observations highlight the importance of accessible soil water content, in addition to thawed stems, for photosynthetic recovery and the role of early spring precipitation events.

Trees are able to access small soil water reservoirs despite partially frozen soils because soil temperatures at (or just below) 0°C do not inhibit photosynthesis or water uptake from the soil (Bergh and Linder, 1999; Sevanto et al., 2006). Frozen soils do, however, limit maximum sap flow and maximum photosynthetic capacity (Bergh and Linder, 1999), which limits the amount of water they are able to extract. This may explain why the spring recovery happens in two distinct steps: before and after complete soil thaw, and why evergreens recover prior to larch leaf-out. Soil temperature was identified as a dominant predictor for $\text{SIF}_{\text{relative}}$ because by the time soil thaw occurs, $\text{SIF}_{\text{relative}}$ is already elevated from the first phase of the spring onset, and therefore, soil thaw becomes a good predictor of elevated SIF.

Phase 2: Black Spruce Pigment Transitions and Larch Leaf-out The second phase of the spring transition is characterized by completely thawed soils (Figure 4.7). Soil temperature increases above 0°C and begins to follow diurnal changes in air temperature on May 15, 2019 and May 16 2020. Shortly after, we observe changes in black spruce PRI and CCI (Figures 4.2 c, d & 4.3 c, d), as well as larch leaf-out (Figures 4.2 a & 4.3 a) and larch transition to a transpiration-induced diurnal cycle (Figures 4.5 d & 4.6 d). Therefore, complete soil thaw is key for black spruce to make more permanent physiological shifts for the growing season. They do this by increasing Chl:Car pigment ratios and reaching maximum photosynthetic capacity, which is limited under frozen soil conditions (Bergh and Linder, 1999). Furthermore, with water access no longer limited, larch are able to use larger water stores to begin the leaf-out process. In 2020, soil VWC was identified as an important predictor of changes in black spruce PRI, CCI, and larch metrics. Figures 4.3 i & 4.6 f show that shortly after soil thaw occurs in 2020, soil VWC dramatically increases. We therefore attribute increases in soil VWC, after soil thaw, to ice melt, making soil temperature the dominant driver.

Soil thaw as a trigger for the spring photosynthetic onset has previously been reported in deciduous forests (Baldocchi et al., 2005), and in Alaskan boreal systems across varied vegetation types (Parazoo et al., 2018). Early photosynthesis prior to soil thaw, however, was observed in predominantly evergreen systems (Parazoo et al., 2018). We suggest that since GPP-based metrics are spatially integrated, they may show landscape thaw as the dominant predictor for carbon uptake in mixed stand forests due to the influence of deciduous species and understory recovery. Furthermore, this may also impact satellite-based measurements, as the larch and other deciduous species have large crown areas compared with black spruce (Pappas et al., 2018), and therefore may impact the satellite signal much more.

4.3.4 Further Implications

Our results, and previous work, show the complexities of wintertime photosynthesis and the spring transition in needleleaf forests and uncertainties associated with future warming scenarios. On the one hand, previous work in a boreal forest in Finland has suggested that wintertime rates of photosynthesis in evergreen systems are possible through small water reservoirs stored in the stems (Sevanto et al., 2006). However, Bowling et al. (2018) found no evidence of wintertime photosynthetic activity in an evergreen system in Colorado despite temperatures being warm enough to thaw stems. While we did not explore wintertime photosynthesis, our results suggest that if there are viable sources of water following precipitation events or soil temperatures at 0°C in thermal equilibrium, wintertime photosynthesis may be possible at the SOBS site. We acknowledge that sustained NPQ during winter may maintain the forests dormant state and prohibit photosynthetic activity during winter (Bowling et al., 2018). However, the recovery of SIF and photosynthetic function prior to the shift in bulk pigment ratios suggests a potential, more dynamic, recovery of photosynthetic activity in winter may be possible. On the other hand, a higher variability of freeze-thaw cycles (Mellander et al., 2007) could have serious consequences for tissue mortality during springtime frosts (Richardson et al., 2018), if the combination of thawed trunks and soils leads to an earlier springtime reactivation, as suggested by our results. Frequent pigment sampling or continuous PAM fluorescence (Porcar-Castell et al., 2012) at a daily or sub-daily resolution, both over winter and during the spring recovery, would provide the necessary information on the reactivation of the rapidly reversible xanthophyll cycle during these times. Furthermore, analysis of wintertime dendrometer and dielectric measurements combined with remote sensing metrics may provide a better view of species-specific wintertime photosynthesis than spatially integrated measures.

The variability of the $\mathrm{SIF}_{\mathrm{relative}}$ signal, and the reversal of photosynthetic recovery due to severe cold weather events (described in Phase 1), means that care must be taken during the spring transition to resolve remote sensing signals. Simple break point metrics that determine a 'cutoff' date for the spring recovery may fail to capture the dynamic nature of evergreens during this time which may therefore account for many of the uncertainties in the timing and drivers of the spring recovery. Furthermore, in mixed forest stands, the different recovery strategies of deciduous and evergreen species will further complicate a break-point method, and pose significant challenges for spatially integrated measures of the spring recovery such as satellite measurements and EC derived GPP.

Our results highlight the necessity of spatially downscaling remote sensing metrics over diverse landscapes during the spring onset. Based on our results, we propose that satellite signals of NDVI and NIRv will be predominantly driven by deciduous dynamics, although further work is necessary to explore these nuances. Furthermore, prior work (Atherton et al., 2017), has shown how PRI is more variable between species than the biochemical responses of each species individually, which will pose significant complications for PRI from satellite measurements. The PRI signals of black spruce and larch agree well in our study, however, further work is necessary to understand how spatial averaging of this data complicates our understanding of LUE and pigment transitions. Finally, species specific responses are spatially averaged in GPP and pose a significant challenge for breaking down the SIF/GPP relationship in mixed forest stands. The larger crown area of deciduous species may contribute to a much higher SIF signal than evergreen species, despite contributing less to the GPP signal. Future work combining dendrometer, GPP, and remote sensing metrics will help to clarify the role that individual species play in these signals.

4.4 Conclusions

We explored the efficacy of remotely sensed metrics for determining the spring transition for deciduous and evergreen species in the boreal forest and examined environmental controls for the spring transition. We found that evergreen black spruce experience a two-phase spring transition which can be observed using remote sensing metrics, and that these two phases have different environmental controls. The first phase of the transition, the onset of photosynthesis, was detected with relative solar-induced chlorophyll fluorescence and depended on warm air temperatures to thaw the tree stems and an increase in plant available water content in the soil through snow-melt or precipitation events. The second phase of the transition, the change in bulk pigment ratios, was detected with vegetation indices PRI and CCI and began after the soil had completely thawed which gave trees greater access to water stored in the soil. Deciduous larch depended on soil thaw for leaf-out and all remotely sensed metrics were able to detect the leaf-out. We suggest that inter-species differences in the timing and drivers of the spring transition contained in integrated GPP-based estimates, or spatially averaged satellite signals, may account for many of the differences and disagreements on the timing and drivers of the spring transition in existing literature. Therefore, incorporating trait information into such estimates is essential for understanding why these differences exist. Finally, our results highlight the value of a multivariate approach combining continuous tree-level observations with tower-based remote sensing products as a way to study physiological processes on a tree-by-tree basis. This approach provides insight into the drivers of spatially averaged EC measurements and satellite observations.

CHAPTER 5

Diurnal and seasonal dynamics of solar-induced chlorophyll fluorescence, vegetation indices, and gross primary productivity in the boreal forest

5.1 Introduction

Uncertainties in future climate projections are, in large part, due to an incomplete understanding of terrestrial carbon and ecosystem feedbacks (Friedlingstein et al., 2014). Among the most poorly understood ecosystems is the boreal forest, which stores a significant amount of carbon and is one of the regions most sensitive to environmental change (Thurner et al., 2014; Bonan, 2008; Schaefer et al., 2014; Fisher et al., 2018; Goetz et al., 2005; Fu et al., 2017). Therefore, a more complete understanding of environmental controls on boreal forest productivity is critical for predicting future carbon cycle feedbacks in this ecosystem (Anav et al., 2015; Parazoo et al., 2018).

Remotely sensed metrics are a powerful tool for understanding and scaling plant responses to the environment across space and time (Frankenberg and Berry, 2017; Gamon et al., 1997, 2016; Jeong et al., 2017; Tucker, 1979). Vegetation indices (VIs) that measure greenness, such as the Normalized Difference Vegetation Index (NDVI) or the Near-Infrared Reflectance from vegetation (NIRv) have proven to be effective at tracking plant productivity in ecosystems where chlorophyll content and carbon uptake are closely correlated, such as deciduous forests and grasslands (Tucker, 1979; Badgley et al., 2017; Yang et al., 2017; Wang et al., 2019).

These measures often fail to predict productivity in evergreen systems, such as the boreal forest, where changes to photosynthesis often occur without significant changes in canopy structure or chlorophyll content (Springer et al., 2017; Sims et al., 2006b; Magney et al., 2019a; Walther et al., 2016; Jeong et al., 2017; Pierrat et al., 2021a). In contrast to greenness based VIs, solar-induced chlorophyll fluorescence (SIF) is a particularly promising remote sensing metric for tracking changes in gross primary productivity (GPP). SIF has been reported to exhibit a linear relationship with GPP at the ecosystem scale across diverse biomes when measured from satellites (Commane et al., 2017; Jeong et al., 2017; Luus et al., 2017; Walther et al., 2016).

SIF has a mechanistic connection to photosynthetic activity (Magney et al., 2019a, 2020; Porcar-Castell et al., 2014, 2021). In all plants, a photon of light absorbed by chlorophyll follows one of three potential pathways: it can be used to drive photochemistry (photochemical quenching (PQ)), it can be dissipated as heat (non-photochemical quenching (NPQ)), or it can be re-emitted as fluorescence (SIF) (Krause and Weis, 1991). The dynamic relationships inherent in these three pathways determine the utility of SIF as a proxy for GPP (Magney et al., 2020). Studies at the leaf level have shown that the yield of fluorescence and yield of photochemistry are proportional under moderate light conditions (Porcar-Castell et al., 2014; Van Der Tol et al., 2014). However, there is a limited understanding of the dynamics of these processes at the canopy scale and under natural conditions such as seasonally varying NPQ and PQ in boreal ecosystems. Recent work has highlighted nuanced relationships between fluorescence and photochemistry, thereby motivating further studies investigating the utility of SIF as a proxy for GPP (Kim et al., 2021; Maguire et al., 2020; Marrs et al., 2020; Dechant et al., 2020).

Fluorescence measured at the canopy scale under natural conditions (SIF) can be described with the following equation:

$$\mathrm{SIF} = \mathrm{APAR} \times \mathrm{LUE_F} \times f_{esc} \tag{5.1}$$

where APAR is the photosynthetically active radiation absorbed by chlorophyll defined as:

$$\mathrm{APAR} = \mathrm{PAR} \times f\mathrm{PAR} \tag{5.2}$$

PAR is photosynthetically active radiation and fPAR is the fraction of PAR absorbed by chlorophyll. $\mathrm{LUE_F}$ is the light use efficiency of fluorescence and f_{esc} is the probability that an emitted photon will escape the canopy. The impact of f_{esc} and canopy structural effects can be considered by calculating the theoretical emitted SIF at the leaf level, $\mathrm{SIF_{total}}$, as:

$$\mathrm{SIF_{total}} = \frac{\mathrm{SIF}}{f_{esc}} \tag{5.3}$$

where SIF is the observed SIF signal from an instrument with a particular viewing geometry. f_{esc} can be estimated in the far-red following Zeng et al. (2019):

$$f_{esc} = \frac{\mathrm{NIRv}}{f\mathrm{PAR}} \tag{5.4}$$

Theoretically, NIRv represents the fraction of near-infrared light that originates from vegetation and minimizes the influence of soil or background reflectances (Badgley et al., 2017). Thus, it is a good measure of canopy structure and chlorophyll content (Badgley et al., 2017) and can be used for estimating f_{esc} of SIF in the near-infrared (Zeng et al., 2019). In cropping systems, the structural influences on SIF (APAR and f_{esc}) have been shown to be the dominant drivers of SIF variability (Dechant et al., 2020). In evergreen needleleaf forests, f_{esc} changes little over the seasonal cycle due to the fact that such forests remain structurally invariant across seasons (Magney et al., 2019a; Stylinski et al., 2002; Badgley et al., 2019; Sims et al., 2006a; Garbulsky et al., 2010). Little empirical evidence for this assumption has been presented and significant questions remain over how f_{esc} impacts SIF over shorter temporal scales and under a variety of illumination conditions. Thus, additional analysis on how canopy structure and illumination conditions impact SIF is necessary.

Canopy integrated carbon uptake via photosynthesis, also known as Gross Primary Productivity (GPP), can be expressed as:

$$\mathrm{GPP} = \mathrm{APAR} \times \mathrm{LUE_P} \tag{5.5}$$

where $\mathrm{LUE_P}$ is the light use efficiency of photosynthesis (Monteith, 1972). $\mathrm{LUE_P}$ is a complex function of leaf biochemistry and APAR, and is often expressed as a hyperbolic function of APAR (Michaelis and Menten, 1913):

$$\mathrm{LUE_P} = \frac{\mathrm{GPP_{max}}}{c + \mathrm{APAR}} \tag{5.6}$$

where c is a coefficient in radiance units and $\mathrm{GPP_{max}}$ is the photosynthetic capacity of the system (i.e. GPP of the canopy at light saturation). In practice, c represents the APAR value at which GPP reaches half of $\mathrm{GPP_{max}}$ in a GPP light response curve. Therefore, it depends on the electron transport rate as well as a plant's rate of carboxylation, which both vary based on plant responses to environmental conditions including temperature and available water. We can combine Equations 5.1 and 5.5 by eliminating APAR to arrive at (Guanter et al., 2014; Frankenberg and Berry, 2017):

$$\mathrm{GPP} = \mathrm{SIF} \times \frac{\mathrm{LUE_P}}{\mathrm{LUE_F} \times f_{esc}} \tag{5.7}$$

Studies at the satellite scale over a variety of ecosystems have shown that SIF and GPP are linearly proportional (Frankenberg and Berry, 2017; Sun et al., 2017, 2018). However, the reason for the linear relationship is unclear, as $\mathrm{LUE_P}$ has a non-linear relationship with light (Equation 5.6). Further combining Equations 5.6 and 5.7, we find a more complete functional relationship between SIF and GPP (Damm et al., 2015):

$$\mathrm{GPP} = \frac{\mathrm{SIF} \times \mathrm{GPP}_{\mathrm{max}}}{a + \mathrm{SIF}} \tag{5.8}$$

where $a = c \times f_{esc} \times \mathrm{LUE}_{\mathrm{F}}$. Damm et al. (2015) notes that because this equation is an approximation of the complex relationships between SIF and GPP, Equation 5.8 performs best when a is assumed constant or SIF corresponds to APAR. This assumption is reasonable under conditions where variations in $\mathrm{LUE}_{\mathrm{F}}$ are substantially smaller than variations in $\mathrm{LUE}_{\mathrm{P}}$, such as cropping systems (Van Der Tol et al., 2014). However, this assumption breaks down in high latitude evergreen systems, such as the boreal forest, which experience strong seasonal changes in $\mathrm{LUE}_{\mathrm{P}}$ associated with photochemical downregulation of photosynthesis over winter (Middleton et al., 1997). Further, it is currently unclear how strong changes in environmental conditions over the course of the season impact $\mathrm{LUE}_{\mathrm{F}}$ and $\mathrm{LUE}_{\mathrm{P}}$. Therefore, there is a critical need for experimental data to better quantify the SIF-GPP relationship in systems with highly dynamic $\mathrm{LUE}_{\mathrm{P}}$ and environmental extremes in light and temperature.

Boreal evergreen needleleaf species experience strong seasonal changes in photosynthesis as a consequence of the physiological stresses of winter as well as dynamic changes in PAR. In order to avoid damage from excess light, both seasonally and diurnally, evergreen needleleaf plants utilize two forms of NPQ, which regulate the dynamics of photochemistry and fluorescence (Verhoeven, 2014; Demmig-Adams and Adams, 1992).

The first form is rapidly reversible and therefore important during times of active photochemistry and high photosynthetically active radiation (PAR). This form involves the rapid conversion of the xanthophyll pigment violaxanthin (V) via antheraxanthin (A) into zeaxanthin (Z) under excess light conditions (Müller et al., 2001; Murchie and Niyogi, 2011). The inter-conversion between xanthophyll pigments has a unique spectral signature and can therefore be measured remotely over shorter timescales (daily) using the photochemical reflectance index (PRI) (Gamon et al., 1992; Gamon and Berry, 2012; Wong and Gamon, 2015b,a). PRI is also a useful indicator for the second form of NPQ, sustained NPQ; however, significant questions remain over its utility for this purpose (Wong and Gamon, 2015b,a;

Pierrat et al., 2021a).

Sustained NPQ is associated with seasonal downregulation of photosynthesis (Adams et al., 2004; Öquist and Huner, 2003; Verhoeven, 2014; Jahns and Holzwarth, 2012; Adams and Demmig-Adams, 1994). This form manifests as an increase in the overall pool size of xanthophyll pigments (V+A+Z) and lutein (an additional carotenoid pigment with photoprotective function) (Verhoeven, 2014; Jahns and Holzwarth, 2012), a dark-retention of xanthophyll pigments A and Z (Adams and Demmig-Adams, 1994), and a subsequent halt in the light-dependent inter-conversion between xanthophyll pigments (Verhoeven, 2014; Öquist and Huner, 2003; Adams et al., 2004). The ratio between chlorophyll and carotenoid pigments therefore changes seasonally to support the winter downregulation of photosynthesis and sustained NPQ (Adams et al., 2004; Ensminger et al., 2004; Porcar-Castell et al., 2012; Wong and Gamon, 2015a). In evergreen systems, the remotely sensed chlorophyll-carotenoid index (CCI) responds to a change in the ratio of chlorophyll to carotenoid pigments and is therefore a potential remote sensing proxy for sustained NPQ (Gamon et al., 2016).

Our current understanding indicates that both the physical (f_{esc}) and the ecophysiological ($\mathrm{LUE_F}$, $\mathrm{LUE_P}$) drivers of the SIF-GPP relationship operate on varying temporal scales and can be measured using a combination of remotely sensed indices. Therefore, a better understanding of these drivers, both at a high temporal resolution and seasonally, is necessary to assess the utility of SIF as a proxy for GPP in boreal ecosystems. In our study, we seek to answer:

1. How do the relationships between SIF, VIs, and GPP change across varying temporal scales?
2. How do the dynamics of $\mathrm{LUE_P}$, $\mathrm{LUE_F}$, and f_{esc} impact the relationship between SIF and GPP?

Tower-based spectrometer systems allow for a deeper investigation of the physical and ecophysiological drivers of the SIF-GPP relationship and aid our ability to scale measurements from the leaf to orbit by filling the spatio-temporal gap between leaf level and satellite level measurements (Grossmann et al., 2018). Here, we present data from a tower-based spectrometer system (Sections 5.2.1-5.2.4) and a statistical analysis (Section 5.2.5) to determine the linkages between SIF and GPP at varying temporal resolutions (Section 5.3.1), to statistically connect changes in SIF and GPP to environmental controls (Section 5.3.2), and to provide a seasonally resolved SIF-GPP parametrization (Section 5.3.3) for the implementation of this ecosystem in carbon cycle models. These results then elucidate the answers to our scientific questions (Section 5.4).

5.2 Materials and Methods

Tower-based SIF spectrometer systems have already provided valuable insights into the SIF-GPP relationship in cropping (Magney et al., 2019b; He et al., 2020), temperate (Kim et al., 2021; Yang et al., 2017, 2015), and sub-alpine evergreen systems (Magney et al., 2019a; Cheng et al., 2020). However, few measurements in boreal ecosystems have been reported (Pierrat et al., 2021a). We collected tower-based SIF and vegetation index (VI) data along with GPP and meteorological data from a boreal field site in Canada to answer our scientific questions. Details of the site, observational methods, and analysis approach are discussed in the following sections.

5.2.1 Site Description: Southern Old Black Spruce

The study site (Southern Old Black Spruce, SOBS, Fluxnet ID CA-Obs) is located near the southern limit of the boreal forest ecotone in Saskatchewan, Canada (53.98°N, 105.12°W) (Figure 5.1) (Jarvis et al., 1997). It is a mixed forest stand with stem density predominantly (90%) black spruce (*Picea mariana*), and scattered (10%) larch (*Larix laricina*) (Pappas et al., 2020a). Average canopy height at the site is ∼16 m with a canopy leaf area index of ∼3.8 m^2m^{-2} (Chen et al., 2006). Long-term (1981-2010) mean annual air temperature

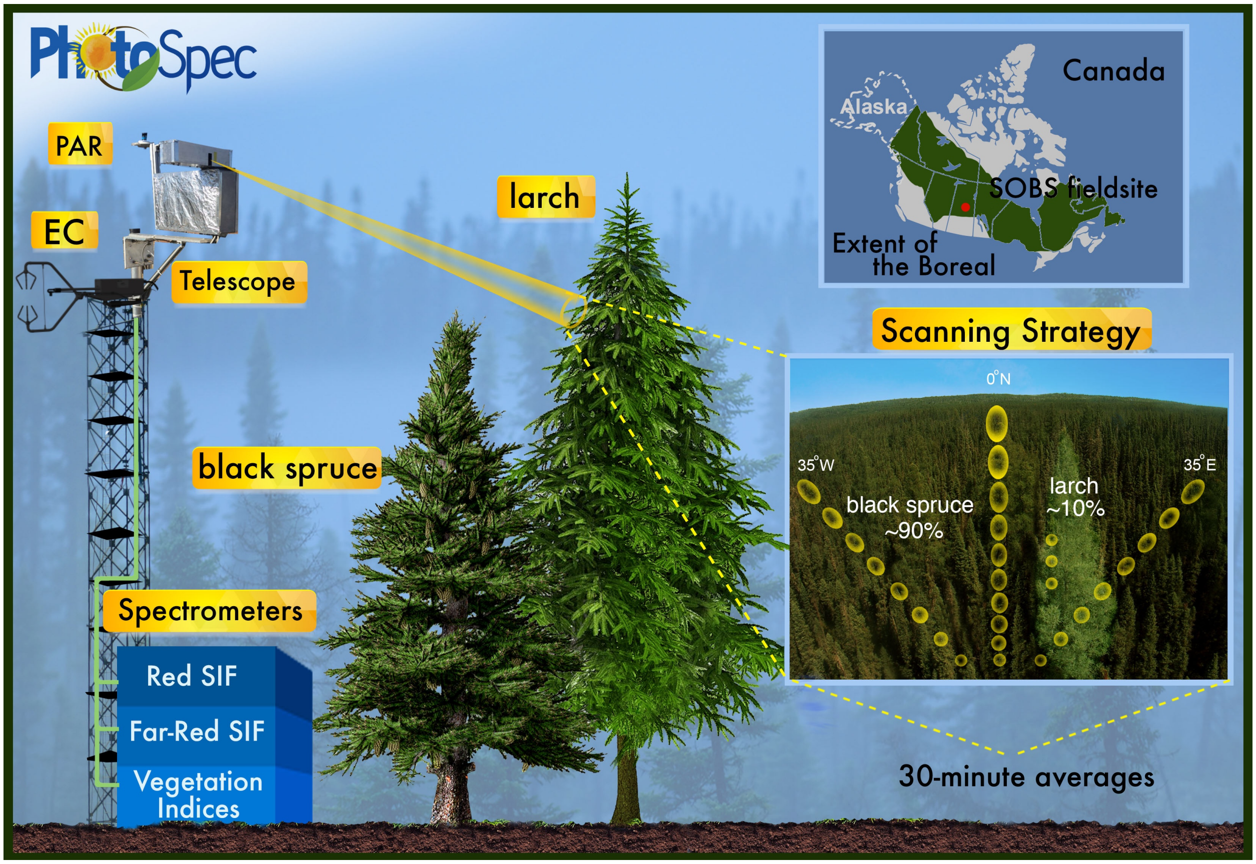

Figure 5.1: Field site location with PhotoSpec and eddy-covariance (EC) measurements at the Southern Old Black Spruce (SOBS) site in Saskatchewan, Canada. PhotoSpec set up is shown with an inset of the scanning strategy and measurement points on both black spruce and larch. Adapted from (Pierrat et al., 2021a).

and total precipitation in the area are 1.4°C and 427.7mm respectively. There is an average of 146 days with a snow depth of 1cm or more (Government of Canada, Prince Albert Station, 2019). The site is equipped with a 26 m above ground level (agl) twin scaffold tower, approximately twice the height of the forest canopy.

5.2.2 Remote Sensing: PhotoSpec

We collected remotely sensed measurements (NDVI, NIRv, PRI, CCI, far-red SIF) using PhotoSpec (see Grossmann et al. (2018) for detailed instrument description) from September

2018 to the end of December 2020. Photospec was installed at the top of the scaffolding tower (26 m agl) facing due north. It has a narrow field of view (0.7°), 2-D scanning capabilities, and can simultaneously measure SIF along with vegetation indices at the same point in the canopy (Grossmann et al., 2018). Our scanning strategy had three 'elevation scans' (scanning vertically with 0° horizontally at the horizon) at 35°W (10 measurements, elevations -50° to -23° in steps of 3°), 0°N (24 measurements, elevations -80° to -11° in steps of 3°), and 35°E (10 measurements, elevations -70° to -25° in steps of 5°) and three individual targets on a larch (Figure 5.1). This scan strategy and subsequent averaging is representative of the forest because it reflects the stem density of the forest with ∼90% of targets hitting black spruce and ∼10% of targets hitting larch. Individual measurements take approximately 20 seconds and the complete scan cycle repeats on a 30 minute loop to compare with GPP and environmental variables.

Vegetation indices were calculated as follows, with $\rho_{nm:nm}$ = the average reflectance across a wavelength range in nm:

$$\text{NDVI} = (\rho_{830:860} - \rho_{620:670})/(\rho_{830:860} + \rho_{620:670}) \tag{5.9}$$

$$\text{NIRv} = (\rho_{830:860} - \rho_{620:670})/(\rho_{830:860} + \rho_{620:670}) \times \rho_{830:860} \tag{5.10}$$

$$\text{PRI} = (\rho_{569:571} - \rho_{520:532})/(\rho_{569:571} + \rho_{520:532}) \tag{5.11}$$

$$\text{CCI} = (\rho_{520:532} - \rho_{620:670})/(\rho_{520:532} + \rho_{620:670}) \tag{5.12}$$

SIF was retrieved in the far-red (745-758 nm) wavelength range using a Fraunhofer-line based fitting algorithm (Grossmann et al., 2018). The Fraunhofer-line based approach makes SIF retrievals insensitive to atmospheric scattering and therefore robust even under cloudy sky conditions (Frankenberg et al., 2011; Mohammed et al., 2019; Chang et al., 2020). We collected 1 second PAR data from a LI-COR LI-190R sensor and used these data to remove PhotoSpec measurements where PAR conditions changed significantly ($\text{PAR}_{\text{std}} >$

$0.2 \times \mathrm{PAR_{avg}}$) over the PhotoSpec integration time. We excluded low-quality retrievals where the SIF retrieval error (Grossmann et al., 2018) was > 0.2 Wm^{-2}sr$^{-1}\mu$m^{-1} and where SIF $<$ -0.1 Wm^{-2}sr$^{-1}\mu$m^{-1} or SIF > 10 Wm^{-2}sr$^{-1}\mu$m^{-1}. Finally, we only considered observations where the Solar Zenith Angle (SZA) $< 80°$ to remove data where low light conditions increase retrieval uncertainty.

We used f_{esc} to calculate $\mathrm{SIF_{total}}$ (Equation 5.3) and to evaluate canopy structure and illumination influences on SIF for each observation. We calculated f_{esc} following Equation 5.4 using NIRv and fPAR, which was estimated as:

$$f\mathrm{PAR} = 1 - \frac{\mathrm{PAR_{canopy}}}{\mathrm{PAR}} \tag{5.13}$$

where $\mathrm{PAR_{canopy}}$ represents outgoing PAR (coming from the canopy) and PAR is the incoming PAR (pointing directly up). $\mathrm{PAR_{canopy}}$ was calculated by integrating the calibrated radiance between 400 and 700 nm measured from PhotoSpec and multiplying by π to convert to hemispheric $\mathrm{PAR_{canopy}}$. PAR was calculated by averaging the 1 second LI-COR LI-190R PAR measurements over the PhotoSpec integration time. We determined APAR following Equation 5.2. We calculated $\mathrm{LUE_F}$ following Equation 5.1 ($\mathrm{LUE_F} = \frac{\mathrm{SIF}}{\mathrm{APAR}*f_{esc}}$) and $\mathrm{LUE_P}$ following Equation 5.5 ($\mathrm{LUE_P} = \frac{\mathrm{GPP}}{\mathrm{APAR}}$).

We calculated averages over each 30-minute period across the full spatial scan to reflect stem density of the canopy and match GPP observations. 30-minute spatial averages were again averaged to report daily and monthly averages. Standard deviation of the diurnal variability was significantly greater than measurement errors (Grossmann et al., 2018) and is thus reported along with daily averages throughout the study.

Days with snow cover were identified visually using phenocam images from the site (`https://phenocam.sr.unh.edu/webcam/sites/canadaOBS/`). Snow cover identification was used to provide context to observed signals but data were not removed from the analysis.

5.2.3 Gross Primary Production

Eddy-covariance (EC) measurements of net ecosystem exchange (NEE) (μmol C m^{-2} s^{-1}) and friction velocity u* (ms^{-1}) were made from atop the site's 26m scaffold tower from July 2019 through the end of December 2020. The EC system consisted of a 3-D sonic anemometer (CSAT3, Campbell Scientific, Logan, UT) in combination with a closed-path infrared gas (CO_2/H_2O) analyzer (LI-7200 analyzer, Li-Cor, Lincoln, NE)) operated in absolute mode. The 30-min eddy fluxes were computed using the Eddy-Pro software (version 7.0.6, Li-Cor, Lincoln, NE). NEE was calculated as the sum of the measured CO_2 eddy flux at the instrument height and the change in CO_2 storage in the air layer between the instruments and the surface (Barr et al., 2006). Nighttime NEE values were rejected under calm conditions using a u* threshold of 0.30 m s^{-1}. Net Ecosystem Production (NEP) was estimated as -NEE assuming no losses via dissolved organic carbon. Finally, gaps in NEP were filled and NEP was partitioned into gross primary production GPP (μmol C m^{-2} s^{-1}) and total ecosystem respiration R_e (μmol C m^{-2} s^{-1}) using the standard Fluxnet-Canada method (Barr et al., 2004).

5.2.4 Environmental Variables

Air temperature and relative humidity were recorded in the canopy at 6 m height with a Vaisala HMP45C probe. Soil temperature measurements were taken with Type-T (copper-constan) thermocouples at two locations at a 10 cm depth below the living-moss layer and averaged together. Soil volumetric water content (VWC) was recorded at two locations at a 7.5 cm depth with Cambell Scientific CS615 Water Content Reflectometers and averaged together. Wind speed and wind direction were measured with an RM Young model 05103-10 wind monitor located at the top of the tower at a height of 26 m. Precipitation was measured with a Geonor T-200B all-weather weighing precipitation gauge located on the roof of the hut at a height of 3.5 m above ground level.

5.2.5 Data Analysis: Curve Fitting and Random Forest Models

We applied the mechanistic equations for the relationships between VI's, SIF, GPP, and PAR at varying temporal scales by fitting curves to SIF/VI's and GPP as well as the light response curves of SIF and GPP. Fitting light response curves allowed us to extract information on $\mathrm{LUE_F}$ and $\mathrm{LUE_P}$ from the fit parameters following Equations 5.1, 5.5, and 5.6. All fitting was done using the fit function within Matlab's curve fitting toolbox (MATLAB, 2021). Fit parameters and goodness of fit statistics (R^2 values) were also extracted using the fit function. All fitted equations are provided within the results and in figure captions where relevant.

We explored the significance of environmental variables as predictors for SIF and GPP at diurnal and seasonal timescales using random forest regression models. We used Matlab's TreeBagger to create four random forest regression models to predict both SIF and GPP at half-hourly and daily resolutions (HH-SIF, HH-GPP, Daily-SIF, Daily-GPP) thereby testing the significance of environmental predictors across diurnal and seasonal scales respectively. Random forest models were chosen due to their high degree of interpretability as well as their non-parametric nature, making them more suitable for approximating nonlinear relationships in complex systems (Breiman, 2001). Both SIF and GPP models were initially trained using the following half-hourly or daily averaged environmental variables as features: PAR, precipitation, soil volumetric water content (VWC) at 7.5 cm, soil temperature at 10 cm, air temperature at canopy height (6 m), relative humidity at canopy height (6 m), friction velocity (u^*), wind speed and wind direction above canopy (26 m), and one column of random numbers for reference. Each model was built with the following sized datasets, which reflect the number of available data during the overlapping collection period, July 24, 2019 to Dec 31, 2020: HH-SIF (25,296), HH-GPP (25,296), Daily-SIF (527), Daily-GPP (527). All 4 models had 100 decision trees, used 70% of data to train, and were sampled without replacement. We checked model performance using the R^2 and out-of-bag (OOB) scores and assessed the predictive power of each feature using the OOB predictor importance estimates (Breiman, 2001). The OOB scores and predictor importance estimates evaluate model performance on unseen data, thereby testing the models generalizability. We then tested each model by systematically removing the lowest performing predictor, retraining the model, and comparing the R^2 and OOB scores (Section 5.3.2). This process was repeated until only one predictor variable remained. The highest performing random forest model for daily average GPP (5 predictors, Figure 5.4) was used to predict GPP from September 9, 2018 (the start of PhotoSpec measurements) to July 24, 2019 (the start of GPP data) and is presented for visualization in Figure 5.2. Modeled GPP was not used in any additional analysis - merely to illustrate approximate GPP prior to the start of flux-tower measurements.

5.3 Results

5.3.1 SIF and VIs as proxies for GPP from half-hourly to seasonal scales

PhotoSpec data (far-red SIF, CCI, PRI, NIRv, NDVI) and flux tower GPP highlight both the dynamic nature of evergreen photochemistry at weekly to seasonal scales at the SOBS site, as well as the utility of remotely sensed measures for explaining seasonal trends in GPP (Figure 5.2).

GPP, PAR, and air temperature exhibit patterns consistent with historical data at SOBS (Liu et al., 2019a) with the growing season extending from approximately late May to early September and the peak of GPP in late July to early August for both 2019 and 2020. Winter dormancy occurs approximately November through March (Pierrat et al., 2021a). PAR values increase in spring, well before the start of the growing season, and explain some of the daily to weekly variability in GPP during the growing season (Figure 5.2 f). Air temperature above 0°C is associated with both the onset (Pierrat et al., 2021a) and cessation of photosynthesis (Figure 5.2 g).

Greenness-based vegetation indices NIRv and NDVI show strong responses to snow cover

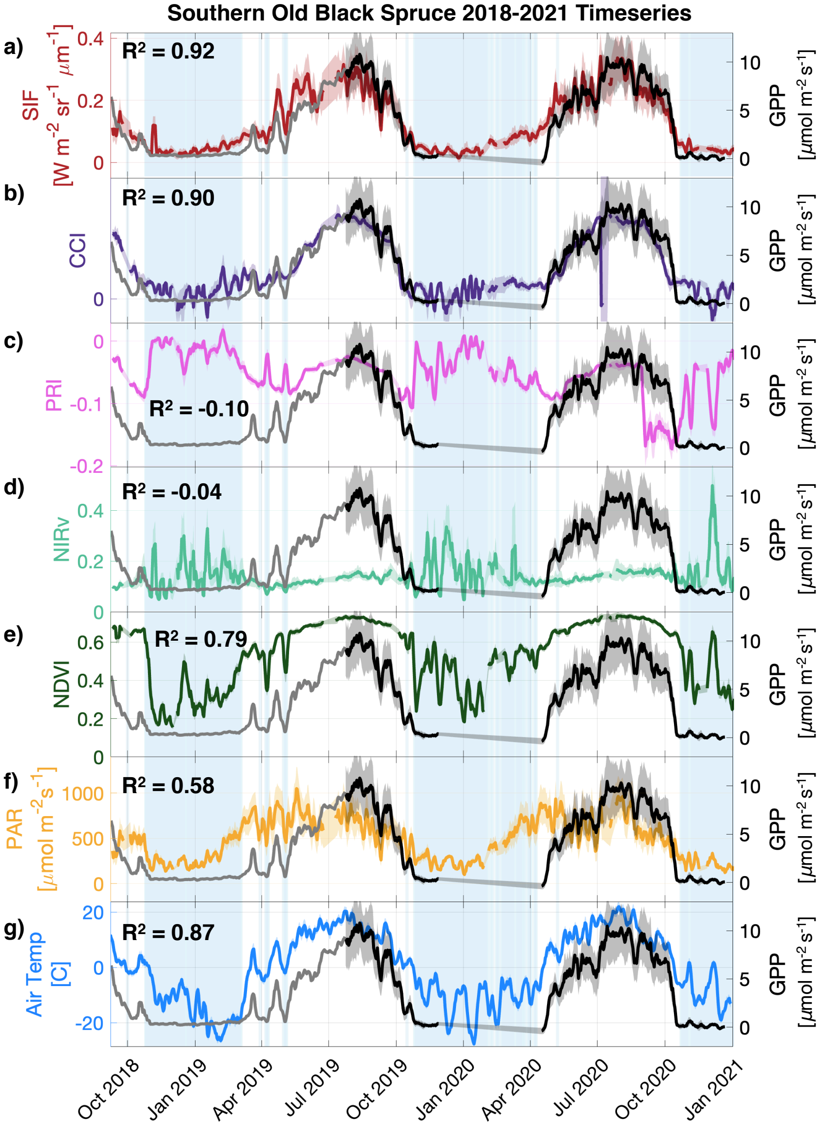

Figure 5.2: a) SIF, b) CCI, c) PRI, d) NIRv, and e) NDVI measurements from PhotoSpec, f) PAR above the canopy (26 m), and g) air temperature at canopy height (6 m) compared with tower-based GPP data for the study period. Solid lines are 5-day moving means of daily averaged data. Shaded error bounds are the standard deviation of diurnal variability. The gray GPP line with no shaded area is the 5-day moving mean of the Daily-GPP random forest model's predicted GPP. R^2 values are the Pearson correlation coefficients between the 5-day moving means of tower-based GPP and the plotted variable. All R^2 values were statistically significant with p-values < 0.005. Light blue background regions are days with snow cover on the canopy as identified by phenocam images.

and poor ability to track the seasonal cycle of tower-based (black line with error bars) and modeled (gray line, Section 5.2.5) GPP (Figure 5.2 d, e). NIRv remains near constant during fall, spring, and summer, despite the strong seasonal cycle of GPP (R^2 = -0.04 for 5-day moving mean). However, NIRv shows a small gradual increase over the growing season, which we interpret as consistent with changes in canopy structure and variability in f_{esc} (Zeng et al., 2019; Badgley et al., 2019). Additionally, NIRv exhibits strong, random, variability over winter due to snow cover or other confounding effects. NDVI shows a stronger correlation with GPP ($R^2 = 0.79$). However, changes in NDVI are predominantly due to a strong snow response of the NDVI signal, notably in early spring and over winter. For the same reason, NDVI increases earlier and remains elevated longer than GPP. Over summer, NDVI shows a slight seasonal curvature with peak NDVI matching peak GPP. Prior work has shown that NDVI tracks photosynthetic phenology well in deciduous temperate ecosystems (Yang et al., 2017), but not in evergreen needleleaf forests (Magney et al., 2019a) where canopy structure and crown architecture have a minor and de-coupled influence on carbon uptake (Pappas et al., 2020a). A species-specific analysis confirms that in the SOBS mixed-stand forest, changes in NDVI and NIRv predominantly reflect changes in deciduous larch, while evergreen NDVI and NIRv remain largely invariant (Pierrat et al., 2021a).

CCI and PRI track the seasonal cycle of GPP well but do not exhibit sharp changes on the scale of days to weeks that we observe with GPP (Figure 5.2 b, c). During spring, CCI and PRI are less responsive to variability in modeled (2019) and tower-based (2020) GPP, and show a delay in the timing of their increase compared with GPP (40 days in 2019, 29 days in 2020) (Pierrat et al., 2021a). Over summer, CCI peaks in early July, prior to maximum GPP in both 2019 and 2020. PRI shows a closer agreement with the summer peak of GPP, but shows less variability over the summer months and is less effective at tracking the seasonal trends in GPP. In fall, CCI shows good agreement with the seasonal downregulation of photosynthesis, while PRI decreases prior to and more rapidly than GPP. Over winter, CCI hovers around zero with a few periods of stronger variability below zero.

This is potentially due to a small response to snow cover. PRI also shows strong responses to snow over winter with increased values during periods of snow cover (Pierrat et al., 2021a). This makes the interpretation of wintertime PRI values significantly more challenging.

SIF tracks tower-based and modeled GPP well, does not show strong responses to snow, and shows similar or stronger correlations with GPP than all other vegetation indices and environmental variables ($R^2 = 0.92$) (Figure 5.2 a). In summer, daily to weekly variability in SIF closely tracks variability in tower-based GPP, most notably at the end of September 2019 and June and July of 2020. In fall, SIF shows the same general decline as GPP. Over winter, unlike GPP, SIF does not go to zero but remains low and less variable compared to its overall seasonal change and the daily to weekly variability over summer. In spring, SIF increases prior to changes in GPP for both years. This is consistent with Magney et al. (2019a) and is explored further in Sections 5.3.3 & 5.4.2.

Because SIF, CCI, and NDVI showed the strongest correlations with GPP at a daily 5-day moving mean resolution ($R^2 = 0.92$, 0.90, 0.79 respectively), we explored their relationships to GPP at varying temporal resolutions in more detail (Figure 5.3). Fitted equations and parameters are summarized in Table A.1. Correlations between SIF, CCI, or NDVI and GPP at monthly, daily, and half-hourly resolutions highlight the strengths and limitations of each index.

At a monthly resolution, linear fits of SIF (a), CCI (d), and NDVI (g) all show strong correlations with tower-based GPP ($R^2 = 0.94$, 0.95, 0.82 respectively). At a daily resolution, a linear fit of SIF shows the strongest correlation with GPP ($R^2 = 0.79$), followed by CCI ($R^2 = 0.75$) and NDVI ($R^2 = 0.56$). A non-linear fit between SIF and GPP did not improve R^2 values ($R^2 = 0.78$ for Equation 5.8, Figure A.1).

At a half-hourly resolution, SIF, fit with Equation 5.8, shows the strongest correlation ($R^2 = 0.64$), while linear fits of CCI and NDVI both show low correlations ($R^2 = 0.02$, 0.30 respectively). At a half-hourly resolution, SIF increases while GPP saturates at high PAR, which leads to a higher degree of non-linearity (Figures 5.3 c, A.1 c, A.2). A linear fit for half-hourly SIF and GPP data resulted in a similar R^2 value ($R^2 = 0.62$ for linear, Figure A.1 c). However, plotting summer data shows that there is in fact a high degree of non-linearity associated with high PAR values (Figure A.2). CCI and NDVI primarily reflect slower seasonal changes in leaf pigments and canopy structure, and therefore do not track the strong variability of GPP with changes in PAR at half-hourly and daily resolutions. In contrast, SIF and GPP both show variability within each season associated with changes in PAR (Figure A.1).

In summary, when measured at higher temporal frequencies, the relationship between GPP and all remotely sensed products decreases and the relationship between SIF and GPP becomes increasingly non-linear. Despite this non-linearity, SIF significantly outperforms all other remotely sensed indices as a proxy for GPP. This non-linearity is explored in further detail in Sections 5.3.3 & 5.4.2.

5.3.2 Environmental drivers of SIF and GPP at half-hourly and daily resolutions

We explored the explanatory power of several environmental parameters using random forest models to determine which variables had the best predictive capacity for SIF and GPP at diurnal and seasonal timescales. All four random forest models (HH-SIF, HH-GPP, Daily-SIF, Daily-GPP) had good performance and high generalizability with all predictors included and when only three predictors were included (Figure 5.4 a).

After systematically eliminating low importance predictors, the three most important predictors for all four models were PAR, soil temperature, and air temperature (Figure 5.4b). HH-SIF and HH-GPP showed PAR as the most important predictor. However, using PAR as the only predictor showed a notable decrease in performance (HH-SIF OOB $R^2 = 0.61$ and HH-GPP OOB $R^2 = 0.31$). These results highlight the fact that variability in SIF cannot simply be explained by changes in PAR. Thus, while the variability in both SIF and GPP over the course of a day (half-hourly resolution) is mostly driven by variability in PAR,

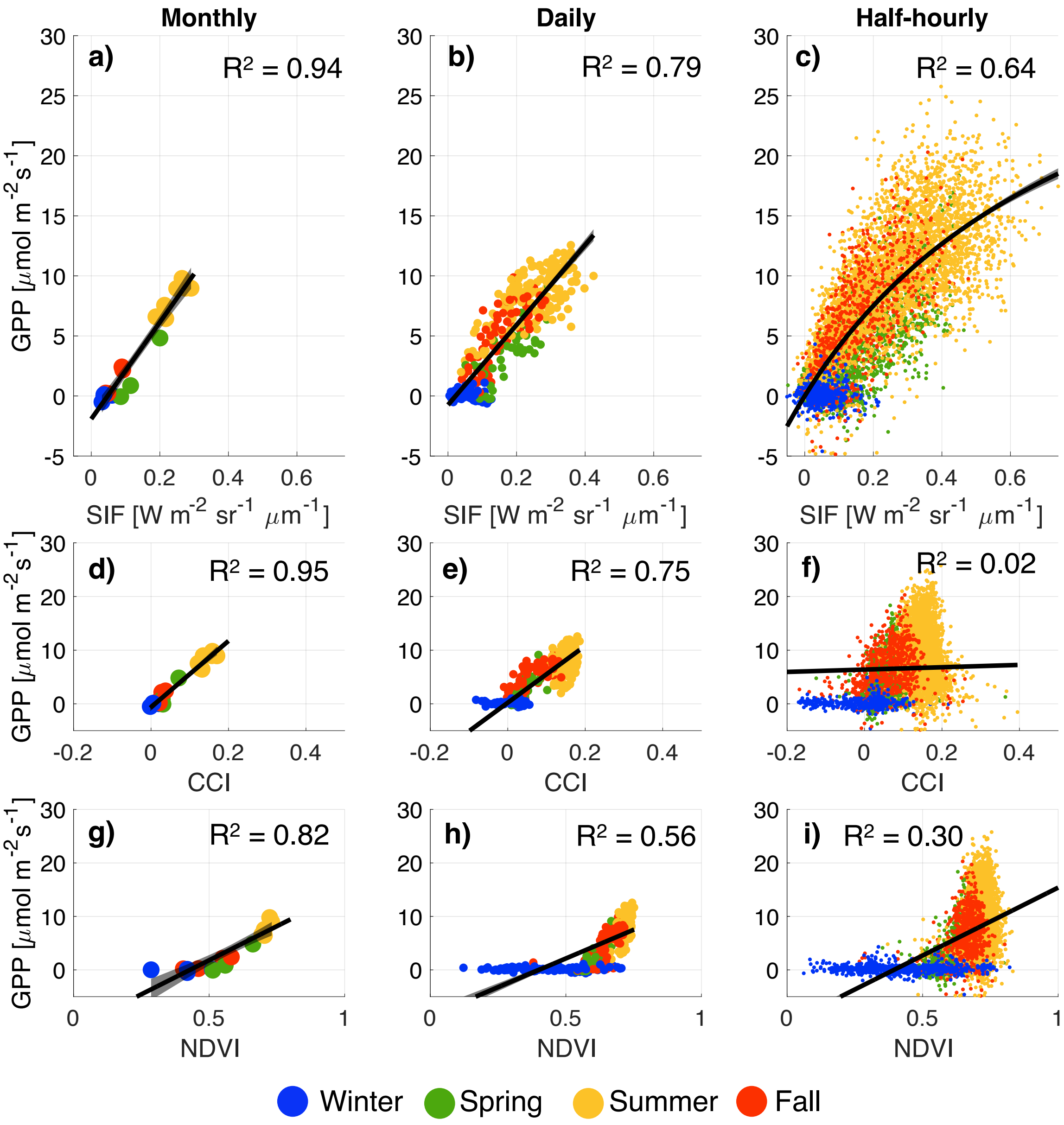

Figure 5.3: The relationships between SIF, CCI, or NDVI, and GPP at monthly, daily, and half-hourly resolutions. Solid black lines are linear fits except c) half-hourly GPP vs. SIF which is based off Equation 5.8. Shaded gray regions are the 95% non-simultaneous functional prediction bounds for the fit. R^2 values are the degree-of-freedom adjusted coefficient of determination of the fit. Fitted parameters and equations are summarized in Table A.1.

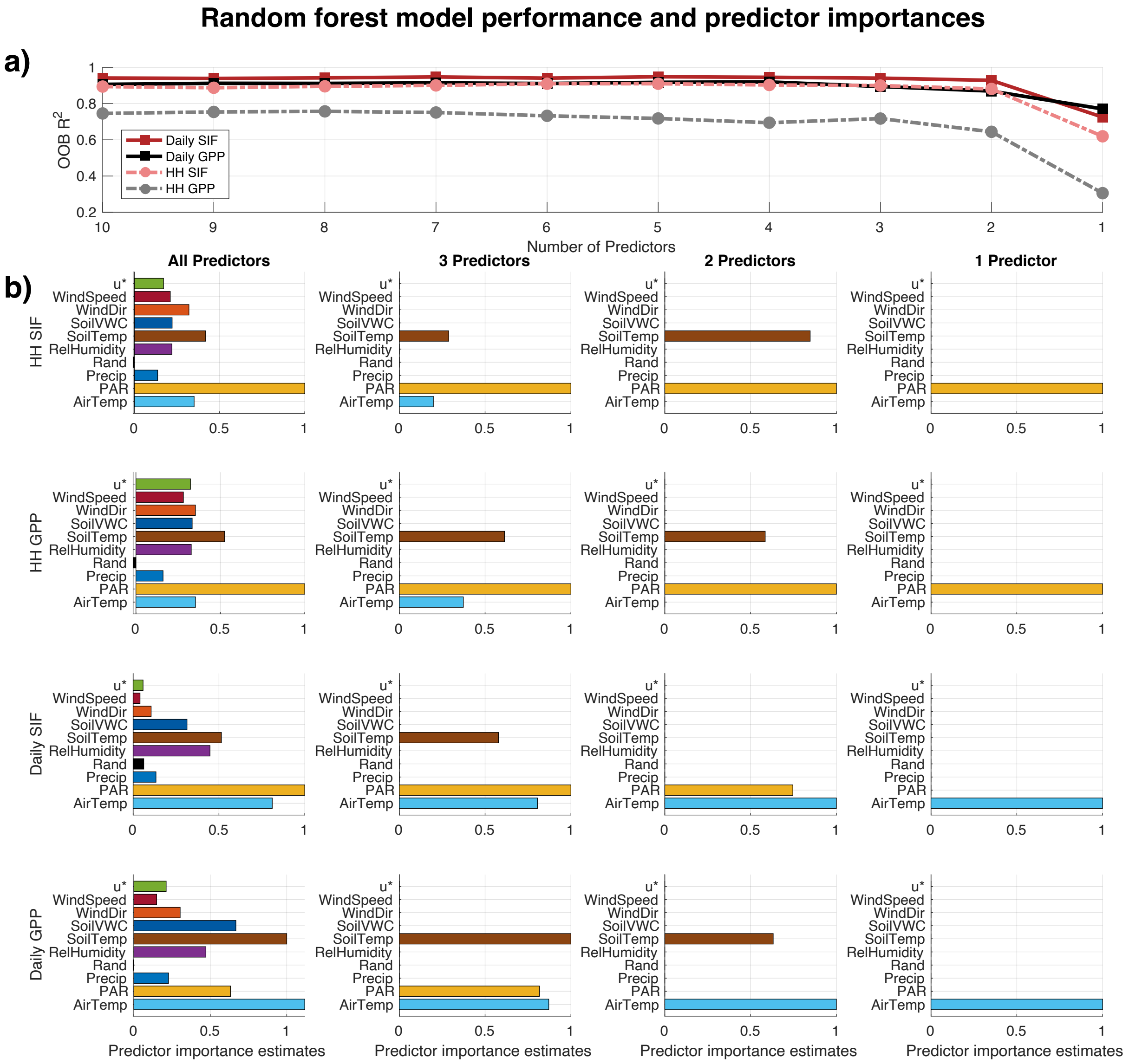

Figure 5.4: Random forest model performance evaluation and predictor importance estimates for all four models: (half-hourly) HH-SIF, HH-GPP, Daily-SIF, Daily-GPP. a) Shows OOB R^2 values for all four models with decreasing numbers of predictors included. b) is the predictor importance estimates for all four models with all predictors included (ten total), three, two, and one predictor included. Predictor importance estimates are normalized to a scale from 0-1 based on the highest performing predictor.

on a seasonal scale, SIF and GPP are regulated by other environmental factors related to temperature.

Daily-SIF and GPP models confirm this seasonal temperature dependence, with air temperature being the most important predictor for both models. Going from three to two predictors, Daily SIF and GPP showed slight decreases in performance (OOB R^2 of 0.94 to 0.92 and 0.89 to 0.87 respectively) and diverged in predictor importance rankings. With two predictors, daily SIF was best predicted using PAR and air temperature, while daily GPP was best predicted using air and soil temperature. Using only one predictor, both daily SIF and GPP were primarily driven by air temperature.

The only notable drops in R^2 and OOB R^2 scores before 3 predictors were reached occurred when removing wind direction from the HH-GPP model (OOB R^2 = 0.72 to 0.69 going from 5 to 4 predictors, Figure 5.4 a). This change was not observed in the HH-SIF or Daily-SIF models. While wind direction does not impact SIF, it determines the part of the forest that is in the eddy-covariance footprint to which GPP is sensitive (Chu et al., 2021). The change in R^2 values thus highlights the importance of considering the GPP footprint in heterogeneous and mixed-species canopies (such as the SOBS site) (Chu et al., 2021).

5.3.3 Light responses of SIF and GPP, and the impact of canopy structure on SIF

Monthly light response curves of SIF and GPP (Figure 5.5) and f_{esc}, $\mathrm{LUE_F}$, and $\mathrm{LUE_P}$ (Figure A.3), illustrate the diurnal and seasonal dynamics of SIF and GPP and highlight why SIF is an effective proxy for GPP despite their non-linear relationship. Figure 5.6 summarizes the monthly physical (f_{esc}) and ecophysiological ($\mathrm{LUE_F}$, $\mathrm{LUE_P}$, $\mathrm{GPP_{max}}$, c) parameters that determine the relationship between SIF and GPP as fitted in Figure 5.5 or averaged monthly. Fitted equations and parameters are summarized in Table A.3.

Figure 5.5 a shows the impact of APAR on f_{esc} while Figure 5.6 a summarizes the monthly

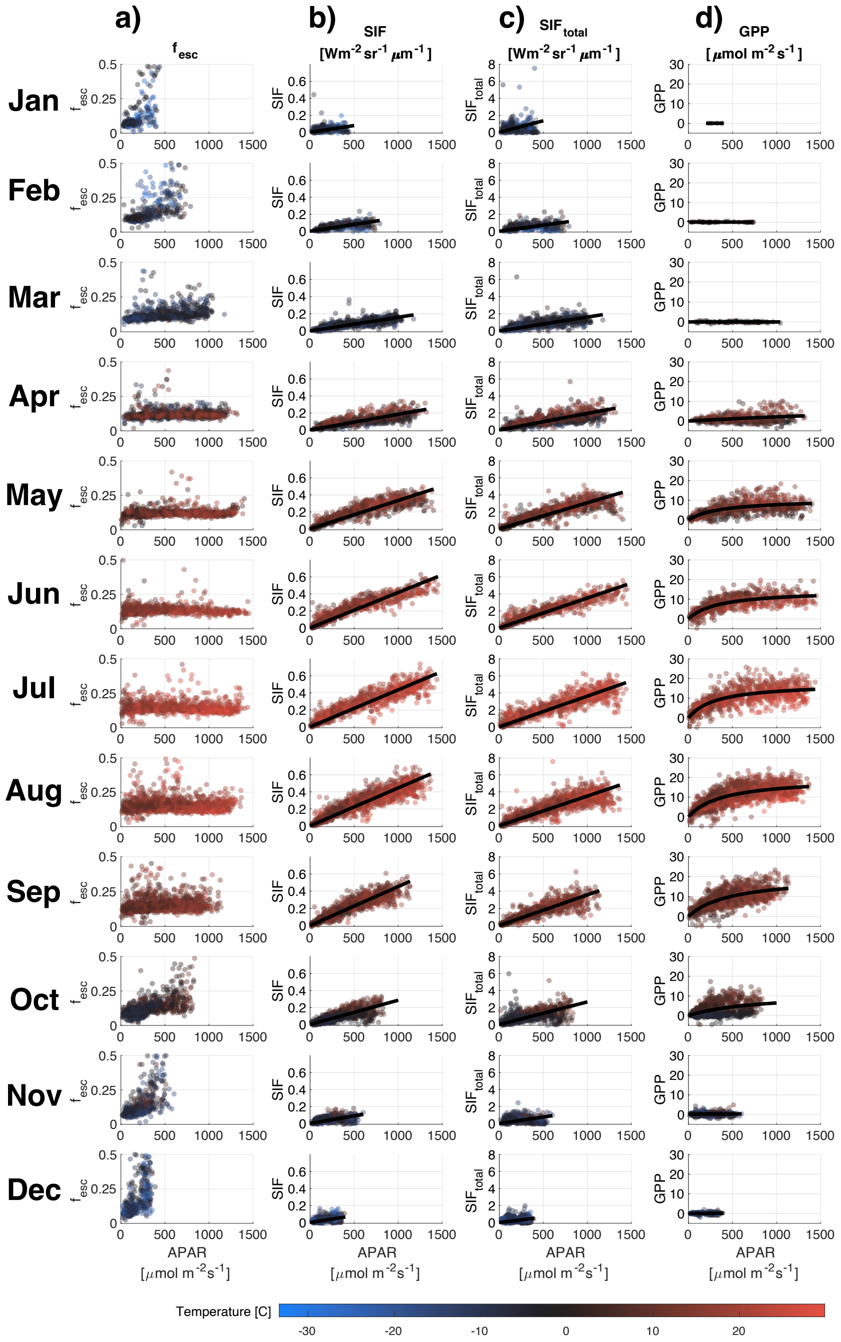

Figure 5.5: Half-hourly data with fitted curves. Column a) f_{esc} calculated from Equation 5.4 plotted against APAR b) light response curves of SIF with a linear fit, c) light response curves of $\text{SIF}_{\text{total}}$ calculated from Equation 5.3 with a linear fit, d) light response curves of GPP fitted with $\text{GPP} = \frac{\text{GPP}_{\text{max}} \times \text{APAR}}{c + \text{APAR}}$ (derived from Equations 5.5 & 5.6). Fitted equations and parameters are summarized in Figure 5.6 and Table A.2.

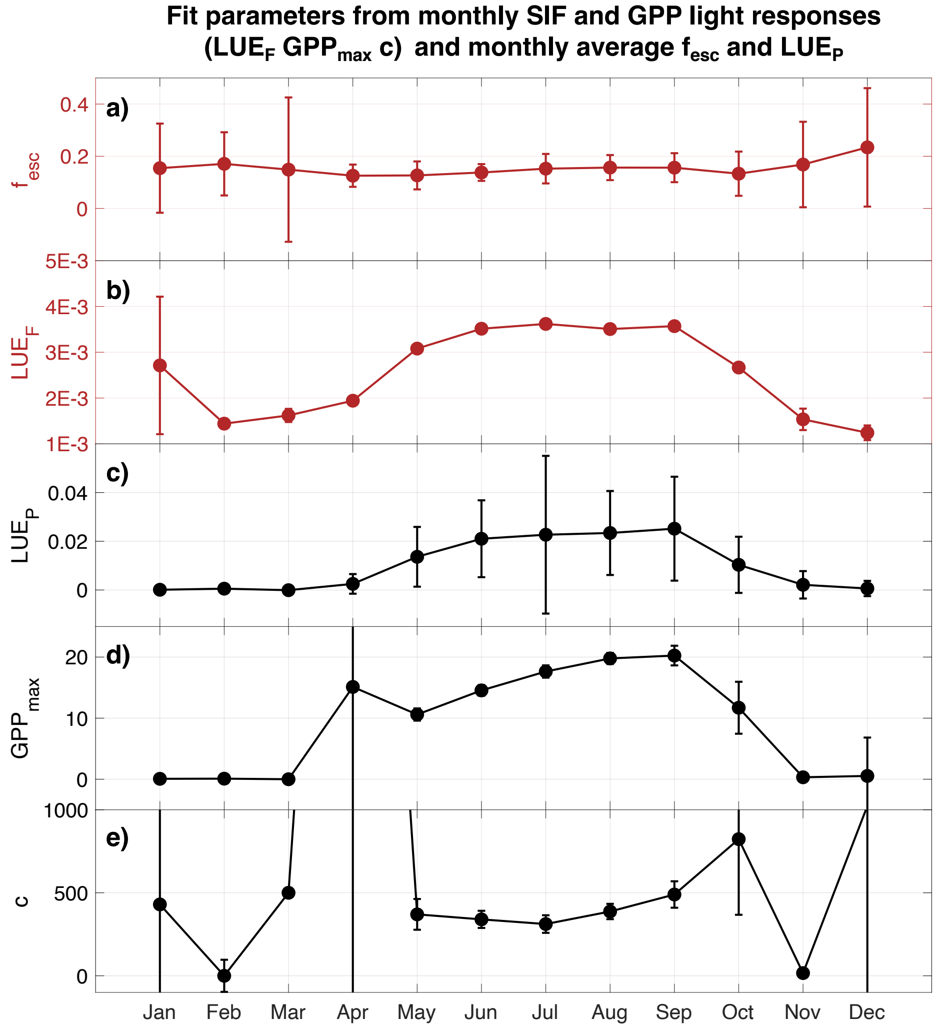

Figure 5.6: Values determined from Figures 5.5 and A.3. Numerical values for b), d), and e) are reported in Table A.2. a) f_{esc} values are monthly averaged f_{esc} as determined with Equation 5.4, b) LUE_{F} $\frac{[\text{Wm}^{-2}\text{sr}^{-1}\mu\text{m}^{-1}]}{[\mu\text{molm}^{-2}\text{s}^{-1}]}$ values are determined from the $\text{SIF}_{\text{total}}$ light response curves in Figure 5.5c, c) LUE_{P} [unitless] values are monthly averaged LUE_{P} (Figure A.3) calculated following Equation 5.5 as $\text{LUE}_{\text{P}} = \frac{\text{GPP}}{\text{APAR}}$. d) GPP_{max} [μmol m^{-2}s^{-1}] and e) c [μmol m^{-2}s^{-1}] are determined from the GPP light response curves in Figure 5.5 d ($\text{GPP} = \frac{\text{GPP}_{\text{max}} \times \text{APAR}}{c + \text{APAR}}$, derived from Equations 5.5&5.6). Error bars in a) and c) are the standard deviations of f_{esc} and LUE_{P} within each month and in b), d), and e) they are the 95% confidence intervals of fitted values. Anomalous values with high fit errors go outside the bounds of the plot but exact values can be found in Table A.2.

average f_{esc} values. Winter f_{esc} values are heavily influenced by the snow response of NIRv (Figure 5.2 d) and therefore make the data more difficult to interpret. When we ignore f_{esc} during snow covered months, the seasonal change in f_{esc} is approximately 20% (Figure 5.6 a). f_{esc} shows a slight decrease at high APAR values over the summer months, which is most pronounced in June and July (Figure 5.5a). The sensitivity of f_{esc} to high APAR values thus impacts the light response of SIF shown in Figure 5.5 b.

Monthly light response curves of SIF in Figure 5.5 b were determined with a linear fit based on Equation 5.1 ($\mathrm{SIF} = a \times \mathrm{APAR}$). Thus, the fit factor a represents average $\mathrm{LUE_F} \times f_{esc}$ for each month. Within each month the light response of SIF shows a slight curvature at high APAR values. This leveling off is most noticeable in April, June, and August. We attribute the curvature in the SIF light response curve to variations in f_{esc} at a high temporal resolution under high light conditions, as shown in Figure 5.5a. When we correct for the effects of f_{esc} by calculating $\mathrm{SIF_{total}}$, the leveling off of SIF at high light is no longer observed (Figure 5.5 c). Light responses of half-hourly $\mathrm{LUE_F}$ values calculated following Equation 5.1 ($\mathrm{LUE_F} = \frac{\mathrm{SIF}}{f_{esc} * \mathrm{APAR}}$) show a subtle decline at high APAR values (Figure A.3 b), however, it is significantly smaller than the decline in $\mathrm{LUE_P}$ (Figure A.3 c) and the light saturation observed with GPP (Figure 5.5 d).

Light response curves of $\mathrm{SIF_{total}}$ in Figure 5.5 c were calculated using a linear fit after correcting SIF for variations in f_{esc} ($\mathrm{SIF_{total}} = \frac{\mathrm{SIF}}{f_{esc}} = a \times \mathrm{APAR}$). Thus, the fit parameter a represents the monthly average $\mathrm{LUE_F}$. Fitted values for $\mathrm{LUE_F}$ from Figure 5.5c are summarized in Figure 5.6b. Over the course of the year, correcting for f_{esc} does not change the fact that both SIF and $\mathrm{SIF_{total}}$ exhibit seasonally variable light response curves and thus, structural and illumination effects cannot fully explain the increase in summer SIF. Seasonal variability in $\mathrm{LUE_F}$ (as calculated from the fitted curves in Figure 5.5c) shows a strong down-regulation, but non-zero values, over winter and a gradual increase towards spring (Figures 5.5 b-c & 5.6 b). This winter light response explains the early spring increase in SIF prior to changes in GPP observed in Figure 5.2 a. This is further explored in Section 5.4.2. In summary, the influence of f_{esc} is important for SIF at a high temporal resolution when high APAR values create more variable radiative conditions, while the influence of LUE_{F} is more dominant over the seasonal cycle.

Figures 5.5 d and A.3 c highlight both the light saturation of GPP during the growing season as well as its seasonal up and downregulation. Light response curves of GPP in Figure 5.5 d are a non-linear least squares fit following Equations 5.5 and 5.6 ($\text{GPP} = \frac{\text{GPP}_{\text{max}} \times \text{APAR}}{c + \text{APAR}}$) and LUE_{P} in Figure A.3 c is calculated following Equation 5.5 ($\text{LUE}_{\text{P}} = \frac{\text{GPP}}{\text{APAR}}$). LUE_{P} is variable over shorter timescales due to changes in APAR Equations 5.5,5.6, Figure A.3 c and seasonally variable due to the seasonal changes in photosynthetic capacity. The response of LUE_{P} to APAR is shown in Figure 5.5 d as the curvature of each GPP light response curve within a particular month at high APAR values and in Figure A.3c as the curvature in the light response of LUE_{P}. The seasonal light response of GPP shows maximum saturation values (GPP_{max}) over summer and minimum values over winter (Figures 5.5 d & 5.6 c, d), with the exception of April where rapid changes during the spring transition led to poor fit statistics. This is in good agreement with the seasonal cycle of monthly averaged LUE_{P} (Figure 5.6 c). Seasonal changes in GPP_{max} and LUE_{P}, which reflect the seasonal cycle of GPP, are driven by the seasonal up and downregulation of photosynthesis and sustained photoprotection over winter. The light response curves of GPP and LUE_{P} show the highest degree of non-linearity over summer, while in winter, spring, and fall, linear fits performed nearly as well as the fitted equation. This is also reflected in the fit parameter c (Figure 5.6 e) which shows a small seasonal cycle with minimum values over summer (excluding winter when GPP is essentially 0 and there is insufficient light for saturation). Lower c values represent a more pronounced curvature in the light response of GPP over summer. This may reflect the fact that non-summer fits involve a smaller range of APAR values and thus do not receive sufficient light to saturate photosynthesis. We attribute the seasonal variation in c as likely due to temperature dependencies. In addition, water limitations or other environmental stresses may impact c over shorter temporal resolutions. Seasonal asymmetry in c may be caused by differences in temperature and water availability between the start and end of the growing season.

Seasonal variations in $\mathrm{GPP_{max}}$ and monthly average $\mathrm{LUE_P}$ largely agree with the seasonal variations in $\mathrm{LUE_F}$, however, they exhibit some important differences (Figure 5.6 b, c, d). In particular, $\mathrm{LUE_F}$ slightly increases in spring prior to significant changes in $\mathrm{LUE_P}$ or $\mathrm{GPP_{max}}$. $\mathrm{LUE_F}$ reaches a summer maximum around July and remains elevated at a near constant value from June through September. On the other hand, $\mathrm{GPP_{max}}$ continues to increase over the summer, peaking in September before decreasing for winter. These subtle changes in shape lead to a seasonally variable relationship between SIF and GPP.

Figure 5.7 a & b shows the relationships between SIF-GPP and $\mathrm{SIF_{total}}$-GPP fitted monthly to half-hourly data. Fitted equations and parameters are summarized in Table A.3. Over the winter months, the relationships between SIF or $\mathrm{SIF_{total}}$ and GPP appear more linear, despite being fit with the non-linear Equation 5.8. Over summer, the non-linear relationship between SIF or $\mathrm{SIF_{total}}$ and GPP becomes more pronounced. This can be attributed to the fact that curvature in the light response curve of GPP is most pronounced over summer (Figure 5.5 d), and thus shows up more prominently in the SIF-GPP relationship. We observe a higher degree of non-linearity in the $\mathrm{SIF_{total}}$-GPP relationship (Figure 5.7 b) than the SIF-GPP relationship (Figure 5.7 a), with the exception of July which can be attributed to a poor overall fit (Figure 5.7 b, Table A.3). The curvature of the SIF light response due to changes in f_{esc} works to linearize the SIF-GPP relationship compared to that of $\mathrm{SIF_{total}}$-GPP. Finally, both SIF and $\mathrm{SIF_{total}}$ show a seasonally variable relationship with GPP. We attribute this seasonal variation to the small light response of SIF over winter and slight differences in the seasonal changes in $\mathrm{LUE_F}$ and $\mathrm{GPP_{max}}$ (Figure 5.6).

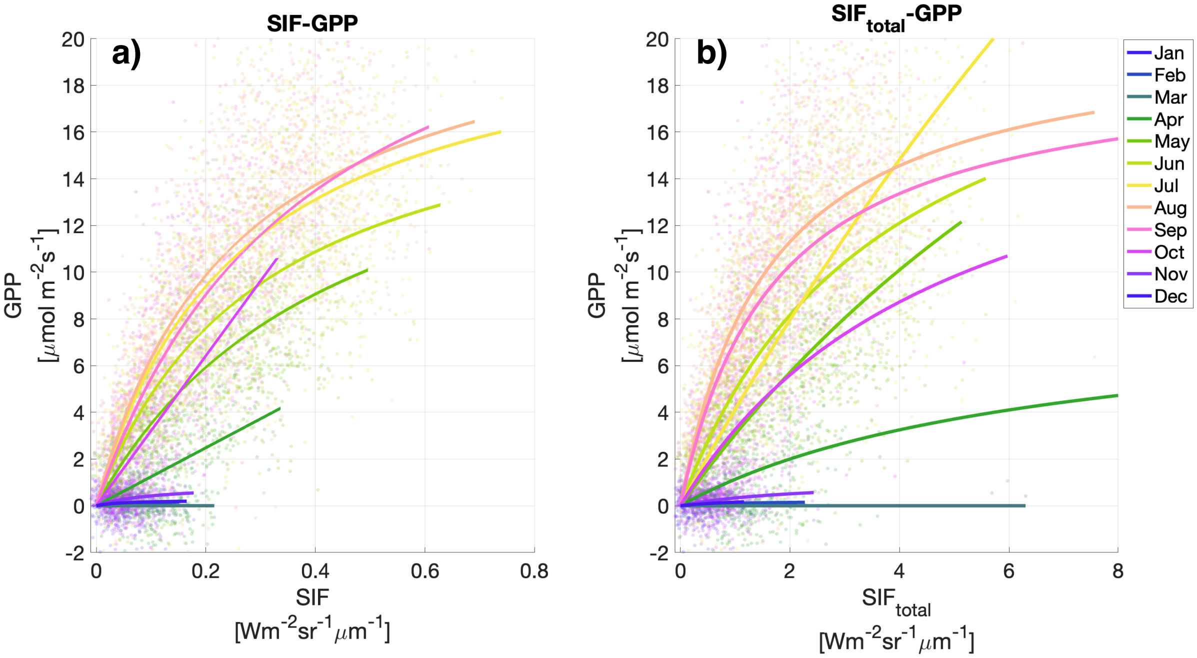

Figure 5.7: Monthly fitted curves to half-hourly data based on Equation 5.8 for a) SIF-GPP and b) SIF$_{\text{total}}$-GPP highlighting the seasonally dynamic SIF-GPP relationship. Curves are only plotted within the data range for that month. Scatter points are half-hourly values.

5.4 Discussion

5.4.1 SIF as a proxy for GPP, and relation to other VIs

Our results highlight SIF as a more effective and comprehensive proxy for GPP than existing vegetation indices from half-hourly to monthly temporal scales in a boreal ecosystem. This can be attributed to the close link between SIF and electron transport rate (ETR, the product of efficiency of photochemistry and absorbed light by chlorophyll), the first step in photosynthetic carbon assimilation (Gu et al., 2019). Our results show the correlation between SIF and GPP strengthens with longer temporal averaging windows (Figure 5.3). Additionally, if one considers the inherent non-linearity in the SIF-GPP relationship (Section 5.4.2), SIF significantly outperforms other remotely sensed metrics as a proxy for GPP.

Finally, SIF shows no strong responses to snow cover - an important consideration for boreal ecosystems (Figures 5.2 & 5.3).

Vegetation indices show substantially decreased effectiveness over shorter temporal scales (daily, half-hourly) compared with SIF (Figures 5.2 & 5.3). The second most effective proxy for GPP (after SIF) was CCI. CCI reflects the ratio of chlorophyll:carotenoids, which change seasonally to support sustained NPQ and the regulation of photosynthesis (Gamon et al., 2016). These bulk pigment ratios are not expected to change at a daily time resolution (Gamon et al., 2016) and are therefore unable to capture the dynamic nature of GPP at sub-seasonal temporal resolutions. CCI is thus a useful metric for satellite observations with only one sample per day for tracking the seasonality of GPP and sustained NPQ, with a few caveats. Our observations show that CCI reaches a maximum over summer, prior to maximum GPP (Figure 5.2 b). The fall increase in carotenoid pigments to support sustained photoprotection over winter may occur prior to fall cessation of GPP due to the inter-conversion between xanthophyll pigments. Furthermore, we observe only small variations in CCI during the spring transition which suggests a potential reactivation of photosynthesis, prior to the spring decrease in carotenoid pigments (Pierrat et al., 2021a). Therefore, CCI is a good metric for tracking general seasonality in evergreen systems and can provide important insights into plant's LUE_P. However, it has limited accuracy for determining spring onset and fall cessation dates and for tracking GPP at finer (daily/half-hourly) resolutions. These subtle differences may indicate a mismatch between the timing of optimal photosynthetic capacity (peak CCI) and optimal environmental, structural, and physiological conditions (peak GPP).

Our results imply that SIF is not solely proportional to the light absorbed by chlorophyll but is also responding dynamically to seasonal variation in NPQ through changes in LUE_F. The yield of fluorescence and the yield of photochemistry are both impacted by PQ and NPQ (Porcar-Castell et al., 2014). Prior work at the leaf level has shown that under high light levels, when there is significant induction of NPQ, the yield of fluorescence and the yield of photochemistry are proportional (Porcar-Castell et al., 2014; Van Der Tol et al., 2014). Our results show that at the canopy scale, seasonal changes in $\mathrm{LUE_F}$ do indeed co-vary with seasonal changes in $\mathrm{LUE_P}$ (Figures 5.5, 5.6, & A.3). The performance of the HH-SIF random forest model decreased considerably when only PAR was included (Figure 5.4) and the Daily-SIF random forest model showed air temperature as the strongest predictor. This confirms the fact that PAR alone is insufficient for explaining the observed variation in SIF, even at a half-hourly resolution.

Air temperature is a useful predictor of sustained NPQ in temperate evergreen ecosystems and sustained NPQ is responsible for shaping the seasonal patterns of SIF (Raczka et al., 2019). Our results provide empirical evidence to support this explanation because both daily average SIF and GPP were best predicted by air temperature (Figure 5.4). We found that accounting for changes in f_{esc} over the course of the season was also insufficient for explaining the seasonal up and downregulation of fluorescence (Figure 5.5). We found that f_{esc} only varied ∼20% over the course of the season, whereas changes in $\mathrm{LUE_F}$ were significantly greater (350% increase over summer) (Figure 5.6). This is particularly important in evergreen needle leaf systems but may not be true for cropping or deciduous systems with high variance in canopy structure (and thus f_{esc}). The observed seasonal pattern in $\mathrm{LUE_F}$ largely co-varied with the seasonal patterns of $\mathrm{LUE_P}$ and $\mathrm{GPP_{max}}$ making SIF an effective proxy for GPP (Figures 5.5 & 5.6).

We view the response of SIF to variations in light absorbed by chlorophyll not as a limitation of SIF as a proxy for GPP, but rather, a strength. SIF has a more dynamic light response than other remotely sensed products (CCI, NDVI, NIRv) and can therefore more effectively capture variations in GPP due to both common physical drivers (light absorbed by chlorophyll) and the ecophysiological connections between $\mathrm{LUE_F}$ and $\mathrm{LUE_P}$ based on the light reactions of photosynthesis.

5.4.2 Dynamics between $\mathrm{LUE_F}$, $\mathrm{LUE_P}$, and f_{esc}, and the convergence and divergence between SIF and GPP

Over half-hourly temporal scales, when SIF and GPP are predominantly influenced by variations in PAR (Figure 5.4), the relationship between SIF and GPP will become non-linear because $\mathrm{LUE_F}$ is largely invariant with APAR compared with $\mathrm{LUE_P}$ which exhibits strong saturation at high APAR values Figures 5.5 & A.3). Within each month, $\mathrm{LUE_F}$ can show a subtle decline with increasing APAR (Figure A.3b) which partially, but incompletely, linearizes the SIF-GPP relationship. This decline in $\mathrm{LUE_F}$ may reflect short-term regulation of the photosynthetic system by rapidly reversible NPQ, although further work should investigate this in more detail. The decrease in f_{esc} at high APAR values also partially linearizes the relationship between SIF and GPP. Although the cause for the decrease in f_{esc} at high APAR is unknown, we hypothesize that complex shading and illumination effects due to different sun geometries throughout the year may explain this decrease. Therefore, future work in this ecosystem and other evergreen needleaf ecosystems should therefore focus on further constraining the effects of f_{esc} under a variety of viewing directions and illumination conditions.

Over longer temporal scales (seasonally), $\mathrm{LUE_P}$ is predominantly driven by changes in $\mathrm{GPP_{max}}$. When temporally averaging, the extreme PAR values that create the curvature in the light response of GPP become less important. Thus, due to the seasonal co-variation between $\mathrm{GPP_{max}}$ and $\mathrm{LUE_F}$ (Figure 5.6), the SIF-GPP relationship converges onto a linear relationship.

Although the light saturation of GPP is the primary driver of divergence in the SIF-GPP relationship, there are other stressors that vary seasonally and impact $\mathrm{LUE_P}$ and $\mathrm{LUE_F}$, consequently impacting the relationship between SIF and GPP. Air and soil temperature, soil water content, and relative humidity were all important drivers of SIF and GPP identified in the random forest model optimization (Figure 5.4) and therefore may be driving divergence between $\mathrm{LUE_F}$ and $\mathrm{LUE_P}$ (and subsequently SIF and GPP). Furthermore, prior work has identified air temperature as an additional potential cause for non-linearity between SIF and GPP over the fall transition (Kim et al., 2021). This is not observed in our fall transition data. However, we observe some non-linearity between SIF and GPP at a daily resolution over summer (Figure 5.3). We attribute this non-linearity to the strong light saturation of GPP over summer and the dependence of $\mathrm{LUE_P}$ on APAR. This means that APAR is the predominant driver for non-linearity, although future work in this area is necessary to explore potential secondary sources of non-linearity.

Our results show a small light response of SIF during winter that has the potential to overestimate GPP in winter and early spring (Figures 5.5 & 5.6). The wintertime light response of SIF may suggest low rates of wintertime photosynthesis that are not captured by flux tower measurements due to low signal-to-noise ratios. This may be possible if temperature is warm enough to thaw boles and allow trees to access small amounts of water stored in the stems (Ensminger et al., 2004; Bowling et al., 2018; Pierrat et al., 2021a). However, we suggest that the observed early spring and winter light response of SIF may be attributed to photosystem I remaining active over winter while photosystem II shuts down more strongly (but not completely) with seasonal downregulation of photosynthesis (Öquist and Huner, 2003; Bag et al., 2020; Porcar-Castell et al., 2008; Porcar-Castell, 2011). This small amount of photosystem activity thus leads to a winter light response that does not reflect carbon assimilation. More work in this area is necessary to explore the nuances of wintertime SIF.

During the spring transition photosynthetic reactivation happens rapidly, in phases, and sometimes reversibly (Pierrat et al., 2021a). Therefore, monthly or monthly averaged SIF and GPP data (Figures 5.5 & 5.6) are inadequate for accurately determining spring transition dates and higher temporal resolution data is necessary. A wintertime light response of SIF adds additional complexity to the use of SIF to determine start of season dates. For a more detailed look at the spring transition and how to effectively use SIF to evaluate the onset of photosynthesis in spring we refer readers to Pierrat et al. (2021a).

In order to account for additional potential non-linearities in the SIF-GPP relationship and adjust for the wintertime SIF light response, users of SIF should treat the SIF-GPP relationship as a seasonally dynamic variable as illustrated in Figure 5.7. This will help account for seasonally variable structural effects, as highlighted by Kim et al. (2021), as well as the seasonal differences between $\mathrm{LUE_P}$ and $\mathrm{LUE_F}$ and the wintertime SIF light response. A seasonally variant SIF-GPP relationship may also help account for additional non-linearities between SIF and GPP that are not due to the light saturation of GPP, including drought or temperature stress.

5.4.3 Implications for Satellite Observations

Spaceborne observations of SIF typically occur around midday and suffer from higher uncertainty under cloudy sky conditions (although this bias is less than typical vegetation indices) (Frankenberg et al., 2011; Parazoo et al., 2019; Köhler et al., 2018). Therefore, they are typically biased towards sunny sky and high light conditions. This bias may lead satellite based retrievals of SIF in boreal ecosystems to exhibit a stronger SIF-GPP non-linearity. This will be exacerbated over summer when midday PAR often falls into the range where GPP is saturated and SIF continues to increase (Figures A.1, A.2, & 5.5). Future work in this area may help us determine the impact of high light, sunny sky bias on satellite-derived SIF-GPP relationships. By introducing the non-linear function (Equation 5.8) for the relationship between SIF and GPP, users of satellite SIF data will more accurately describe the light saturation of GPP. Additionally, a seasonally dynamic SIF-GPP relationship allows users of SIF to better account for seasonal differences in $\mathrm{LUE_F}$ and $\mathrm{LUE_P}$.

5.5 Conclusions

This work provides a direct comparison between SIF and several other remote sensing metrics as proxies for GPP in the boreal forest and explains how the relationship between SIF and

GPP becomes increasingly linear from half-hourly to monthly time scales.

We find that at daily to monthly resolutions, SIF shows a linear relationship with GPP and outperforms other commonly used vegetation indices (NDVI, NIRv, PRI, CCI) as a proxy for GPP. At a half-hourly resolution, the relationship between SIF and GPP becomes non-linear, as we would expect based on theory and the leaf level response of SIF and GPP to APAR. Nevertheless, SIF still provides a more effective proxy for GPP than other remote sensing metrics.

We use an entirely data-driven approach for separating out structural and physiological effects on SIF and GPP and the relationship between the two. The dynamics between $\mathrm{LUE_P}$, $\mathrm{LUE_F}$, and f_{esc} dictate the nature of the relationship between SIF and GPP at varying temporal scales. At a half-hourly resolution, APAR is the primary driver of both SIF and GPP. Therefore, non-linearity between SIF and GPP at a half-hourly resolution is primarily driven by the light saturation of GPP. Temporal averaging reduces this non-linearity by reducing the impact of light saturated GPP at high PAR. Variations in f_{esc} become more important to SIF at a half-hourly resolution and lead to a slight reduction in SIF at high light levels. Seasonally, SIF and GPP both vary with temperature and the light use efficiencies of fluorescence and photosynthesis ($\mathrm{LUE_F}$, $\mathrm{GPP_{max}}$) generally co-vary across the seasonal cycle with sustained non-photochemical quenching. f_{esc} does not play a significant role in the seasonal relationship between SIF and GPP. A small light response of SIF in winter, as well as small differences in the seasonal cycles of $\mathrm{LUE_F}$ and $\mathrm{GPP_{max}}$ lead to a seasonally variable SIF-GPP relationship. Accounting for this seasonally variable relationship will help improve the accuracy for SIF as a proxy for GPP.

Our results strongly support the value of SIF as a proxy for GPP in boreal forests, and emphasize the need for future research to further constrain the relationship under varying illumination and environmental conditions.

CHAPTER 6

Forests for forests: combining vegetation indices with solar-induced chlorophyll fluorescence in random forest models improves gross primary productivity prediction in the boreal forest

6.1 Introduction

Uncertainty in future climate projections is largely driven by terrestrial ecosystem feedbacks on the carbon cycle (Friedlingstein et al., 2014). A major contributor to terrestrial ecosystem feedbacks is plant carbon uptake via photosynthesis. Plant carbon uptake can be estimated locally at the tower/site level, as gross primary productivity (GPP), but remote sensing is necessary to scale and understand carbon exchange across space and time (Anav et al., 2015). This is especially relevant in arctic-boreal ecosystems which play a major, but highly uncertain, role in the global carbon cycle (Bonan, 2008; Thurner et al., 2014). Arctic-boreal carbon cycle uncertainty can be attributed to unevenly distributed field observations and challenges in using remote sensing (e.g. high sun angles, snow cover, short growing seasons, persistent greenness) (Nelson et al., 2022). Therefore, improvements must be made in how we connect remotely sensed measurements to GPP in arctic-boreal ecosystems.

GPP can be described using the light-use-efficiency model (Monteith, 1972):

$$\mathrm{GPP} = \mathrm{PAR} \times f\mathrm{PAR} \times \mathrm{LUE_P} \tag{6.1}$$

where PAR is the photosynthetically active radiation, fPAR is the fraction of photosynthetically active radiation absorbed by chlorophyll, and $\mathrm{LUE_P}$ is the light-use-efficiency of photosynthesis. Proposed remote sensing metrics for approximating GPP typically track either the physical (fPAR) or the physiological ($\mathrm{LUE_P}$) components of this equation. Solar-induced chlorophyll fluorescence is an especially powerful remote sensing metric for understanding GPP over a variety of ecosystems (Sun et al., 2017, 2018) and across a variety of scales (Magney et al., 2020; Mohammed et al., 2019; Pierrat et al., 2022a; Porcar-Castell et al., 2021; Yang et al., 2017) due to its connection to both the physical (PAR×fPAR) and the physiological ($\mathrm{LUE_P}$) components of GPP. SIF can be described using the light-use-efficiency model:

$$\mathrm{SIF} = \mathrm{PAR} \times f\mathrm{PAR} \times \mathrm{LUE_F} \times f_{esc} \tag{6.2}$$

where $\mathrm{LUE_F}$ is the light-use-efficiency of fluorescence, and f_{esc} is the fraction of emitted SIF photons which escape the canopy. SIF and GPP share the physical drivers PAR×fPAR, which largely explains the relationship between SIF and GPP in cropping systems (Dechant et al., 2020). Equations 1 and 2 can be combined to eliminate the absorbed photosynthetically active radiation (APAR = PAR×fPAR):

$$\mathrm{GPP} = \mathrm{SIF} \times \frac{\mathrm{LUE_P}}{\mathrm{LUE_F} \times f_{esc}} \tag{6.3}$$

The physiological component of SIF, $\mathrm{LUE_F}$ co-varies with $\mathrm{LUE_P}$ under moderate light conditions (Porcar-Castell et al., 2014; Van Der Tol et al., 2014) and averaged over broad spatio-temporal scales (Magney et al., 2020; Pierrat et al., 2022a). This is the basis for SIF as a proxy for GPP when measured from space across a broad range of ecosystems (Sun et al., 2017, 2018). However, these conditions are not necessarily always met (Marrs et al., 2020), especially in the boreal forest where complex canopy structure and divergence between the light and carbon fixation reactions of photosynthesis can complicate these signals (Maguire et al., 2020; Pierrat et al., 2022a). Therefore, a more nuanced relationship between SIF and GPP that takes into consideration divergence between variations in LUE_F, LUE_P, and f_esc will further improve the utility of SIF as a proxy for GPP. Additional reflectance-based remotely sensed metrics, i.e. vegetation indices (VIs), can provide more information on both the structural and physiological processes impacting GPP and can therefore improve our ability to track and understand GPP with remote sensing.

Physically, SIF and GPP are impacted by illumination conditions and canopy structure (i.e. the combined effects of leaf-area index (LAI), vertical distribution of LAI, leaf orientation, clumping, etc.) which mediate both fPAR and f_esc. At a constant PAR and LUE_P, GPP amplifies under cloudy sky conditions because a higher diffuse fraction allows light to penetrate deeper into the canopy, thus increasing fPAR (Alton et al., 2007; Gu et al., 2002; Durand et al., 2021). Although the amplification of GPP under diffuse skies has been well documented, it is often not considered when approximating GPP with remote sensing proxies.

Canopy structure is often approximated using greenness based VIs which are sensitive to chlorophyll content in an instrument field of view. Thus, they are generally a good approximation for fPAR. The Normalized Difference Vegetation Index (NDVI) effectively tracks vegetation productivity in ecosystems where chlorophyll content and carbon uptake are closely correlated (i.e. larger variations in fPAR than LUE_P) (Tucker, 1979; Wang et al., 2019; Yang et al., 2017). This is not the case in the boreal forest where changes in carbon uptake do not correlate with changes in chlorophyll content (Gamon et al., 2013; Garbulsky et al., 2010; Sims et al., 2006b). Additionally, NDVI is extremely sensitive to the presence of snow cover (Pierrat et al., 2021a, 2022a). The near-infrared reflectance from vegetation (NIRv) expands on NDVI by multiplying NDVI by the total scene NIR reflectance, thereby amplifying the vegetated signal. NIRv has shown stronger correlations with fPAR and GPP than NDVI alone (Badgley et al., 2019, 2017). NIRv can also be used as a proxy for f_esc (Zeng et al., 2019). Both NDVI and NIRv provide useful information on the physical/structural influences on SIF and GPP, however, it is unclear how sensitive these indices are to changes in fPAR and f_{esc} and if there exists a universal relationship across ecosystems.

Physiologically, the light-use-efficiencies of both fluorescence and photosynthesis are mediated by non-photochemical quenching - a heat dissipation mechanism that plants utilize to avoid damage from excess sunlight (Raczka et al., 2019; Walter-McNeill et al., 2021). The extent to which non-photochemical quenching is necessary to protect plant tissue depends on a host of environmental controls that determine a plant's ability to photosynthesize (Demmig-Adams and Adams, 2006). Of particular relevance in this respect is plant's sensitivity to temperature. Freezing over winter or heat waves over summer create stress conditions which subsequently impact $\mathrm{LUE_P}$. Monitoring the extent of non-photochemical quenching thus provides insight into $\mathrm{LUE_P}$ (Adams et al., 2004), and likely $\mathrm{LUE_F}$, although those dependencies are not yet well quantified.

Non-photochemical quenching manifests in two forms of photoprotection in boreal ecosystems, both of which can be detected with remote sensing measures (Demmig-Adams et al., 2006; Gamon et al., 1997, 2016). The first is rapidly reversible and therefore important under short-term high light stress. It can be detected using the Photochemical Reflectance Index (PRI). Therefore, PRI tracks changes in $\mathrm{LUE_P}$ over the diurnal cycle (Gamon et al., 1997; Wong and Gamon, 2015a,b). The second form is sustained and thus important over longer time periods such as winter in regions where freezing temperatures limit the ability for plants to (Verhoeven, 2014). This form can be tracked using the Chlorophyll-Carotenoid Index (CCI) (Gamon et al., 2016). CCI has successfully tracked variations in GPP over the seasonal cycle because it is sensitive to long-term changes in $\mathrm{LUE_P}$.

Including information on heat dissipation dynamics through remotely sensed products (PRI and CCI) improves modelling of photosynthetic phenology (Wong et al., 2022), especially when used in conjunction with SIF (Hikosaka and Tsujimoto, 2021; Wang et al., 2020). In addition, correcting the SIF signal for canopy and structural effects using structurally sensitive metrics also improves its relationship with GPP (Liu et al., 2020b; Lu et al., 2020). It has been well documented and mechanistically explained why vegetation indices are sensitive to changes in non-photochemical quenching or canopy structure but there are no universal quantitative relationships among them. To develop such a relationship, the impacts from canopy structure, view/sun angle effects, snow cover, and potential differences in instrumentation (field of view, instrument sensitivity) must all be accounted for. Until mechanistic models are able to effectively account for all the aforementioned effects, the capacity for these indices to inform SIF and GPP is limited to qualitative or site-specific empirical relationships. In order to make more effective use of remote sensing as a proxy for GPP, it is necessary to have a quantitative framework that can relate SIF, VIs, and GPP.

Advances in machine learning have provided exciting opportunities for data analysis and predictive modeling. In particular, random forest models are non-parametric in nature and are therefore well suited for approximating non-linear, multi-parameter relationships in complex systems (Breiman, 2001). Because random forest models do not assume functional dependencies between input variables and predicted output and rather 'learn' relationships based on input data, they are particularly useful for systems where statistical parameterized models either do not exist or are not well constrained. Random forest models are also highly interpretable compared with other machine learning techniques due to predictor importance estimates, which make them more useful for explaining and understanding observed relationships. Finally, random forest models have already been used to understand nuance in the SIF-GPP relationship (Bai et al., 2022; Jiao et al., 2019; Pierrat et al., 2022a). We propose that using random forest models as a tool to understand and predict GPP based on a combination of remote sensing metrics will present a significant improvement over traditional parameterized models (Dechant et al., 2020; Monteith, 1972; Van Der Tol et al., 2014) or other machine learning approaches.

The central question of this study is therefore: Can we improve our ability to predict GPP from SIF by using random forest models as a quantitative framework that can incorporate additional physical and physiological information provided by VIs? To answer this question, we present 2.5 years of tower-based remote sensing data across two boreal forest locations, qualitatively evaluate the seasonal and diurnal trends among them, and present an interpretation on the physical and physiological information contained in them (Section 6.3.1). We justify the use of random forest models as a tool for understanding SIF, VI, and GPP dynamics by showing that they can accurately reproduce SIF-GPP-PAR relationships (Section 6.3.2). Finally, we explore the utility of random forest models and remotely sensed products for improving GPP estimation by showing how random forest models driven by SIF, VIs, and temperature improve the prediction of GPP and shed light on important physical and physiological processes (Sections 6.3.3 & 6.3.4).

6.2 Materials and Methods

6.2.1 Site Description: Southern Old Black Spruce and NEON Delta Junction

We collected data at the Southern Old Black Spruce site (SOBS, FLUXNET site code CA-Obs) and the National Ecological Observatory Network (NEON), Delta Junction (DEJU) which represent the northern and southern limits of the North American boreal forest and associated environmental conditions (Figure 6.1, Table 6.1). SOBS is located near the southern limit of the boreal forest in Saskatchewan, Canada (53.98°N, 105.12°W) (Jarvis et al., 1997). It is a mixed forest stand with stem density predominantly (90%) black spruce (*Picea mariana*), and scattered (10%) larch (*Larix laricina*). DEJU is located towards the northern end of the boreal forest outside Delta Junction, Alaska (63.88°N, 145.75°W). It is an evergreen forest dominated by black and white spruce (*Picea mariana & Picea glauca*).

6.2.2 Data Collection: Tower-based Remote Sensing, GPP, and Environmental Variables

We collected tower-based remotely sensed measurements (far-red SIF, NDVI, NIRv, CCI, PRI) using PhotoSpec (see Grossmann et al. (2018) for detailed instrument description) at

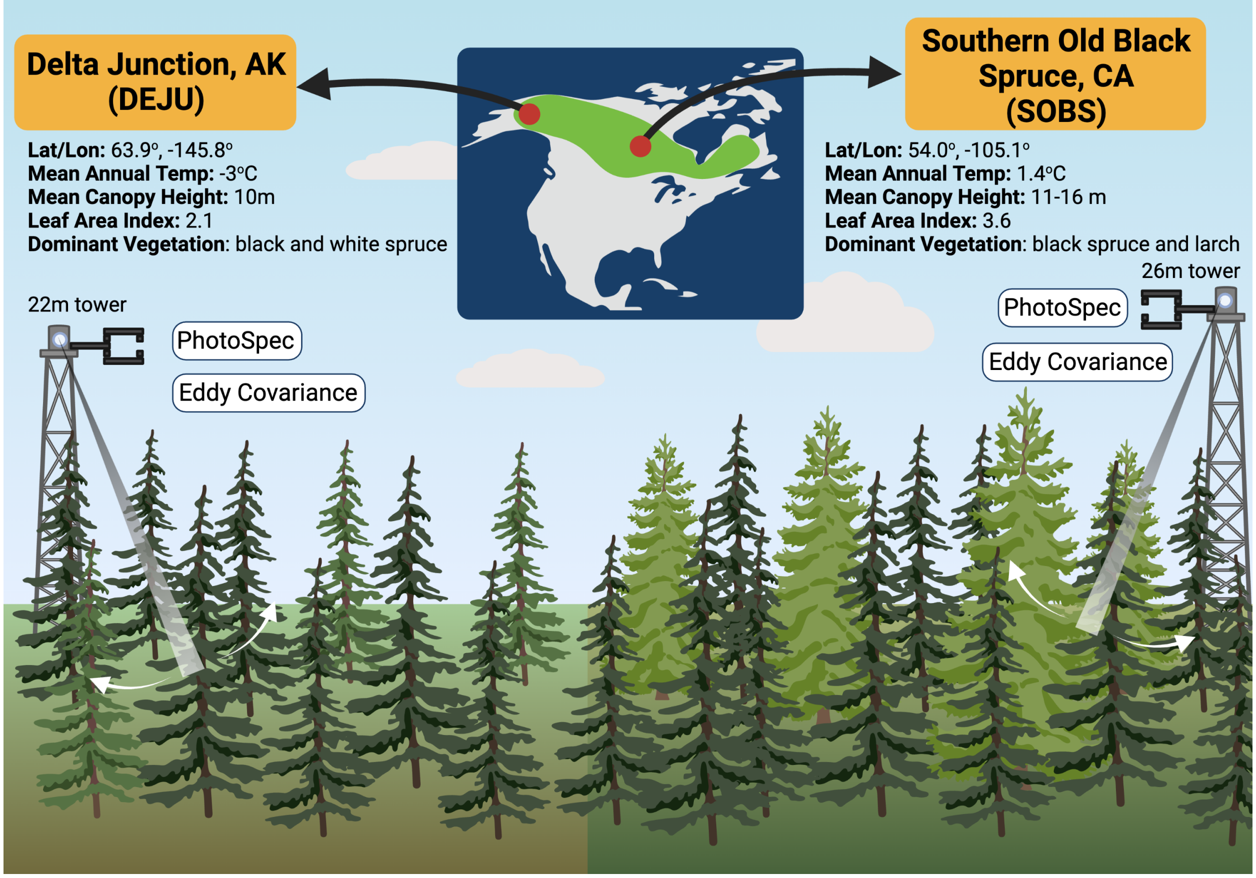

Figure 6.1: Experimental setup at the two boreal forest field locations. Site information for SOBS from (Pappas et al., 2020a; Chen et al., 2006). Site information for DEJU from the National Ecological Observation Network (NEON). Figure created with BioRender.com.

both the SOBS and DEJU field sites. Measurements ran from August 2019 - December 2021 at both field locations (Figures 6.2 & 6.3). At both sites, Photospec was installed atop the scaffolding tower facing due north. It has a narrow field of view (0.7°), 2-D scanning capabilities, and simultaneously measures SIF and VIs at the same point in the canopy (Grossmann et al., 2018). Individual measurements take approximately 20 seconds. We took canopy representative scans at both field locations within a 30-minute window and averaged measurements together to compare with the temporal resolution of GPP and environmental variables. SIF was retrieved in the far-red (745-758 nm) wavelength range using a Fraunhofer-line based fitting algorithm (Grossmann et al., 2018). The Fraunhofer-line based approach makes SIF retrievals insensitive to atmospheric scattering and therefore robust even under cloudy sky conditions (Chang et al., 2020; Frankenberg et al., 2011; Mohammed et al., 2019). We filtered data for low quality retrievals and retrievals with unstable sky conditions (Pierrat et al., 2022a, 2021a) for both sites. The VIs were calculated as follows, with $\rho_{nm:nm}$ = the average reflectance across a wavelength range in nm:

$$\text{NDVI} = (\rho_{830:860} - \rho_{620:670})/(\rho_{830:860} + \rho_{620:670}) \tag{6.4}$$

$$\text{NIRv} = (\rho_{830:860} - \rho_{620:670})/(\rho_{830:860} + \rho_{620:670}) \times \rho_{830:860} \tag{6.5}$$

$$\text{PRI} = (\rho_{569:571} - \rho_{520:532})/(\rho_{569:571} + \rho_{520:532}) \tag{6.6}$$

$$\text{CCI} = (\rho_{520:532} - \rho_{620:670})/(\rho_{520:532} + \rho_{620:670}) \tag{6.7}$$

In boreal ecosystems, the onset of photosynthesis often occurs prior to complete snow melt (Parazoo et al., 2018; Starr and Oberbauer, 2003). Therefore, any proposed approach for predicting GPP based on remote metrics must be effective even in the presence of snow. Because of this, we did not filter for snow but visually identified snow dates using phenocam imagery (Richardson et al., 2018). Filtering for snow using an NDVI threshold > 0.5 (Cheng et al., 2020; Magney et al., 2019a) did not change the results of this study (Figures B.1-B.4).

To include impacts of illumination conditions on our analysis, we determined a measure of direct vs. diffuse radiation (Df). Df reflects the deviation of PAR at a given solar zenith angle from the expected PAR during a clear sky reference day so that Df=1 is clear sky conditions (Pierrat et al., 2021b). Df values were calculated for every PhotoSpec measurement ($\approx$20 second resolution) and averaged together in 30-minute windows to compare with GPP and environmental measurements (Table 6.1). Values where Df $>$ 0.8 are considered clear sky conditions.

Data collection and processing for eddy covariance and meteorological data for both SOBS and DEJU are summarized in Table 6.1.

Table 6.1: Summary of methods for measurement and data processing at the two field locations.

Measurement	**SOBS**	**DEJU**
SIF, VIs, PAR, & Df	PhotoSpec mounted atop the tower and processed following Grossmann et al. (2018); Pierrat et al. (2022a)	PhotoSpec mounted atop the tower and processed following Grossmann et al. (2018); Pierrat et al. (2022a)
GPP **Eddy-covariance**	Taken using a 3-D sonic anemometer (CSAT3, Campbell Scientific, Logan, UT) in combination with a closed-path infrared gas (CO2/H2O) analyzer (LI-7200 analyzer, Li-Cor, Lincoln, NE) operated in absolute mode.	Obtained from National Ecological Observatory Network (NEON) (2022a) using a Campbell Scientific CSAT-3 3-D Sonic Anemometer and LI-COR - LI7200 gas analyzer.

Continued on next page

Table 6.1: Summary of methods for measurement and data processing at the two field locations. (Continued)

Measurement	**SOBS**	**DEJU**
	We performed quality assurance on the data using the standard Fluxnet-Canada method following Barr et al. (2004, 2006).	We performed quality assurance on carbon fluxes based on turbulent and storage fluxes separately, using a bivariate statistical procedure for each, to overcome quality flag restrictions in the "expanded" NEON eddy-covariance bundle. 3% outliers (3% of rarest events from the tails of each distribution) were excluded from joint probability distributions for all available data for 1) turbulent flux and PPFD, and separately for 2) storage flux and time of day. NEE data were considered valid if both the turbulent and storage fluxes passed this quality control step (and NEE is equal to their sum).

Continued on next page

Table 6.1: Summary of methods for measurement and data processing at the two field locations. (Continued)

Measurement	**SOBS**	**DEJU**
Partitioning	Data for NEE and meteorological variables were filtered to remove low turbulence (low friction velocity) periods and then gap-filled via the R package REddyProc (Wutzler et al., 2018). REddyProc was used to partition NEE into GPP and Reco using the method of Lasslop et al. (2010), with air temperature used as the driving temperature for Reco.	Data for NEE and meteorological variables were filtered to remove low turbulence (low friction velocity) periods and then gap-filled via the R package REddyProc (Wutzler et al., 2018). REddyProc was used to partition NEE into GPP and Reco using the method of (Lasslop et al., 2010), with air temperature used as the driving temperature for Reco.
Air Temperature (Tair) & Relative Humidity (RH)	Vaisala HMP45C probe at 6 m	Vaisala HUMICAP Humidity and Temperature Probe - HMP 155 at 22 m (National Ecological Observatory Network (NEON), 2022b)
Soil Temperature (Tsoil)	Type-T (copper-constan) thermocouples at a 10 cm depth	Thermometrics - Climate RTD 100-ohm Probe at 6 cm depth (National Ecological Observatory Network (NEON), 2022c)
Soil Volumetric Water Content (SWC)	Cambell Scientific CS615 Water Content Reflectometers at a 7.5 cm depth	Sentek - EnviroSCAN TriSCAN at 6 cm depth (National Ecological Observatory Network (NEON), 2022d)

6.2.3 Data Analysis: Random Forest and Parameterized Models

We trained and tested a variety of random forest models (Table 6.2). All random forest models were produced using Matlab's TreeBagger function (MATLAB, 2019) which is based on the random forest algorithm from Breiman (2001). We used the full data collection window (Aug 2019-Dec 2021, Figure 6.2) to train all models. All models were created using 100 regression trees and sampled with replacement on an in bag fraction of 0.7 (i.e. 70% of the data were randomly chosen to train the models saving 30% to test the models). Out-of-bag (OOB) predictor importance estimates were determined using the permuted predictor delta error following the standard CART algorithm (Breiman, 2001) using the remaining 30% of data. Model performance was evaluated by calculating the Pearson's correlation coefficient (Gibbons et al., 2003) between measurements and predictions on the full dataset (R^2) and the reserved test dataset (OOB R^2 score). Specific models are identified in Section 3 with the naming conventions in Table 6.2.

We compared random forest models with common parameterized light-use-efficiency models for the relationships among SIF, GPP, and PAR (Equations 6.1, 6.2, and 6.3). All curve fitting and goodness of fit statistics (R^2 values) were done using Matlab's fit function (MATLAB, 2019). Specifics of fitted equations are provided in Section 6.3.3 and figure captions where relevant.

Table 6.2: Naming conventions and descriptions of the random forest models used in this study. ENV describes models driven with environmental inputs. RS describes models driven with remote sensing and meteorological inputs. Parentheses indicate the same model setup tested with a different variable or location.

Model Name	**Number of Data Points**	**Temporal Resolution**	**Site**	**Inputs**	**Output**	**Purpose**
ENV-SIF	12,482 (3,969)	Half-hourly	SOBS (DEJU)	PAR, Tair, Tsoil, SWC, RH, Df	SIF	To test the ability of random forest models to reproduce quantitative SIF-GPP dynamics (Section 6.3.2)
ENV-GPP	12,482 (3,969)	Half-hourly	SOBS (DEJU)	PAR, Tair, Tsoil, SWC, RH, Df	GPP	To test the ability of random forest models to reproduce quantitative SIF-GPP dynamics (Section 6.3.2)
RS-SOBS	12,482	Half-hourly	SOBS	SIF, CCI, PRI, NDVI, NIRv, Tair, Df	GPP	To test our ability to improve GPP prediction from SIF by including additional remote sensing metrics (Section 6.3.3)

Continued on next page

Table 6.2: Naming conventions and descriptions of the random forest models used in this study. ENV describes models driven with environmental inputs. RS describes models driven with remote sensing and meteorological inputs. Parentheses indicate the same model setup tested with a different variable or location. (Continued)

Model Name	**Number of Data Points**	**Temporal Resolution**	**Site**	**Inputs**	**Output**	**Purpose**
RS-DEJU	10,433	Half-hourly	DEJU	SIF, CCI, PRI, NDVI, NIRv, Tair, Df	GPP	To test our ability to improve GPP prediction from SIF by including additional remote sensing metrics (Section 6.3.3)
RS-Total	1,157 (833 clear sky)	Daily midday (10:00-14:00) average	SOBS & DEJU	SIF, CCI, NDVI, NIRv, Tair, (site)	GPP	To test the applicability of our random forest approach across multiple sites (Section 6.3.4)
RS-DSOBS	622	Daily midday (10:00-14:00) average	SOBS	SIF, CCI, NDVI, NIRv, Tair	GPP	To compare our random forest approach with existing models for GPP based on SIF (Section 6.3.4)

Continued on next page

Table 6.2: Naming conventions and descriptions of the random forest models used in this study. ENV describes models driven with environmental inputs. RS describes models driven with remote sensing and meteorological inputs. Parentheses indicate the same model setup tested with a different variable or location. (Continued)

Model Name	**Number of Data Points**	**Temporal Resolution**	**Site**	**Inputs**	**Output**	**Purpose**
RS-DDEJU	535	Daily midday (10:00-14:00) average	DEJU	SIF, CCI, NDVI, NIRv, Tair	GPP	To compare our random forest approach with existing models for GPP based on SIF (Section 6.3.4)

6.3 Results and Discussion

6.3.1 Trends among SIF, VIs, and GPP

We present the relationships and trends among SIF, VIs, and environmental parameters across seasonal and diurnal scales for both field locations in Figures 6.2 and 6.3. Compared with SOBS, DEJU generally exhibits a shorter growing season, a smaller summer maximum GPP, and lower values for all remotely sensed metrics (Figures 6.2 & 6.3).

SIF tracks the seasonal cycle and daily-weekly variability in GPP (Figure 6.2 row a). Monthly diurnal profiles of SIF show good agreement with monthly diurnal profiles of GPP across both sites (Figure 6.3 row a). SIF increases in spring prior to changes in GPP (Figure 6.2 row a) and shows a small diurnal profile over winter at both sites, while GPP does not (Figure 6.3 row a). This early spring increase has been reported in other evergreen locations

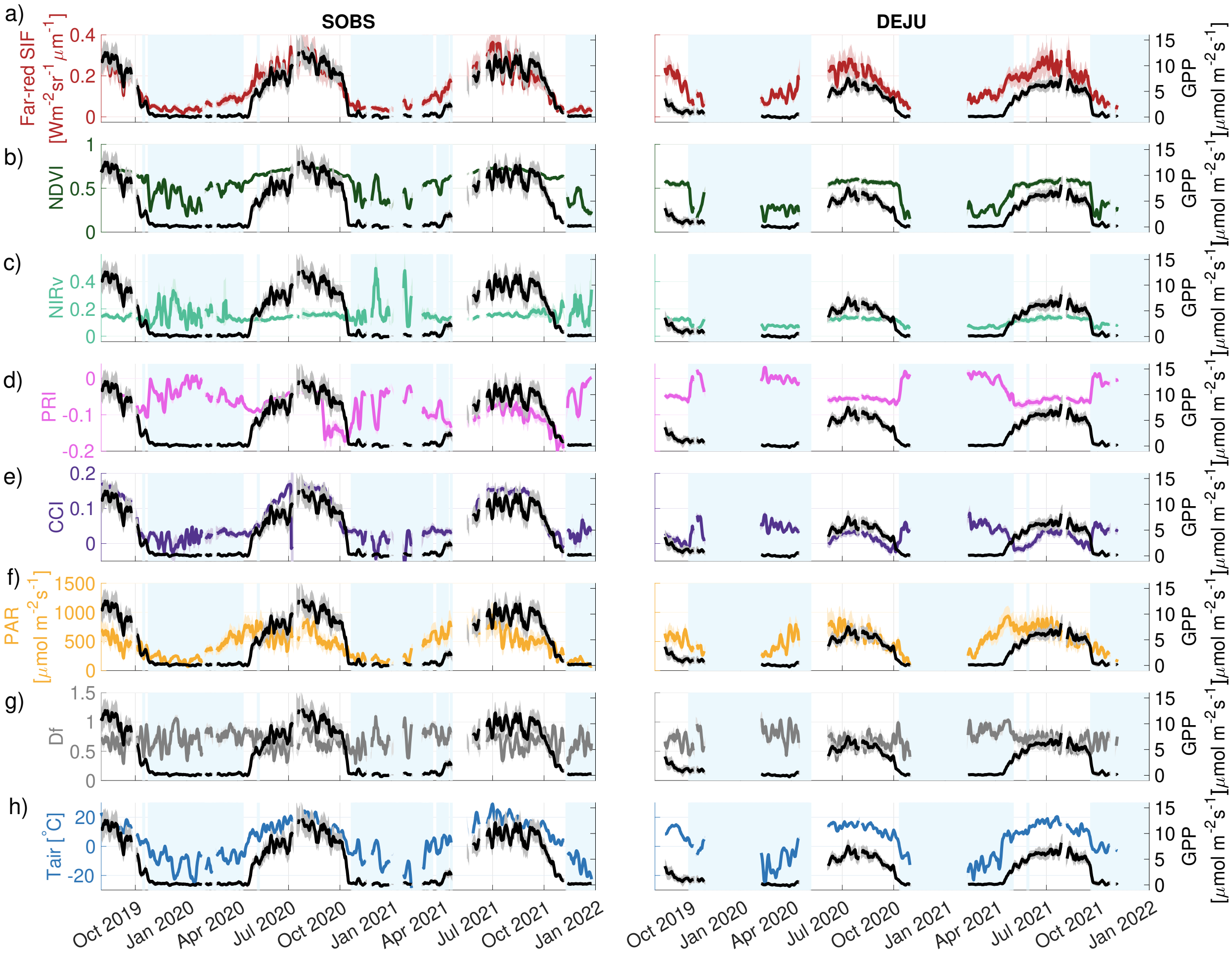

Figure 6.2: 5-day moving mean of daily average GPP compared with a) SIF, b) NDVI, c) NIRv, d) PRI, e) CCI, f) PAR, g) Df and h) Air Temperature over the entire data collection period for both the SOBS and DEJU sites. Shaded regions are the 5-day moving mean of the standard deviation of diurnal variability. Blue shaded regions are periods of snow cover as visually identified using phenocam imagery.

(Magney et al., 2019a; Pierrat et al., 2022a; Yang et al., 2022) and is attributed to persistent photosystem II activity (Bowling et al., 2018; Porcar-Castell, 2011). This leads to a winter light response of SIF which means SIF increases coincident with PAR in winter/early spring in a way that does not reflect changes in GPP. This does not preclude the use of SIF as a proxy for GPP, but it must be accounted for to prevent overestimation of GPP in winter (Pierrat et al., 2021a, 2022a).

Structurally sensitive indices (NDVI and NIRv) show little variability over summer and are sensitive to snow in winter across both sites (Figure 6.2 rows b & c). Over summer at SOBS, NDVI and NIRv show greater changes than at DEJU, which reflects the fact that SOBS is a mixed-species forest with scattered deciduous larch trees. SOBS therefore experiences greater changes in canopy structure over the seasonal cycle than evergreen DEJU. NDVI peaks in mid-morning and mid-afternoon over the summer months at SOBS and has no clear pattern at DEJU (Figure 6.3 row b). NIRv is slightly higher in the morning at DEJU and has no clear pattern at SOBS (Figure 6.3 row c). These patterns suggest that NDVI and NIRv are useful for accounting for shifts in viewing geometry and illumination effects across the diurnal cycle.

Physiologically sensitive indices (CCI and PRI) generally track the seasonal cycle of GPP but show sensitivity to snow cover in winter. CCI is more sensitive to snow at DEJU due to a higher fraction of snow cover on the canopy. Both CCI and PRI increase in spring following GPP at both sites (Figure 6.2 rows d & e). This is consistent with a two-phased spring transition beginning with the onset of photosynthesis, followed by a reduction in sustained photoprotection (Pierrat et al., 2021a). CCI at DEJU is lower than at SOBS which may indicate differences in chlorophyll:carotenoid ratios between the sites. Diurnally, PRI shows a small decrease around midday during summer months at both sites (Figure 6.3 row d). This highlights the sensitivity of PRI to rapidly reversible photoprotection which will occur under high-light, high-stress conditions. CCI shows a slight diurnal pattern at SOBS and does not show a consistent diurnal pattern at DEJU. The lack of a diurnal pattern at DEJU supports the idea that CCI is sensitive to sustained cold-season photoprotection which will not change over the course of the diurnal cycle. PRI and CCI thus provide information on plant heat dissipation processes at both seasonal and diurnal timescales.

Environmental conditions at the two sites (PAR, Df, and Tair) are consistent with expected environmental patterns (Figures 6.2 & 6.3 rows f-h). PAR increases prior to an increase in GPP and begins to decrease in fall prior to a decline in GPP at both sites. Df does not show a defined seasonal cycle, nor does it show a prominent diurnal pattern at either site. Thus, diffuse sky conditions are largely independent of season or time of day. Air temperature tracks the seasonal cycle of GPP, and air temperatures above 0°C are a good indicator of growing season length (Parazoo et al., 2018; Pierrat et al., 2021a; Stettz et al., 2022). Air temperature peaks in the afternoon following the peak in SIF and GPP.

6.3.2 SIF and GPP light response curves: light-use-efficiency and random forest models

We tested the ability of random forest models to reproduce quantitative SIF-GPP dynamics by comparing light response curves following the parameterized light-use-efficiency model (Figure 6.4 row a) with light response curves produced by environmentally driven random forest models (Table 6.2, ENV-SIF & ENV-GPP, Figure 6.4 row b), at a half-hourly resolution at the SOBS site. The same analysis tested at the DEJU site shows consistent results (Figures B.5 & B.6).

The half-hourly data and parameterized light-use-efficiency model ($\mathrm{GPP} = \frac{\mathrm{GPP_{max}} \times \mathrm{PAR}}{c \times \mathrm{PAR}}$, Michaelis and Menten, 1913; Monteith, 1972) and ($\mathrm{SIF} = c \times \mathrm{PAR}$, Equation 6.2) show a curved light response for GPP, consistent with the light saturation of GPP, and a near linear light response for SIF (Figure 6.4 row a). Both GPP and SIF show a seasonally dynamic light response with minima over winter and maxima over summer. The light response of SIF approaches but does not go to zero over the winter months due to persistent winter photosystem II activity (Bowling et al., 2018; Porcar-Castell, 2011; Yang et al., 2022).

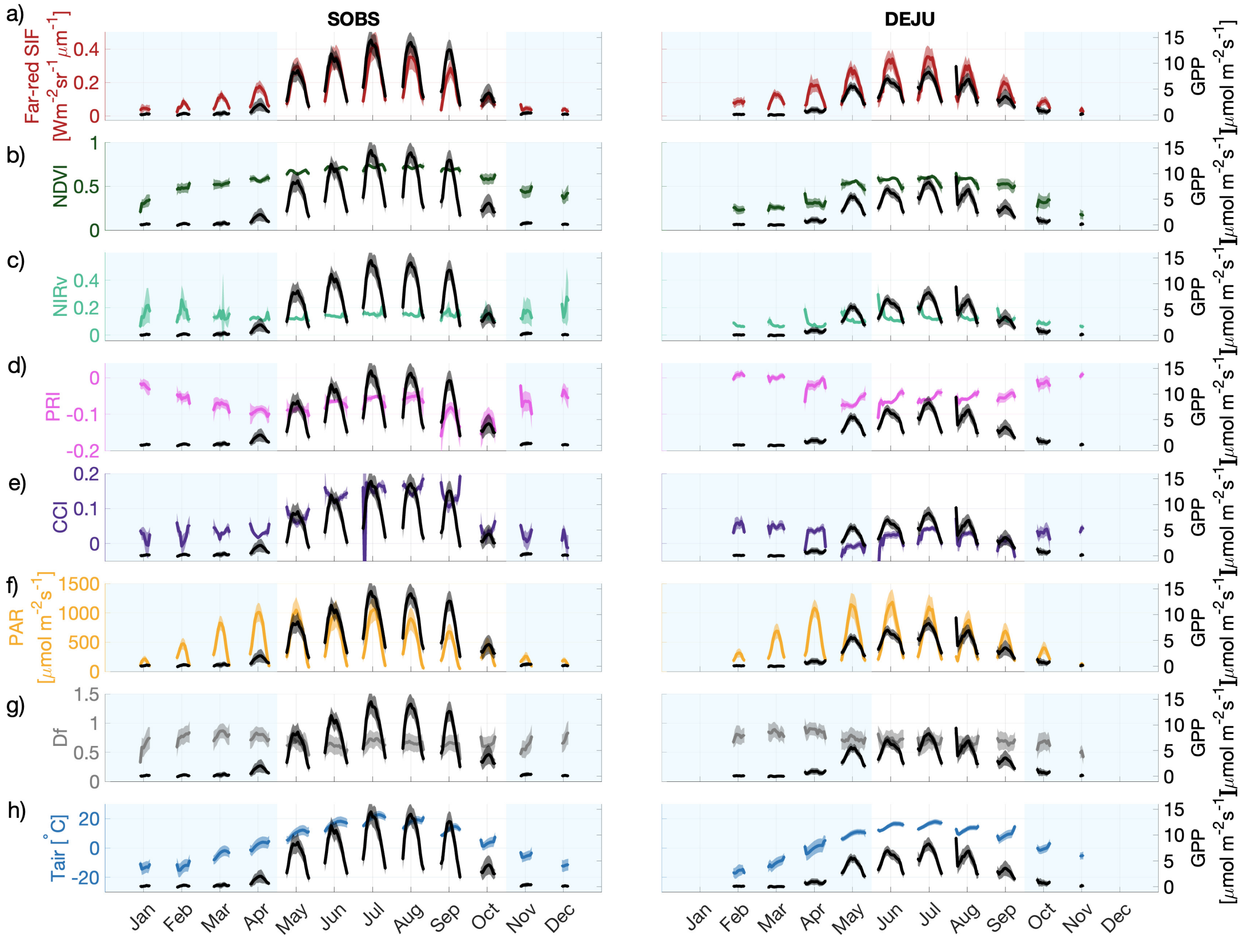

Figure 6.3: Average monthly diurnal patterns of GPP compared with a) SIF, b) NDVI, c) NIRv, d) PRI, e) CCI, f) PAR, g) Df and h) Air Temperature over the entire data collection period for both the SOBS and DEJU sites. Shaded regions are the standard deviation for each hourly average within the month. Blue shaded regions represent months with snow cover as visually identified using phenocam imagery.

Both ENV-SIF and ENV-GPP models had strong performance with high R^2 ($R^2 = 0.93$ and 0.94 respectively) and OOB R^2 scores (OOB $R^2 = 0.86$ and 0.89 respectively) (Figure B.7). This highlights the ability of random forest models to capture the environmental dependencies of both SIF and GPP. The two trained models were run for each month using the range of PAR values for that month and the monthly average for the rest of the environmental predictor variables to reproduce the light response curves of SIF and GPP (Figure 6.4 row b). The monthly light response curves produced by the random forest models have the same patterns as both the data and the parameterized light-use-efficiency models. The light response of GPP is curved and the light response of SIF is largely linear. SIF shows a slight curvature at high PAR values which we attribute to changes in f_{esc} at high PAR (Pierrat et al., 2022a). Both GPP and SIF exhibit a monthly variable light response and the light response of SIF does not drop to zero over winter, consistent with the light-use-efficiency model.

These results highlight the efficacy of random forest models for reproducing quantitative relationships and environmental dependencies for GPP and SIF without prescribing a parameterized model onto the data (Chen et al., 2021). Because of this, and the additional information that can be provided by additional remote sensing metrics (Section 6.3.1), we justify the use of random forest models for GPP prediction.

6.3.3 Random forest models compared with parameterized models for predicting GPP

We tested the ability of random forest models to improve GPP prediction by testing traditional parameterized models (a linear SIF-GPP relationship, a non-linear SIF-GPP relationship that takes into account the light saturation of GPP (Monteith, 1972) and a monthly variable non-linear SIF-GPP relationship (Damm et al., 2015; Pierrat et al., 2022a) against our new random forest approach combining multiple remote sensing indices for predicting GPP (Figures 5 & 6). The two random forest models used to test this (Table 6.2, RS-

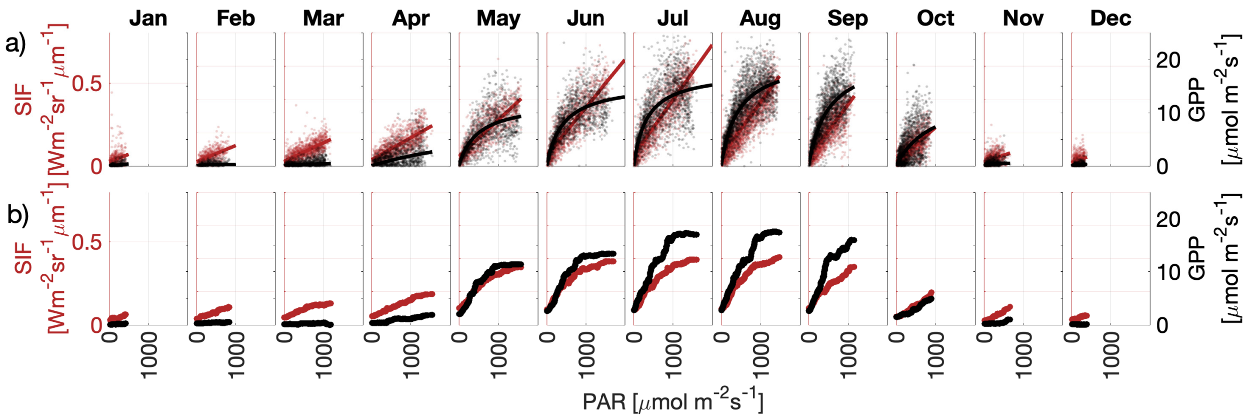

Figure 6.4: Row a) shows half-hourly SIF and GPP data against PAR fitted with the parameterized light-use-efficiency models: (GPP $= \frac{\text{GPPmax} \times \text{PAR}}{c \times \text{PAR}}$, Michaelis and Menten, 1913; Monteith, 1972) and (SIF $= c \times$ PAR, Equation 6.2). Row b) shows light response curves of half-hourly GPP and SIF produced from two random forest models (ENV-GPP and ENV-SIF).

SOBS & RS-DEJU) were driven by remote sensing and meteorological variables that reflect the physical and physiological controls on photosynthesis relevant at a half-hourly temporal resolution.

The linear fit between SIF and GPP (Figure 6.5 row a) performs moderately-poorly with an R^2 = 0.58 at SOBS and R^2 = 0.43 at DEJU (Figure 6.6 row a). The non-linear fit based on (Damm et al., 2015) shows little to no improvement from the linear fit with R^2 = 0.60 at SOBS and R^2 = 0.43 at DEJU (Figure 6.6 row b). Both models with a fixed SIF-GPP relationship overestimate GPP in winter due to a persistent winter light response of SIF. The monthly variable non-linear SIF-GPP relationship (Figure 6.5 row c) shows a marked improvement in the predictability of GPP at both the SOBS and DEJU sites with R^2 = 0.76 and R^2 = 0.66 respectively (Figure 6.6 row c). In addition to improved R^2 values, the monthly variable non-linear SIF-GPP relationship helps account for the persistent winter light response and the winter overestimation of GPP is no longer observed. The random forest models driven by remotely sensed products (Figure 6.5 row d) improved the predictability of GPP compared to all parameterized models at both sites with R^2 = 0.90 and 0.86 and OOB

$R^2 = 0.81$ and 0.73 at SOBS and DEJU respectively (Figure 6.6 row d). The overestimation of GPP in winter is not observed using the random forest approach and residuals between predicted and measured GPP are more homoscedastic across seasons.

The predictive power of input variables is evaluated with the predictor importance estimates (Figure 6.5 row d). SIF was the most important predictor at SOBS and second most important predictor at DEJU, highlighting the power of SIF for GPP prediction. DEJU showed a higher dependence on air temperature than SOBS which could point to stronger temperature limitations at this site. Df was an important predictor across both sites which highlights the dependence of GPP on diffuse vs. direct radiative conditions (Durand et al., 2021; Pierrat et al., 2021b). NIRv was the third most important predictor at SOBS which could reflect the fact that SOBS is a mixed-species forest interspersed with deciduous trees and will thus have more dramatic changes in canopy structure over the course of the season than DEJU. CCI was moderately important at both SOBS and DEJU which highlights the relevance of CCI for capturing changes in sustained photoprotection over winter. NDVI was not a particularly important predictor for either SOBS or DEJU which could reflect the fact that NIRv is more effective at capturing changes in canopy structure (Badgley et al., 2017, 2019) than NDVI. PRI was also not particularly important for either SOBS or DEJU which suggests that rapidly reversible non-photochemical quenching dynamics may be more effectively captured in the SIF signal when a prescribed relationship between SIF and GPP is not used. Including PAR as an input variable does not improve model results but does decrease the predictor importance of SIF (Figures B.8 & B.9). Substituting PAR for SIF as a predictor variable also does not change model performance (Figures B.10 & B.11). This suggests that vegetation indices effectively capture the structural (fPAR) and physiological ($\mathrm{LUE_P}$) factors relevant for predicting GPP.

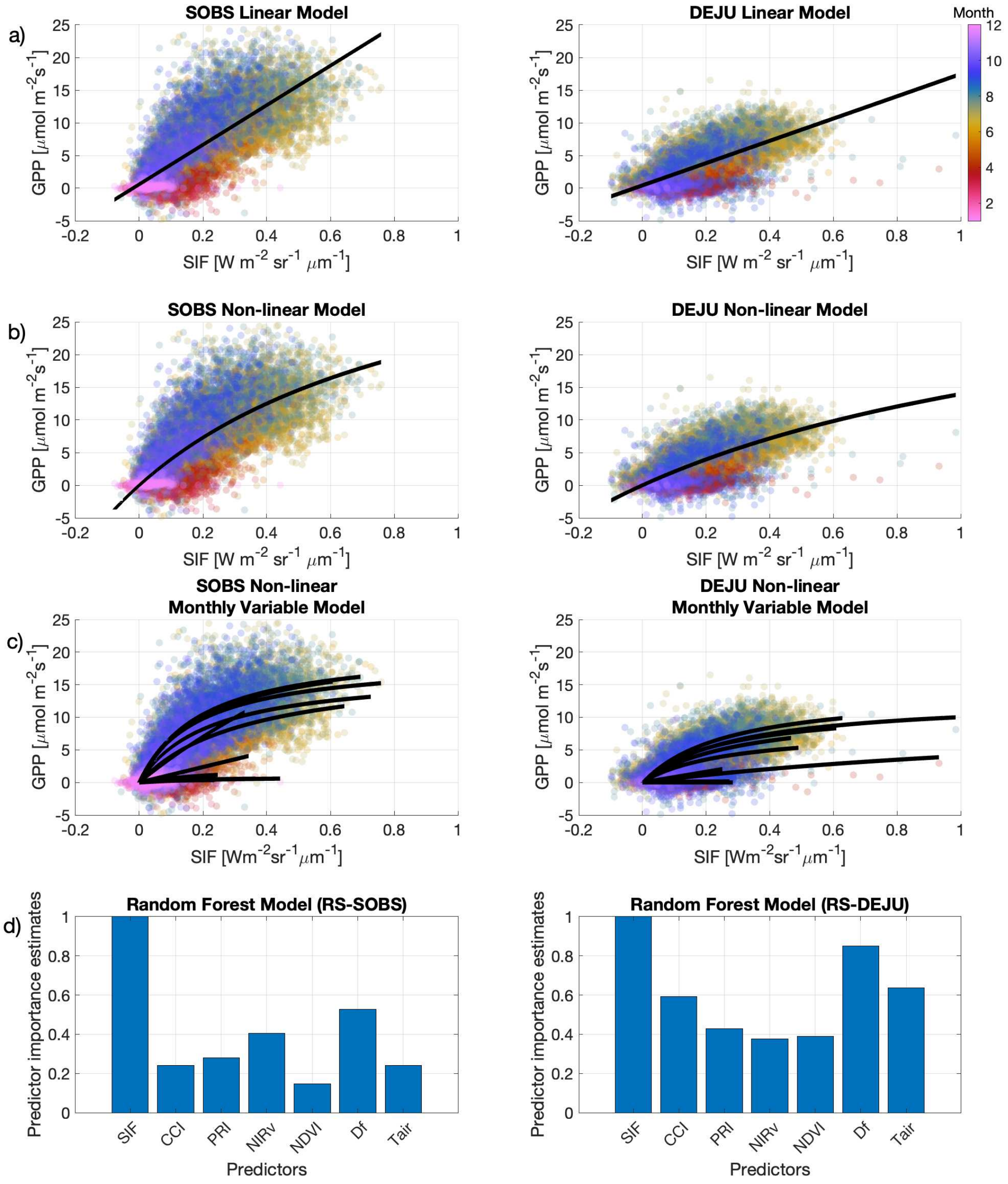

Figure 6.5: Setup of traditional parameterized models for SIF as a proxy for GPP with our proposed random forest modelling approach for both SOBS and DEJU. Row a) shows a linear fit between SIF and GPP. Row b) shows a non-linear fit based on the light use efficiency model ($\text{GPP} = \frac{\text{SIF} \times \text{GPP}_{\text{max}}}{\text{a+SIF}}$, Damm et al., 2015). Row c) shows the same non-linear fit but fitted monthly to create a monthly variable SIF-GPP relationship (Pierrat et al., 2022a). Row d) shows the input variables predictor importance estimates for random forest models RS-SOBS and RS-DEJU.

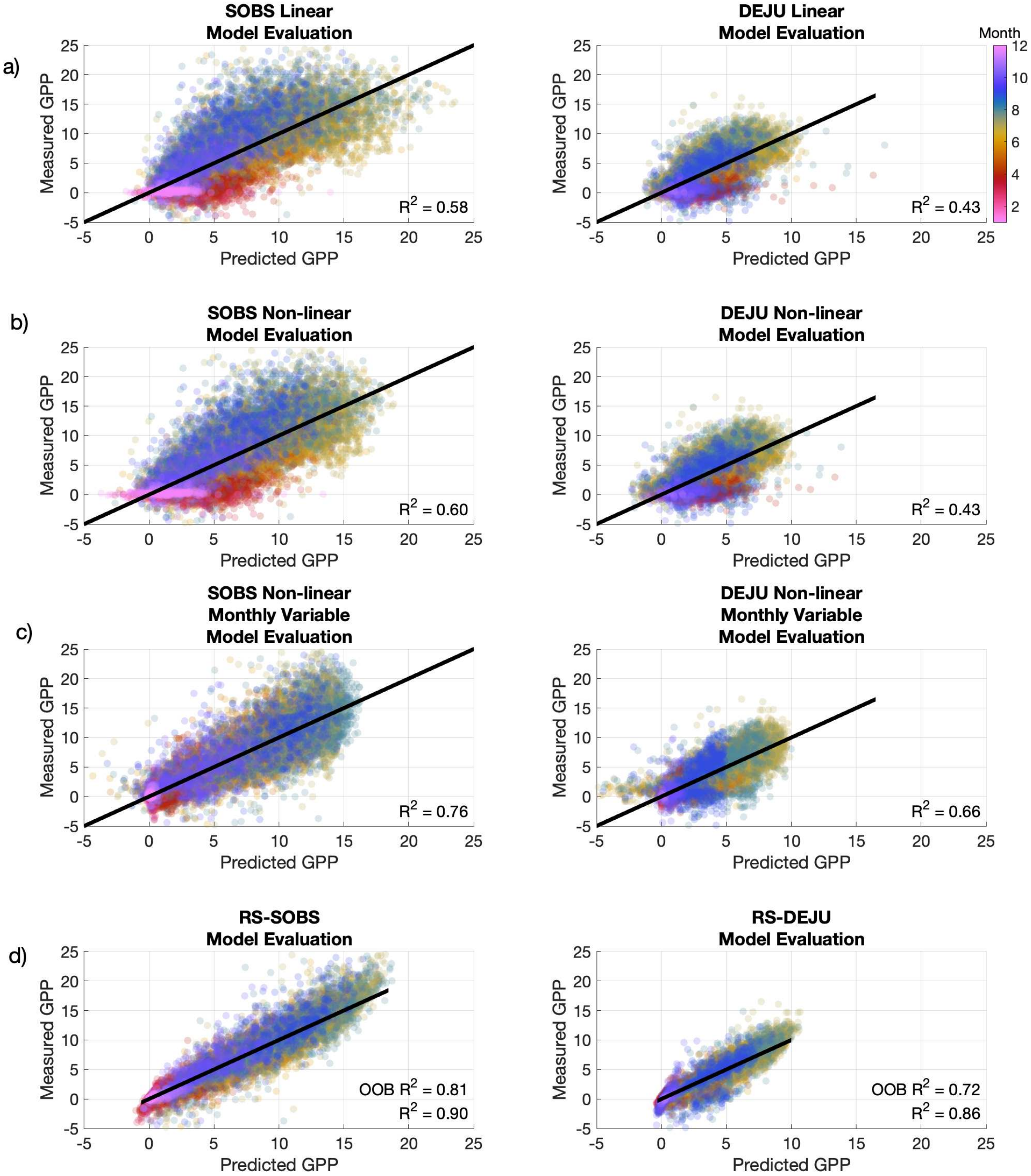
SOBS Linear Model Evaluation

DEJU Linear Model Evaluation

SOBS Non-linear Model Evaluation

DEJU Non-linear Model Evaluation

SOBS Non-linear Monthly Variable Model Evaluation

DEJU Non-linear Monthly Variable Model Evaluation

RS-SOBS Model Evaluation

RS-DEJU Model Evaluation

Figure 6.6: Evaluation of model performance for traditional parameterized models compared with our proposed random forest modelling approach for both SOBS and DEJU. Rows a), b), c), and d) show the correlation between measured GPP and predicted GPP based on the models presented in Figure 6.5 as row a) a linear fit between SIF and GPP, row b) a non-linear fit based on the light use efficiency model, row c) a monthly variable non-linear fit, row d) random forest models RS-SOBS and RS-DEJU (Table 6.2).

6.3.4 Random forest models for predicting GPP across boreal forest sites

Satellite remote sensing enables the approximation of GPP over a broader spatial range than tower-based measurements, making it essential for understanding regional GPP dynamics. However, relationships between remotely sensed products and GPP are often site specific and thus require a new model or set of parameters for each ecosystem or plant functional type. We tested the potential of our random forest modeling approach across sites for a "universal" model for GPP based on remotely sensed products. We trained a model (RS-Total) to predict GPP from data that are readily accessible or can be inferred from satellite measurements (Table 6.2, RS-Total). We used data at a daily resolution averaged between 10:00-14:00 under all (Figure 6.7) and only sunny (Figure B.12) sky conditions to replicate satellite observations across both the SOBS and DEJU sites together. SOBS and DEJU are at the latitudinal extremes of the boreal ecosystem, thus, testing the feasibility of interpolation across the boreal region.

Our results show excellent performance on the predictability of GPP based on remotely sensed metrics ($R^2 = 0.94$ and OOB $R^2 = 0.89$) (Figure 6.7). Residuals between predicted and measured GPP are highly homoscedastic and GPP is not overestimated in winter. Predictor importance estimates show that SIF is the most valuable predictor for GPP, but air temperature, NDVI, CCI, and NIRv are all relevant predictors. To test the universality of this approach, we tested the same model but included a site flag as a predictor (either SOBS or DEJU) (Figure B.13). This model showed no improvement in performance ($R^2 = 0.94$ and OOB $R^2 = 0.89$) and had site flag as the least relevant predictor. This may be because importance estimates are biased towards predictors with many classes or different values (Loh and Shih, 1997) and we only had two flags for the two sites. Alternatively, this, as well as the success of the model without the site flag, points to our random forest modeling approach being independent of site, and therefore potentially generalizable across the boreal biome at the satellite level (Li et al., 2018; Sun et al., 2017). This approach also works whether or not the data have been filtered for snow contamination (Figure B.4)

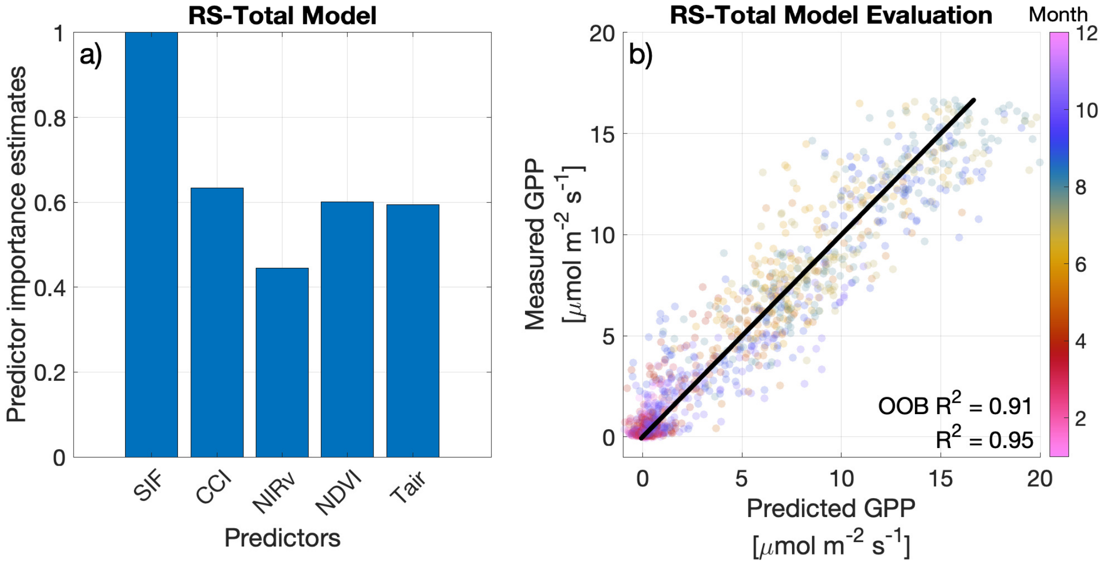

Figure 6.7: Random forest model trained with daily midday average data across both sites (RS-Total) with a) predictor importance estimates and b) model performance on out-of-bag data with predicted and measured GPP.

and shows near identical results when only clear sky days are used (Figure B.12) which are both advantageous in the boreal. The combined random forest modeling approach also outperformed all other parameterized models at a daily midday resolution for the two sites separately (Figures B.14 & B.15) and worked well for the combined sites at a half-hourly resolution (Figure B.16). Substituting PAR for SIF also showed good model performance and similar predictor importance estimates (Figure B.17). This suggests that vegetation indices are effective at capturing the physical and physiological effects relevant for predicting GPP. Our results support the use of this approach for improving the predictability of GPP from remote sensing observations because it can account for physical and physiological mechanisms impacting remotely sensed signals.

6.4 Conclusions

In this paper, we present a quantitative framework for predicting GPP using random forest models driven by a set of remotely sensed products and air temperature. Multiple years of tower-based remote sensing and GPP data across two field locations at the northern and southern ends of the North American boreal forest show that VIs and SIF contain valuable information on the physical and physiological drivers of GPP. Additionally, random forest models driven by environmental variables are able to reproduce light response curves of SIF and GPP and are thus able to capture quantitative relationships of plant physiology. These results justify the use of random forest models to predict GPP based on a set of random forest parameters. Random forest models outperform traditional parameterized models based on SIF alone for predicting GPP because they are able to incorporate physical and physiological information provided by additional remote sensing metrics without prescribing a parameterized model. This approach is not site specific and therefore has the potential to be scaled across the boreal domain using satellite measurements. Finally, this approach has potential for use in other ecosystems where remote sensing data is available. Random forest models improve the utility of SIF and vegetation index data for scaling and understanding GPP across space and time and thus present an exciting opportunity to better understand vegetation's role in the global carbon cycle.

CHAPTER 7

Conclusions

In this chapter, I conclude by revisiting the overarching science questions presented in Chapter 1 and connecting them with the results in Chapters 2-6. I then provide a brief synopsis of recent and ongoing work that targets unanswered aspects of these science questions as well as new ones that have emerged. Finally, I close with long-term aspirations inspired by this thesis work.

7.1 Summary

The overarching aim of this work is to disentangle the physical and biological drivers of optical signals in evergreen needleleaf forests with tower-based spectrometer systems, to build a framework for understanding and monitoring evergreen needleleaf photosynthesis in a changing climate. We have done this by answering the following scientific questions:

1. What environmental conditions drive changes in photochemical and biochemical regulation of photosynthesis in ENFs?

In Chapter 2 we provided a broad overview of the environmental drivers of photochemical and biochemical regulation of photosynthesis in ENFs. We highlight how light is the primary energetic driver of photosynthesis. Then, depending on temperature and water availability, the plant will partition the absorbed light energy to 1) drive photosynthesis, 2) damage the plant tissue, 3) thermal energy dissipation, or 4) re-emit as fluorescence. Over the diurnal cycle, plants use a form of rapidly reversible thermal energy dissipation to avoid damage and conserve water resources during periods of high-light and high-temperature (i.e., midday). Over the seasonal cycle, ENF in regions which experience sub-zero temperatures in winter (e.g., Alaska, Canada, Colorado) will employ a form of sustained thermal energy dissipation. This allows them to protect against damage over the entire winter season when they are absorbing appreciable amounts of light but unable to perform photosynthesis due to temperature and water limitations. We also show that this sustained thermal energy dissipation does not occur in ENF which show environmental conditions favorable for photosynthesis year round (e.g., Florida). During the spring transition, evergreen and deciduous needleleaf species have different environmental controls on the onset of photosynthesis (Chapter 4). Because evergreen species already have needles, they are able to begin photosynthesis earlier in the spring when the tree trunks have thawed and while soils are still frozen/thawing. Deciduous species on the other hand must wait until soils have thawed to access greater water resources and begin the leaf-out process. We show that seasonally air temperature is the main driver of ENF photosynthesis, while diurnally light is the primary driver (Chapter 5).

2. What are the fundamental biological and physical processes influencing observed optical metrics?

Photosynthesis is dependent on both the amount of absorbed light and the energy partitioning among the four different pathways. Therefore, we can use optical metrics sensitive to both the absorbed light and energy partitioning to probe photosynthesis (Chapter 2). Metrics sensitive to canopy greenness (NDVI and NIRv) are an effective probe of chlorophyll content and thus the fraction of available light absorbed by chlorophyll. This renders them an effective probe of photosynthetic activity for deciduous species (Chapter 4) but not for evergreens (Chapters 5 & 6). Metrics sensitive to xanthophyll pigments which are responsible for both rapidly reversible and sustained thermal energy dissipation (PRI and CCI) are a good probe of photosynthetic activity in ENF but generally sensitive to the presence of snow

(Chapters 4, 5, & 6). Finally, SIF is sensitive to both absorbed light and the yield of fluorescence which tends to co-vary with the yield of photosynthesis over broad spatio-temporal scales (Chapters 4, 5 & 6).

3. How do the relationships among different optical metrics and underlying biologic processes change across varying temporal scales?

The two main temporal scales investigated in this dissertation are diurnal and seasonal. Across both diurnal and seasonal scales, greenness based metrics (NDVI and NIRv) remain approximately constant (with the exception of sensitivity to snow) because there are no significant changes in canopy structure and chlorophyll content (Chapter 5). Over the course of a season, PRI and CCI (sensitive to xanthophyll pigments and thermal energy dissipation) and SIF all do a good job at tracking GPP. At finer temporal resolutions (daily-half-hourly) SIF outperforms other metrics for tracking GPP because it is more sensitive to the more rapid changes in light. However, the relationship between SIF and GPP is nuanced due to the light responses of SIF and GPP. The light response of both SIF and GPP changes seasonally as thermal energy dissipation induces a shutdown of photosynthesis. Over winter, the light response of SIF does not drop to zero while the light response of GPP does. This leads to an early increase in SIF prior to changes in GPP in spring. This early increase can be accounted for by using $\text{SIF}_{\text{relative}}$ which is a proxy for the light-use-efficiency of fluorescence and co-varies seasonally with the light-use-efficiency of photosynthesis (Chapters 4 & 5). Across the diurnal cycle, at high light intensities, the light response of GPP saturates while SIF does not (Chapter 5). The combination of these processes leads to a seasonally-dependent and curved relationship between SIF and GPP.

4. How can we improve our ability to track ENF photosynthesis by combining optical metrics?

Optical metrics can provide information on both the structure and function of plants

(Chapter 2). While SIF contains information on both the absorbed light and energy partitioning of that light, the exact relationship between SIF and GPP is nuanced and depends on the temporal resolution as well as the environmental controls on photosynthesis. Therefore, we can improve our ability to predict GPP from SIF by incorporating additional information on canopy structure and thermal energy dissipation provided by reflectance based vegetation indices (Chapter 6). In this dissertation, we do this by using random forest models which are non-parametric in nature and more interpretable than other machine learning approaches. Using random forest models to predict GPP from optical metrics (SIF and vegetation indices) shows both an improvement over traditional parameterizations and is not site-specific making it potentially applicable across ENF more broadly.

7.2 Looking Ahead

The work presented in this dissertation presents a framework for understanding ENF photosynthesis using optical metrics. The majority of this research has therefore gone into understanding the empirical trends and drivers of collected data across ENF locations along with qualitative descriptions of their mechanistic drivers. To do this, the research has remained data driven in nature and limited in its spatial scale (site-level observations). Future research can therefore expand on the understandings gleaned in this dissertation, and using the data collected during this research, in two main ways. First, by fusing data and modeling frameworks we can improve our mechanistic understanding of biologic responses to environmental drivers and ability to predict forest carbon uptake in a changing climate. Second, by expanding the spatial range of observations and linking satellite and tower-based data, we can do a better job at monitoring and understanding ENF carbon dynamics more broadly.

7.2.1 Fusing data and modeling frameworks

When embarking on this dissertation research, our funded proposals included incorporating modeling frameworks to understand mechanistic drivers of observed signals. This included the Soil-Canopy-Observation of Photosynthesis and Energy Fluxes (SCOPE) model (van der Tol et al., 2009; Van Der Tol et al., 2014; van der Tol et al., 2016) and the Discrete Anisotropic Radiative Transfer (DART) model (Gastellu-Etchegorry et al., 2017; Liu et al., 2019b). What we quickly learned by using the SCOPE model at the Southern Old Black Spruce site (Pierrat et al., 2021b) was that SCOPE was unable to capture the seasonal cycle in SIF and unable to capture the magnitude of the SIF signal. We tuned the model to the site using data from Chen et al. (2006) and ran sensitivity tests based on realistic input parameters. Nowhere in these tests were we able to get the magnitude or the seasonal cycle to match the model with observations. The issues we encountered at our study site are also not unique. Prior work has shown wide discrepancies in the magnitude and direction of modeled SIF in response to light conditions (Parazoo et al., 2020). In order to effectively use models to understand biologic processes we cannot observe and to use them to predict what will happen to ecosystems in the future, we must reconcile these differences.

We believe the two main issues with existing models be attributed to issues in the radiative transfer scheme as well as issues with the photosynthesis model used. With respect to radiative transfer, ENF are known for canopy clumping. Therefore introducing a canopy clumping scheme (Braghiere et al., 2019) should theoretically improve radiative transfer in the model (Wang and Frankenberg, 2022). With respect to photosynthesis, we believe that the misrepresentation of the seasonal cycle of SIF can be attributed to an insufficient representation of non-photochemical quenching dynamics (Raczka et al., 2019). Additionally, recently developed photosynthesis models (Johnson et al., 2021; Johnson and Berry, 2021) should be able to better capture the relationships among photosynthesis, fluorescence, and thermal energy dissipation.

Through close collaboration between modelers and observationalists, we can hopefully reconcile these issues. Projects such as the SIF Model Inter-comparison Project (a followup on Parazoo et al., 2020) are helping to identify discrepancies between existing models and measurements. This will help us understand how and why different models are arriving at different results for the SIF signal and what we need to to do improve such models. Additional projects such as the Climate Modeling Alliance are also working to implement the aforementioned changes into models (Wang et al., 2023). Ultimately, these efforts will result in an improved ability to model and predict the fate of the terrestrial biosphere.

7.2.2 Linking tower and satellite observations

Satellite remote sensing is an essential tool for understanding and monitoring ecosystems and their responses to environmental change. Upcoming satellite missions aim to advance spaceborne remote sensing capabilities by expanding the spectral range and resolution of existing missions. Specifically, the Surface Biology and Geology (SBG) component of the National Aeronautics and Space Administration's (NASA) new Earth System Observatory will include an imaging spectrometer in the solar-reflected range (400-2,500 nm) with coverage at biweekly intervals and pixel size as fine as 30 m (Cawse-Nicholson et al., 2021, 2023). The reflectance data collected as part of this mission will be a huge advancement in comprehensive spectral monitoring of the earth system (Schneider et al., 2019). However, due to the inherent nature of spaceborne missions, it is still limited in its spatiotemporal resolution compared with tower-based spectral measurements. Therefore, tower-based spectral measurements will be an essential tool in the validation, interpretation, and spatiotemporal downscaling of spaceborne measurements (Parazoo et al., 2019) and comparison with model outputs (Poulter et al., 2023). In addition, tower-based optical measurements alone can provide an enhanced mechanistic understanding of ecosystem processes and are useful tool for assessing ecosystem health and productivity at the site level (Nelson et al., 2022; Gamon, 2015).

To fully realize the promise of spaceborne measurements, careful integration with tower-based data is essential. This can be accomplished by expanding the number of sites equipped with spectral data and developing standards to make tower-based remote sensing comparable across sites. The self-described "coalition of the willing", FLUXNET, has been able to standardize and make accessible hundreds of sites of eddy-covariance derived flux data. This has enabled a dirth of new science and intersite comparisons. With the dramatic growth in spectral imaging in earth science and global ecology communities, now is the time for increased coordination and collaboration between remote sensing scientists. Using the FLUXNET model hopefully remote sensing scientists can begin to standardize remotely sensed products and make datasets more accessible and usable. Efforts such as the Ameriflux Year of Remote Sensing and the upcoming affiliated workshop "Linking Optical and Energy Fluxes" (`https://fluxnet.org/community/linking-optical-and-energy-fluxes-workshop/`) will be key steppingstones in this process.

7.3 Final Remarks

The emission of carbon dioxide by humans has irreversibly changed our climate and climate system (Solomon et al., 2009). Being able to prepare and protect against the inevitable changes to our planet is essential for the future survival humankind. My biggest hope for the work presented in this dissertation is that it may play a small part in protecting our planet's ecosystems in a rapidly changing climate.

APPENDIX A

Supplementary Materials for Chapter 5

Table A.1: Summary of fitted equations and fit parameters for Figure 5.3 (with 95% confidence intervals)

Figure 5.3 fit parameters (with 95% confidence)	**Monthly** y=a×x+b	**Daily** 1) y=a1×x+b1 2) y=a2×x/(b2+x)	**Half-Hourly** 1) y=a1×x+b1 2) y=a2×x/(b2+x)
SIF-GPP	a = 40.26 (35.23, 45.3) b = -1.918 (-2.764, -1.071)	a1 = 33.29 (31.57, 35.02) b1 = -0.7411 (-1.073, -0.4089) a2 = 701.9 (-6162, 7566) b2 = 23.08 (-205.2, 251.4)	a1 = 30.13 (29.6, 30.66) b1 = 0.8396 (0.7132, 0.9661) a2 = 40.6 (37.11, 44.09) b2 = 0.8817 (0.7789, 0.9845)
CCI-GPP	a = 61.76 (54.86, 68.67) b = -0.6264 (-1.269, 0.01627)	a1 = 53 (49.96, 56.03) b1 = 0.2168 (-0.1029, 0.5365)	a1 = 2.174 (1.79, 2.559) b1 = 6.384 (6.257, 6.511)
NDVI-GPP	a = 25.47 (19.27, 31.66) b = -10.93 (-14.59, -7.259)	a1 = 21.47 (19.58, 23.37) b1 = -8.596 (-9.792, -7.4)	a1 = 25.39 (24.52, 26.27) b1 = -10.01 (-10.59, -9.424)

Table A.2: Summary of fitted equations and fit parameters for Figure 5.5 (with 95% confidence intervals)

Figure 5.5 fit parameters (with 95% confidence)	**SIF-APAR** y=a×x	**$\text{SIF}_{\text{total}}$-APAR** y=a×x	**GPP-APAR** y=a×x/(b+x)
Jan	a = 0.000159 (0.0001348, 0.0001832)	a = 0.002713 (0.001212, 0.004213)	a = 0.09222 (0.0235, 0.1609) b = 1.612e-08 (-96.7, 96.7)
Feb	a = 0.0001609 (0.000152, 0.0001697)	a = 0.001441 (0.001331, 0.001551)	a1 = 2.174 (1.79, 2.559) b1 = 6.384 (6.257, 6.511)
Mar	a = 0.0001598 (0.0001547, 0.0001649)	a = 0.001621 (0.001477, 0.001765)	a = 0 (fixed at bound) b = 500 (-Inf, Inf)
Apr	a = 0.0001844 (0.0001795, 0.0001893)	a = 0.001942 (0.00186, 0.002024)	a = 15.11 (-50.43, 80.65) b = 6214 (-2.444e+04, 3.686e+04)
May	a = 0.0003348 (0.0003288, 0.0003408)	a = 0.00308 (0.003014, 0.003145)	a = 10.59 (9.594, 11.59) b = 370.1 (277.4, 462.7)
Jun	a = 0.0004163 (0.0004094, 0.0004232)	a = 0.003513 (0.00346, 0.003567)	a = 14.54 (13.67, 15.42) b = 339.9 (288.2, 391.5)

Continued on next page

Table A.2: Summary of fitted equations and fit parameters for Figure 5.5 (with 95% confidence intervals) (Continued)

Figure 5.5 fit parameters (with 95% confidence)	**SIF-APAR** y=a×x	**$\mathbf{SIF_{total}}$-APAR** y=a×x	**GPP-APAR** y=a×x/(b+x)
Jul	a = 0.0004353 (0.0004291, 0.0004416)	a = 0.003618 (0.003551, 0.003685)	a = 17.63 (16.63, 18.64) b = 311.7 (258.8, 364.7)
Aug	a = 0.0004457 (0.0004409, 0.0004504)	a = 0.003506 (0.00346, 0.003552)	a = 19.78 (18.86, 20.69) b = 387.3 (341.2, 433.4)
Sep	a = 0.0004536 (0.0004477, 0.0004595)	a = 0.00357 (0.003508, 0.003632)	a = 20.24 (18.63, 21.86) b = 489.7 (410, 569.3)
Oct	a = 0.0002864 (0.0002788, 0.000294)	a = 0.002666 (0.00257, 0.002763)	a = 11.7 (7.45, 15.96) b = 823.1 (367.5, 1279)
Nov	a = 0.0001792 (0.0001689, 0.0001895)	a = 0.001535 (0.001301, 0.001769)	a = 0.3199 (0.2411, 0.3987) b =16.37 (-4.927, 37.66)
Dec	a = 0.0001617 (0.0001479, 0.0001755)	a = 0.001242(0.001082, 0.001402)	a = 0.5382 (-5.745, 6.821) b = 1023 (-1.388e+04, 1.593e+04)

Table A.3: Summary of fitted equations and fit parameters for Figure 5.7 (with 95% confidence intervals)

Figure 5.7 fit parameters (with 95% confidence)	**SIF-GPP** y=a×x/(b+x)	**$\mathbf{SIF_{total}}$-GPP** y=a×x/(b+x)
Jan	a = 0.07597 (-4.812e+05, 4.812e+05) b = 49.72 (-3.149e+08, 3.149e+08)	a = 0.00533 (-4.847e+05, 4.847e+05) b = 111.2 (-1.011e+10, 1.011e+10)
Feb	a = 0.4593 (-2, 2.918) b = 0.2986 (-1.753, 2.35)	a = 0.2125 (-0.2523, 0.6773) b = 0.9927 (-3.112, 5.098)
Mar	a = 6.732e-06 (-305.5, 305.5) b = 59.7 (-2.723e+09, 2.723e+09)	a = 6.765e-09 (fixed at bound) b = 3.775 (-1.632e+08, 1.632e+08)
Apr	a = 2.184e+05 (-6.091e+09, 6.091e+09) b = 1.76e+04 (-4.908e+08, 4.908e+08)	a = 8.634 (0.7435, 16.52) b = 6.632 (-1.338, 14.6)
May	a = 19.23 (15.16, 23.3) b = 0.4489 (0.2978, 0.6)	a = 43.62 (25.29, 61.95) b = 13.28 (6.614, 19.96)
Jun	a = 19.07 (17.09, 21.05) b = 0.3016 (0.2421, 0.3611)	a = 23.39 (20.94, 25.83) b = 3.73 (3.106, 4.354)
Jul	a = 21.68 (19.78, 23.58) b = 0.2616 (0.2107, 0.3125)	a = 108.8 (65.41, 152.2) b = 25.38 (13.99, 36.76)
Aug	a = 22.6 (21.16, 24.03) b = 0.2583 (0.2227, 0.294)	a = 20.46 (19.29, 21.62) b = 1.622 (1.4, 1.843)
Sep	a = 26.61 (23.55, 29.66) b = 0.3886 (0.3141, 0.4632)	a = 19.06 (18.1, 20.02) b = 1.706 (1.538, 1.874)

Continued on next page

Table A.3: Summary of fitted equations and fit parameters for Figure 5.7 (with 95% confidence intervals) (Continued)

Figure 5.7 fit parameters (with 95% confidence)	**SIF-GPP** y=a×x/(b+x)	**$\mathbf{SIF_{total}}$-GPP** y=a×x/(b+x)
Oct	a = 9.558e+04 (-1.628e+08, 1.63e+08) b = 2978 (-5.073e+06, 5.079e+06)	a = 19.73 (11.12, 28.34) b = 5.048 (2.227, 7.869)
Nov	a = 0.8852 (0.1863, 1.584) b = 0.1096 (-0.01847, 0.2377)	a = 1.09 (0.6217, 1.559) b = 2.277 (1.298, 3.256)
Dec	a = 0.2482 (0.03798, 0.4585) b = 0.04845 (0.009215, 0.08768)	a = 0.3963 (-0.5688, 1.362) b = 1.612 (-2.386, 5.61)

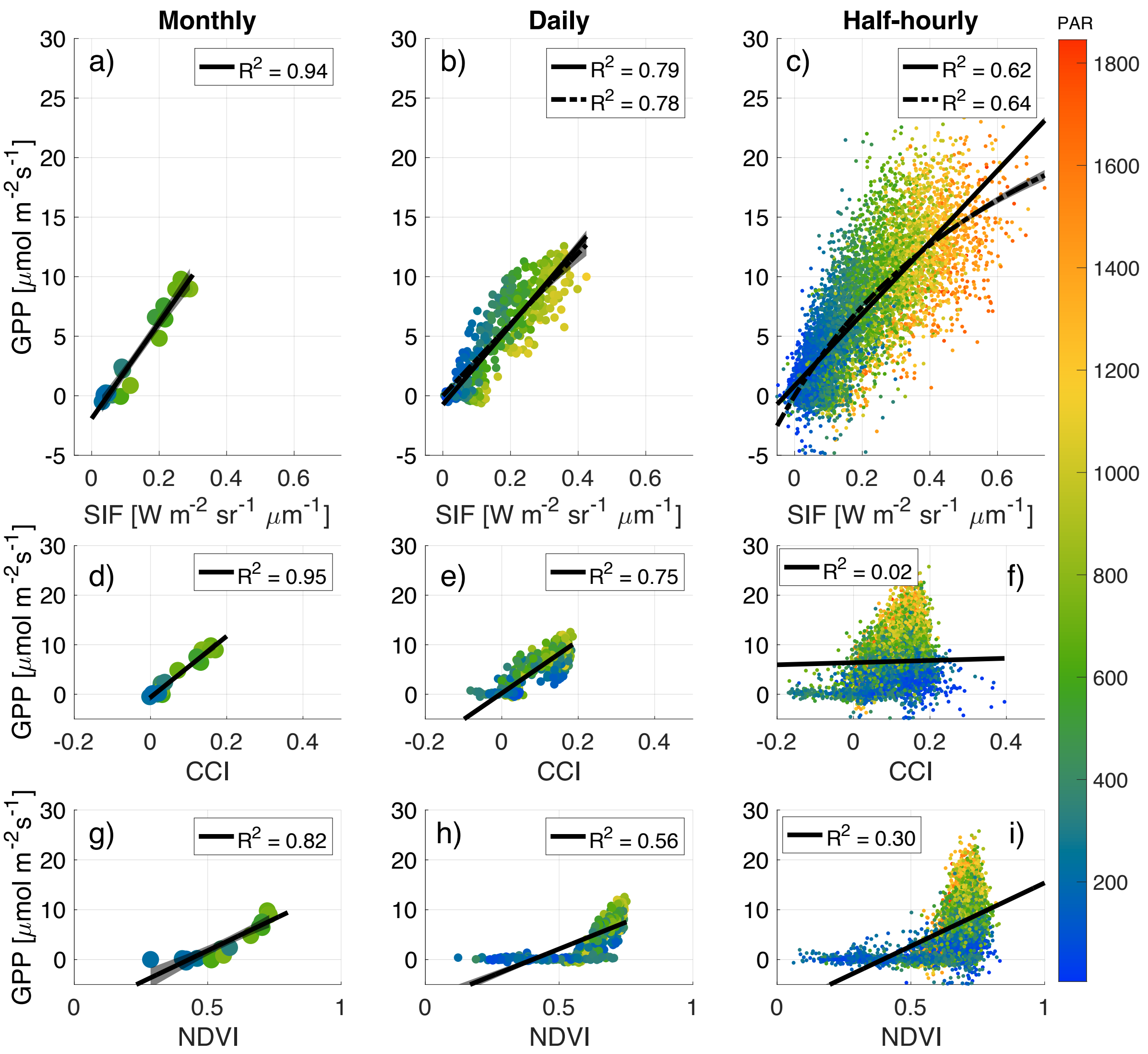

Figure A.1: The relationships between SIF, CCI, or NDVI, and GPP at monthly, daily, and half-hourly resolutions colored by PAR in [μmolm^{-2}s^{-1}]. Solid black lines are linear fits and dashed lines in b) and c) are based off Equation 5.8. Shaded gray regions are the 95% non-simultaneous functional prediction bounds for the fit. R^2 values are the degree-of-freedom adjusted coefficient of determination of the fit. Fitted parameters and equations are summarized in Table A.1.

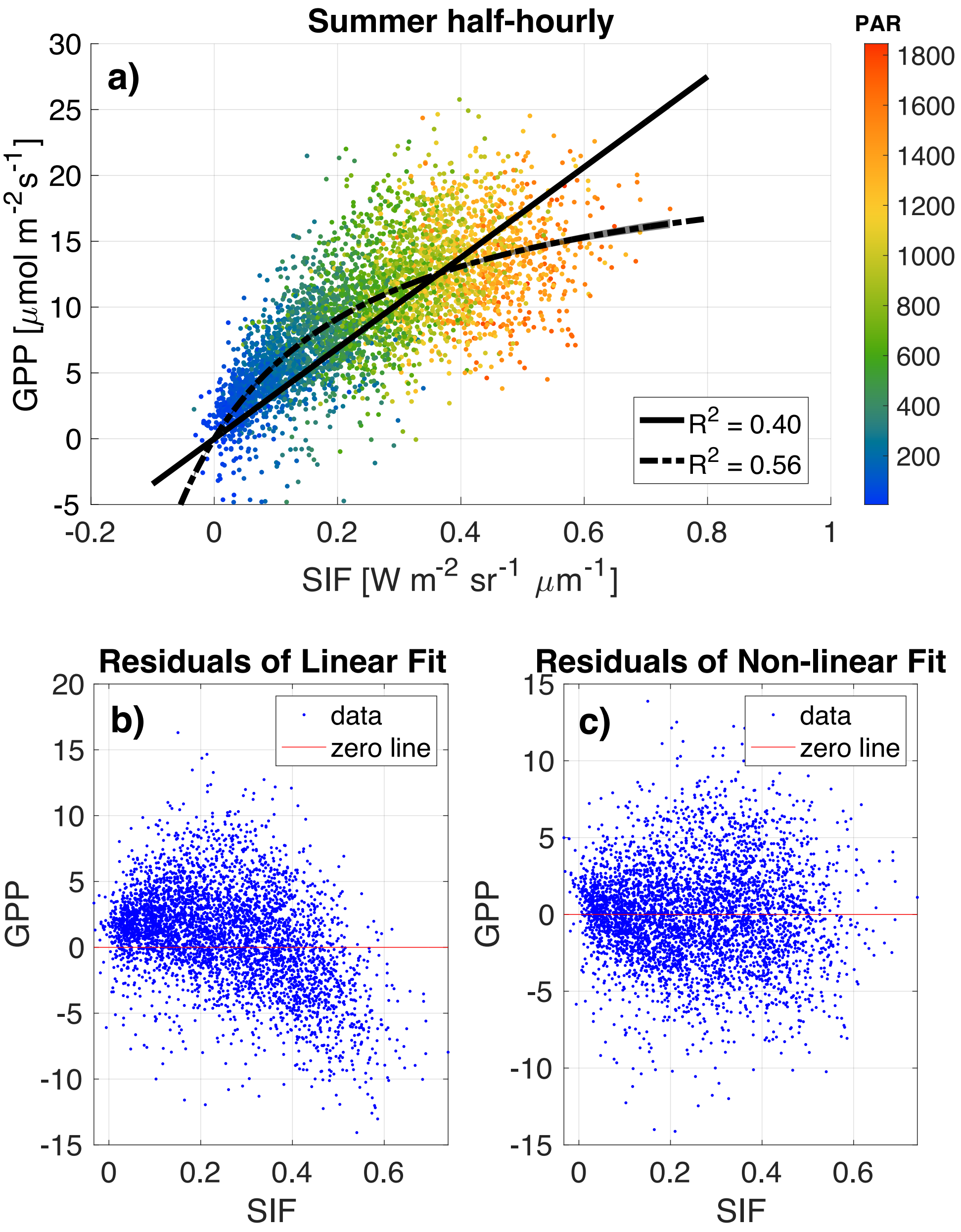

Figure A.2: a) The relationship between SIF and GPP at a half-hourly resolution colored by PAR in [μmolm^{-2}s^{-1}] for summertime data (between May 26 and September 16). The solid black line is a linear fit and the dashed line in is based off Equation 5.8. Shaded gray regions are the 95% non-simultaneous functional prediction bounds for the fit. R^2 values are the degree-of-freedom adjusted coefficient of determination of the fit. b) and c) show the residuals for both the linear and non-linear fits.

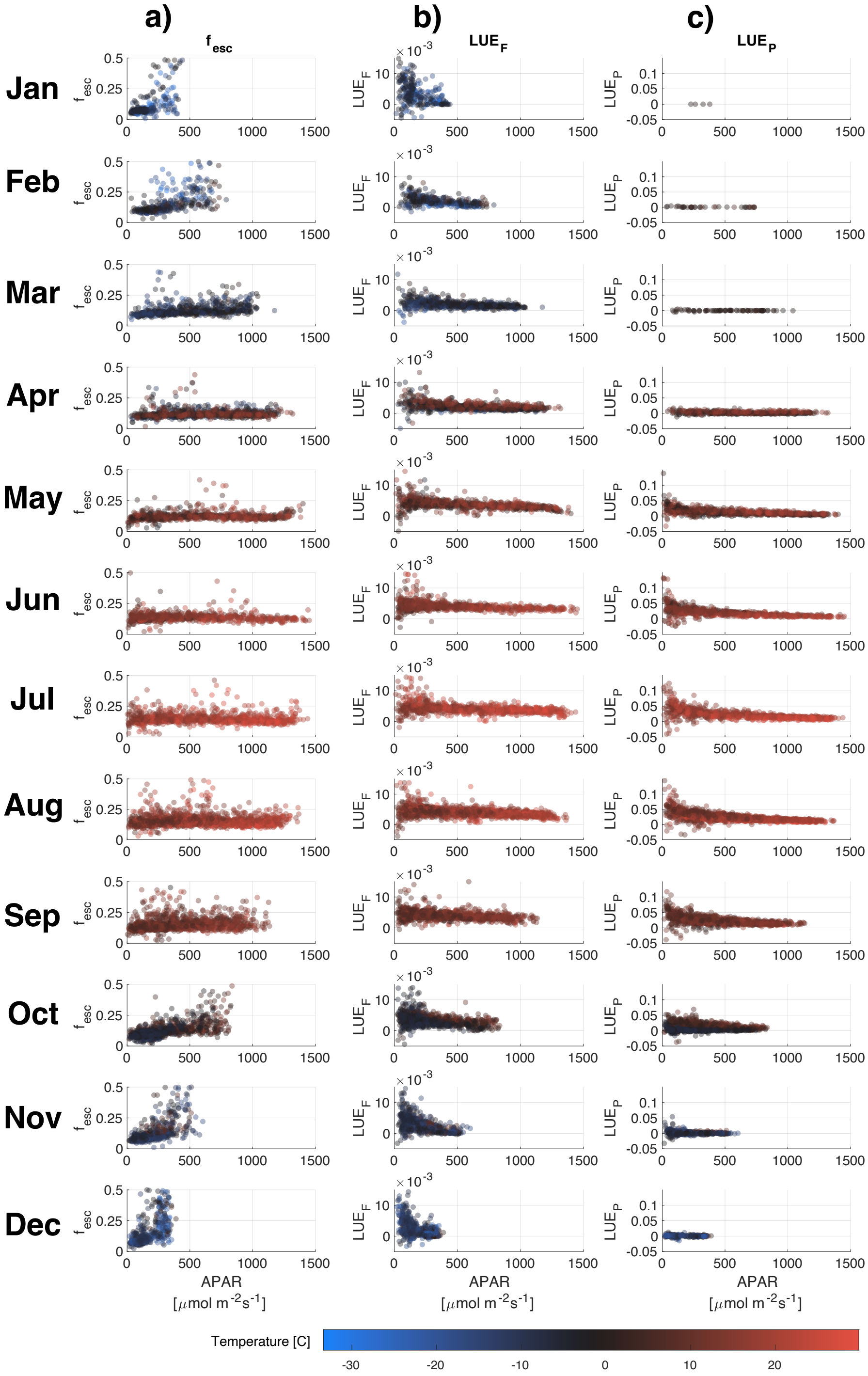

Figure A.3: Half-hourly data light response curves broken up monthly. Column a) f_{esc} calculated from Equation 4 plotted against APAR. Column b) LUEF in [Wm^{-2}sr$^{-1}\mu$m^{-1}]/[μmolm^{-2}s^{-1}] values determined from Equation 5.1 (LUE_F = SIF/[APAR*fesc]). Column c) LUE_P [unitless] calculated from Equation 6.1 (LUE_P = GPP/APAR).

APPENDIX B

Supplementary Materials for Chapter 6

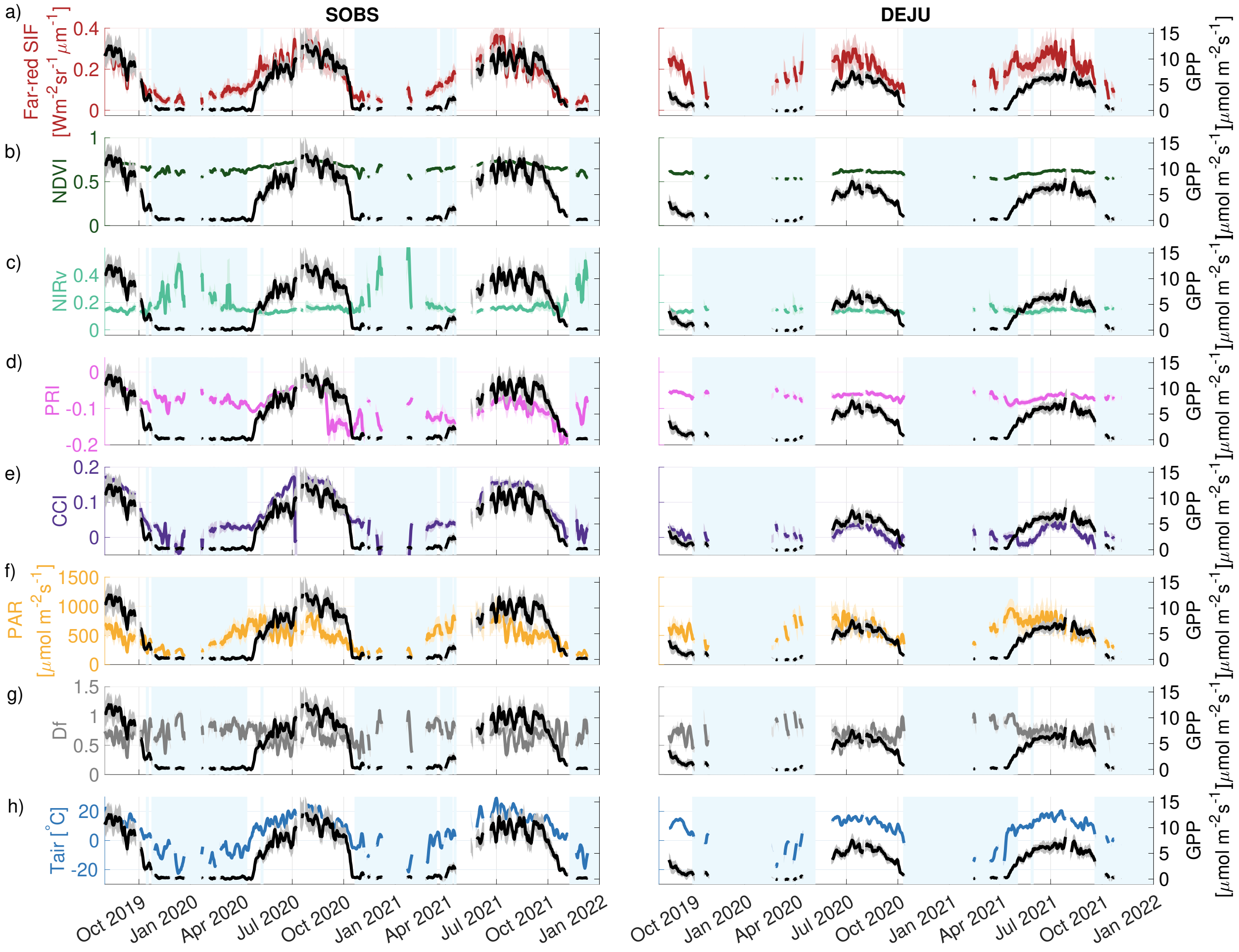

Figure B.1: The same as main text Figure 6.2 but showing data filtered to remove snow cover impacts. 5-day moving mean of daily average GPP compared with a) SIF, b) NDVI, c) NIRv, d) PRI, e) CCI, f) PAR, g) Df and h) Air Temperature over the entire data collection period for both the SOBS and DEJU sites. Shaded regions are the 5-day moving mean of the standard deviation of diurnal variability.

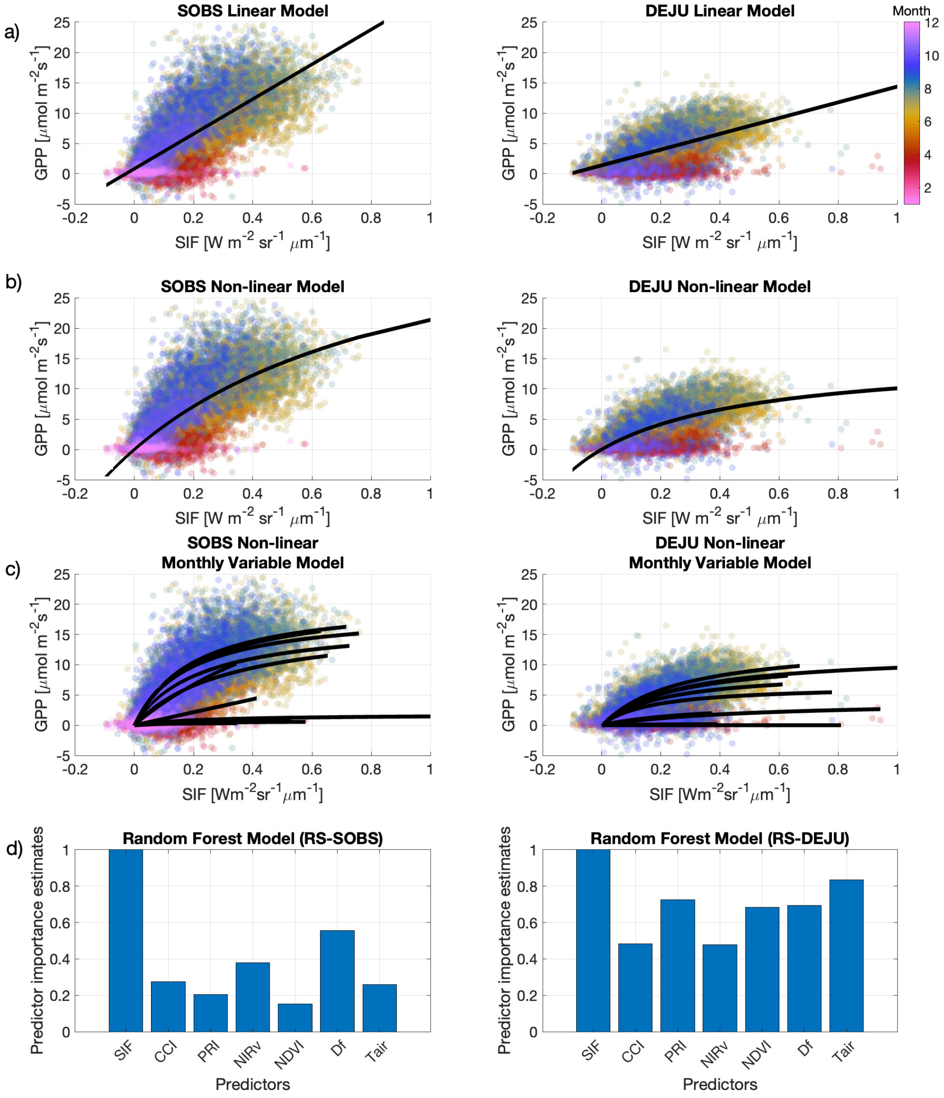

Figure B.2: The same as main text Figure 6.5 but using data filtered to remove snow impacts. Setup of traditional parameterized models for SIF as a proxy for GPP with our proposed random forest modelling approach for both SOBS and DEJU. Row a) shows a linear fit between SIF and GPP. Row b) shows a non-linear fit based on the light use efficiency model as ($\mathrm{GPP} = \frac{\mathrm{SIF} \times \mathrm{GPP_{max}}}{\mathrm{a+SIF}}$, Damm et al., 2015). Row c) shows the same non-linear fit but fitted monthly to create a monthly variable SIF-GPP relationship (Pierrat et al., 2022a). Row d) shows the input variables predictor importance estimates for random forest models RS-SOBS and RS-DEJU.

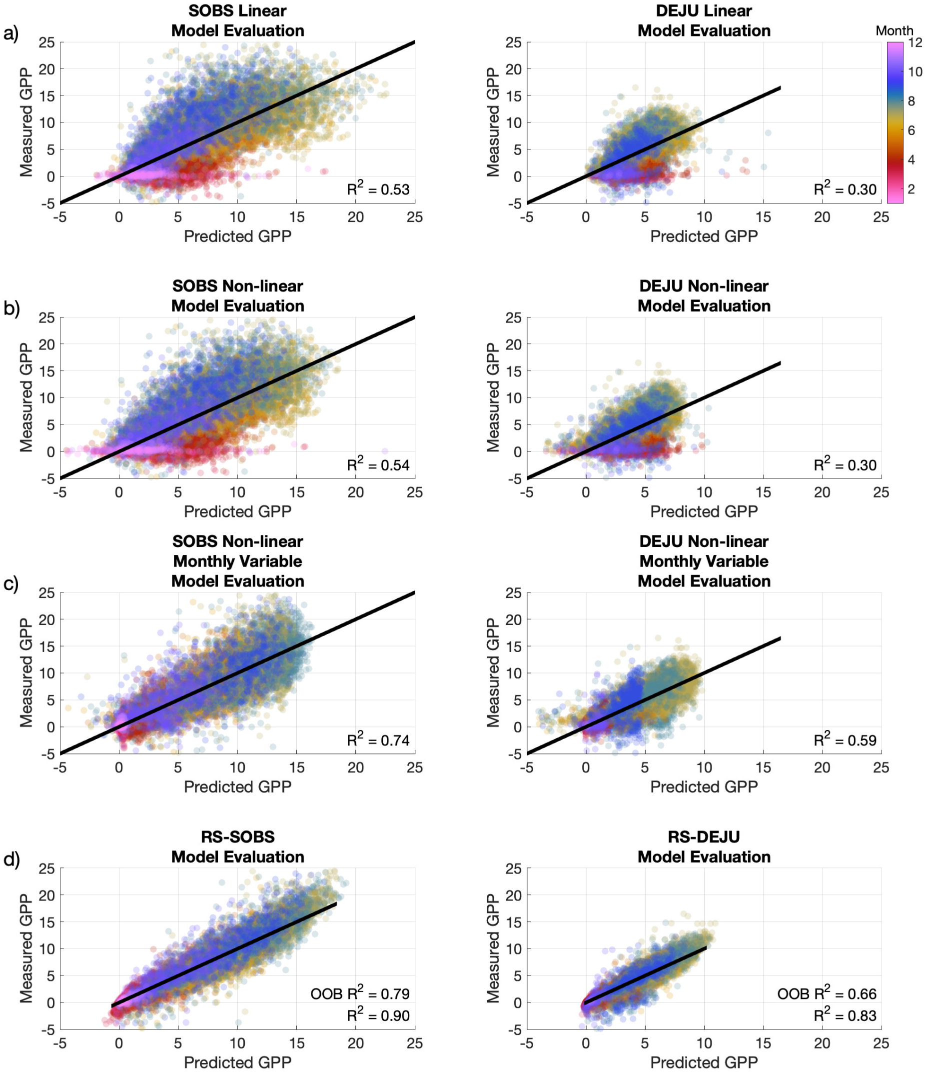

Figure B.3: The same as main text Figure 6.6 but using data filtered to remove snow cover impacts. Evaluation of model performance for traditional parameterized models compared with our proposed random forest modelling approach for both SOBS and DEJU. Rows a), b), c), and d) show the correlation between measured GPP and predicted GPP based on the models presented in Figure B.2 as row a) a linear fit between SIF and GPP, row b) a non-linear fit based on the light use efficiency model, row c) a monthly variable non-linear fit, row d) random forest models RS-SOBS and RS-DEJU (Table 6.2).

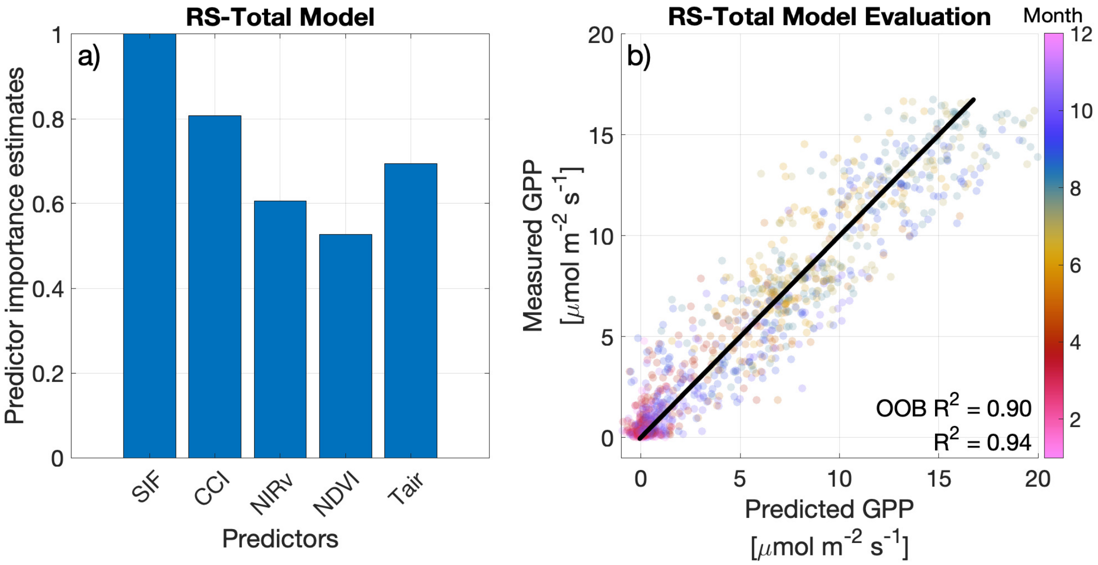

Figure B.4: The same as main text Figure 6.7 but using data filtered to remove snow cover impacts. Random forest model trained with daily midday average data across both sites (RS-Total) with a) predictor importance estimates and b) model performance on out-of-bag data with predicted and measured GPP.

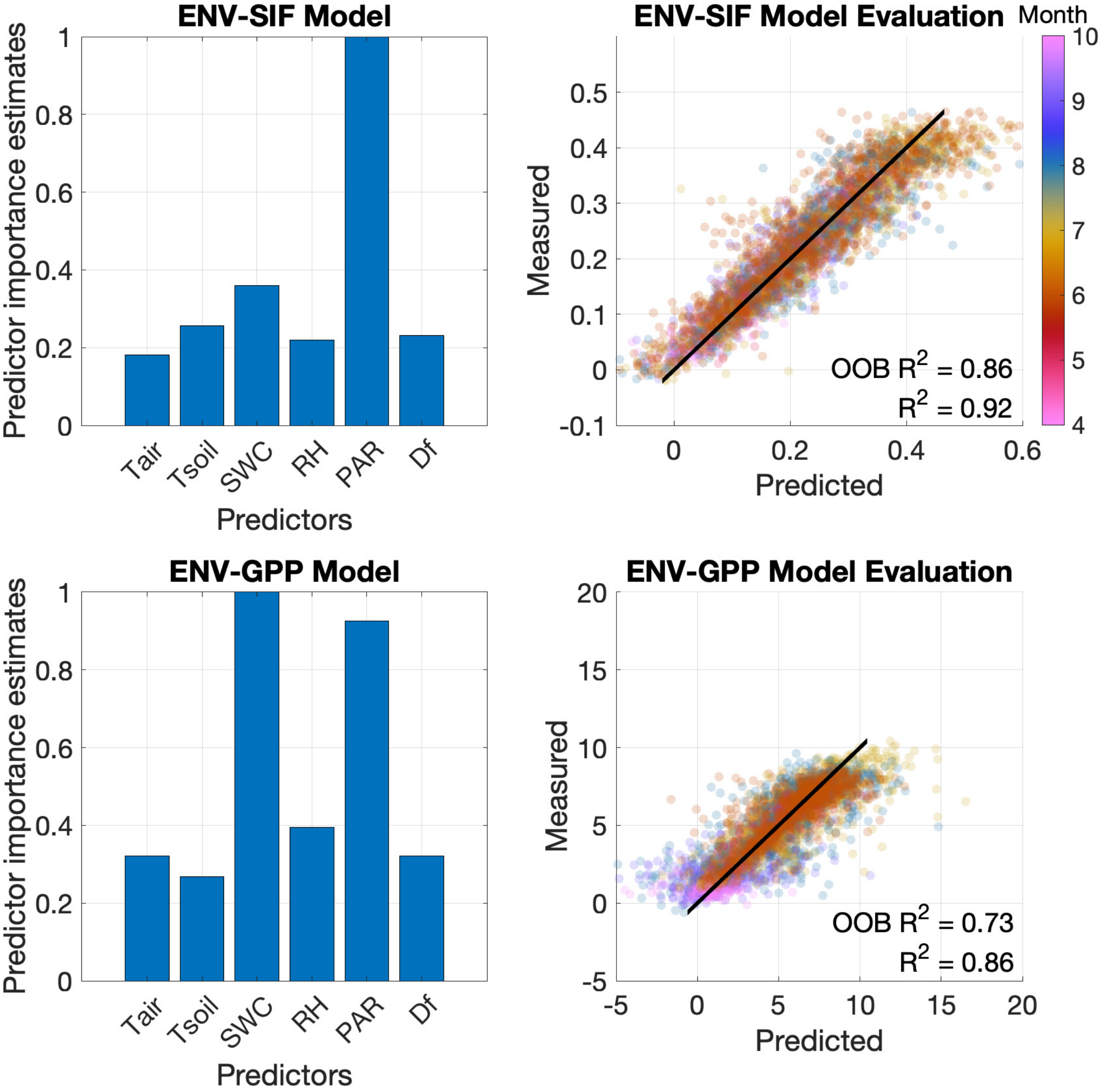

Figure B.5: Predictor importance estimates and model performance evaluation for two random forest models (ENV-GPP and ENV-SIF, Table 6.2) at the Delta Junction site (DEJU).

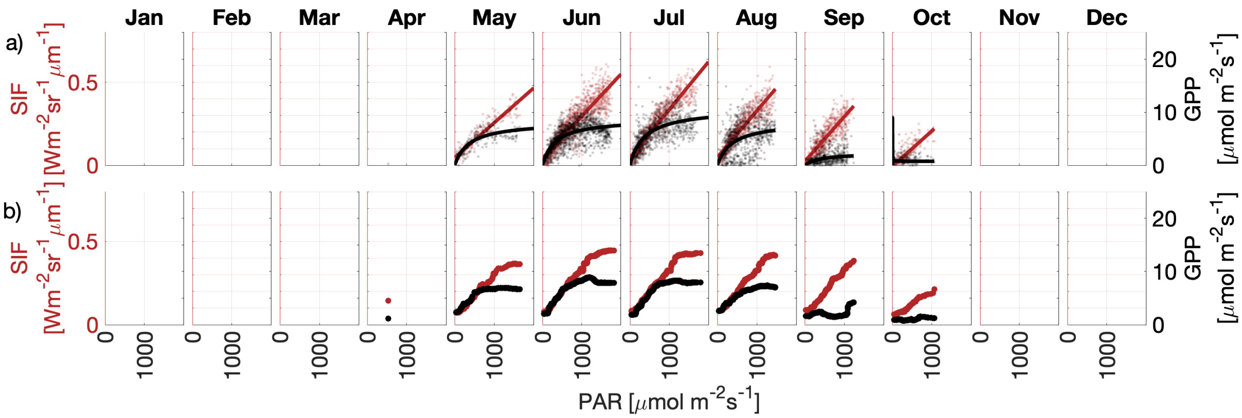

Figure B.6: Row a) shows half-hourly SIF and GPP data against PAR fitted with the parameterized light-use-efficiency models: (GPP $= \frac{\mathrm{GPP_{max}} \times \mathrm{PAR}}{c \times \mathrm{PAR}}$, Michaelis and Menten, 1913; Monteith, 1972) and (SIF $= c \times$ PAR, Equation 6.2). Row b) shows light response curves of half-hourly GPP and SIF produced from two random forest models (ENV-GPP and ENV-SIF) at the Delta Junction site (DEJU).

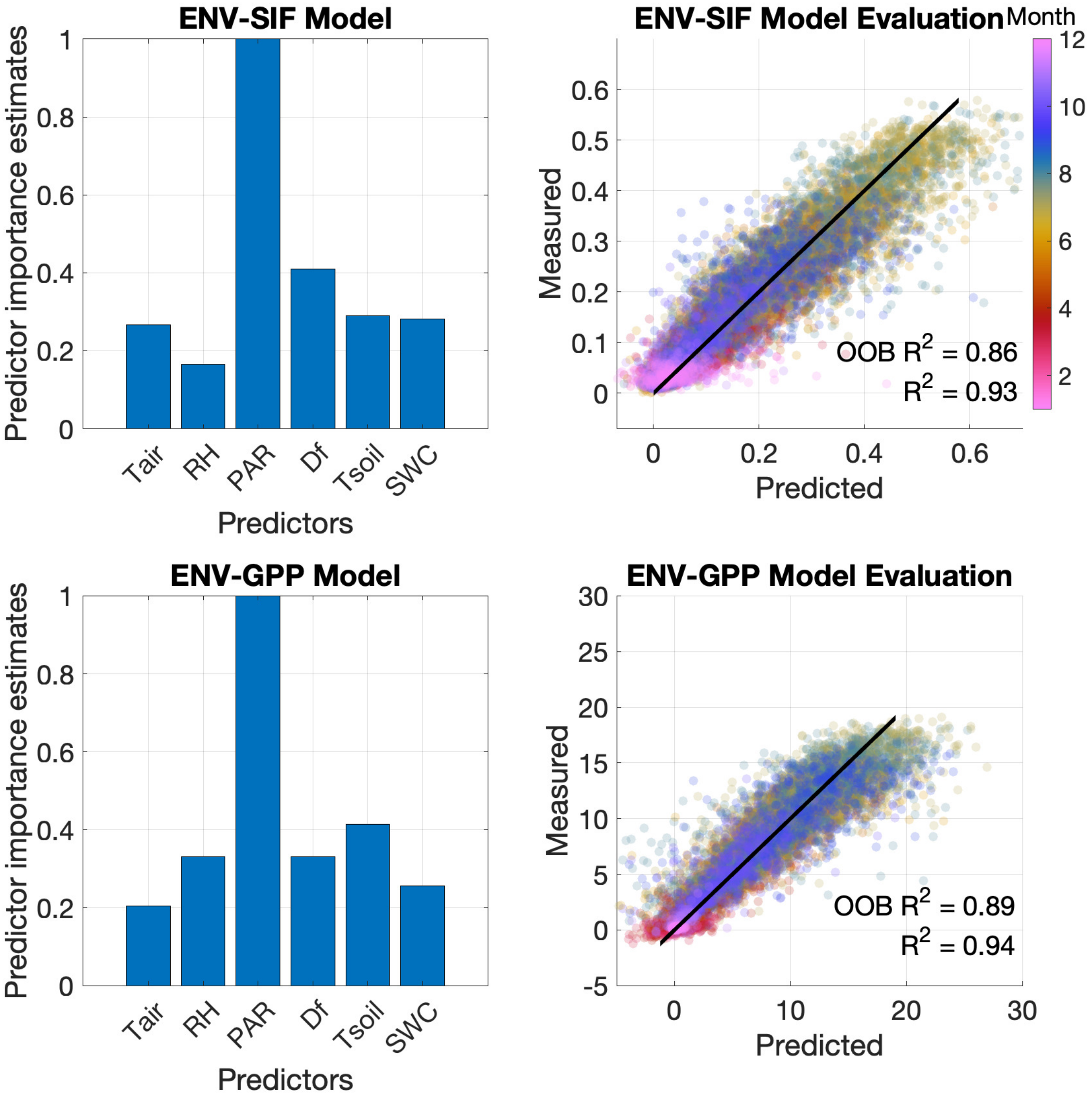

Figure B.7: Predictor importance estimates and model performance evaluation for two random forest models (ENV-GPP and ENV-SIF, Table 6.2) at the Southern Old Black Spruce site (SOBS).

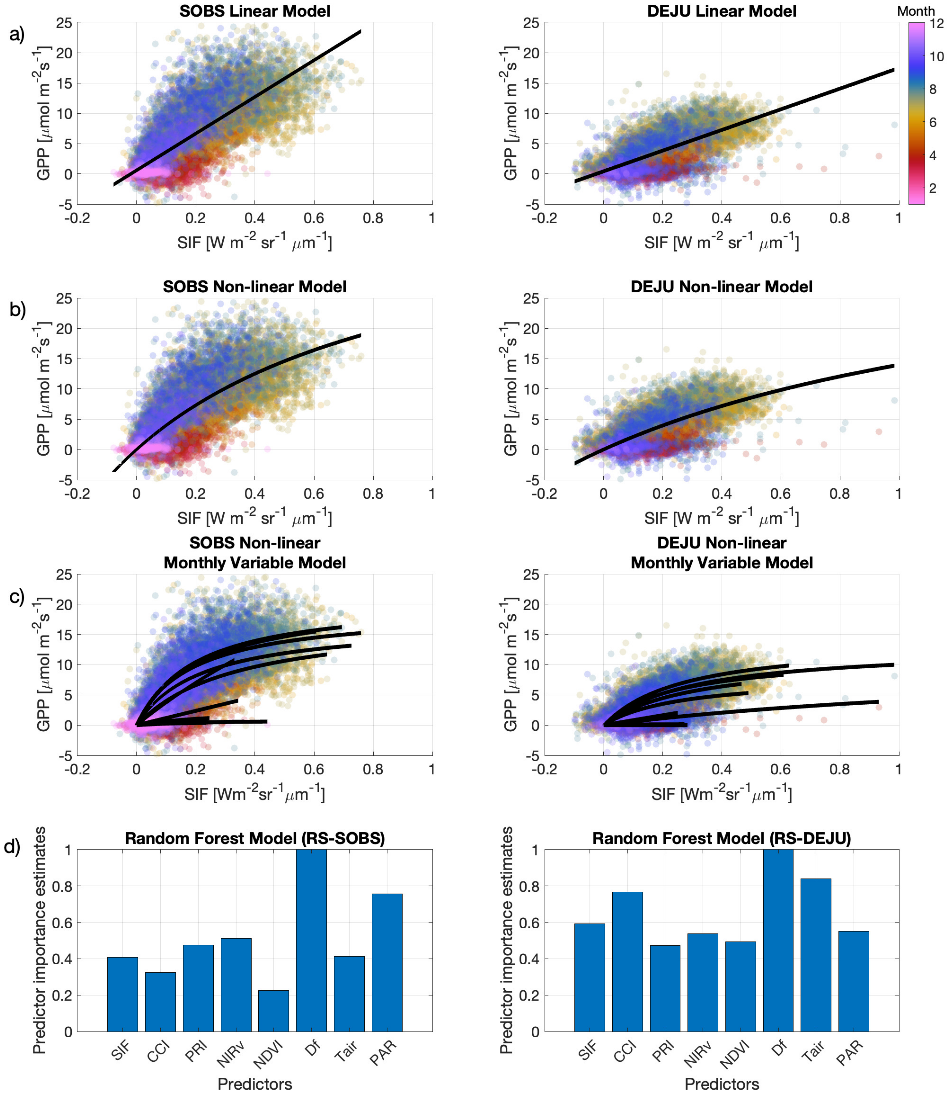

Figure B.8: The same as main text Figure 6.5 but including PAR as a predictor variable. Setup of traditional parameterized models for SIF as a proxy for GPP with our proposed random forest modelling approach for both SOBS and DEJU. Row a) shows a linear fit between SIF and GPP. Row b) shows a non-linear fit based on the light use efficiency model as ($\mathrm{GPP} = \frac{\mathrm{SIF} \times \mathrm{GPP_{max}}}{\mathrm{a} + \mathrm{SIF}}$, Damm et al., 2015). Row c) shows the same non-linear fit but fitted monthly to create a monthly variable SIF-GPP relationship (Pierrat et al., 2022a). Row d) shows the input variables predictor importance estimates for random forest models RS-SOBS and RS-DEJU with the addition of PAR as a predictor variable.

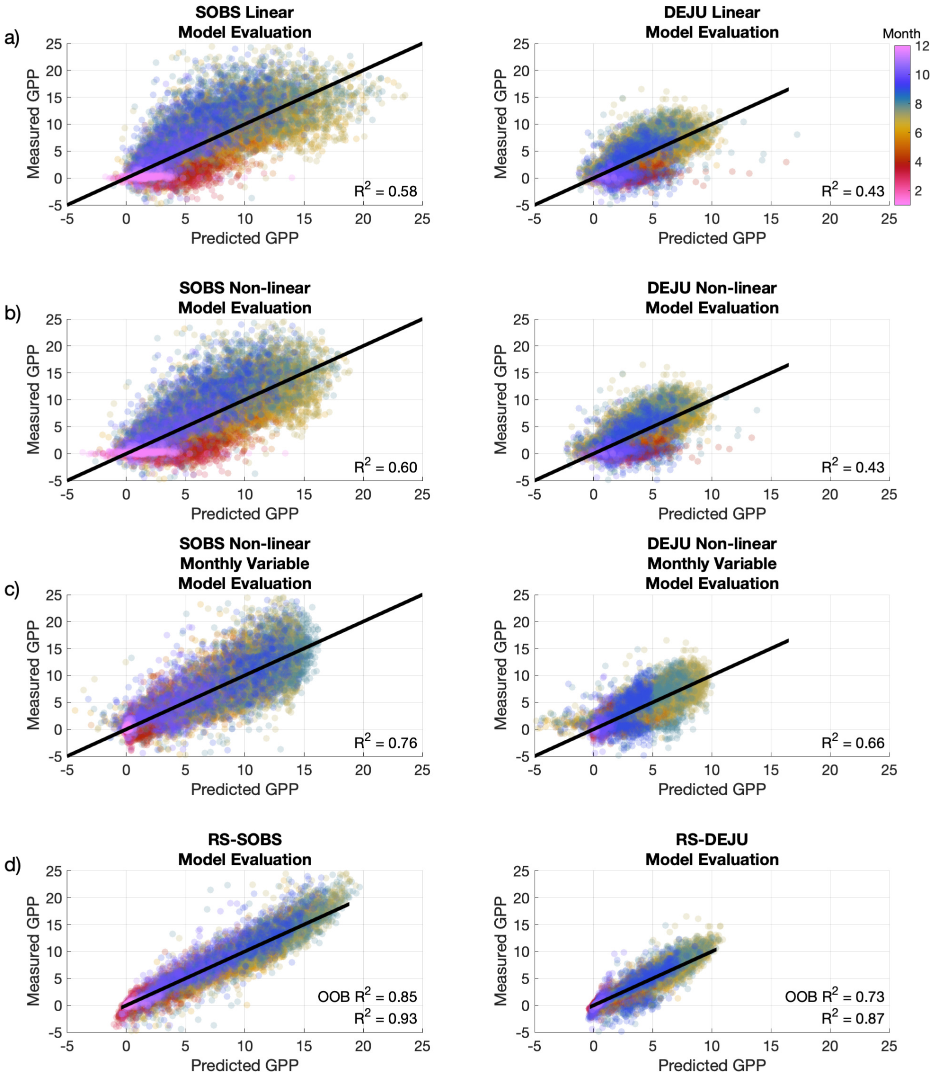

Figure B.9: The same as main text Figure 6.6 but including PAR as a predictor variable. Evaluation of model performance for traditional parameterized models compared with our proposed random forest modelling approach for both SOBS and DEJU. Rows a), b), c), and d) show the correlation between measured GPP and predicted GPP based on the models presented in Figure B.8 as row a) a linear fit between SIF and GPP, row b) a non-linear fit based on the light use efficiency model, row c) a monthly variable non-linear fit, row d) random forest models RS-SOBS and RS-DEJU (Table 2) but with the addition of PAR as a predictor variable.

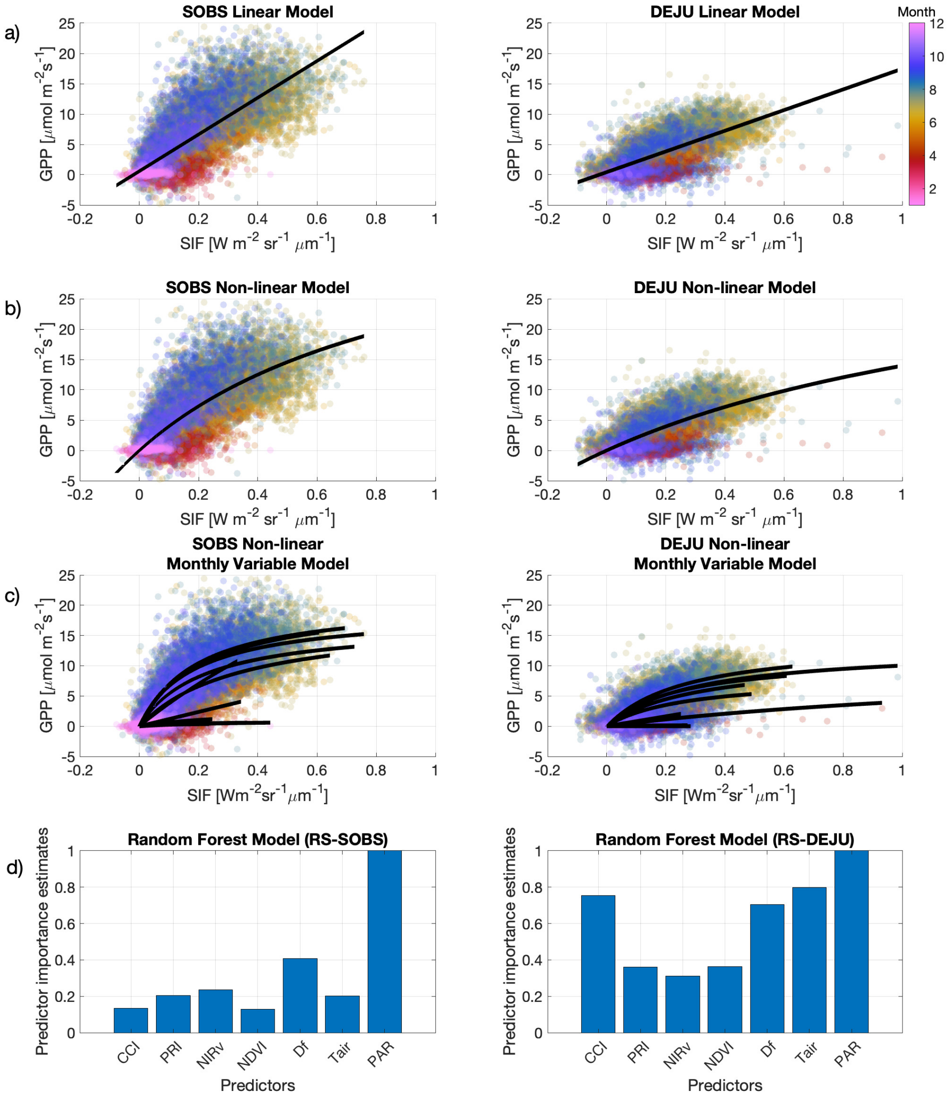

Figure B.10: The same as main text Figure 6.5 but including PAR as a predictor variable instead of SIF. Setup of traditional parameterized models for SIF as a proxy for GPP with our proposed random forest modelling approach for both SOBS and DEJU. Row a) shows a linear fit between SIF and GPP. Row b) shows a non-linear fit based on the light use efficiency model as (GPP $= \frac{\text{SIF}\times\text{GPP}_{\text{max}}}{\text{a+SIF}}$, Damm et al., 2015). Row c) shows the same non-linear fit but fitted monthly to create a monthly variable SIF-GPP relationship (Pierrat et al., 2022a). Row d) shows the input variables predictor importance estimates for random forest models RS-SOBS and RS-DEJU with the addition of PAR as a predictor variable.

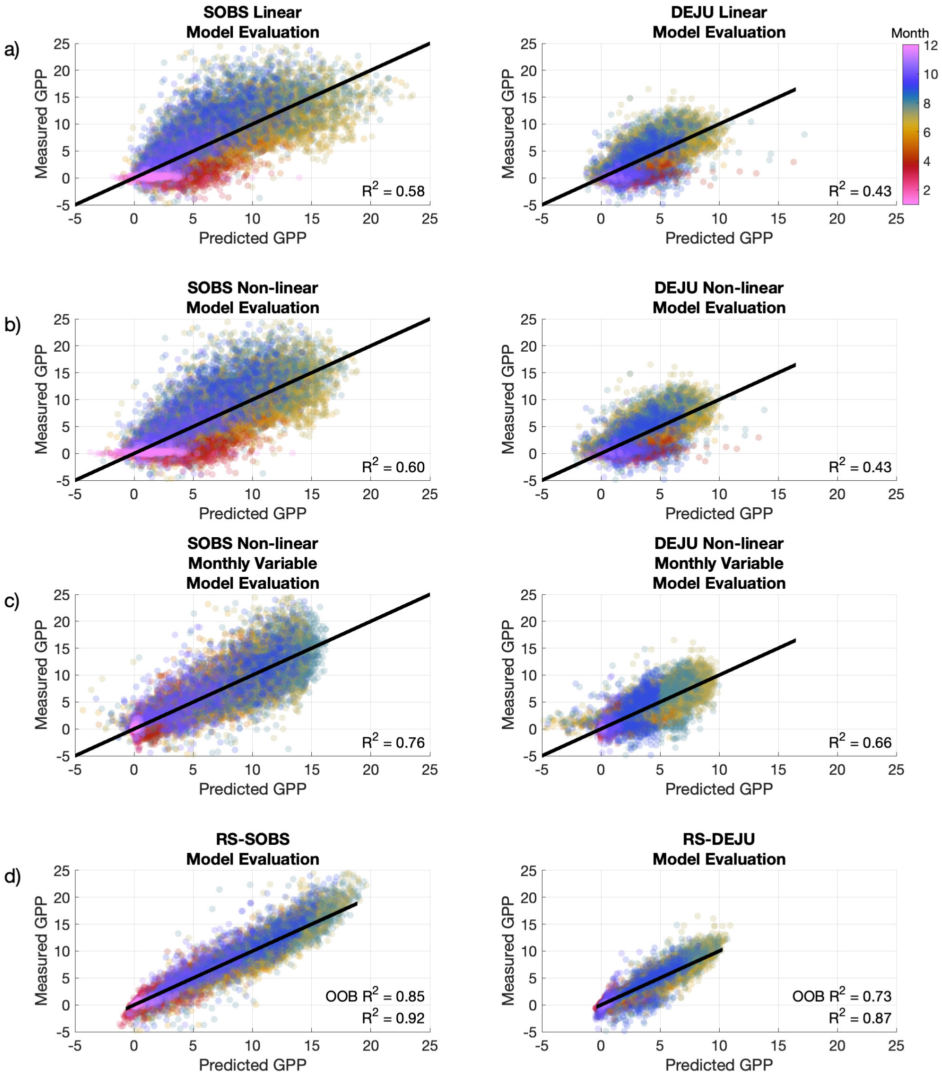

Figure B.11: The same as main text Figure 6.6 but including PAR as a predictor variable instead of SIF. Evaluation of model performance for traditional parameterized models compared with our proposed random forest modelling approach for both SOBS and DEJU. Rows a), b), c), and d) show the correlation between measured GPP and predicted GPP based on the models presented in Figure B.10 as row a) a linear fit between SIF and GPP, row b) a non-linear fit based on the light use efficiency model, row c) a monthly variable non-linear fit, row d) random forest models RS-SOBS and RS-DEJU (Table 6.2) but with the addition of PAR as a predictor variable.

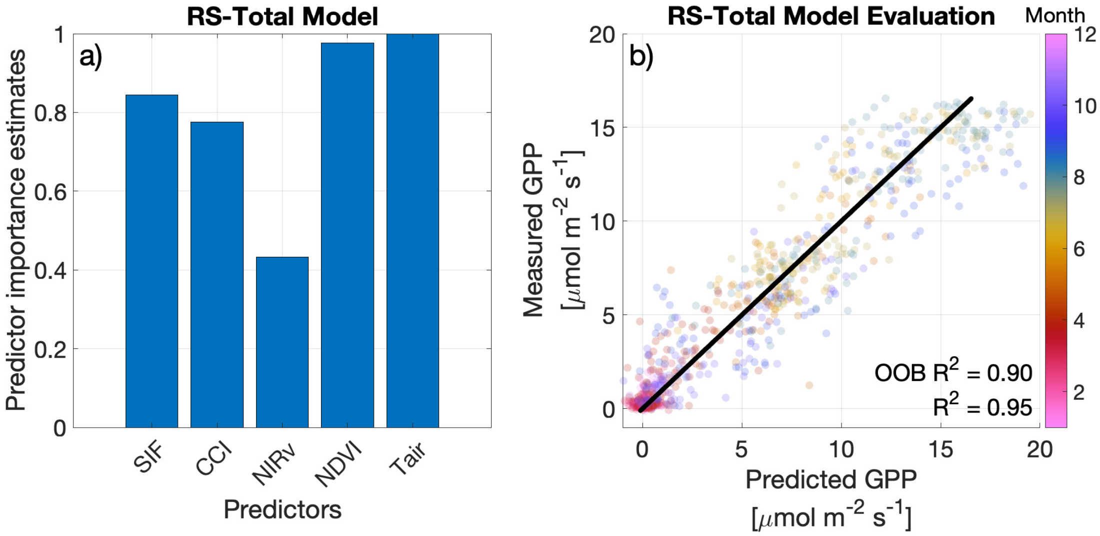

Figure B.12: The same as main text Figure 6.7 but only including clear sky days. Random forest model trained with daily midday average data across both sites (RS-Total) with a) predictor importance estimates and b) model performance on out-of-bag data with predicted and measured GPP.

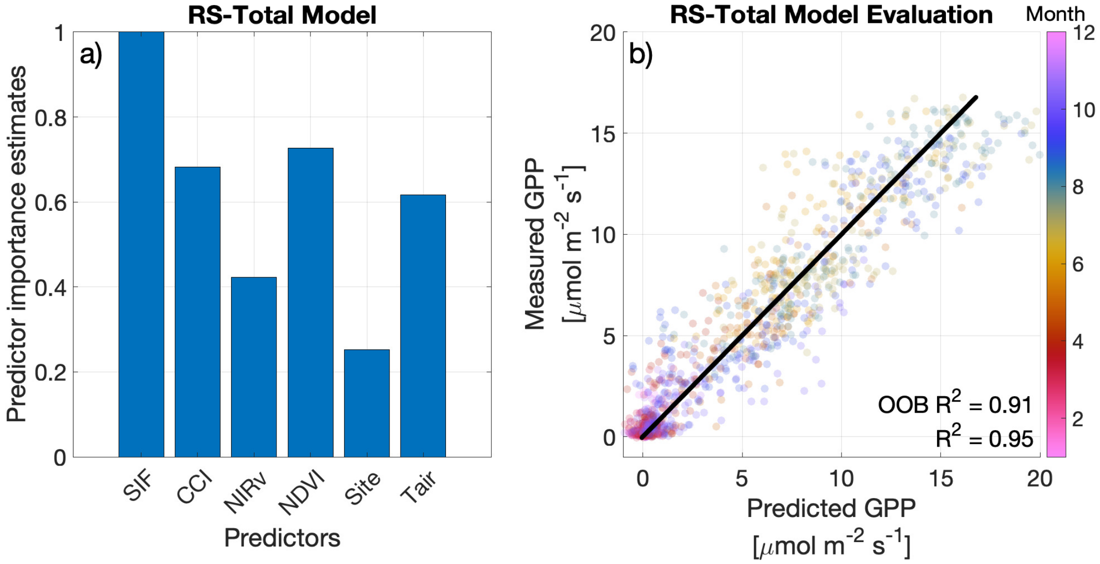

Figure B.13: The same as main text Figure 6.7 but including a site flag. Random forest model trained with daily midday average data across both sites (RS-Total) with a) predictor importance estimates and b) model performance on out-of-bag data with predicted and measured GPP.

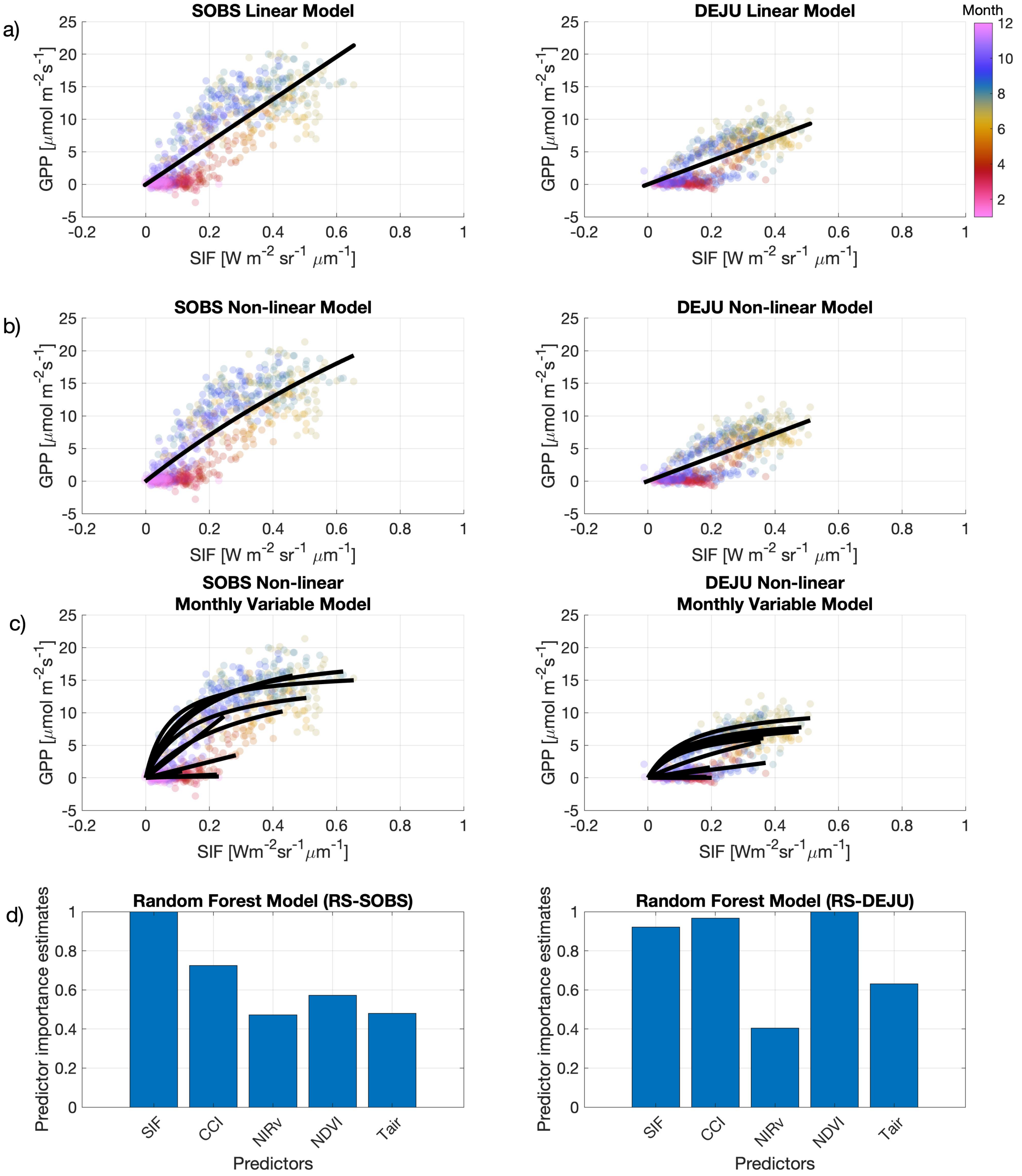

Figure B.14: Setup of traditional parameterized models for SIF as a proxy for GPP with our proposed random forest modelling approach for both SOBS and DEJU at a daily resolution. Row a) shows a linear fit between SIF and GPP. Row b) shows a non-linear fit based on the light use efficiency model as (GPP $= \frac{\text{SIF} \times \text{GPP}_{\text{max}}}{\text{a+SIF}}$, Damm et al., 2015). Row c) shows the same non-linear fit but fitted monthly to create a monthly variable SIF-GPP relationship (Pierrat et al., 2022a). Row d) shows the input variables predictor importance estimates for random forest models RS-SOBS and RS-DEJU with the addition of PAR as a predictor variable.

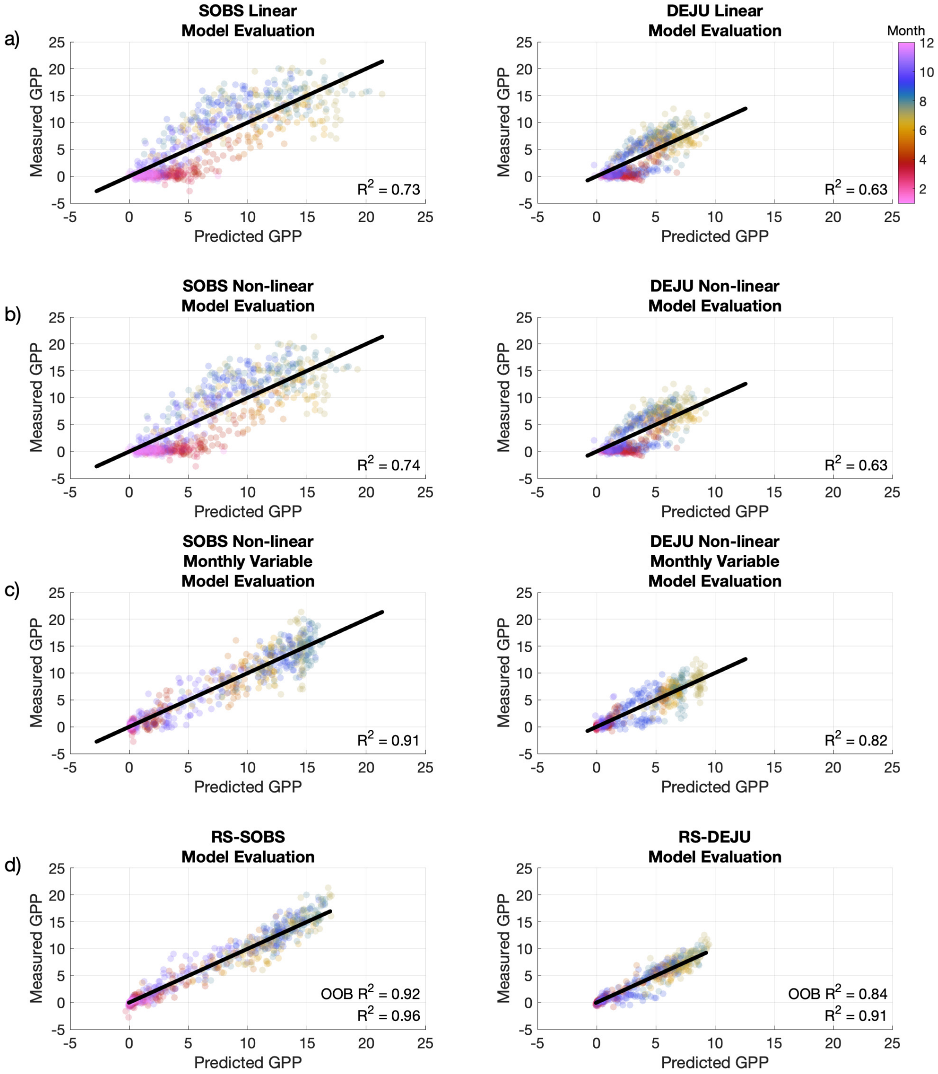

Figure B.15: Evaluation of model performance for traditional parameterized models compared with our proposed random forest modelling approach for both SOBS and DEJU at a daily resolution. Rows a), b), c), and d) show the correlation between measured GPP and predicted GPP based on the models presented in Figure B.14 as row a) a linear fit between SIF and GPP, row b) a non-linear fit based on the light use efficiency model, row c) a monthly variable non-linear fit, row d) random forest models RS-SOBS and RS-DEJU (Table 6.2) but with the addition of PAR as a predictor variable.

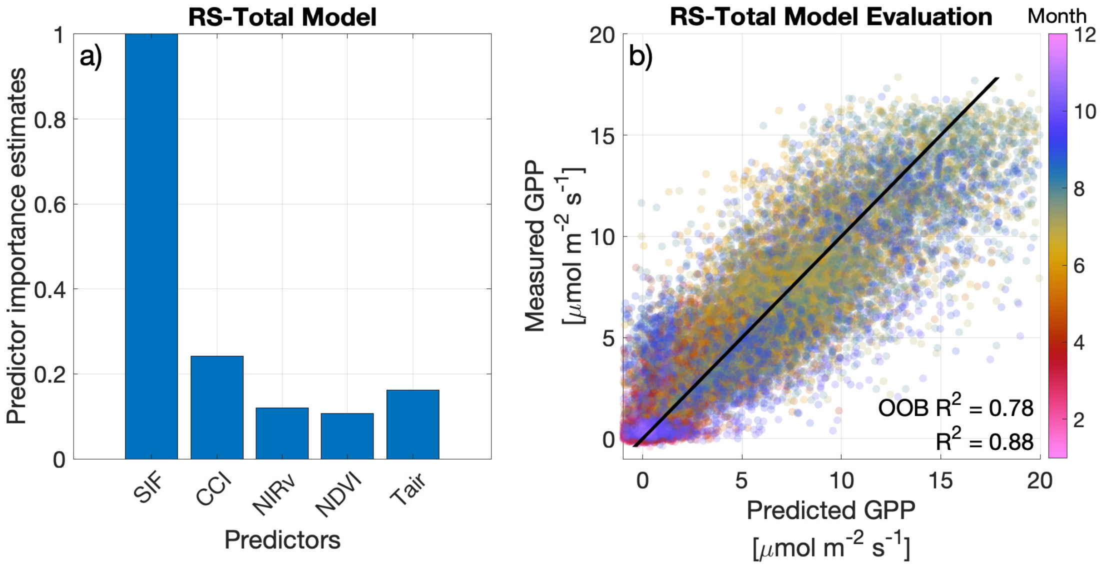

Figure B.16: The same as main text Figure 6.7 but trained with half-hourly data across both sites (RS-Total) with a) predictor importance estimates and b) model performance on out-of-bag data with predicted and measured GPP.

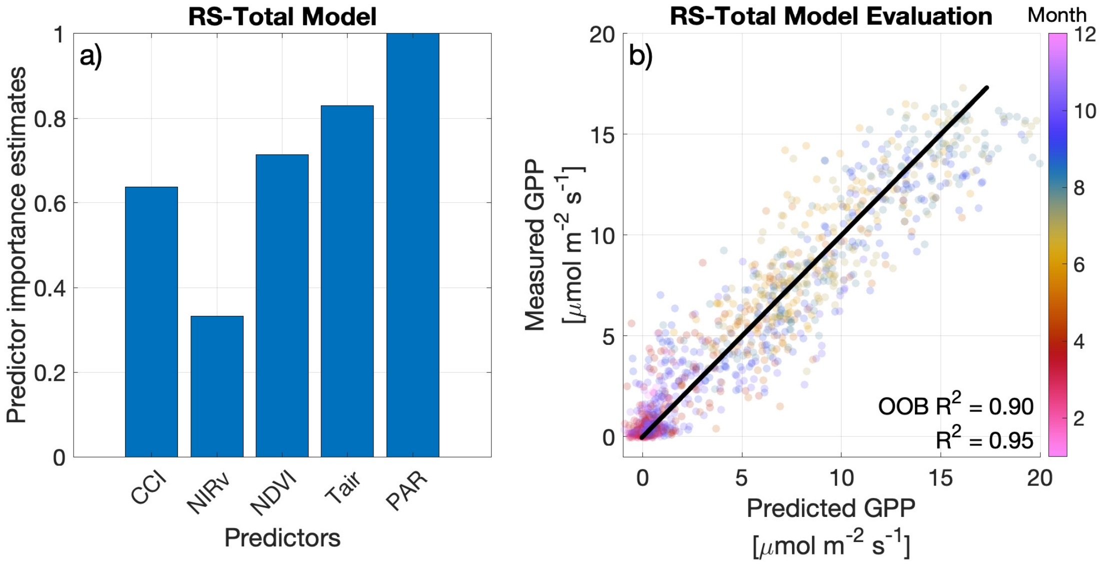

Figure B.17: The same as main text Figure 6.7 but using PAR instead of SIF. Random forest model trained with daily midday average data across both sites (RS-Total) with a) predictor importance estimates and b) model performance on out-of-bag data with predicted and measured GPP.

Bibliography

W. W. Adams and B. Demmig-Adams. Carotenoid composition and down regulation of photosystem II in three conifer species during the winter. *Physiologia Plantarum*, 92(3): 451–458, 1994. ISSN 13993054. doi: 10.1111/j.1399-3054.1994.tb08835.x.

W. W. Adams, C. R. Zarter, V. Ebbert, and B. Demmig-Adams. Photoprotective Strategies of Overwintering Evergreens. *BioScience*, 54(1):41, 2004. ISSN 0006-3568. doi: 10.1641/0006-3568(2004)054[0041:PSOOE]2.0.CO;2.

W. W. Adams III, B. Demmig-Adams, T. N. Rosenstiel, A. K. Brightwell, and V. Ebbert. Photosynthesis and Photoprotection in Overwintering Plants. *Plant Biology*, 4(5):545–557, 2002. ISSN 1438-8677. doi: 10.1055/s-2002-35434. _eprint: https://onlinelibrary.wiley.com/doi/pdf/10.1055/s-2002-35434.

D. Alcaraz-Segura, E. Chuvieco, H. E. Epstein, E. S. Kasischke, and A. Trishchenko. Debating the greening vs. browning of the North American boreal forest: differences between satellite datasets. *Global Change Biology*, 16(2):760–770, 2010. ISSN 1365-2486. doi: 10.1111/j.1365-2486.2009.01956.x.

C. D. Allen, A. K. Macalady, H. Chenchouni, D. Bachelet, N. McDowell, M. Vennetier, T. Kitzberger, A. Rigling, D. D. Breshears, E. H. T. Hogg, P. Gonzalez, R. Fensham, Z. Zhang, J. Castro, N. Demidova, J.-H. Lim, G. Allard, S. W. Running, A. Semerci, and N. Cobb. A global overview of drought and heat-induced tree mortality reveals emerging climate change risks for forests. *Forest Ecology and Management*, 259(4):660–684, Feb. 2010. ISSN 0378-1127. doi: 10.1016/j.foreco.2009.09.001.

P. B. Alton, P. R. North, and S. O. Los. The impact of diffuse sunlight on canopy light-use efficiency, gross photosynthetic product and net ecosystem exchange in three forest biomes. *Global Change Biology*, 13(4):776–787, jan 2007. ISSN 13541013. doi: 10.1111/j.1365-2486.2007.01316.x.

T. Ameglio, F. W. Ewers, U. M. R. P. Inra, B. Pascal, and S. I. D. Crouelle. Stem diameter variations and cold hardiness in walnut trees. *Journal of Experimental Botany*, 52(364): 2135–2142, 2001.

A. Anav, P. Friedlingstein, C. Beer, P. Ciais, A. Harper, C. Jones, G. Murray-Tortarolo, D. Papale, N. C. Parazoo, P. Peylin, S. Piao, S. Sitch, N. Viovy, A. Wiltshire, and M. Zhao. Reviews of Geophysics primary production : A review. *Reviews of Geophysics*, pages 1–34, 2015. ISSN 87551209. doi: 10.1002/2015RG000483.

W. R. L. Anderegg, A. Flint, C.-y. Huang, L. Flint, J. A. Berry, F. W. Davis, J. S. Sperry, and C. B. Field. Tree mortality predicted from drought-induced vascular damage. *Nature Geoscience*, 8(5):367–371, May 2015. ISSN 1752-0908. doi: 10.1038/ngeo2400.

W. R. L. Anderegg, A. T. Trugman, G. Badgley, C. M. Anderson, A. Bartuska, P. Ciais, D. Cullenward, C. B. Field, J. Freeman, S. J. Goetz, J. A. Hicke, D. Huntzinger, R. B. Jackson, J. Nickerson, S. Pacala, and J. T. Randerson. Climate-driven risks to the climate mitigation potential of forests. *Science (New York, N.Y.)*, 368(6497):eaaz7005, June 2020. ISSN 1095-9203. doi: 10.1126/science.aaz7005.

W. R. L. Anderegg, O. S. Chegwidden, G. Badgley, A. Trugman, D. Cullenward, J. T. Abatzoglou, J. Hicke, J. Freeman, and J. J. Hamman. Future climate risks from stress, insects and fire across US forests. *Ecology Letters*, 25(6):1510–1520, June 2022. ISSN 1461-023X. doi: 10.1111/ele.14018.

G. P. Asner. Biophysical and Biochemical Sources of Variability in Canopy Reflectance. *Remote Sensing of Environment*, 64(3):234–253, June 1998. ISSN 0034-4257. doi: 10.1016/S0034-4257(98)00014-5.

J. Atherton, B. Olascoaga, L. Alonso, and A. Porcar-Castell. Spatial variation of leaf optical properties in a boreal forest is influenced by species and light environment. *Frontiers in Plant Science*, 8:309, 2017. ISSN 1664462X. doi: 10.3389/fpls.2017.00309.

C. B. Eller, F. de V. Barros, P. R.L. Bittencourt, L. Rowland, M. Mencuccini, and R. S. Oliveira. Xylem hydraulic safety and construction costs determine tropical tree growth. *Plant Cell and Environment*, 41(3):548–562, 2018. ISSN 13653040. doi: 10.1111/pce.13106.

G. Badgley, C. B. Field, and J. A. Berry. Canopy near-infrared reflectance and terrestrial photosynthesis. *Science Advances*, 3(3):e1602244, 2017. ISSN 23752548. doi: 10.1126/sciadv.1602244.

G. Badgley, L. D. Anderegg, J. A. Berry, and C. B. Field. Terrestrial gross primary production: Using NIRV to scale from site to globe. *Global Change Biology*, 25(11):3731–3740, 2019. ISSN 13652486. doi: 10.1111/gcb.14729.

P. Bag, V. Chukhutsina, Z. Zhang, S. Paul, A. G. Ivanov, T. Shutova, R. Croce, A. R. Holzwarth, and S. Jansson. Direct energy transfer from photosystem II to photosystem I confers winter sustainability in Scots Pine. *Nature Communications*, 11(1):1–13, 2020. ISSN 20411723. doi: 10.1038/s41467-020-20137-9.

J. Bai, H. Zhang, R. Sun, X. Li, J. Xiao, and Y. Wang. Estimation of global GPP from GOME-2 and OCO-2 SIF by considering the dynamic variations of GPP-SIF relationship. *Agricultural and Forest Meteorology*, 326:109180, Nov. 2022. ISSN 0168-1923. doi: 10.1016/j.agrformet.2022.109180.

D. D. Baldocchi. Assessing the eddy covariance technique for evaluating carbon dioxide exchange rates of ecosystems: Past, present and future. *Global Change Biology*, 9(4):479–492, 2003. ISSN 13541013. doi: 10.1046/j.1365-2486.2003.00629.x.

D. D. Baldocchi. How eddy covariance flux measurements have contributed to our understanding of Global Change Biology. *Global Change Biology*, 26(1):242–260, 2020. ISSN 1365-2486. doi: 10.1111/gcb.14807.

D. D. Baldocchi, B. B. Hicks, and T. P. Meyers. Measuring biosphere-atmosphere exchanges of biologically related gases with micrometeorological methods. *Ecology*, 69(5):1331–1340, 1988. ISSN 00129658. doi: 10.2307/1941631.

D. D. Baldocchi, T. A. Black, P. S. Curtis, E. Falge, J. D. Fuentes, A. Granier, L. Gu, A. Knohl, K. Pilegaard, H. P. Schmid, R. Valentini, K. Wilson, S. Wofsy, L. Xu, and S. Yamamoto. Predicting the onset of net carbon uptake by deciduous forests with soil temperature and climate data: A synthesis of FLUXNET data. *International Journal of Biometeorology*, 49(6):377–387, 2005. ISSN 00207128. doi: 10.1007/s00484-005-0256-4.

D. D. Baldocchi, Y. Ryu, B. Dechant, E. Eichelmann, K. Hemes, S. Ma, C. R. Sanchez, R. Shortt, D. Szutu, A. Valach, J. Verfaillie, G. Badgley, Y. Zeng, and J. A. Berry. Outgoing Near-Infrared Radiation From Vegetation Scales With Canopy Photosynthesis Across a Spectrum of Function, Structure, Physiological Capacity, and Weather. *Journal of Geophysical Research: Biogeosciences*, 125(7), 2020. ISSN 21698961. doi: 10.1029/2019JG005534.

A. Baldridge, S. Hook, C. Grove, and G. Rivera. The ASTER spectral library version 2.0. *Remote Sensing of Environment*, 113(4):711–715, Apr. 2009. ISSN 00344257. doi: 10.1016/j.rse.2008.11.007.

J. Barichivich, K. R. Briffa, R. B. Myneni, T. J. Osborn, T. M. Melvin, P. Ciais, S. Piao, and C. Tucker. Large-scale variations in the vegetation growing season and annual cycle of atmospheric CO2 at high northern latitudes from 1950 to 2011. *Global Change Biology*, 19(10):3167–3183, 2013. ISSN 13541013. doi: 10.1111/gcb.12283.

A. G. Barr, T. A. Black, E. H. Hogg, N. Kljun, K. Morgenstern, and Z. Nesic. Interannual variability in the leaf area index of a boreal aspen-hazelnut forest in relation to net ecosystem production. *Agricultural and Forest Meteorology*, 126(3-4):237–255, 2004. ISSN 01681923. doi: 10.1016/j.agrformet.2004.06.011.

A. G. Barr, K. Morgenstern, T. A. Black, J. H. McCaughey, and Z. Nesic. Surface energy balance closure by the eddy-covariance method above three boreal forest stands and implications for the measurement of the CO2 flux. *Agricultural and Forest Meteorology*, 140 (1-4):322–337, 2006. ISSN 01681923. doi: 10.1016/j.agrformet.2006.08.007.

P. S. A. Beck, S. J. Goetz, M. C. Mack, H. D. Alexander, Y. Jin, J. T. Randerson, and M. M. Loranty. The impacts and implications of an intensifying fire regime on Alaskan boreal forest composition and albedo. *Global Change Biology*, 17(9):2853–2866, 2011. ISSN 1365-2486. doi: 10.1111/j.1365-2486.2011.02412.x.

C. Beer, M. Reichstein, E. Tomelleri, P. Ciais, M. Jung, N. Carvalhais, C. Rödenbeck, M. A. Arain, D. Baldocchi, G. B. Bonan, A. Bondeau, A. Cescatti, G. Lasslop, A. Lindroth, M. Lomas, S. Luyssaert, H. Margolis, K. W. Oleson, O. Roupsard, E. Veenendaal, N. Viovy, C. Williams, F. I. Woodward, and D. Papale. Terrestrial Gross Carbon Dioxide Uptake: Global Distribution and Covariation with Climate. *Science*, 329(5993):834–838, Aug. 2010. doi: 10.1126/science.1184984.

B. J. Bentz, A. M. Jönsson, M. Schroeder, A. Weed, R. A. I. Wilcke, and K. Larsson. Ips typographus and dendroctonus ponderosae models project thermal suitability for intra- and inter-continental establishment in a changing climate. *Frontiers in Forests and Global Change*, 2, 2019. ISSN 2624-893X.

J. Bergh and S. Linder. Effects of soil warming during spring on photosynthetic recovery in boreal Norway spruce stands. *Global Change Biology*, 5(3):245–253, 1999. ISSN 13541013. doi: 10.1046/j.1365-2486.1999.00205.x.

L. T. Berner, R. Massey, P. Jantz, B. C. Forbes, M. Macias-Fauria, I. Myers-Smith, T. Kumpula, G. Gauthier, L. Andreu-Hayles, B. V. Gaglioti, P. Burns, P. Zetterberg, R. D'Arrigo, and S. J. Goetz. Summer warming explains widespread but not uniform greening in the Arctic tundra biome. *Nature Communications*, 11(1):4621, Sept. 2020. ISSN 2041-1723. doi: 10.1038/s41467-020-18479-5.

J. Berry and O. Bjorkman. Photosynthetic Response and Adaptation to Temperature in Higher Plants. *Annual Review of Plant Physiology*, 31(1):491–543, 1980. doi: 10.1146/annurev.pp.31.060180.002423.

G. B. Bonan. Forests and climate change: Forcings, feedbacks, and the climate benefits of forests. *Science*, 320(5882):1444–1449, 2008. ISSN 00368075. doi: 10.1126/science.1155121.

D. R. Bowling, B. A. Logan, K. Hufkens, D. M. Aubrecht, A. D. Richardson, S. P. Burns, W. R. Anderegg, P. D. Blanken, and D. P. Eiriksson. Limitations to winter and spring photosynthesis of a Rocky Mountain subalpine forest. *Agricultural and Forest Meteorology*, 252:241–255, 2018. ISSN 01681923. doi: 10.1016/j.agrformet.2018.01.025.

R. K. Braghiere, T. Quaife, E. Black, L. He, and J. M. Chen. Underestimation of Global Photosynthesis in Earth System Models Due to Representation of Vegetation Structure. *Global Biogeochemical Cycles*, 33(11):1358–1369, nov 2019. ISSN 19449224. doi: 10.1029/2018GB006135.

L. Breiman. Random Forests. *Machine Learning*, 45(1):5–32, Oct. 2001. ISSN 1573-0565. doi: 10.1023/A:1010933404324.

T. J. Brodribb, J. Powers, H. Cochard, and B. Choat. Hanging by a thread? Forests and drought. *Science (New York, N.Y.)*, 368(6488):261–266, Apr. 2020. ISSN 1095-9203. doi: 10.1126/science.aat7631.

W. Buermann, M. Forkel, M. O'Sullivan, S. Sitch, P. Friedlingstein, V. Haverd, A. K. Jain, E. Kato, M. Kautz, S. Lienert, D. Lombardozzi, J. E. Nabel, H. Tian, A. J. Wiltshire, D. Zhu, W. K. Smith, and A. D. Richardson. Widespread seasonal compensation effects of spring warming on northern plant productivity. *Nature*, 562(7725):110–114, Oct. 2018. ISSN 0028-0836. doi: 10.1038/s41586-018-0555-7.

Z. Butterfield, W. Buermann, and G. Keppel-Aleks. Satellite observations reveal seasonal redistribution of northern ecosystem productivity in response to interannual climate variability. *Remote Sensing of Environment*, 242:111755, June 2020. ISSN 0034-4257. doi: 10.1016/j.rse.2020.111755.

K. Cawse-Nicholson, P. A. Townsend, D. Schimel, A. M. Assiri, P. L. Blake, M. F. Buongiorno, P. Campbell, N. Carmon, K. A. Casey, R. E. Correa-Pabón, K. M. Dahlin, H. Dashti, P. E. Dennison, H. Dierssen, A. Erickson, J. B. Fisher, R. Frouin, C. K. Gatebe, H. Gholizadeh, M. Gierach, N. F. Glenn, J. A. Goodman, D. M. Griffith, L. Guild, C. R. Hakkenberg, E. J. Hochberg, T. R. H. Holmes, C. Hu, G. Hulley, K. F. Huemmrich, R. M. Kudela, R. F. Kokaly, C. M. Lee, R. Martin, C. E. Miller, W. J. Moses, F. E. Muller-Karger, J. D. Ortiz, D. B. Otis, N. Pahlevan, T. H. Painter, R. Pavlick, B. Poulter, Y. Qi, V. J. Realmuto, D. Roberts, M. E. Schaepman, F. D. Schneider, F. M. Schwandner, S. P. Serbin, A. N. Shiklomanov, E. N. Stavros, D. R. Thompson, J. L. Torres-Perez, K. R. Turpie, M. Tzortziou, S. Ustin, Q. Yu, Y. Yusup, and Q. Zhang. NASA's surface biology and geology designated observable: A perspective on surface imaging algorithms. *Remote Sensing of Environment*, 257:112349, May 2021. ISSN 0034-4257. doi: 10.1016/j.rse.2021.112349.

K. Cawse-Nicholson, A. M. Raiho, D. R. Thompson, G. C. Hulley, C. E. Miller, K. R. Miner, B. Poulter, D. Schimel, F. D. Schneider, P. A. Townsend, and S. K. Zareh. Surface Biology and Geology imaging spectrometer: A case study to optimize the mission design using intrinsic dimensionality. *Remote Sensing of Environment*, 290:113534, May 2023. ISSN 0034-4257. doi: 10.1016/j.rse.2023.113534.

C. Y. Chang, L. Guanter, C. Frankenberg, P. Köhler, L. Gu, T. S. Magney, K. Grossmann, and Y. Sun. Systematic assessment of retrieval methods for canopy far-red solar-induced chlorophyll fluorescence using high-frequency automated field spectroscopy.

Journal of Geophysical Research: Biogeosciences, 125, 7 2020. ISSN 21698961. doi: 10.1029/2019JG005533/FORMAT/PDF.

A. Chen, J. Mao, D. Ricciuto, J. Xiao, C. Frankenberg, X. Li, P. E. Thornton, L. Gu, and A. K. Knapp. Moisture availability mediates the relationship between terrestrial gross primary production and solar-induced chlorophyll fluorescence: Insights from global-scale variations. *Global Change Biology*, 27(6):1144–1156, 2021. ISSN 1365-2486. doi: 10.1111/gcb.15373.

J. M. Chen, A. Govind, O. Sonnentag, Y. Zhang, A. Barr, and B. Amiro. Leaf area index measurements at Fluxnet-Canada forest sites. *Agricultural and Forest Meteorology*, 140 (1-4):257–268, 2006. ISSN 01681923. doi: 10.1016/j.agrformet.2006.08.005.

R. Cheng, T. S. Magney, D. Dutta, D. R. Bowling, B. A. Logan, S. P. Burns, P. D. Blanken, K. Grossmann, S. Lopez, A. D. Richardson, J. Stutz, and C. Frankenberg. Decomposing reflectance spectra to track gross primary production in a subalpine evergreen forest. *Biogeosciences*, 17(18):4523–4544, 2020. ISSN 17264189. doi: 10.5194/bg-17-4523-2020.

R. Cheng, T. S. Magney, E. L. Orcutt, Z. Pierrat, P. Köhler, D. R. Bowling, M. S. Bret-Harte, E. S. Euskirchen, M. Jung, H. Kobayashi, A. V. Rocha, O. Sonnentag, J. Stutz, S. Walther, D. Zona, and C. Frankenberg. Evaluating photosynthetic activity across Arctic-Boreal land cover types using solar-induced fluorescence. *Environmental Research Letters*, 17(11):115009, Nov. 2022. ISSN 1748-9326. doi: 10.1088/1748-9326/ac9dae.

H. Chu, X. Luo, Z. Ouyang, W. S. Chan, S. Dengel, S. C. Biraud, M. S. Torn, S. Metzger, J. Kumar, M. A. Arain, T. J. Arkebauer, D. Baldocchi, C. Bernacchi, D. Billesbach, T. A. Black, P. D. Blanken, G. Bohrer, R. Bracho, S. Brown, N. A. Brunsell, J. Chen, X. Chen, K. Clark, A. R. Desai, T. Duman, D. Durden, S. Fares, I. Forbrich, J. A. Gamon, C. M. Gough, T. Griffis, M. Helbig, D. Hollinger, E. Humphreys, H. Ikawa, H. Iwata, Y. Ju, J. F. Knowles, S. H. Knox, H. Kobayashi, T. Kolb, B. Law, X. Lee,

M. Litvak, H. Liu, J. W. Munger, A. Noormets, K. Novick, S. F. Oberbauer, W. Oechel, P. Oikawa, S. A. Papuga, E. Pendall, P. Prajapati, J. Prueger, W. L. Quinton, A. D. Richardson, E. S. Russell, R. L. Scott, G. Starr, R. Staebler, P. C. Stoy, E. Stuart-Haëntjens, O. Sonnentag, R. C. Sullivan, A. Suyker, M. Ueyama, R. Vargas, J. D. Wood, and D. Zona. Representativeness of Eddy-Covariance flux footprints for areas surrounding AmeriFlux sites. *Agricultural and Forest Meteorology*, 301-302:108350, may 2021. ISSN 01681923. doi: 10.1016/j.agrformet.2021.108350.

R. Commane, J. Lindaas, J. Benmergui, K. A. Luus, R. Y. Chang, B. C. Daube, E. S. Euskirchen, J. M. Henderson, A. Karion, J. B. Miller, S. M. Miller, N. C. Parazoo, J. T. Randerson, C. Sweeney, P. Tans, K. Thoning, S. Veraverbeke, C. E. Miller, and S. C. Wofsy. Carbon dioxide sources from Alaska driven by increasing early winter respiration from Arctic tundra. *Proceedings of the National Academy of Sciences of the United States of America*, 114(21):5361–5366, 2017. ISSN 10916490. doi: 10.1073/pnas.1618567114.

A. Damm, L. Guanter, E. Paul-Limoges, C. van der Tol, A. Hueni, N. Buchmann, W. Eugster, C. Ammann, and M. E. Schaepman. Far-red sun-induced chlorophyll fluorescence shows ecosystem-specific relationships to gross primary production: An assessment based on observational and modeling approaches. *Remote Sensing of Environment*, 166:91–105, 2015. ISSN 00344257. doi: 10.1016/j.rse.2015.06.004.

T. De Swaef, V. De Schepper, M. W. Vandegehuchte, and K. Steppe. Stem diameter variations as a versatile research tool in ecophysiology. *Tree Physiology*, 35(10):1047–1061, Oct. 2015. ISSN 17584469. doi: 10.1093/treephys/tpv080.

B. Dechant, Y. Ryu, G. Badgley, Y. Zeng, J. A. Berry, Y. Zhang, Y. Goulas, Z. Li, Q. Zhang, M. Kang, J. Li, and I. Moya. Canopy structure explains the relationship between photosynthesis and sun-induced chlorophyll fluorescence in crops. *Remote Sensing of Environment*, 241, 2020. ISSN 00344257. doi: 10.1016/j.rse.2020.111733.

B. Demmig-Adams and W. W. Adams. Photoprotection and other responses of plants to high light stress. *Annual Review of Plant Physiology and Plant Molecular Biology*, 43(1): 599–626, 1992. ISSN 10402519. doi: 10.1146/annurev.pp.43.060192.003123.

B. Demmig-Adams and W. W. Adams. Photoprotection in an ecological context: the remarkable complexity of thermal energy dissipation. *New Phytologist*, 172(1):11–21, Oct. 2006. ISSN 1469-8137. doi: 10.1111/J.1469-8137.2006.01835.X.

B. Demmig-Adams, V. Ebbert, C. R. Zarter, and W. W. Adams. Characteristics and Species-Dependent Employment of Flexible Versus Sustained Thermal Dissipation and Photoinhibition. In B. Demmig-Adams, W. W. Adams, and A. K. Mattoo, editors, *Photoprotection, Photoinhibition, Gene Regulation, and Environment*, Advances in Photosynthesis and Respiration, pages 39–48. Springer Netherlands, Dordrecht, 2006. ISBN 978-1-4020-3579-1. doi: 10.1007/1-4020-3579-9_4. URL `https://doi.org/10.1007/1-4020-3579-9_4`.

A. R. Desai, A. D. Richardson, A. M. Moffat, J. Kattge, D. Y. Hollinger, A. Barr, E. Falge, A. Noormets, D. Papale, M. Reichstein, and V. J. Stauch. Cross-site evaluation of eddy covariance GPP and RE decomposition techniques. *Agricultural and Forest Meteorology*, 148(6-7):821–838, June 2008. ISSN 01681923. doi: 10.1016/j.agrformet.2007.11.012.

J. Dong, R. K. Kaufmann, R. B. Myneni, C. J. Tucker, P. E. Kauppi, J. Liski, W. Buermann, V. Alexeyev, and M. K. Hughes. Remote sensing estimates of boreal and temperate forest woody biomass: carbon pools, sources, and sinks. *Remote Sensing of Environment*, 84(3): 393–410, Mar. 2003. ISSN 00344257. doi: 10.1016/S0034-4257(02)00130-X.

R. Doughty, P. Köhler, C. Frankenberg, T. S. Magney, X. Xiao, Y. Qin, X. Wu, and B. Moore. TROPOMI reveals dry-season increase of solar-induced chlorophyll fluorescence in the Amazon forest. *Proceedings of the National Academy of Sciences of the United States of America*, 116(44):22393–22398, Oct. 2019. ISSN 0027-8424. doi: 10.1073/pnas.1908157116.

D. M. Drew and G. M. Downes. The use of precision dendrometers in research on daily stem size and wood property variation: A review. *Dendrochronologia*, 27(2):159–172, 2009. ISSN 11257865. doi: 10.1016/j.dendro.2009.06.008.

M. Durand, E. H. Murchie, A. V. Lindfors, O. Urban, P. J. Aphalo, and T. M. Robson. Diffuse solar radiation and canopy photosynthesis in a changing environment. *Agricultural and Forest Meteorology*, 311:108684, Dec. 2021. ISSN 01681923.

J. U. Eitel, K. L. Griffin, N. T. Boelman, A. J. Maguire, A. J. Meddens, J. Jensen, L. A. Vierling, S. C. Schmiege, and J. S. Jennewein. Remote sensing tracks daily radial wood growth of evergreen needleleaf trees. *Global Change Biology*, 26(7):4068–4078, 2020. ISSN 13652486. doi: 10.1111/gcb.15112.

J. U. H. Eitel, P. E. Gessler, A. M. S. Smith, and R. Robberecht. Suitability of existing and novel spectral indices to remotely detect water stress in Populus spp. *Forest Ecology and Management*, 229(1):170–182, July 2006. ISSN 0378-1127. doi: 10.1016/j.foreco.2006.03.027.

L. Eklundh, T. Johansson, and S. Solberg. Mapping insect defoliation in Scots pine with MODIS time-series data. *Remote Sensing of Environment*, 113(7):1566–1573, July 2009. ISSN 0034-4257. doi: 10.1016/j.rse.2009.03.008.

I. Ensminger, D. Sveshnikov, D. A. Campbell, C. Funk, S. Jansson, J. Lloyd, O. Shibistova, and G. Öquist. Intermittent low temperatures constrain spring recovery of photosynthesis in boreal Scots pine forests. *Global Change Biology*, 10(6):995–1008, 2004. ISSN 13541013. doi: 10.1111/j.1365-2486.2004.00781.x.

G. D. Farquhar, S. von Caemmerer, and J. A. Berry. A biochemical model of photosynthetic CO2 assimilation in leaves of C3 species. *Planta*, 149(1):78–90, June 1980. ISSN 1432-2048. doi: 10.1007/BF00386231.

M. R. Felipe-Lucia, S. Soliveres, C. Penone, P. Manning, F. van der Plas, S. Boch, D. Prati, C. Ammer, P. Schall, M. M. Gossner, J. Bauhus, F. Buscot, S. Blaser, N. Blüthgen, A. de Frutos, M. Ehbrecht, K. Frank, K. Goldmann, F. Hänsel, K. Jung, T. Kahl, T. Nauss, Y. Oelmann, R. Pena, A. Polle, S. Renner, M. Schloter, I. Schöning, M. Schrumpf, E.-D. Schulze, E. Solly, E. Sorkau, B. Stempfhuber, M. Tschapka, W. W. Weisser, T. Wubet, M. Fischer, and E. Allan. Multiple forest attributes underpin the supply of multiple ecosystem services. *Nature Communications*, 9(1):4839, Nov. 2018. ISSN 2041-1723. doi: 10.1038/s41467-018-07082-4.

I. Filella, J. Peñuelas, L. Llorens, and M. Estiarte. Reflectance assessment of seasonal and annual changes in biomass and CO2 uptake of a Mediterranean shrubland submitted to experimental warming and drought. *Remote Sensing of Environment*, 90(3):308–318, 2004. ISSN 00344257. doi: 10.1016/j.rse.2004.01.010.

I. Filella, A. Porcar-Castell, S. Munné-Bosch, J. Bäck, M. F. Garbulsky, and J. Peñuelas. PRI assessment of long-term changes in carotenoids/chlorophyll ratio and short-term changes in de-epoxidation state of the xanthophyll cycle. *International Journal of Remote Sensing*, 30(17):4443–4455, 2009. ISSN 13665901. doi: 10.1080/01431160802575661.

J. B. Fisher, D. J. Hayes, C. R. Schwalm, D. N. Huntzinger, E. Stofferahn, K. Schaefer, Y. Luo, S. D. Wullschleger, S. Goetz, C. E. Miller, P. Griffith, S. Chadburn, A. Chatterjee, P. Ciais, T. A. Douglas, H. Genet, A. Ito, C. S. Neigh, B. Poulter, B. M. Rogers, O. Sonnentag, H. Tian, W. Wang, Y. Xue, Z. L. Yang, N. Zeng, and Z. Zhang. Missing pieces to modeling the Arctic-Boreal puzzle. *Environmental Research Letters*, 13(2), 2018. ISSN 17489326. doi: 10.1088/1748-9326/aa9d9a.

C. Frankenberg and J. Berry. Solar induced chlorophyll fluorescence: Origins, relation to photosynthesis and retrieval. *Comprehensive Remote Sensing*, 1-9(1986):143–162, 2017. ISSN 0036-8075. doi: 10.1016/B978-0-12-409548-9.10632-3.

C. Frankenberg, A. Butz, and G. C. Toon. Disentangling chlorophyll fluorescence from atmospheric scattering effects in O2 A-band spectra of reflected sun-light. *Geophysical Research Letters*, 38(3):n/a–n/a, 2011. ISSN 00948276. doi: 10.1029/2010GL045896.

C. Frankenberg, C. O'Dell, J. Berry, L. Guanter, J. Joiner, P. Köhler, R. Pollock, and T. E. Taylor. Prospects for chlorophyll fluorescence remote sensing from the Orbiting Carbon Observatory-2. *Remote Sensing of Environment*, 147:1–12, May 2014. ISSN 00344257. doi: 10.1016/j.rse.2014.02.007.

N. H. F. French, E. S. Kasischke, R. J. Hall, K. A. Murphy, D. L. Verbyla, E. E. Hoy, J. L. Allen, N. H. F. French, E. S. Kasischke, R. J. Hall, K. A. Murphy, D. L. Verbyla, E. E. Hoy, and J. L. Allen. Using Landsat data to assess fire and burn severity in the North American boreal forest region: an overview and summary of results. *International Journal of Wildland Fire*, 17(4):443–462, Aug. 2008. ISSN 1448-5516, 1448-5516. doi: 10.1071/WF08007.

M. Friedl and D. Sulla-Menashe. MCD12Q1 MODIS/Terra+Aqua Land Cover Type Yearly L3 Global 500m SIN Grid V006, 2019. Type: dataset.

P. Friedlingstein, M. Meinshausen, V. K. Arora, C. D. Jones, A. Anav, S. K. Liddicoat, and R. Knutti. Uncertainties in CMIP5 climate projections due to carbon cycle feedbacks. *Journal of Climate*, 27(2):511–526, 2014. ISSN 08948755. doi: 10.1175/JCLI-D-12-00579.1.

P. Friedlingstein, M. W. Jones, M. O'Sullivan, R. M. Andrew, D. C. E. Bakker, J. Hauck, C. Le Quéré, G. P. Peters, W. Peters, J. Pongratz, S. Sitch, J. G. Canadell, P. Ciais, R. B. Jackson, S. R. Alin, P. Anthoni, N. R. Bates, M. Becker, N. Bellouin, L. Bopp, T. T. T. Chau, F. Chevallier, L. P. Chini, M. Cronin, K. I. Currie, B. Decharme, L. M. Djeutchouang, X. Dou, W. Evans, R. A. Feely, L. Feng, T. Gasser, D. Gilfillan, T. Gkritzalis, G. Grassi, L. Gregor, N. Gruber, Ö. Gürses, I. Harris, R. A. Houghton,

G. C. Hurtt, Y. Iida, T. Ilyina, I. T. Luijkx, A. Jain, S. D. Jones, E. Kato, D. Kennedy, K. Klein Goldewijk, J. Knauer, J. I. Korsbakken, A. Körtzinger, P. Landschützer, S. K. Lauvset, N. Lefèvre, S. Lienert, J. Liu, G. Marland, P. C. McGuire, J. R. Melton, D. R. Munro, J. E. M. S. Nabel, S.-I. Nakaoka, Y. Niwa, T. Ono, D. Pierrot, B. Poulter, G. Rehder, L. Resplandy, E. Robertson, C. Rödenbeck, T. M. Rosan, J. Schwinger, C. Schwingshackl, R. Séférian, A. J. Sutton, C. Sweeney, T. Tanhua, P. P. Tans, H. Tian, B. Tilbrook, F. Tubiello, G. R. van der Werf, N. Vuichard, C. Wada, R. Wanninkhof, A. J. Watson, D. Willis, A. J. Wiltshire, W. Yuan, C. Yue, X. Yue, S. Zaehle, and J. Zeng. Global Carbon Budget 2021. *Earth System Science Data*, 14(4):1917–2005, Apr. 2022. ISSN 1866-3508. doi: 10.5194/essd-14-1917-2022.

Z. Fu, P. C. Stoy, Y. Luo, J. Chen, J. Sun, L. Montagnani, G. Wohlfahrt, A. F. Rahman, S. Rambal, C. Bernhofer, J. Wang, G. Shirkey, and S. Niu. Climate controls over the net carbon uptake period and amplitude of net ecosystem production in temperate and boreal ecosystems. *Agricultural and Forest Meteorology*, 243:9–18, 2017. ISSN 01681923. doi: 10.1016/j.agrformet.2017.05.009.

J. A. Gamon. Reviews and Syntheses: optical sampling of the flux tower footprint. *Biogeosciences*, 12(14):4509–4523, July 2015. ISSN 1726-4189. doi: 10.5194/bg-12-4509-2015.

J. A. Gamon and J. A. Berry. Facultative and constitutive pigment effects on the Photochemical Reflectance Index (PRI) in sun and shade conifer needles. *Israel Journal of Plant Sciences*, 60(1-2):85–95, 2012. ISSN 07929978. doi: 10.1560/IJPS.60.1-2.85.

J. A. Gamon, J. Peñuelas, and C. B. Field. A narrow-waveband spectral index that tracks diurnal changes in photosynthetic efficiency. *Remote Sensing of Environment*, 41(1):35–44, 1992. ISSN 00344257. doi: 10.1016/0034-4257(92)90059-S.

J. A. Gamon, L. Serrano, and J. S. Surfus. The photochemical reflectance index: An optical indicator of photosynthetic radiation use efficiency across species, functional types, and nutrient levels. *Oecologia*, 112(4):492–501, 1997. ISSN 00298549. doi: 10.1007/s004420050337.

J. A. Gamon, K. F. Huemmrich, R. S. Stone, and C. E. Tweedie. Spatial and temporal variation in primary productivity (NDVI) of coastal Alaskan tundra: Decreased vegetation growth following earlier snowmelt. *Remote Sensing of Environment*, 129(March 2016): 144–153, 2013. ISSN 00344257. doi: 10.1016/j.rse.2012.10.030.

J. A. Gamon, O. Kovalchuck, C. Y. S. Wong, A. Harris, and S. R. Garrity. Monitoring seasonal and diurnal changes in photosynthetic pigments with automated PRI and NDVI sensors. *Biogeosciences*, 12(13):4149–4159, July 2015. ISSN 1726-4170. doi: 10.5194/bg-12-4149-2015.

J. A. Gamon, K. F. Huemmrich, C. Y. Wong, I. Ensminger, S. Garrity, D. Y. Hollinger, A. Noormets, and J. Peñuelask. A remotely sensed pigment index reveals photosynthetic phenology in evergreen conifers. *Proceedings of the National Academy of Sciences of the United States of America*, 113(46):13087–13092, 2016. ISSN 10916490. doi: 10.1073/pnas.1606162113.

F. Gao, J. Masek, M. Schwaller, and F. Hall. On the blending of the Landsat and MODIS surface reflectance: predicting daily Landsat surface reflectance. *IEEE Transactions on Geoscience and Remote Sensing*, 44(8):2207–2218, Aug. 2006. ISSN 1558-0644. doi: 10.1109/TGRS.2006.872081.

M. F. Garbulsky, J. Peñuelas, D. Papale, J. Ardö, M. L. Goulden, G. Kiely, A. D. Richardson, E. Rotenberg, E. M. Veenendaal, and I. Filella. Patterns and controls of the variability of radiation use efficiency and primary productivity across terrestrial ecosystems. *Global Ecology and Biogeography*, 19(2):253–267, 2010. ISSN 1466822X. doi: 10.1111/j.1466-8238.2009.00504.x.

S. R. Garrity, J. U. Eitel, and L. A. Vierling. Disentangling the relationships between plant pigments and the photochemical reflectance index reveals a new approach for remote estimation of carotenoid content. *Remote Sensing of Environment*, 115(2):628–635, 2011. ISSN 00344257. doi: 10.1016/j.rse.2010.10.007.

J.-P. Gastellu-Etchegorry, N. Lauret, T. Yin, L. Landier, A. Kallel, Z. Malenovský, A. A. Bitar, J. Aval, S. Benhmida, J. Qi, G. Medjdoub, J. Guilleux, E. Chavanon, B. Cook, D. Morton, N. Chrysoulakis, and Z. Mitraka. DART: Recent Advances in Remote Sensing Data Modeling With Atmosphere, Polarization, and Chlorophyll Fluorescence. *IEEE Journal of Selected Topics in Applied Earth Observations and Remote Sensing*, 10(6): 2640–2649, June 2017. ISSN 2151-1535. doi: 10.1109/JSTARS.2017.2685528.

D. Gaumont-Guay, T. A. Black, A. G. Barr, T. J. Griffis, R. S. Jassal, P. Krishnan, N. Grant, and Z. Nesic. Eight years of forest-floor CO2 exchange in a boreal black spruce forest: Spatial integration and long-term temporal trends. *Agricultural and Forest Meteorology*, 184:25–35, 2014. ISSN 01681923. doi: 10.1016/j.agrformet.2013.08.010.

A. Gettelman, A. J. Geer, R. M. Forbes, G. R. Carmichael, G. Feingold, D. J. Posselt, G. L. Stephens, S. C. van den Heever, A. C. Varble, and P. Zuidema. The future of Earth system prediction: Advances in model-data fusion. *Science Advances*, 8(14):eabn3488, Apr. 2022. doi: 10.1126/sciadv.abn3488.

J. Gibbons, B. Gibbons, S. Chakraborti, and G. Gibbons. *Nonparametric Statistical Inference, Fourth Edition: Revised and Expanded*. Statistics: A Series of Textbooks and Monographs. Taylor & Francis, 2003. ISBN 978-0-8247-4052-8.

A. M. Gilmore and M. C. Ball. Protection and storage of chlorophyll in overwintering evergreens. *Proceedings of the National Academy of Sciences*, 97(20):11098–11101, Sept. 2000. doi: 10.1073/pnas.150237697.

A. A. Gitelson and J. A. Gamon. The need for a common basis for defining light-use efficiency: Implications for productivity estimation. *Remote Sensing of Environment*, 156: 196–201, 2015. ISSN 00344257. doi: 10.1016/j.rse.2014.09.017.

T. J. Givnish. Adaptive significance of evergreen vs. deciduous leaves: solving the triple paradox. *Silva Fennica*, 36(3), Dec. 2002.

S. J. Goetz, A. G. Bunn, G. J. Fiske, and R. A. Houghton. Satellite-observed photosynthetic trends across boreal North America associated with climate and fire disturbance. *Proceedings of the National Academy of Sciences*, 102(38):13521–13525, Sept. 2005. doi: 10.1073/pnas.0506179102.

A. Gonsamo, J. M. Chen, D. T. Price, W. A. Kurz, and C. Wu. Land surface phenology from optical satellite measurement and CO2 eddy covariance technique. *Journal of Geophysical Research: Biogeosciences*, 117(G3), 2012. ISSN 2156-2202. doi: 10.1029/2012JG002070.

Government of Canada, Prince Albert Station. Canadian Climate Normals - Climate - Environment and Climate Change Canada, Prince Albert Station, 2019.

K. Grossmann, C. Frankenberg, T. S. Magney, S. C. Hurlock, U. Seibt, and J. Stutz. PhotoSpec: A new instrument to measure spatially distributed red and far-red Solar-Induced Chlorophyll Fluorescence. *Remote Sensing of Environment*, 216(November 2017):311–327, 2018. ISSN 00344257. doi: 10.1016/j.rse.2018.07.002.

L. Gu, D. Baldocchi, S. B. Verma, T. A. Black, T. Vesala, E. M. Falge, and P. R. Dowty. Advantages of diffuse radiation for terrestrial ecosystem productivity. *Journal of Geophysical Research Atmospheres*, 107(5-6):ACL 2–1–ACL 2–23, 2002. ISSN 01480227. doi: 10.1029/2001jd001242.

L. Gu, J. Han, J. D. Wood, C. Y. Chang, and Y. Sun. Sun-induced Chl fluorescence and its importance for biophysical modeling of photosynthesis based on light reactions. *New Phytologist*, 223(3):1179–1191, 2019. ISSN 14698137. doi: 10.1111/nph.15796.

L. Guanter, Y. Zhang, M. Jung, J. Joiner, M. Voigt, J. A. Berry, C. Frankenberg, A. R. Huete, P. Zarco-Tejada, J.-E. Lee, M. S. Moran, G. Ponce-Campos, C. Beer, G. Camps-Valls, N. Buchmann, D. Gianelle, K. Klumpp, A. Cescatti, J. M. Baker, and T. J. Griffis. Global and time-resolved monitoring of crop photosynthesis with chlorophyll fluorescence. *Proceedings of the National Academy of Sciences*, 111(14):E1327–E1333, 2014. ISSN 0027-8424. doi: 10.1073/PNAS.1320008111.

L. He, T. Magney, D. Dutta, Y. Yin, P. Köhler, K. Grossmann, J. Stutz, C. Dold, J. Hatfield, K. Guan, B. Peng, and C. Frankenberg. From the Ground to Space: Using Solar-Induced Chlorophyll Fluorescence to Estimate Crop Productivity. *Geophysical Research Letters*, 47(7):e2020GL087474, apr 2020. ISSN 19448007. doi: 10.1029/2020GL087474.

K. Hikosaka and K. Tsujimoto. Linking remote sensing parameters to CO2 assimilation rates at a leaf scale. *Journal of Plant Research*, 134(4):695–711, July 2021. ISSN 16180860. doi: 10.1007/S10265-021-01313-4/FIGURES/9.

D. Y. Hollinger and A. D. Richardson. Uncertainty in eddy covariance measurements and its application to physiological models. *Tree Physiology*, 25(7):873–885, July 2005. ISSN 0829-318X. doi: 10.1093/treephys/25.7.873.

N. E. Holt, G. R. Fleming, and K. K. Niyogi. Toward an Understanding of the Mechanism of Nonphotochemical Quenching in Green Plants. *Biochemistry*, 43(26):8281–8289, July 2004. ISSN 0006-2960, 1520-4995. doi: 10.1021/bi0494020.

A. R. Holzwarth and P. Jahns. Non-Photochemical Quenching Mechanisms in Intact Organisms as Derived from Ultrafast-Fluorescence Kinetic Studies. volume 40, pages 129–156, Dordrecht, 2014. Springer Netherlands. ISBN 978-94-017-9031-4 978-94-017-9032-1. doi: 10.1007/978-94-017-9032-1_5. Book Title: Non-Photochemical Quenching and Energy Dissipation in Plants, Algae and Cyanobacteria Series Title: Advances in Photosynthesis and Respiration.

N. P. A. Huner, G. Öquist, V. M. Hurry, M. Krol, S. Falk, and M. Griffith. Photosynthesis, photoinhibition and low temperature acclimation in cold tolerant plants. *Photosynthesis Research*, 37(1):19–39, July 1993. ISSN 1573-5079. doi: 10.1007/BF02185436.

T. E. Huxman, A. A. Turnipseed, J. P. Sparks, P. C. Harley, and R. K. Monson. Temperature as a control over ecosystem CO2 fluxes in a high-elevation, subalpine forest. *Oecologia*, 134(4):537–546, Mar. 2003. ISSN 1432-1939. doi: 10.1007/s00442-002-1131-1.

P. Jahns and A. R. Holzwarth. The role of the xanthophyll cycle and of lutein in photoprotection of photosystem II. *Biochimica Et Biophysica Acta*, 1817(1):182–193, Jan. 2012. ISSN 0006-3002. doi: 10.1016/j.bbabio.2011.04.012.

P. G. Jarvis, J. M. Massheder, S. E. Hale, J. B. Moncrieff, M. Rayment, and S. L. Scott. Seasonal variation of carbon dioxide, water vapor, and energy exchanges of a boreal black spruce forest. *Journal of Geophysical Research Atmospheres*, 102(24):28953–28966, 1997. ISSN 01480227. doi: 10.1029/97jd01176.

S. J. Jeong, C. H. Ho, H. J. Gim, and M. E. Brown. Phenology shifts at start vs. end of growing season in temperate vegetation over the Northern Hemisphere for the period 1982-2008. *Global Change Biology*, 17(7):2385–2399, 2011. ISSN 13541013. doi: 10.1111/j.1365-2486.2011.02397.x.

S. J. Jeong, D. Schimel, C. Frankenberg, D. T. Drewry, J. B. Fisher, M. Verma, J. A. Berry, J. E. Lee, and J. Joiner. Application of satellite solar-induced chlorophyll fluorescence to understanding large-scale variations in vegetation phenology and function over northern high latitude forests. *Remote Sensing of Environment*, 190:178–187, 2017. ISSN 00344257. doi: 10.1016/j.rse.2016.11.021.

W. Jiao, Q. Chang, and L. Wang. The Sensitivity of Satellite Solar-Induced Chlorophyll Fluorescence to Meteorological Drought. *Earth's Future*, 7(5):558–573, 2019. ISSN 2328-4277. doi: 10.1029/2018EF001087.

J. E. Johnson and J. A. Berry. The role of Cytochrome b6f in the control of steady-state photosynthesis: a conceptual and quantitative model. *Photosynthesis Research*, 148(3): 101–136, June 2021. ISSN 1573-5079. doi: 10.1007/s11120-021-00840-4.

J. E. Johnson, C. B. Field, and J. A. Berry. The limiting factors and regulatory processes that control the environmental responses of C3, C3–C4 intermediate, and C4 photosynthesis. *Oecologia*, 197(4):841–866, Dec. 2021. ISSN 1432-1939. doi: 10.1007/s00442-021-05062-y.

M. Jung, M. Reichstein, H. A. Margolis, A. Cescatti, A. D. Richardson, M. A. Arain, A. Arneth, C. Bernhofer, D. Bonal, J. Chen, D. Gianelle, N. Gobron, G. Kiely, W. Kutsch, G. Lasslop, B. E. Law, A. Lindroth, L. Merbold, L. Montagnani, E. J. Moors, D. Papale, M. Sottocornola, F. Vaccari, and C. Williams. Global patterns of land-atmosphere fluxes of carbon dioxide, latent heat, and sensible heat derived from eddy covariance, satellite, and meteorological observations. *Journal of Geophysical Research: Biogeosciences*, 116 (G3), 2011. ISSN 2156-2202. doi: 10.1029/2010JG001566.

M. Jung, C. Schwalm, M. Migliavacca, S. Walther, G. Camps-Valls, S. Koirala, P. Anthoni, S. Besnard, P. Bodesheim, N. Carvalhais, F. Chevallier, F. Gans, D. S. Goll, V. Haverd, P. Köhler, K. Ichii, A. K. Jain, J. Liu, D. Lombardozzi, J. E. M. S. Nabel, J. A. Nelson, M. O'Sullivan, M. Pallandt, D. Papale, W. Peters, J. Pongratz, C. Rödenbeck, S. Sitch, G. Tramontana, A. Walker, U. Weber, and M. Reichstein. Scaling carbon fluxes from eddy covariance sites to globe: synthesis and evaluation of the FLUXCOM approach. *Biogeosciences*, 17(5):1343–1365, Mar. 2020. ISSN 1726-4170. doi: 10.5194/bg-17-1343-2020.

M. Kautz, A. J. H. Meddens, R. J. Hall, and A. Arneth. Biotic disturbances in Northern Hemisphere forests – a synthesis of recent data, uncertainties and implications for forest monitoring and modelling. *Global Ecology and Biogeography*, 26(5):533–552, 2017. ISSN 1466-8238. doi: 10.1111/geb.12558.

R. J. Keenan, G. A. Reams, F. Achard, J. V. de Freitas, A. Grainger, and E. Lindquist. Dynamics of global forest area: Results from the FAO Global Forest Resources Assessment

2015. *Forest Ecology and Management*, 352:9–20, Sept. 2015. ISSN 0378-1127. doi: 10.1016/j.foreco.2015.06.014.

T. F. Keenan, J. Gray, M. A. Friedl, M. Toomey, G. Bohrer, D. Y. Hollinger, J. W. Munger, J. O'Keefe, H. P. Schmid, I. S. Wing, B. Yang, and A. D. Richardson. Net carbon uptake has increased through warming-induced changes in temperate forest phenology. *Nature Climate Change*, 4(7):598–604, July 2014. ISSN 1758-6798. doi: 10.1038/nclimate2253.

J. Kim, Y. Ryu, B. Dechant, H. Lee, H. Seok, A. Kornfeld, and J. A. Berry. Remote Sensing of Environment Solar-induced chlorophyll fluorescence is non-linearly related to canopy photosynthesis in a temperate evergreen needleleaf forest during the fall transition. *Remote Sensing of Environment*, 258(August 2020):112362, 2021. ISSN 0034-4257. doi: 10.1016/j.rse.2021.112362.

G. King, P. Fonti, D. Nievergelt, U. Büntgen, and D. Frank. Climatic drivers of hourly to yearly tree radius variations along a 6C natural warming gradient. *Agricultural and Forest Meteorology*, 168:36–46, 2013. ISSN 01681923. doi: 10.1016/j.agrformet.2012.08.002.

M. Köhl, R. Lasco, M. Cifuentes, ö. Jonsson, K. T. Korhonen, P. Mundhenk, J. de Jesus Navar, and G. Stinson. Changes in forest production, biomass and carbon: Results from the 2015 UN FAO Global Forest Resource Assessment. *Forest Ecology and Management*, 352:21–34, Sept. 2015. ISSN 0378-1127. doi: 10.1016/j.foreco.2015.05.036.

P. Köhler, C. Frankenberg, T. S. Magney, L. Guanter, J. Joiner, and J. Landgraf. Global Retrievals of Solar-Induced Chlorophyll Fluorescence With TROPOMI: First Results and Intersensor Comparison to OCO-2. *Geophysical Research Letters*, 45(19):10,456–10,463, 2018. ISSN 19448007. doi: 10.1029/2018GL079031.

T. T. Kozlowski and C. H. Winget. Diurnal and Seasonal Variation in Radii of Tree Stem. *Ecological Society of America*, 45(1):149–155, 1964.

T. T. Kozlowski, C. H. Winget, and J. . H. . Torrie. Daily Radial Growth of Oak in Relation to Maximum and Minimum Temperature. *The University of Chicago Press*, 124(1):9–17, 1962.

G. H. Krause and E. Weis. Chlorophyll fluorescence and photosynthesis: The basics. *Annual Review of Plant Physiology and Plant Molecular Biology*, 42(1):313–349, 1991. ISSN 10402519. doi: 10.1146/annurev.pp.42.060191.001525.

G. Lasslop, M. Reichstein, D. Papale, A. Richardson, A. Arneth, A. Barr, P. Stoy, and G. Wohlfahrt. Separation of net ecosystem exchange into assimilation and respiration using a light response curve approach: Critical issues and global evaluation. *Global Change Biology*, 16(1):187–208, 2010. ISSN 13541013. doi: 10.1111/j.1365-2486.2009.02041.x.

X. Li, J. Xiao, B. He, M. Altaf Arain, J. Beringer, A. R. Desai, C. Emmel, D. Y. Hollinger, A. Krasnova, I. Mammarella, S. M. Noe, P. S. Ortiz, A. C. Rey-Sanchez, A. V. Rocha, and A. Varlagin. Solar-induced chlorophyll fluorescence is strongly correlated with terrestrial photosynthesis for a wide variety of biomes: First global analysis based on OCO-2 and flux tower observations. *Global Change Biology*, 24(9):3990–4008, Sept. 2018. ISSN 13652486. doi: 10.1111/GCB.14297.

J. Liu, P. O. Wennberg, N. C. Parazoo, Y. Yin, and C. Frankenberg. Observational Constraints on the Response of High-Latitude Northern Forests to Warming. *AGU Advances*, 1(4):e2020AV000228, 2020a. ISSN 2576-604X. doi: 10.1029/2020AV000228.

P. Liu, T. A. Black, R. S. Jassal, T. Zha, Z. Nesic, A. G. Barr, W. D. Helgason, X. Jia, Y. Tian, J. J. Stephens, and J. Ma. Divergent long-term trends and interannual variation in ecosystem resource use efficiencies of a southern boreal old black spruce forest 1999–2017. *Global Change Biology*, 25(9):3056–3069, 2019a. ISSN 13652486. doi: 10.1111/gcb.14674.

W. Liu, J. Atherton, M. Mõttus, J.-P. Gastellu-Etchegorry, Z. Malenovský, P. Raumonen, M. Åkerblom, R. Mäkipää, and A. Porcar-Castell. Simulating solar-induced chlorophyll fluorescence in a boreal forest stand reconstructed from terrestrial laser scanning measurements. *Remote Sensing of Environment*, 232:111274, Oct. 2019b. ISSN 0034-4257. doi: 10.1016/j.rse.2019.111274.

X. Liu, L. Liu, J. Hu, J. Guo, and S. Du. Improving the potential of red SIF for estimating GPP by downscaling from the canopy level to the photosystem level. *Agricultural and Forest Meteorology*, 281:107846, Feb. 2020b. ISSN 0168-1923.

B. A. Logan. Oxygen Metabolism and Stress Physiology. In G. Jee, R. R. Wise, and J. K. Hoober, editors, *The Structure and Function of Plastids*, volume 23, pages 539–553. Springer Netherlands, Dordrecht, 2007. ISBN 978-1-4020-4060-3 978-1-4020-4061-0. doi: 10.1007/978-1-4020-4061-0_27. Series Title: Advances in Photosynthesis and Respiration.

B. A. Logan, S. C. Grace, W. W. Adams Iii, and B. Demmig-Adams. Seasonal differences in xanthophyll cycle characteristics and antioxidants in Mahonia repens growing in different light environments. *Oecologia*, 116(1-2):9–17, Aug. 1998. ISSN 1432-1939. doi: 10.1007/PL00013823.

W.-Y. Loh and Y.-S. Shih. Split Selection Methods For Classification Trees. *Statistica Sinica*, 7:815–840, 1997.

K. Loris, W. M. Havranek, and G. Wieser. The Ecological Significance of Thickness Changes in Stem , Branches and Twigs of Pinus cembra L . during Winter. *Phyton-Horn*, 39(4): 117–122, 1999.

X. Lu, Z. Liu, F. Zhao, and J. Tang. Comparison of total emitted solar-induced chlorophyll fluorescence (SIF) and top-of-canopy (TOC) SIF in estimating photosynthesis. *Remote Sensing of Environment*, 251:112083, Dec. 2020. ISSN 0034-4257. doi: 10.1016/j.rse.2020.112083.

K. A. Luus, R. Commane, N. C. Parazoo, J. Benmergui, E. S. Euskirchen, C. Frankenberg, J. Joiner, J. Lindaas, C. E. Miller, W. C. Oechel, D. Zona, S. Wofsy, and J. C.

Lin. Tundra photosynthesis captured by satellite-observed solar-induced chlorophyll fluorescence. *Geophysical Research Letters*, 44(3):1564–1573, 2017. ISSN 19448007. doi: 10.1002/2016GL070842.

S. Luyssaert, I. Inglima, M. Jung, A. D. Richardson, M. Reichstein, D. Papale, S. L. Piao, E. D. Schulze, L. Wingate, G. Matteucci, L. Aragao, M. Aubinet, C. Beer, C. Bernhofer, K. G. Black, D. Bonal, J. M. Bonnefond, J. Chambers, P. Ciais, B. Cook, K. J. Davis, A. J. Dolman, B. Gielen, M. Goulden, J. Grace, A. Granier, A. Grelle, T. Griffis, T. Grünwald, G. Guidolotti, P. J. Hanson, R. Harding, D. Y. Hollinger, L. R. Hutyra, P. Kolari, B. Kruijt, W. Kutsch, F. Lagergren, T. Laurila, B. E. Law, G. Le Maire, A. Lindroth, D. Loustau, Y. Malhi, J. Mateus, M. Migliavacca, L. Misson, L. Montagnani, J. Moncrieff, E. Moors, J. W. Munger, E. Nikinmaa, S. V. Ollinger, G. Pita, C. Rebmann, O. Roupsard, N. Saigusa, M. J. Sanz, G. Seufert, C. Sierra, M. L. Smith, J. Tang, R. Valentini, T. Vesala, and I. A. Janssens. CO2 balance of boreal, temperate, and tropical forests derived from a global database. *Global Change Biology*, 13(12):2509–2537, 2007. ISSN 1365-2486. doi: 10.1111/j.1365-2486.2007.01439.x.

T. S. Magney, D. R. Bowling, B. A. Logan, K. Grossmann, J. Stutz, P. D. Blanken, S. P. Burns, R. Cheng, M. A. Garcia, P. Köhler, S. Lopez, N. C. Parazoo, B. Raczka, D. Schimel, and C. Frankenberg. Mechanistic evidence for tracking the seasonality of photosynthesis with solar-induced fluorescence. *Proceedings of the National Academy of Sciences of the United States of America*, 116(24):11640–11645, 2019a. ISSN 10916490. doi: 10.1073/pnas.1900278116.

T. S. Magney, C. Frankenberg, P. Köhler, G. North, T. S. Davis, C. Dold, D. Dutta, J. B. Fisher, K. Grossmann, A. Harrington, J. Hatfield, J. Stutz, Y. Sun, and A. Porcar-Castell. Disentangling Changes in the Spectral Shape of Chlorophyll Fluorescence: Implications for Remote Sensing of Photosynthesis. *Journal of Geophysical Research: Biogeosciences*, 124(6):1491–1507, 2019b. ISSN 21698961. doi: 10.1029/2019JG005029.

T. S. Magney, M. L. Barnes, and X. Yang. On the Covariation of Chlorophyll Fluorescence and Photosynthesis Across Scales. *Geophysical Research Letters*, 47(23), 2020. ISSN 0094-8276. doi: 10.1029/2020gl091098.

A. Maguire, J. Eitel, T. Magney, C. Frankenberg, P. Köhler, E. Orcutt, N. Parazoo, R. Pavlick, Z. Pierrat, and P. Townsend. Spatial covariation between solar induced fluorescence and vegetation indices from Arctic-Boreal landscapes. *in review at Environmental Research Letters*, 2021.

A. J. Maguire, J. U. Eitel, K. L. Griffin, T. S. Magney, R. A. Long, L. A. Vierling, S. C. Schmiege, J. S. Jennewein, W. A. Weygint, N. T. Boelman, and S. G. Bruner. On the Functional Relationship Between Fluorescence and Photochemical Yields in Complex Evergreen Needleleaf Canopies. *Geophysical Research Letters*, 47(9), 2020. ISSN 19448007. doi: 10.1029/2020GL087858.

J. K. Marrs, J. S. Reblin, B. A. Logan, D. W. Allen, A. B. Reinmann, D. M. Bombard, D. Tabachnik, and L. R. Hutyra. Solar-Induced Fluorescence Does Not Track Photosynthetic Carbon Assimilation Following Induced Stomatal Closure. *Geophysical Research Letters*, 47(15), 2020. ISSN 19448007. doi: 10.1029/2020GL087956.

A. M. Matheny, G. Bohrer, S. R. Garrity, T. H. Morin, C. J. Howard, and C. S. Vogel. Observations of stem water storage in trees of opposing Hydraulic strategies. *Ecosphere*, 6(9):art165, 2015. ISSN 21508925. doi: 10.1890/ES15-00170.1.

MATLAB. *version 9.11.0 (R2021b).* The MathWorks Inc., Natick, Massachusetts, 2021.

K. Maxwell and G. N. Johnson. Chlorophyll fluorescence—a practical guide. *Journal of Experimental Botany*, 51(345):659–668, Apr. 2000. ISSN 0022-0957. doi: 10.1093/jexbot/51.345.659.

S. K. Meerdink, S. J. Hook, D. A. Roberts, and E. A. Abbott. The ECOSTRESS spectral library version 1.0. *Remote Sensing of Environment*, 230:111196, Sept. 2019. ISSN 0034-4257. doi: 10.1016/j.rse.2019.05.015.

P. E. Mellander, M. O. Löfvenius, and H. Laudon. Climate change impact on snow and soil temperature in boreal Scots pine stands. *Climatic Change*, 85(1-2):179–193, 2007. ISSN 01650009. doi: 10.1007/s10584-007-9254-3.

M. Michaelian, E. H. Hogg, R. J. Hall, and E. Arsenault. Massive mortality of aspen following severe drought along the southern edge of the Canadian boreal forest. *Global Change Biology*, 17(6):2084–2094, June 2011. ISSN 1354-1013. doi: 10.1111/j.1365-2486.2010.02357.x.

L. Michaelis and M. L. Menten. Kinetik der Invertinwirkung. *Biochem. z*, 49(333–369):352, 1913. ISSN 03660753.

E. M. Middleton, J. H. Sullivan, B. D. Bovard, A. J. Deluca, S. S. Chan, and T. A. Cannon. Seasonal variability in foliar characteristics and physiology for boreal forest species at the five Saskatchewan tower sites during the 1994 Boreal Ecosystem-Atmosphere Study. *Journal of Geophysical Research Atmospheres*, 102(24):28831–28844, 1997. ISSN 01480227. doi: 10.1029/97jd02560.

K. Mohammadi, Y. Jiang, and G. Wang. Flash drought early warning based on the trajectory of solar-induced chlorophyll fluorescence. *Proceedings of the National Academy of Sciences*, 119(32):e2202767119, Aug. 2022. doi: 10.1073/pnas.2202767119.

G. H. Mohammed, R. Colombo, E. M. Middleton, U. Rascher, C. van der Tol, L. Nedbal, Y. Goulas, O. Pérez-Priego, A. Damm, M. Meroni, J. Joiner, S. Cogliati, W. Verhoef, Z. Malenovský, J.-P. Gastellu-Etchegorry, J. R. Miller, L. Guanter, J. Moreno, I. Moya, J. A. Berry, C. Frankenberg, and P. J. Zarco-Tejada. Remote sensing of solar-induced chlorophyll fluorescence (SIF) in vegetation: 50 years of progress. *Remote Sensing of Environment*, 231:111177, sep 2019. ISSN 0034-4257. doi: 10.1016/J.RSE.2019.04.030.

J. L. Monteith. Solar Radiation and Productivity in Tropical Ecosystems. *The Journal of Applied Ecology*, 9(3):747, 1972. ISSN 00218901. doi: 10.2307/2401901.

J. L. Monteith, C. J. Moss, G. W. Cooke, N. W. Pirie, and G. D. H. Bell. Climate and the efficiency of crop production in Britain. *Philosophical Transactions of the Royal Society of London. B, Biological Sciences*, 281(980):277–294, Jan. 1997. doi: 10.1098/rstb.1977.0140.

E. H. Murchie and K. K. Niyogi. Manipulation of photoprotection to improve plant photosynthesis. *Plant Physiology*, 155(1):86–92, 2011. ISSN 00320889. doi: 10.1104/pp.110.168831.

I. H. Myers-Smith, J. T. Kerby, G. K. Phoenix, J. W. Bjerke, H. E. Epstein, J. J. Assmann, C. John, L. Andreu-Hayles, S. Angers-Blondin, P. S. Beck, L. T. Berner, U. S. Bhatt, A. D. Bjorkman, D. Blok, A. Bryn, C. T. Christiansen, J. H. C. Cornelissen, A. M. Cunliffe, S. C. Elmendorf, B. C. Forbes, S. J. Goetz, R. D. Hollister, R. de Jong, M. M. Loranty, M. Macias-Fauria, K. Maseyk, S. Normand, J. Olofsson, T. C. Parker, F. J. W. Parmentier, E. Post, G. Schaepman-Strub, F. Stordal, P. F. Sullivan, H. J. Thomas, H. Tømmervik, R. Treharne, C. E. Tweedie, D. A. Walker, M. Wilmking, and S. Wipf. Complexity revealed in the greening of the Arctic. *Nature Climate Change*, 10(2):106–117, Feb. 2020. ISSN 1758-678X. doi: 10.1038/s41558-019-0688-1.

R. B. Myneni, J. Dong, C. J. Tucker, R. K. Kaufmann, P. E. Kauppi, J. Liski, L. Zhou, V. Alexeyev, and M. K. Hughes. A large carbon sink in the woody biomass of Northern forests. *Proceedings of the National Academy of Sciences*, 98(26):14784–14789, Dec. 2001. doi: 10.1073/pnas.261555198.

P. Müller, X.-P. Li, and K. K. Niyogi. Non-Photochemical Quenching. A Response to Excess Light Energy. *Plant Physiology*, 125(4):1558–1566, Apr. 2001. ISSN 0032-0889. doi: 10.1104/pp.125.4.1558.

National Ecological Observatory Network (NEON). Bundled data products - eddy covariance (dp4.00200.001), 2022a. URL `https://data.neonscience.org/data-products/DP4.00200.001/RELEASE-2022`.

National Ecological Observatory Network (NEON). Relative humidity (dp1.00098.001), 2022b. URL `https://data.neonscience.org/data-products/DP1.00098.001/RELEASE-2022`.

National Ecological Observatory Network (NEON). Soil temperature (dp1.00041.001), 2022c. URL `https://data.neonscience.org/data-products/DP1.00041.001/RELEASE-2022`.

National Ecological Observatory Network (NEON). Soil water content and water salinity (dp1.00094.001), 2022d. URL `https://data.neonscience.org/data-products/DP1.00094.001/RELEASE-2022`.

M. F. Nehemy, J. Maillet, N. Perron, C. Pappas, O. Sonnentag, J. L. Baltzer, C. P. Laroque, and J. J. McDonnell. Snowmelt Water Use at Transpiration Onset: Phenology, Isotope Tracing, and Tree Water Transit Time. *Water Resources Research*, 58(9), Sept. 2022. ISSN 0043-1397, 1944-7973. doi: 10.1029/2022WR032344.

M. F. Nehemy, Z. Pierrat, J. Maillet, A. D. Richardson, J. Stutz, B. Johnson, W. Helgason, A. G. Barr, C. P. Laroque, and J. J. McDonnell. Phenological assessment of transpiration: The stem-temp approach for determining start and end of season. *Agricultural and Forest Meteorology*, 331:109319, Mar. 2023. ISSN 0168-1923. doi: 10.1016/j.agrformet.2023.109319.

P. R. Nelson, A. J. Maguire, Z. Pierrat, E. L. Orcutt, D. Yang, S. Serbin, G. V. Frost, M. J. Macander, T. S. Magney, D. R. Thompson, J. A. Wang, S. F. Oberbauer, S. V. Zesati, S. J. Davidson, H. E. Epstein, S. Unger, P. K. E. Campbell, N. Carmon, M. Velez-Reyes, and K. F. Huemmrich. Remote Sensing of Tundra Ecosystems Using High Spectral Resolution Reflectance: Opportunities and Challenges. *Journal of Geophysical Research: Biogeosciences*, 127(2), Feb. 2022. ISSN 2169-8953. doi: 10.1029/2021JG006697.

K. K. Niyogi. PHOTOPROTECTION REVISITED: Genetic and Molecular Approaches. *Annual Review of Plant Physiology and Plant Molecular Biology*, 50(1):333–359, 1999. doi: 10.1146/annurev.arplant.50.1.333.

K. K. Niyogi, A. R. Grossman, and O. Björkman. Arabidopsis mutants define a central role for the xanthophyll cycle in the regulation of photosynthetic energy conversion. *The Plant Cell*, 10(7):1121–1134, July 1998. ISSN 1040-4651. doi: 10.1105/tpc.10.7.1121.

S. Oh, W. Adams, B. Demmig-Adams, and S. Koh. Seasonal photoprotective responses in needles of Korean fir (abies Koreana) over an altitudinal gradient on Mount Halla, Jeju Island, Korea. *Arctic, Antarctic, and Alpine Research*, 2013. ISSN 15230430. doi: 10.1657/1938-4246-45.2.238.

G. Öquist and N. P. Huner. Photosynthesis of Overwintering Evergreen Plants. *Annual Review of Plant Biology*, 54:329–355, 2003. ISSN 15435008. doi: 10.1146/annurev.arplant.54.072402.115741.

C. Ottander, D. Campbell, and G. Öquist. Seasonal changes in photosystem II organisation and pigment composition in Pinus sylvestris. *Planta*, 1995. ISSN 00320935. doi: 10.1007/BF00239954.

D. Papale, M. Reichstein, M. Aubinet, E. Canfora, C. Bernhofer, W. Kutsch, B. Longdoz, S. Rambal, R. Valentini, T. Vesala, and D. Yakir. Towards a standardized processing of Net Ecosystem Exchange measured with eddy covariance technique: algorithms and uncertainty estimation. *Biogeosciences*, 3(4):571–583, Nov. 2006. ISSN 1726-4170. doi: 10.5194/bg-3-571-2006.

C. Pappas, A. M. Matheny, J. L. Baltzer, A. G. Barr, T. A. Black, G. Bohrer, M. Detto, J. Maillet, A. Roy, O. Sonnentag, and J. Stephens. Boreal tree hydrodynamics: Asynchronous, diverging, yet complementary. *Tree Physiology*, 38(7):953–964, 2018. ISSN 17584469. doi: 10.1093/treephys/tpy043.

C. Pappas, J. Maillet, S. Rakowski, J. L. Baltzer, A. G. Barr, T. A. Black, S. Fatichi, C. P. Laroque, A. M. Matheny, A. Roy, O. Sonnentag, and T. Zha. Aboveground tree growth is a minor and decoupled fraction of boreal forest carbon input. *Agricultural and Forest Meteorology*, 290(December 2019):108030, 2020a. ISSN 01681923. doi: 10.1016/j.agrformet.2020.108030.

C. Pappas, R. L. Peters, and P. Fonti. Linking variability of tree water use and growth with species resilience to environmental changes. *Ecography*, 43(9):1386–1399, 2020b. ISSN 16000587. doi: 10.1111/ecog.04968.

N. C. Parazoo, A. Arneth, T. A. Pugh, B. Smith, N. Steiner, K. Luus, R. Commane, J. Benmergui, E. Stofferahn, J. Liu, C. Rödenbeck, R. Kawa, E. Euskirchen, D. Zona, K. Arndt, W. Oechel, and C. Miller. Spring photosynthetic onset and net CO2 uptake in Alaska triggered by landscape thawing. *Global Change Biology*, 24(8):3416–3435, 2018. ISSN 13652486. doi: 10.1111/gcb.14283.

N. C. Parazoo, C. Frankenberg, P. Köhler, J. Joiner, Y. Yoshida, T. Magney, Y. Sun, and V. Yadav. Towards a Harmonized Long-Term Spaceborne Record of Far-Red Solar-Induced Fluorescence. *Journal of Geophysical Research: Biogeosciences*, 124(8):2518–2539, 2019. ISSN 21698961. doi: 10.1029/2019JG005289.

N. C. Parazoo, T. Magney, A. Norton, B. Raczka, C. Bacour, F. Maignan, I. Baker, Y. Zhang, B. Qiu, M. Shi, N. MacBean, D. R. Bowling, S. P. Burns, P. D. Blanken, J. Stutz, K. Grossmann, and C. Frankenberg. Wide discrepancies in the magnitude and direction of modeled solar-induced chlorophyll fluorescence in response to light conditions. *Biogeosciences*, 17 (13):3733–3755, 2020. ISSN 1726-4189. doi: 10.5194/bg-17-3733-2020.

R. Pearce. Plant Freezing and Damage. *Annals of Botany*, 87:417–424, 2001. doi: 10.1006/anbo.2000.1352.

S. Peng, P. Ciais, F. Chevallier, P. Peylin, P. Cadule, S. Sitch, S. Piao, A. Ahlström, C. Huntingford, P. Levy, X. Li, Y. Liu, M. Lomas, B. Poulter, N. Viovy, T. Wang, and X. Wang. Global Biogeochemical Cycles simulated by terrestrial ecosystem models. *Global Biogeochemical Cycles*, 29:46–64, 2014. doi: 10.1002/2014GB004931.Received.

M. Perämäki, E. Nikinmaa, S. Sevanto, H. Ilvesniemi, E. Siivola, P. Hari, and T. Vesala. Tree stem diameter variations and transpiration in Scots pine: an analysis using a dynamic sap flow model. *Tree Physiology*, 21(12-13):889–897, Aug. 2001. ISSN 0829-318X. doi: 10.1093/treephys/21.12-13.889.

S. Piao, X. Wang, P. Ciais, B. Zhu, T. Wang, and J. Liu. Changes in satellite-derived vegetation growth trend in temperate and boreal Eurasia from 1982 to 2006. *Global Change Biology*, 17(10):3228–3239, oct 2011. ISSN 13541013. doi: 10.1111/j.1365-2486.2011.02419.x.

Z. Pierrat, M. F. Nehemy, A. Roy, T. Magney, N. C. Parazoo, C. Laroque, C. Pappas, O. Sonnentag, K. Grossmann, D. R. Bowling, U. Seibt, A. Ramirez, B. Johnson, W. Helgason, A. Barr, and J. Stutz. Tower-Based Remote Sensing Reveals Mechanisms Behind a Two-phased Spring Transition in a Mixed-Species Boreal Forest. *Journal of Geophysical Research: Biogeosciences*, 126(5):e2020JG006191, 2021a. ISSN 2169-8961. doi: 10.1029/2020JG006191.

Z. Pierrat, A. J. Norton, L. Baskin Monk, N. Parazoo, A. Maguire, K. Grossmann, T. Magney, A. Barr, and J. Stutz. Radiative transfer and viewing geometry considerations for remote sensing as a proxy for carbon uptake in boreal ecosystems. *ESS Open Archive*, 2021b. doi: https://doi.org/10.1002/essoar.10509278.1.

Z. Pierrat, T. Magney, N. C. Parazoo, K. Grossmann, D. R. Bowling, U. Seibt, B. Johnson, W. Helgason, A. Barr, J. Bortnik, A. Norton, A. Maguire, C. Frankenberg, and J. Stutz. Diurnal and Seasonal Dynamics of Solar-Induced Chlorophyll Fluorescence, Vegetation

Indices, and Gross Primary Productivity in the Boreal Forest. *Journal of Geophysical Research: Biogeosciences*, 127(2):e2021JG006588, 2022a. ISSN 2169-8961. doi: 10.1029/2021JG006588.

Z. A. Pierrat, J. Bortnik, B. Johnson, A. Barr, T. Magney, D. R. Bowling, N. Parazoo, C. Frankenberg, U. Seibt, and J. Stutz. Forests for forests: combining vegetation indices with solar-induced chlorophyll fluorescence in random forest models improves gross primary productivity prediction in the boreal forest. *Environmental Research Letters*, 17(12): 125006, Dec. 2022b. ISSN 1748-9326. doi: 10.1088/1748-9326/aca5a0.

A. Porcar-Castell. A high-resolution portrait of the annual dynamics of photochemical and non-photochemical quenching in needles of Pinus sylvestris. *Physiologia Plantarum*, 143 (2):139–153, 2011. ISSN 00319317. doi: 10.1111/j.1399-3054.2011.01488.x.

A. Porcar-Castell, E. Juurola, E. Nikinmaa, F. Berninger, I. Ensminger, and P. Hari. Seasonal acclimation of photosystem II in Pinus sylvestris. I. Estimating the rate constants of sustained thermal energy dissipation and photochemistry. *Tree Physiology*, 28(10):1475–1482, 2008. ISSN 0829318X. doi: 10.1093/treephys/28.10.1475.

A. Porcar-Castell, J. I. Garcia-Plazaola, C. J. Nichol, P. Kolari, B. Olascoaga, N. Kuusinen, B. Fernández-Marín, M. Pulkkinen, E. Juurola, and E. Nikinmaa. Physiology of the seasonal relationship between the photochemical reflectance index and photosynthetic light use efficiency. *Oecologia*, 170(2):313–323, 2012. ISSN 00298549. doi: 10.1007/s00442-012-2317-9.

A. Porcar-Castell, E. Tyystjärvi, J. Atherton, C. Van Der Tol, J. Flexas, E. E. Pfündel, J. Moreno, C. Frankenberg, and J. A. Berry. Linking chlorophyll a fluorescence to photosynthesis for remote sensing applications: Mechanisms and challenges. *Journal of Experimental Botany*, 65(15):4065–4095, 2014. ISSN 14602431. doi: 10.1093/jxb/eru191.

A. Porcar-Castell, Z. Malenovský, T. Magney, S. Van Wittenberghe, B. Fernández-Marín,

F. Maignan, Y. Zhang, K. Maseyk, J. Atherton, L. P. Albert, T. M. Robson, F. Zhao, J.-I. Garcia-Plazaola, I. Ensminger, P. A. Rajewicz, S. Grebe, M. Tikkanen, J. R. Kellner, J. A. Ihalainen, U. Rascher, and B. Logan. Chlorophyll a fluorescence illuminates a path connecting plant molecular biology to Earth-system science. *Nature Plants*, 7(8):998–1009, 2021. ISSN 2055-0278. doi: 10.1038/s41477-021-00980-4.

B. Poulter, B. Currey, L. Calle, A. N. Shiklomanov, C. H. Amaral, E. N. J. Brookshire, P. Campbell, A. Chlus, K. Cawse-Nicholson, F. Huemmrich, C. E. Miller, K. Miner, Z. Pierrat, A. M. Raiho, D. Schimel, S. Serbin, W. K. Smith, N. Stavros, J. Stutz, P. Townsend, D. R. Thompson, and Z. Zhang. Simulating Global Dynamic Surface Reflectances for Imaging Spectroscopy Spaceborne Missions: LPJ-PROSAIL. *Journal of Geophysical Research: Biogeosciences*, 128(1): e2022JG006935, 2023. ISSN 2169-8961. doi: 10.1029/2022JG006935. _eprint: https://onlinelibrary.wiley.com/doi/pdf/10.1029/2022JG006935.

B. Raczka, A. Porcar-Castell, T. Magney, J. E. Lee, P. Köhler, C. Frankenberg, K. Grossmann, B. A. Logan, J. Stutz, P. D. Blanken, S. P. Burns, H. Duarte, X. Yang, J. C. Lin, and D. R. Bowling. Sustained Nonphotochemical Quenching Shapes the Seasonal Pattern of Solar-Induced Fluorescence at a High-Elevation Evergreen Forest. *Journal of Geophysical Research: Biogeosciences*, 124(7):2005–2020, 2019. ISSN 21698961. doi: 10.1029/2018JG004883.

P. B. Reich. The world-wide 'fast-slow' plant economics spectrum: A traits manifesto. *Journal of Ecology*, 102(2):275–301, 2014. ISSN 00220477. doi: 10.1111/1365-2745.12211.

M. Reichstein, E. Falge, D. Baldocchi, D. Papale, M. Aubinet, P. Berbigier, C. Bernhofer, N. Buchmann, T. Gilmanov, A. Granier, T. Grünwald, K. Havránková, H. Ilvesniemi, D. Janous, A. Knohl, T. Laurila, A. Lohila, D. Loustau, G. Matteucci, T. Meyers, F. Miglietta, J.-M. Ourcival, J. Pumpanen, S. Rambal, E. Rotenberg, M. Sanz, J. Tenhunen, G. Seufert, F. Vaccari, T. Vesala, D. Yakir, and R. Valentini. On the separation of net ecosystem exchange into assimilation and ecosystem respiration: review and improved algorithm. *Global Change Biology*, 11(9):1424–1439, 2005. ISSN 1365-2486. doi: 10.1111/j.1365-2486.2005.001002.x.

A. D. Richardson. Tracking seasonal rhythms of plants in diverse ecosystems with digital camera imagery. *New Phytologist*, 222(4):1742–1750, 2019. ISSN 1469-8137. doi: 10.1111/nph.15591.

A. D. Richardson, T. A. Black, P. Ciais, N. Delbart, M. A. Friedl, N. Gobron, D. Y. Hollinger, W. L. Kutsch, B. Longdoz, S. Luyssaert, M. Migliavacca, L. Montagnani, J. W. Munger, E. Moors, S. Piao, C. Rebmann, M. Reichstein, N. Saigusa, E. Tomelleri, R. Vargas, and A. Varlagin. Influence of spring and autumn phenological transitions on forest ecosystem productivity. *Philosophical Transactions of the Royal Society B: Biological Sciences*, 365 (1555):3227–3246, 2010. ISSN 14712970. doi: 10.1098/rstb.2010.0102.

A. D. Richardson, R. S. Anderson, M. A. Arain, A. G. Barr, G. Bohrer, G. Chen, J. M. Chen, P. Ciais, K. J. Davis, A. R. Desai, M. C. Dietze, D. Dragoni, S. R. Garrity, C. M. Gough, R. Grant, D. Y. Hollinger, H. A. Margolis, H. Mccaughey, M. Migliavacca, R. K. Monson, J. W. Munger, B. Poulter, B. M. Raczka, D. M. Ricciuto, A. K. Sahoo, K. Schaefer, H. Tian, R. Vargas, H. Verbeeck, J. Xiao, and Y. Xue. Terrestrial biosphere models need better representation of vegetation phenology: Results from the North American Carbon Program Site Synthesis. *Global Change Biology*, 18(2):566–584, 2012. ISSN 13541013. doi: 10.1111/j.1365-2486.2011.02562.x.

A. D. Richardson, K. Hufkens, T. Milliman, D. M. Aubrecht, M. E. Furze, B. Seyednasrollah, M. B. Krassovski, J. M. Latimer, W. R. Nettles, R. R. Heiderman, J. M. Warren, and P. J. Hanson. Ecosystem warming extends vegetation activity but heightens vulnerability to cold temperatures. *Nature*, 560(7718):368–371, 2018. ISSN 14764687. doi: 10.1038/s41586-018-0399-1.

A. Roy, P. Toose, A. Mavrovic, C. Pappas, A. Royer, C. Derksen, A. Berg, T. Rowlandson, M. El-Amine, A. Barr, A. Black, A. Langlois, and O. Sonnentag. L-Band response to freeze/thaw in a boreal forest stand from ground- and tower-based radiometer observations. *Remote Sensing of Environment*, 237(September 2019):111542, 2020. ISSN 00344257. doi: 10.1016/j.rse.2019.111542.

K. Schaefer, H. Lantuit, V. E. Romanovsky, E. A. Schuur, and R. Witt. The impact of the permafrost carbon feedback on global climate. *Environmental Research Letters*, 9(8), 2014. ISSN 17489326. doi: 10.1088/1748-9326/9/8/085003.

D. Schimel, R. Pavlick, J. B. Fisher, G. P. Asner, S. Saatchi, P. Townsend, C. Miller, C. Frankenberg, K. Hibbard, and P. Cox. Observing terrestrial ecosystems and the carbon cycle from space. *Global Change Biology*, 21(5):1762–1776, 2015. ISSN 1365-2486. doi: 10.1111/gcb.12822.

D. Schimel, F. D. Schneider, and JPL Carbon and Ecosystem Participants. Flux towers in the sky: global ecology from space. *New Phytologist*, 224(2):570–584, 2019. ISSN 1469-8137. doi: 10.1111/nph.15934.

F. Schneider, A. Ferraz, and D. Schimel. Watching earth's interconnected systems at work. *Eos*, 100, 2019.

U. Schreiber. Pulse-Amplitude-Modulation (PAM) Fluorometry and Saturation Pulse Method: An Overview. In G. C. Papageorgiou and Govindjee, editors, *Chlorophyll a Fluorescence: A Signature of Photosynthesis*, Advances in Photosynthesis and Respiration, pages 279–319. Springer Netherlands, Dordrecht, 2004. ISBN 978-1-4020-3218-9. doi: 10.1007/978-1-4020-3218-9_11.

R. Seidl, D. Thom, M. Kautz, D. Martin-Benito, M. Peltoniemi, G. Vacchiano, J. Wild, D. Ascoli, M. Petr, J. Honkaniemi, M. J. Lexer, V. Trotsiuk, P. Mairota, M. Svoboda,

M. Fabrika, T. A. Nagel, and C. P. O. Reyer. Forest disturbances under climate change. *Nature Climate Change*, 7:395–402, June 2017. ISSN 1758-678X. doi: 10.1038/nclimate3303.

S. Sevanto, T. Suni, J. Pumpanen, T. Grönholm, P. Kolari, E. Nikinmaa, P. Hari, and T. Vesala. Wintertime photosynthesis and water uptake in a boreal forest. *Tree Physiology*, 26(6):749–757, 2006. ISSN 0829-318X. doi: 10.1093/treephys/26.6.749.

B. Seyednasrollah, D. R. Bowling, R. Cheng, B. A. Logan, T. S. Magney, C. Frankenberg, J. C. Yang, A. M. Young, K. Hufkens, M. A. Arain, T. A. Black, P. D. Blanken, R. Bracho, R. Jassal, D. Y. Hollinger, B. E. Law, Z. Nesic, and A. D. Richardson. Seasonal variation in the canopy color of temperate evergreen conifer forests. *New Phytologist*, 2020. ISSN 0028-646X. doi: 10.1111/nph.17046.

Q. Shen, L. Liu, W. Zhao, J. Yang, X. Han, F. Tian, and J. Wu. Relationship of surface soil moisture with solar-induced chlorophyll fluorescence and normalized difference vegetation index in different phenological stages: a case study of Northeast China. *Environmental Research Letters*, 16(2):024039, Feb. 2021. ISSN 1748-9326. doi: 10.1088/1748-9326/abd2f1.

D. A. Sims, H. Luo, S. Hastings, W. C. Oechel, A. F. Rahman, and J. A. Gamon. Parallel adjustments in vegetation greenness and ecosystem CO2 exchange in response to drought in a Southern California chaparral ecosystem. *Remote Sensing of Environment*, 103(3):289–303, 2006a. ISSN 00344257. doi: 10.1016/j.rse.2005.01.020.

D. A. Sims, A. F. Rahman, V. D. Cordova, B. Z. El-Masri, D. D. Baldocchi, L. B. Flanagan, A. H. Goldstein, D. Y. Hollinger, L. Misson, R. K. Monson, W. C. Oechel, H. P. Schmid, S. C. Wofsy, and L. Xu. On the use of MODIS EVI to assess gross primary productivity of North American ecosystems. *Journal of Geophysical Research: Biogeosciences*, 111(4), 2006b. ISSN 01480227. doi: 10.1029/2006JG000162.

W. B. Smith, P. D. Miles, C. H. Perry, and S. A. Pugh. Forest resources of the United States, 2007: a technical document supporting the forest service 2010 RPA Assessment. *General Technical Report - USDA Forest Service*, (No.WO-78), 2009.

W. K. Smith, A. M. Fox, N. MacBean, D. J. P. Moore, and N. C. Parazoo. Constraining estimates of terrestrial carbon uptake: new opportunities using long-term satellite observations and data assimilation. *New Phytologist*, 225(1):105–112, 2020. ISSN 1469-8137. doi: 10.1111/nph.16055.

S. Solomon, G.-K. Plattner, R. Knutti, and P. Friedlingstein. Irreversible climate change due to carbon dioxide emissions. *Proceedings of the National Academy of Sciences*, 106 (6):1704–1709, Feb. 2009. doi: 10.1073/pnas.0812721106.

J. S. Sperry and J. E. M. Sullivan. Xylem Embolism in Response to Freeze-Thaw Cycles and Water Stress in Ring-Porous, Diffuse-Porous, and Conifer Species 1. *Plant Physiology*, 100 (2):605–613, Oct. 1992. ISSN 0032-0889.

K. R. Springer, R. Wang, and J. A. Gamon. Parallel seasonal patterns of photosynthesis, fluorescence, and reflectance indices in boreal trees. *Remote Sensing*, 9(7), 2017. ISSN 20724292. doi: 10.3390/rs9070691.

G. Starr and S. F. Oberbauer. PHOTOSYNTHESIS OF ARCTIC EVERGREENS UNDER SNOW: IMPLICATIONS FOR TUNDRA ECOSYSTEM CARBON BALANCE. *Ecology*, 84(6):1415–1420, June 2003. ISSN 1939-9170. doi: 10.1890/02-3154.

K. Steppe, D. J. W. De Pauw, R. Lemeur, and P. a. Vanrolleghem. A mathematical model linking tree sap flow dynamics to daily stem diameter fluctuations and radial stem growth. *Tree physiology*, 26(3):257–273, 2006. ISSN 0829-318X. doi: 10.1093/treephys/26.3.257.

S. G. Stettz, N. C. Parazoo, A. A. Bloom, P. D. Blanken, D. R. Bowling, S. P. Burns, C. Bacour, F. Maignan, B. Raczka, A. J. Norton, I. Baker, M. Williams, M. Shi, Y. Zhang, and B. Qiu. Resolving temperature limitation on spring productivity in an evergreen conifer forest using a model-data fusion framework. *Biogeosciences*, 19(2):541–558, Jan. 2022. ISSN 17264189. doi: 10.5194/BG-19-541-2022.

E. Stofferahn, J. B. Fisher, D. J. Hayes, C. R. Schwalm, D. N. Huntzinger, W. Hantson, B. Poulter, and Z. Zhang. The Arctic-Boreal vulnerability experiment model benchmarking system. *Environmental Research Letters*, 14(5):055002, May 2019. ISSN 1748-9326. doi: 10.1088/1748-9326/ab10fa.

C. D. Stylinski, J. A. Gamon, and W. C. Oechel. Seasonal patterns of reflectance indices, carotenoid pigments and photosynthesis of evergreen chaparral species. *Oecologia*, 131(3): 366–374, 2002. ISSN 00298549. doi: 10.1007/s00442-002-0905-9.

Y. Sun, C. Frankenberg, J. D. Wood, D. S. Schimel, M. Jung, L. Guanter, D. T. Drewry, M. Verma, A. Porcar-Castell, T. J. Griffis, L. Gu, T. S. Magney, P. Köhler, B. Evans, and K. Yuen. OCO-2 advances photosynthesis observation from space via solar-induced chlorophyll fluorescence. *Science*, 358(6360), 2017. ISSN 10959203. doi: 10.1126/science.aam5747.

Y. Sun, C. Frankenberg, M. Jung, J. Joiner, L. Guanter, P. Köhler, and T. Magney. Overview of Solar-Induced chlorophyll Fluorescence (SIF) from the Orbiting Carbon Observatory-2: Retrieval, cross-mission comparison, and global monitoring for GPP. *Remote Sensing of Environment*, 209(February):808–823, 2018. ISSN 00344257. doi: 10.1016/j.rse.2018.02.016.

S. Tanja, F. Berninger, T. Vesala, T. Markkanen, P. Hari, A. Mäkelä, H. Ilvesniemi, H. Hänninen, E. Nikinmaa, T. Huttula, T. Laurila, M. Aurela, A. Grelle, A. Lindroth, A. Arneth, O. Shibistova, and J. Lloyd. Air temperature triggers the recovery of evergreen boreal forest photosynthesis in spring. *Global Change Biology*, 9(10):1410–1426, 2003. ISSN 13541013. doi: 10.1046/j.1365-2486.2003.00597.x.

J. Tardif, M. Flannigan, and Y. Bergeron. An analysis of the daily radial activity of 7 boreal tree species, northwestern quebec. *Environmental Monitoring and Assessment*, 67: 141–160, 2001.

M. Thurner, C. Beer, M. Santoro, N. Carvalhais, T. Wutzler, D. Schepaschenko, A. Shvidenko, E. Kompter, B. Ahrens, S. R. Levick, and C. Schmullius. Carbon stock and density of northern boreal and temperate forests. *Global Ecology and Biogeography*, 23(3):297–310, 2014. ISSN 1466822X. doi: 10.1111/geb.12125.

M. W. Trahan and B. A. Schubert. Temperature-induced water stress in high-latitude forests in response to natural and anthropogenic warming. *Global Change Biology*, 22(2):782–791, feb 2016. ISSN 13652486. doi: 10.1111/gcb.13121.

G. Tramontana, K. Ichii, G. Camps-Valls, E. Tomelleri, and D. Papale. Uncertainty analysis of gross primary production upscaling using Random Forests, remote sensing and eddy covariance data. *Remote Sensing of Environment*, 168:360–373, Oct. 2015. ISSN 0034-4257. doi: 10.1016/j.rse.2015.07.015.

G. Tramontana, M. Migliavacca, M. Jung, M. Reichstein, T. F. Keenan, G. Camps-Valls, J. Ogee, J. Verrelst, and D. Papale. Partitioning net carbon dioxide fluxes into photosynthesis and respiration using neural networks. *Global Change Biology*, 26(9):5235–5253, 2020. ISSN 1365-2486. doi: 10.1111/gcb.15203.

A. T. Trugman, L. D. L. Anderegg, W. R. L. Anderegg, A. J. Das, and N. L. Stephenson. Why is Tree Drought Mortality so Hard to Predict? *Trends in Ecology & Evolution*, 36 (6):520–532, June 2021. ISSN 1872-8383. doi: 10.1016/j.tree.2021.02.001.

C. J. Tucker. Red and photographic infrared linear combinations for monitoring vegetation. *Remote Sensing of Environment*, 8(2):127–150, 1979. ISSN 00344257. doi: 10.1016/0034-4257(79)90013-0.

A. Turcotte, H. Morin, C. Krause, A. Deslauriers, and M. Thibeault-Martel. The timing of spring rehydration and its relation with the onset of wood formation in black spruce.

Agricultural and Forest Meteorology, 149(9):1403–1409, 2009. ISSN 01681923. doi: 10.1016/j.agrformet.2009.03.010.

S. L. Ustin, A. Gitelson, S. Jacquemoud, M. Schaepman, G. P. Asner, J. A. Gamon, and P. Zarco-Tejada. Retrieval of foliar information about plant pigment systems from high resolution spectroscopy. *Remote Sensing of Environment*, 113:S67–S77, Sept. 2009. ISSN 00344257. doi: 10.1016/j.rse.2008.10.019.

C. van der Tol, W. Verhoef, and A. Rosema. A model for chlorophyll fluorescence and photosynthesis at leaf scale. *Agricultural and Forest Meteorology*, 149(1):96–105, jan 2009. ISSN 01681923. doi: 10.1016/j.agrformet.2008.07.007.

C. Van Der Tol, J. A. Berry, P. K. Campbell, and U. Rascher. Models of fluorescence and photosynthesis for interpreting measurements of solar-induced chlorophyll fluorescence. *Journal of Geophysical Research: Biogeosciences*, 119(12):2312–2327, dec 2014. ISSN 21698961. doi: 10.1002/2014JG002713.

C. van der Tol, M. Rossini, S. Cogliati, W. Verhoef, R. Colombo, U. Rascher, and G. Mohammed. A model and measurement comparison of diurnal cycles of sun-induced chlorophyll fluorescence of crops. *Remote Sensing of Environment*, 186:663–677, dec 2016. ISSN 00344257. doi: 10.1016/j.rse.2016.09.021.

A. Verhoeven. Sustained energy dissipation in winter evergreens, 2014. ISSN 0028646X.

A. Walter-McNeill, M. A. Garcia, B. A. Logan, D. M. Bombard, J. S. Reblin, S. Lopez, C. D. Southwick, E. L. Sparrow, and D. R. Bowling. Wide variation of winter-induced sustained thermal energy dissipation in conifers: a common-garden study. *Oecologia 2021 197:3*, 197(3):589–598, Sept. 2021. ISSN 1432-1939. doi: 10.1007/S00442-021-05038-Y.

S. Walther, M. Voigt, T. Thum, A. Gonsamo, Y. Zhang, P. Köhler, M. Jung, A. Varlagin, and L. Guanter. Satellite chlorophyll fluorescence measurements reveal large-scale decoupling of photosynthesis and greenness dynamics in boreal evergreen forests. *Global change biology*, 22(9):2979–2996, 2016. ISSN 13652486. doi: 10.1111/gcb.13200.

B. Wang, Z. Tian, W. Zhang, G. Chen, Y. Guo, and M. Wang. Retrieval of Green-up Onset Date from MODIS Derived NDVI in Grasslands of Inner Mongolia. *IEEE Access*, 7:77885–77893, 2019. ISSN 21693536. doi: 10.1109/ACCESS.2019.2922003.

J. A. Wang and M. A. Friedl. The role of land cover change in Arctic-Boreal greening and browning trends. *Environmental Research Letters*, 14(12):125007, 2019. ISSN 17489326. doi: 10.1088/1748-9326/ab5429.

X. Wang, J. M. Chen, and W. Ju. Photochemical reflectance index (PRI) can be used to improve the relationship between gross primary productivity (GPP) and sun-induced chlorophyll fluorescence (SIF). *Remote Sensing of Environment*, 246:111888, Sept. 2020. ISSN 0034-4257. doi: 10.1016/j.rse.2020.111888.

Y. Wang and C. Frankenberg. On the impact of canopy model complexity on simulated carbon, water, and solar-induced chlorophyll fluorescence fluxes. *Biogeosciences*, 19(1): 29–45, Jan. 2022. ISSN 1726-4170. doi: 10.5194/bg-19-29-2022.

Y. Wang, R. K. Braghiere, M. Longo, A. J. Norton, P. Köhler, R. Doughty, Y. Yin, A. A. Bloom, and C. Frankenberg. Modeling Global Vegetation Gross Primary Productivity, Transpiration and Hyperspectral Canopy Radiative Transfer Simultaneously Using a Next Generation Land Surface Model—CliMA Land. *Journal of Advances in Modeling Earth Systems*, 15(3):e2021MS002964, 2023. ISSN 1942-2466. doi: 10.1029/2021MS002964.

M. A. White, K. M. De BEURS, K. Didan, D. W. Inouye, A. D. Richardson, O. P. Jensen, J. O'keefe, G. Zhang, R. R. Nemani, W. J. D. Van LEEUWEN, J. F. Brown, A. De WIT, M. Schaepman, X. Lin, M. Dettinger, A. S. Bailey, J. Kimball, M. D. Schwartz, D. D. Baldocchi, J. T. Lee, and W. K. Lauenroth. Intercomparison, interpretation, and assessment of spring phenology in North America estimated from remote sensing for 1982–2006. *Global Change Biology*, 15(10):2335–2359, 2009. ISSN 1365-2486. doi: 10.1111/j.1365-2486.2009.01910.x.

M. Wisniewski, L. Gusta, and G. Neuner. Adaptive mechanisms of freeze avoidance in plants: A brief update. *Environmental and Experimental Botany*, 99:133–140, 2014. ISSN 00988472. doi: 10.1016/j.envexpbot.2013.11.011.

C. Y. Wong and J. A. Gamon. Three causes of variation in the photochemical reflectance index (PRI) in evergreen conifers. *New Phytologist*, 206(1):187–195, 2015a. ISSN 14698137. doi: 10.1111/nph.13159.

C. Y. Wong and J. A. Gamon. The photochemical reflectance index provides an optical indicator of spring photosynthetic activation in evergreen conifers. *New Phytologist*, 206 (1):196–208, 2015b. ISSN 14698137. doi: 10.1111/nph.13251.

C. Y. Wong, L. M. Mercado, M. A. Arain, and I. Ensminger. Remotely sensed carotenoid dynamics improve modelling photosynthetic phenology in conifer and deciduous forests. *Agricultural and Forest Meteorology*, 321:108977, June 2022. ISSN 01681923. doi: 10.1016/J.AGRFORMET.2022.108977.

J. Wu, D. Guan, F. Yuan, A. Wang, and C. Jin. Soil Temperature Triggers the Onset of Photosynthesis in Korean Pine. *PLoS ONE*, 8(6):e65401, 2013. ISSN 19326203. doi: 10.1371/journal.pone.0065401.

T. Wutzler, A. Lucas-Moffat, M. Migliavacca, J. Knauer, K. Sickel, L. Šigut, O. Menzer, and M. Reichstein. Basic and extensible post-processing of eddy covariance flux data with REddyProc. *Biogeosciences*, 15(16):5015–5030, 2018. ISSN 17264189. doi: 10.5194/bg-15-5015-2018.

J. Xiao, F. Chevallier, C. Gomez, L. Guanter, J. A. Hicke, A. R. Huete, K. Ichii, W. Ni, Y. Pang, A. F. Rahman, G. Sun, W. Yuan, L. Zhang, and X. Zhang. Remote sensing of the terrestrial carbon cycle: A review of advances over 50 years. *Remote Sensing of Environment*, 233:111383, Nov. 2019. ISSN 00344257. doi: 10.1016/j.rse.2019.111383.

H. Yang, X. Yang, M. Heskel, S. Sun, and J. Tang. Seasonal variations of leaf and canopy properties tracked by ground-based NDVI imagery in a temperate forest. *Scientific Reports*, 7(1), 2017. ISSN 20452322. doi: 10.1038/s41598-017-01260-y.

J. C. Yang, T. S. Magney, D. Yan, J. F. Knowles, W. K. Smith, R. L. Scott, and G. A. Barron-Gafford. The Photochemical Reflectance Index (PRI) Captures the Ecohydrologic Sensitivity of a Semiarid Mixed Conifer Forest. *Journal of Geophysical Research: Biogeosciences*, 125(11):e2019JG005624, 2020. ISSN 2169-8961. doi: 10.1029/2019JG005624.

J. C. Yang, T. S. Magney, L. P. Albert, A. D. Richardson, C. Frankenberg, J. Stutz, K. Grossmann, S. P. Burns, B. Seyednasrollah, P. D. Blanken, and D. R. Bowling. Gross primary production (GPP) and red solar induced fluorescence (SIF) respond differently to light and seasonal environmental conditions in a subalpine conifer forest. *Agricultural and Forest Meteorology*, 317:108904, Apr. 2022. ISSN 0168-1923. doi: 10.1016/J.AGRFORMET.2022.108904.

X. Yang, J. Tang, J. F. Mustard, J. E. Lee, M. Rossini, J. Joiner, J. W. Munger, A. Kornfeld, and A. D. Richardson. Solar-induced chlorophyll fluorescence that correlates with canopy photosynthesis on diurnal and seasonal scales in a temperate deciduous forest. *Geophysical Research Letters*, 42(8):2977–2987, 2015. ISSN 19448007. doi: 10.1002/2015GL063201.

Y. Zeng, G. Badgley, B. Dechant, Y. Ryu, M. Chen, and J. A. Berry. A practical approach for estimating the escape ratio of near-infrared solar-induced chlorophyll fluorescence. *Remote Sensing of Environment*, 232(July):111209, 2019. ISSN 00344257. doi: 10.1016/j.rse.2019.05.028.

Y. Zeng, D. Hao, A. Huete, B. Dechant, J. Berry, J. M. Chen, J. Joiner, C. Frankenberg, B. Bond-Lamberty, Y. Ryu, J. Xiao, G. R. Asrar, and M. Chen. Optical vegetation indices for monitoring terrestrial ecosystems globally. *Nature Reviews Earth & Environment*, May 2022. ISSN 2662-138X. doi: 10.1038/s43017-022-00298-5.

X. Zhang, M. A. Friedl, C. B. Schaaf, A. H. Strahler, J. C. F. Hodges, F. Gao, B. C. Reed, and A. Huete. Monitoring vegetation phenology using MODIS. *Remote Sensing of Environment*, 84(3):471–475, Mar. 2003. ISSN 0034-4257. doi: 10.1016/S0034-4257(02)00135-9.

R. Zweifel. Radial stem variations – a source of tree physiological information not fully exploited yet. *Plant, Cell & Environment*, 39(2):231–232, 2016. ISSN 1365-3040. doi: 10.1111/pce.12613.

R. Zweifel and R. Häsler. Frost-induced reversible shrinkage of bark of mature subalpine conifers. *Agricultural and Forest Meteorology*, 102(March):213–222, 2000.

R. Zweifel and R. Häsler. Dynamics of water storage in mature subalpine Picea abies: temporal and spatial patterns of change in stem radius. *Tree Physiology*, 21(9):561–569, June 2001. ISSN 0829-318X. doi: 10.1093/treephys/21.9.561.

R. Zweifel, W. Eugster, S. Etzold, M. Dobbertin, N. Buchmann, and R. Häsler. Link between continuous stem radius changes and net ecosystem productivity of a subalpine Norway spruce forest in the Swiss Alps. *New Phytologist*, 187(3):819–830, 2010. ISSN 0028646X. doi: 10.1111/j.1469-8137.2010.03301.x.

R. Zweifel, M. Haeni, N. Buchmann, and W. Eugster. Are trees able to grow in periods of stem shrinkage? *New Phytologist*, 211(3):839–849, 2016. ISSN 14698137. doi: 10.1111/nph.13995.